Technical University of Munich
TUM School of Engineering and Design

Structural Loads of a Mach-Scaled Rotor in Dynamic Stall – An Experimental Hover Analysis

Verena M. Heuschneider

Vollständiger Abdruck der von der TUM School of Engineering and Design der Technischen Universität München zur Erlangung eines

Doktors der Ingenieurwissenschaften (Dr.-Ing.)

genehmigten Dissertation.

Vorsitz:	Prof. Dr. Ilkay Yavrucuk
Prüfende der Dissertation:	1. Prof. Dr.-Ing. Manfred Hajek 2. Prof. Jayant Sirohi, Ph.D. 3. apl. Prof. Dr.-Ing. Christian W. M. Breitsamter

Die Dissertation wurde am 18.03.2024 bei der Technischen Universität München eingereicht und durch die TUM School of Engineering and Design am 24.06.2024 angenommen.

Kurzfassung

Der dynamische Strömungsabriss ist ein instationäres, aerodynamisches Phänomen, das an hochbelasteten Hubschrauberrotorblättern auftritt. Mit diesem Phänomen sind hohe Vibrationen und Strukturlasten verbunden, die den Hubschrauberbetrieb im Vorwärts- und Manöverflug einschränken. Trotz zahlreicher experimenteller und numerischer Untersuchungen in der Vergangenheit fehlt noch immer ein tiefgehendes Verständnis über Strömungsmorphologie und Parameterabhängigkeiten dieses komplexen Phänomens. Ziel dieser Arbeit ist es, den Einfluss der Rotorsteuergrößen – Drehzahl, kollektiver und zyklischer Einstellwinkel – auf dynamische Strömungsablösung an einem rotierenden, aufnickenden Rotorblatt zu untersuchen und daraus Interessensbereiche für weitergehende Forschung abzuleiten. Dieses Ziel wird erreicht durch eine experimentelle Untersuchung des instationären aerodynamischen Phänomens an einem Mach-skalierten Rotor im Schwebeflug mit Hilfe von Blattwurzelmomenten und Steuerstangenkräften.
Für diese Analyse wurde ein Rotorprüfstand entwickelt, der im dynamischen Strömungsabriss sowohl in Schwebe- als auch Vorwärtsflugbedingungen betrieben werden kann. Der untersuchte Rotor umfasst zwei Rotorblätter. Jedes Rotorblatt hat einen gelenklosen Blattanschluss, einen rechteckigen Grundriss und das NACA0012-Profil mit einer 0° Quetschkante. Dieser experimentelle Aufbau ermöglicht den Vergleich von Strömungsablösungsdaten eines rotierenden, aufnickenden Blattes mit bereits veröffentlichten Daten eines aufnickenden Profils im Windkanal.
Die Rotorexperimente in dieser Arbeit konzentrieren sich auf verschiedene Strömungsablösungsfälle mit variierenden kollektiven und zyklischen Einstellwinkeln: $14, 16, 18, 20^\circ \pm 6^\circ$ und $14^\circ \pm 4, 5, 6, 7, 8, 9, 10^\circ$. Die Strukturlasten während der dynamischen Strömungsablösung werden mit den entsprechenden Lasten der statischen Ablösungspolare verglichen. Statische und dynamische Strömungsablösung werden bei jeweils drei verschiedenen Rotordrehzahlen gemessen und analysiert: 900, 1200 und 1500 U/min. Die höchste Drehzahl geht mit folgenden Mach- und Reynoldszahlen an der Blattspitze einher: $Ma_{tip} = 0.41$ und $Re_{tip} = 1.2 \cdot 10^6$. Die gemessenen Schub- und Leistungspolaren werden mit Hilfe eines elastischen Rotormodells validiert.
Die Analyse der Auswirkungen der Parameter kollektiver Einstellwinkel, zyklischer Einstellwinkel und Drehzahl auf die Strukturlasten zeigt einen klar zunehmenden Trend. Im Speziellen weisen der zyklische Einstellwinkel und die Drehzahl einen linearen Zusammenhang mit Lasterhöhung, Lastspanne, und Hysterese des Schlagmoments auf. Darüber hinaus haben Drehzahl und zyklisches Steuer den stärksten sowie einen bilinearen Einfluss auf Schwenkmoment, Torsion und Steuerstangenkräfte.
Lastvariationen zwischen Rotorumläufen mit Bifurkation treten in zwei von zehn Fällen dynamischer Strömungsablösung bei moderaten kollektiven Blatteinstellwinkeln auf. In diesen Fällen beschränkt sich die Bifurkation nicht nur auf die Bereiche von Ablösung und Wiederanliegen der Strömung, vor allem beim Schwenkmoment.
Der eigens entwickelte und für dynamische Strömungsablösung konfigurierte Rotorprüfstand ist eine Forschungsplattform für phänomenologische Untersuchungen verschiedener Rotorkonfigu-

rationen, Blattgeometrien und Flugzustände unter Laborbedingungen. Die gezeigten Forschungsergebnisse haben eine wegweisende Funktion für weitere Forschungsarbeiten zu dynamischer Strömungsablösung an Rotoren, da sie auf Bereiche kritischer dynamischer Lasten und unerwarteter Trends hindeuten und damit eine Grundlage für weiterführende Forschungsarbeiten liefern.

Abstract

Dynamic stall is an unsteady aerodynamic phenomenon that occurs on a highly loaded helicopter rotor blade. The vibrations and high structural loads associated with this phenomenon limit the operation of the helicopter in forward and maneuvering flight. Despite numerous experimental and numerical studies in the past, the flow morphology and parameter dependence of this complex phenomenon are not well understood. The objective of this thesis is to investigate the effect of rotor control parameters – rotor speed, collective pitch, and cyclic pitch – on the structural loads of a rotating pitching blade during dynamic stall and to identify areas of interest for future research. This objective is achieved through an experimental investigation of the unsteady aerodynamic phenomenon on a Mach-scaled rotor in hover using the blade root moments and pitch link forces. For this analysis, a rotor test rig has been developed to operate in dynamic stall in hover and forward flight conditions. The investigated rotor contains two blades; each blade has a hingeless blade attachment, a rectangular planform and a NACA0012 0° tab airfoil. This experimental setup allows the comparison of data from the rotating and pitching blade with previously published data from a pitching airfoil during dynamic stall in free-stream conditions.

The rotor experiments in this thesis focus on dynamic stall cases with varying collective and cyclic pitch angles: $14, 16, 18, 20^\circ \pm 6^\circ$ and $14^\circ \pm 4, 5, 6, 7, 8, 9, 10^\circ$. The dynamic stall loads are examined in relation to the corresponding static stall loads. Static and dynamic stall data are measured and analyzed at three different rotor speeds: 900, 1200, and 1500 RPM. The maximum speed implies a corresponding tip Mach number of $Ma_{tip} = 0.41$ and a Reynolds number of $Re_{tip} = 1.2 \cdot 10^6$. The measured thrust and power polars are validated using a numerical elastic rotor model.

The analysis of the effect of the parameters collective pitch, cyclic pitch, and rotor speed on the structural loads shows significant increasing trends. In particular, increasing cyclic pitch and rotor speed show a considerable linear positive trend in the dynamic load overshoot, load range and hysteresis of the flapping moment. Furthermore, the combination of the highest rotor speed (1500 RPM) and high cyclic pitch angles ($\Theta_C \geq 6^\circ$) represents the most significant load increase of lead-lag moment, torsion, and pitch link forces.

Cycle-to-cycle variations with bifurcation occur in two out of the ten selected dynamic stall cases, where moderate mean pitch angles are prevalent. For these cases, bifurcation is not only restricted to the stall onset and reattachment areas, especially in the lead-lag moment.

The specially designed and configured rotor test rig for dynamic stall is a research platform for phenomenological investigations of different rotor configurations, blade shapes and flight states in a laboratory environment. The presented research results have directional implications for dynamic stall research, as they reveal further regions of interest for future work by highlighting areas of critical load dynamics and unexpected trend changes.

Acknowledgments

This work could not have been accomplished without the help and support of various personalities, to whom I owe my sincere gratitude. First of all, I would like to thank my supervisor and doctoral father, Prof. Dr.-Ing. M. Hajek, for his untiring support during the construction of the test rig and throughout the work of this thesis. He has given me room for personal, professional, and technical development and the confidence to make important project-related decisions that have contributed to broadening my horizons and professional development. Prof. Dr. phil. J. Sirohi supported this work with his enriching ability to combine theoretical knowledge with experimental expertise. His willingness and enthusiasm to explain physical phenomena with appropriate theoretical models enriched my work with a more profound understanding and excitement for helicopter theory and experiments in general. Furthermore, I would like to thank my mentor, Prof. Dr.-Ing. S. Greiser, for his professional advice and guidance. His insight and qualified feedback helped me in my development towards publications and scientific discussions. I also want to express my thanks towards Prof. Dr.-Ing. F. Holzapfel for his decisive support in my career choice through a short-term cooperation at his institute, thus giving me an insight into and a passion for aerospace research during my pre-university years. Special thanks go to M. Thieme, the secretary of the institute, who handled the organizational and social matters in a very professional and uplifting way. Her positive and helpful attitude in dealing with challenges has always been encouraging and has always resulted in the best outcome. Colleagues and students have continuously contributed to this work with technical discussions and exchange of critical views, therefore, I express my thanks to Prof. Dr. phil. I. Yavrucuk and the whole team at the Center of Rotorcraft and Vertical Flight.

Additional thanks go to the Laboratory for Product Development and Lightweight Design at the Technical University of Munich, especially L. Krämer, M. Bauer, B. Lerch, and J. Stokic for their fantastic support with installation help, test equipment, and practical advice. The mechanical workshop of the Physics Department of the Technical University of Munich, under the direction of M. Pfaller and M. Reither, has contributed essentially to the manufacturing quality of the mechanical components. In addition, their professional work and expertise have always shortened the machining time in a clever and appropriate way. Furthermore, I thank my colleagues from the Institute of Materials Science and Mechanics of Materials (A. Fillafer, M. Olenberg), the Chair of Carbon Composites (T. Witteczek, R. Rauch), the Chair of Aerodynamics and Fluid Mechanics (C. Breitsamter, W. Lützenburg), and the Chair of Thermodynamics (H. Koller, T. Schleussner, G. Giel), Technical University of Munich, for their continuous support with advice and assistance when needed. Special thanks to D. Maraite and G. Sanow of Carl Zeiss GOM Metrology GmbH for their support in DIC measurement campaigns and data processing.

Last but not least, this thanks goes to my family and friends for their unconditional love and moral support, there is not enough space to mention all of them! Special appreciation goes to Hayford, who has been a mentor, coach, and friend to me in every challenge. Thank you!

Contents

Abbreviations and Symbols

Acronyms

2D	Two-Dimensional
3D	Three-Dimensional
A/D	Analog/Digital
ACT	Actuator
AKD	Advanced Kollmorgen Servo Drive
ANSYS Mechanical	Structural FE Analysis Software
AoA	Angle of Attack
AREA	Autonomous Rotorcraft for Extreme Altitudes
ARO	Army Research Office
BOS	Background Oriented Schlieren
CAD	Computer Aided Design
CAMRAD II	Comprehensive Analytical Model of Rotorcraft Aerodynamics and Dynamics
CFD	Computational Fluid Dynamics
CPL	Telemetry Coupler
cRIO	CompactRIO
CSD	Computational Structural Dynamics
CU	Coupling Unit
DAQ	Data Acquisition
DIC	Digital Image Correlation
DIT	Differential Infrared Thermography
DLR	German Aerospace Center
DMT	Differential Momentum Theory
DS	Dynamic Stall
DYMORE	Finite Element Based Tool for the Analysis of Nonlinear Flexible Multibody Systems
ELAMX^2	Java-Written Composite Calculator
EMA	Experimental Modal Analysis

EN AW	European Norm Aluminum Wrought
ENC	Encoder
ENG	Engine
EtherCAT	Ethernet for Control Automation Technology
FBG	Fiber Bragg Grating
FEM	Finite Element Method
FFT	Fast Fourier Transformation
FPR	Frames per Rotation
FPS	Frames per Second
FS	Full Scale
FU	Frequency Converter Unit
GARTEUR	Group for Aeronautical Research and Technology in EURope
GLMWT	Glenn L. Martin Wind Tunnel
GoAHEAD	Generation of Advanced Helicopter Experimental Aerodynamic Database
HARF	High Advance Ratio Facility
HMI	Human Machine Interface
HS	Hall Sensor
JPDF	Joint Probability Density Function
LC	Load Cell
LED	Light Emitting Diode
LEV	Leading-Edge Vortex
LL	Limit Load
LRTA	Large Rotor Test Apparatus
MAC	Modal Assurance Criterion
MERIT	Munich Experimental Rotor Investigation Testbed
MSL	Mean Sea Level
NACA	National Advisory Committee for Aeronautics
NASA	National Aeronautics and Space Administration
NFAC	USAF National Full-Scale Aerodynamics Complex
ONERA	French National Office for Aerospace Studies and Research
PCMM	Programmable Controller Multi-Axis Master

PDF	Probability Density Function
PH	Pitch Horn
PIV	Particle Image Velocimetry
PL	Pitch Link
POD	Proper Orthogonal Decomposition
PR	Push Rod
PS	Pressure Sensor
PSP	Pressure Sensitive Paint
RANS	Reynolds-Averaged Navier-Stokes
REnc	Rotating Encoder
rev	Revolution
RMSE	Root Mean Square Error
RPM	Revolutions per Minute
RTG	Rotor Test Stand Göttingen
SA	Spalart-Allmaras One-Equation Model
SG	Strain Gauge
SN	Serial Number
SONATA	Structural Optimization and Aeroelastic Analysis Framework
SP	Swashplate
SS	Static Stall
STB	Shake the Box – 3D Lagrangian Particle Tracking at High Particle Densities
STD	Standard Deviation
TAU	Unstructured Computational Fluid Dynamics Solver
TE	Trailing Edge
TPU	Telemetry Processing Unit
TSP	Temperature Sensitive Paint
TTL	Transistor-Transistor Logic
TUM	Technical University of Munich
TW	Twill Weave
UD	Unidirectional Fiber
UL	Ultimate Load
UMD	University of Maryland
URANS	Unsteady Reynolds-Averaged Navier-Stokes
USAF	United States Air Force
UTTAS	Utility Tactical Transport Aircraft System
VABS	Variational Asymptotic Beam Sectional Analysis

WS	Workspace

Symbols

A	Rotor disk area
C	Sutherland constant
C_d	Aerodynamic drag coefficient
C_l	Aerodynamic lift coefficient
C_m	Aerodynamic moment coefficient
$C_{F_{PL,1/2}}$	Non-dimensionalized pitch link force
$C_{M_{\beta,\zeta,\theta},\Delta}$	Dynamic load range between maximum and minimum value of the hysteresis
$C_{M_{\beta,\zeta,\theta},hys}$	Hysteresis area
$C_{M_{\beta,\zeta,\theta},max}$	Dynamic load increase or load overshoot
$C_{M_{\beta,\zeta,\theta}}$	Non-dimensionalized blade flapping, lead-lag, and torsional moments
E	Young's modulus
F_y	Radial blade attachment force
F_{PL}	Axial pitch link force
$F_{y,short}$	Short time lateral hub force
Fz	Rotor thrust
G	Shear modulus
I	Area moment of inertia
I_c	Confidence interval of a data set
I_Θ	Torsional moment of inertia
K	Blade moments calibration matrix
M_T	Rotor torque
M_x	Rotor hub moment
M_Θ	Blade torsion
M_β	Blade flapping moment
M_ζ	Blade lead-lag moment
Ma	Mach number
N	Number of revolutions
O_T	Telemetry amplifier offset
R	Rotor radius
R_T	Telemetry amplifier reduction factor
R_s	Ideal gas constant
$R_{1/2/3/4}$	Full bridge strain gauge resistance
Re	Reynolds number
S_T	Telemetry amplifier sensitivity
T	Air temperature

U_e	Excitation voltage
U_{SG}	Strain gauge bridge detuning voltage
V	Free stream velocity
$\Delta\Psi$	Azimuth delta between pitch axis and pitch horn attachment point
Λ	Sweep angle
Ω	Rotational speed
Ψ	Rotor azimuth
Θ	Blade pitch angle
Θ_0	Collective pitch control angle
Θ_{1C}	Longitudinal 1/rev cyclic pitch control angle
Θ_{1S}	Lateral 1/rev cyclic pitch control angle
Θ_{SS}	Static stall pitch angle
$\Theta_{x,SP}$	Swashplate tilt angle around x-axis of the body frame
$\Theta_{y,SP}$	Swashplate tilt angle around y-axis of the body frame
α	Angle of attack
α_T	Temperature coefficient
β	Blade flapping angle
$\dot{\Theta}_m$	Maximum pitch rate
ε	Strain
ε_y	Normal strain
ε_{xy}	Torsional strain
η	Dynamic viscosity
γ	Lock number
κ	Gas constant
μ	Advance ratio; Mean
ν	Kinematic viscosity
$\nu_{12,13,23}$	Poisson's ratio
ρ	Air density
σ	Rotor solidity ratio; Standard deviation
θ	Blade feathering angle
ζ	Blade lead-lag angle
a	Speed of sound
c	Airfoil chord
c_P	Power coefficient
c_T	Thrust coefficient
e	Error
e_{PH}	Radial pitch horn station
f_A	Nonrotating data sampling frequency
f_T	Rotating data sampling frequency
h_{SP}	Swashplate spherical center height
k	Gauge factor; reduced frequency

k_{PL}	Axial pitch link stiffness
k_{tip}	Reduced frequency at blade tip
l	Short pitch link length
l_{PL}	Rotating pitch link length
m_{Bl}	Blade mass
p	Atmospheric pressure
r	Radial blade station
r_i	Blade's most inner radial position of aerodynamic efficiency
r_{CG}	Blade's radial center of gravity
r_{PH}	Radius of pitch horn attachment point
r_{SG}	Radius of blade moment strain gauges
$r_{SP,i}$	Radius of stationary pitch link attachment point
$r_{SP,o}$	Radius of rotating pitch link attachment point
t	Time
v	Radial speed
v_{tip}	Blade tip speed
x_a	Amplified and corrected bridge detuning voltage
x_d	Digital bridge detuning voltage
x_{PH}	Radius of pitch horn attachment point from pitch axis
$z_{1,2,3}$	Actuator rod positions

List of Figures

List of Tables

1 Introduction

1.1 Problem Statement and Research Questions

Helicopters are unrivaled aerial artists. Their agility and versatility give them a unique edge in certain air missions. However, they are composed of many complex subsystems that require careful attention in design and manufacturing processes, as well as in operation and maintenance. One of the helicopter's most complex systems is the main rotor, which provides lift. In addition to the complexity of the mechanical components associated with a main rotor system, the rotor's aerodynamics are subject to several transient effects that occur during all phases of flight. Due to the helicopter's forward speed, superimposed on the rotor blade's rotational and pitching motion – necessary to direct the rotor thrust in the desired flight direction – each rotor blade experiences unsteady flow conditions and varying Angle of Attack (AoA). These unsteady flow conditions vary with blade radius and rotor azimuth.

According to Leishman [2], there are several sources of unsteady aerodynamic effects that affect blade airloads. They can be divided into two groups: Blade motion and flowfield structure. Blade motion includes controlled collective and cyclic pitch motion, flapping and lead-lag motion, and elastic bending and twisting. The flowfield structure has periodic and aperiodic components. Rotational speed, inflow, and sweep are attributed to the low-frequency, periodic flowfield, while fuselage flow effects, the three-dimensional vortex wake system and distortion, and atmospheric gusts contribute to the high-frequency, aperiodic flowfield, also known as velocity field perturbations [2]. At the blade element level, unsteady airflow conditions (angle of attack and velocity) affect local aerodynamic loads that vary with time, radius, and azimuth. For low angles of attack and attached flow, these perturbations cause air loads with moderate amplitudes and phase variations compared to quasi-steady flow conditions. However, at high angles of attack and unsteady flow separation, *dynamic stall* can occur, a phenomenon accompanied by significant airload increases (lift, drag, and pitch moment), flow hystereses, and cycle-to-cycle variations [30, 32, 33]. On a helicopter rotor, it occurs mainly in flight phases with very high blade loading, such as in fast forward or maneuvering flight. Dynamic stall can lead to severe aeroelastic stability problems and performance degradation, resulting in operational limitations due to high vibration levels, structural load amplitudes, and fatigue problems [34–36]. A comprehensive understanding of dynamic stall on a helicopter rotor is essential for reliable load prediction in the early stages of rotor design. The ability to predict and eliminate dynamic stall from the flight envelope is necessary to improve safety standards and incorporate it into new designs [37].

Over the past few decades, numerous experimental and numerical studies have been conducted on pitching airfoils undergoing dynamic stall in the wind tunnel. Early investigations focused on understanding the flow physics and the sensitivity of the phenomenon to flow parameters – such as Reynolds number, Mach number, AoA mean and range – as well as various parameters describing the airfoil motion – pitching, heaving, and lagging, without accounting for rotational and three-dimensional flow effects, such as radial flow, the effect of coriolis forces, and the interaction of the dynamic stall vortex with the blade tip vortex. Recent experimental studies have increasingly focused on flow visualization to understand stall events, as well as surface pressure measurements to determine stall onset areas and provide validation data for Computational Fluid Dynamics (CFD) simulations. On the one hand, these measurements provide an insight into local unsteady flow effects, which is helpful for code validation purposes and for detecting and tracing stall mechanisms; on the other hand, these investigations can lead to an over-interpretation of local unsteady flow phenomena, which may still have a minor impact on the effective, integrated structural loads. Given the history of dynamic stall investigations, the research question that arises here is the following:

How do the load trends and unsteady effects observed on pitching airfoils translate to a rotating pitching blade under three-dimensional flow conditions in dynamic stall?

Three sub-questions are embedded in this central research question and need to be answered in this thesis:

1. *How does rotor speed affect the load dynamics of a rotating pitching airfoil in Three-Dimensional (3D) flow conditions during dynamic stall?*
2. *How do collective and cyclic pitch angles affect the load dynamics of a rotating pitching airfoil in 3D flow conditions during dynamic stall?*
3. *To what extent do cycle-to-cycle variations of local aerodynamic loads affect integrated structural loads of a rotating pitching airfoil during dynamic stall?*

Before defining the objective of this thesis and approach to answer these questions, the following two sections provide a deeper insight into the flow morphology of the dynamic stall phenomenon and the state of the art of experimental dynamic stall research.

1.2 Dynamic Stall Flow Morphology

According to the definition of McCroskey et al. [38, 39], dynamic stall occurs on any lifting surface when it is subjected to time-dependent, unsteady movements, like pitching or plunging, that results in an effective angle of attack above its normal static stall angle and a rapid angle of attack change in the static stall angle region. It is accompanied by complex flow separation mechanisms including shear layers and vortices interacting with one another and with the lifting surface. The resulting effects are highly dynamic airloads, that exceed static flow load maxima by far.

As mentioned above, a helicopter rotor blade experiences complex flow conditions, especially in maneuvering and fast forward flight. While the advancing blade operates at high Mach numbers and low angle of attack – therefore close to its shock induced flow separation boundary – the retreating blade experiences significantly lower Mach numbers at higher angles of attack close to stall. In addition, each rotor blade performs low-frequency and high-frequency pitch, flapping, and lead-lag motion, and interacts with discrete blade vortices and shed rotor wakes. These interactions lead to highly unsteady flow conditions within the rotor disk. Moreover, aeroelasticity can have a significant influence on locus, form and strength of dynamic stall. The following section explains in more detail how unsteady aerodynamics affect airfoil behavior, to promote a better understanding of dynamic stall formation and mechanisms.

Unsteady effects on airfoil behavior

The physics of dynamic flow separation differ substantially from those under static or quasi-steady conditions. When compared to static flow separation, dynamic flow separation is characterized by a delay of stall onset to higher angles of attack. It is usually accompanied by leading-edge vortex shedding and vortex sweep over the chord towards the airfoil's trailing edge. This causes a rapid aft movement of the center of pressure and a large nose-down pitching moment. These airload nonlinearities can cause critically high control loads, vibrations, and structural loads. In particular, high blade torsion loads are of concern as they may cause structural fatigue and damage, and degrade the control and handling qualities of a helicopter [40].

According to Leishman [2], there are three main effects of unsteady motion on unsteady airfoil behavior, which lead to dynamic and delayed flow separation:

1. The flow unsteadiness resulting from alternating circulation (induced by the blade's pitching motion), which is shed into the wake at the airfoil's trailing edge. This shedding causes reduction in lift and adverse pressure gradients when compared to the steady case at the same angle of attack.

2. The kinematic induced camber effect due to a positive pitch rate, which leads to a decrease in leading edge pressure and pressure gradients for a given value of lift.

3. Unsteady boundary layer effects such as flow reversal without significant large-scale flow separation.

These unsteady effects play a major role in the dynamic stall mechanism on an airfoil. They delay stall onset, flow separation, and flow reattachment. The various stages of a classic dynamic stall process are explained in the following.

Dynamic Stall Process

According to state-of-the-art research, there are three different dynamic stall mechanisms or a combination thereof: leading-edge separation, trailing-edge separation, and shock-induced separation. They vary depending on free stream Reynolds number and reduced frequency. The reduced frequency is a parameter commonly used to characterize unsteadiness of flow conditions related to dynamic stall. It is associated with the pitch rate and free-stream velocity [37].

Leading-edge stall is accompanied by a Leading-Edge Vortex (LEV) and is most common on helicopter rotor airfoils, such as the NACA 0012 airfoil. Moreover, dynamic stall events are strongly dependent on airfoil geometries. There are different stall types that were detected with hot-wire anemometer probes by Carr et al. [1, 41] dependent on the airfoil geometry: Trailing-edge stall on a cambered airfoil, leading-edge bubble bursting stall on a sharp leading-edge airfoil, and turbulent leading-edge stall on the NACA 0012 airfoil, which is a modified form of the leading-edge stall due to its abrupt turbulent leading-edge separation.

According to Leishman [2], the flow morphology of the dynamic stall phenomenon, which is associated with turbulent leading-edge separation, can be described in five stages using the example of an oscillating airfoil, see Fig. 1.1:

1. The airfoil strokes upward under unsteady attached flow conditions, while the nose-up pitch rate kinematics induce a virtual camber reduction. As soon as the static stall angle is exceeded, flow reversal in the boundary layer occurs. The onset of flow separation is delayed as a result of a reduction in adverse pressure gradients, the shed wake influence, and the unsteady boundary layer response.

2. Flow separation and vortex disturbance develop near the leading edge. This shear layer instability generates small-scale vortices with increasing interaction and a subsequent shear layer roll-up into a large-scale vortex, that sweeps over the upper profile surface towards the trailing edge. During this process, the global airfoil flow shows no significant separation characteristics. According to Mulleners et al. [3], dynamic stall onset is marked by primary stall vortex detachment due to vortex-induced separation. Lift increases far beyond maximum static lift (50 to 100% static lift increase), as long as the vortex stays over the upper surface. Simultaneously, a significant increase of nose-down pitch moment occurs due to the rapid aft movement of the center of pressure (moment stall).

3. The vortex reaches the trailing edge and passes into the wake downstream, which marks the onset of lift stall, while pressure drag and nose-down pitching moment reach their maximum values.

4. After the vortex passes the trailing edge, flow conditions on the upper airfoil surface develop into full separation.

5. The flow reattachment is delayed until angles of attack far below the static stall angle because of flow reorganization and a reverse induced camber effect (due to the dynamic pitch-down movement).

The mentioned delays in stall onset and flow reattachment cause significant hystereses in all three airload coefficients, which can cause reduced aerodynamic damping and aeroelastic stability problems. As there are many parameters that influence the development and process of dynamic stall, a broad and reliable experimental database is necessary to detect trends and correlations and to understand the phenomenon and increase prediction capability. The number of research efforts in the last decades shows the phenomenon's complexity and investigation potential it offers.

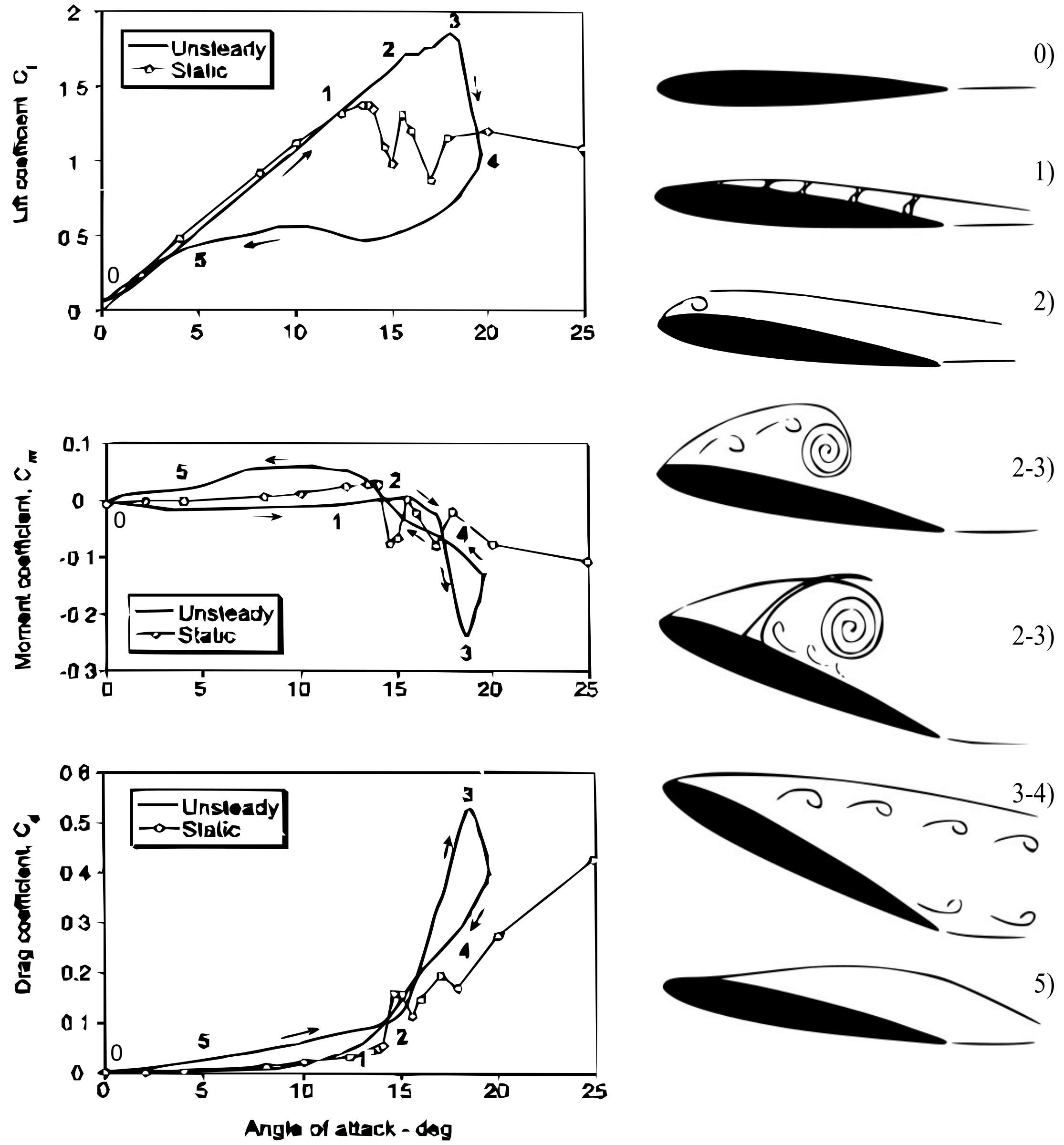

Figure 1.1: Dynamic stall flow morphology in five stages, adapted from Carr [1], Leishman [2], and Mulleners [3]

1.3 Current State of Experimental Dynamic Stall Research

Dynamic stall is dependent on a variety of parameters and conditions, especially in rotorcraft environments. Its complexity and nonlinear behavior have been the focus in experimental and computational helicopter research for more than the last five decades. Due to the large amount of published research within the last century, there have been several early literature reviews in the past on developments in dynamic stall analysis [2,37,42–46]. Smith et al. [37,46] and Gardner et al. [47] provided an extensive summary on recent dynamic stall research, which resulted from the 2019 Army Research Office (ARO) dynamic stall workshop at the Georgia Institute of Technology. It covers the current research status of understanding, predicting, and controlling dynamic stall with a focus on future directions.

The following sections focus on the current state of experimental dynamic stall research together with their results that are most relevant for this thesis. Most of the published experimental studies vary widely in the setup and quality of measurements. They range from two-dimensional tests on airfoil sections to three-dimensional finite wings undergoing various kinematic motions or free stream flow with different ranges of Reynolds and Mach numbers, scaled rotating blade experiments, and fully instrumented flight tests.

Pitching Airfoil

The unsteady phenomenon of dynamic stall was initially observed in the 1920s and 1930s on wing airfoils undergoing gusts and on autogiro rotor blades in flight [48–51]. The initial detection of a correlation between lift increase of an airfoil and unsteady change in angle of attack led to a large set of two-dimensional dynamic stall experiments on oscillating airfoils under different flow conditions, environmental parameters, airfoil shapes and motion, ranging from the late 1960s to the mid 1990s, see e.g. Liiva [52–54], Gray [55], Carr [5,6,45,56], Chandrasekhara [57,58], McAlister [41,59], McCroskey [39,42,60–63], Scruggs [64], Lorber [65], Carta [66], Martin [67], and Piziali [68]. The oscillating airfoils were predominantly examined in a sinusoidal pitching movement, but also in sweeping or plunging motion. Most recent pitching airfoil investigations made use of high-quality measurement equipment and visualization techniques, such as [3,69–75], adding substantial value to the understanding of the dynamic stall vortex formation.

Previous experiments cover a broad variety of airflow parameters, such as reduced frequency (k), Reynolds number (Re), and Mach number (Ma) to create different unsteady flow conditions. The reduced frequency k is a dimensionless parameter that describes the degree of unsteadiness for a certain flow condition around a lifting surface. It is defined to be

$$k = \frac{\omega c}{2V} \tag{1.1}$$

with the airfoil section's chord c, the angular (pitching) frequency ω, and the free stream flow velocity V. The reduced frequency is used as a standard parameter to correlate dynamic stall data. It changes with the radius of a rotor blade and needs to be considered for all elastic and rigid body blade motions (pitch, flap, lead-lag). For $0 \leq k \leq 0.05$ the flow is considered quasi-steady (small, often negligible unsteady effects), whereas values above $k = 0.05$ describe unsteady flow. For $k > 0.2$, an aerodynamic problem is considered highly unsteady [2].

Among others, the two-dimensional pitching airfoil experiments of McCroskey et al. contributed to a fundamental understanding of the dynamic stall process for low Re numbers ($Re \ll 500,000$) and incompressible flow. They explained different stages of this process, like leading-edge flow separation, vortex shedding, stall delay, and reattachment delay, specifically for the NACA 0012 airfoil. Carr et al. delivered a seminal study on the effects of the parameters reduced frequency, Mach number, Reynolds number, mean angle of attack, and pitch range on various airfoils, including the NACA 0012. The most relevant findings are summarized in the following sections. Since the airfoil shape has a strong influence on dynamic stall events and type of stall, the following sections are restricted to parameter studies on the NACA 0012 airfoil, which is used in this thesis.

Influence of Reduced Frequency The reduced frequency of a pitching airfoil has a major impact on dynamic stall behavior and aerodynamic loads. Increasing the reduced frequency delays stall onset and flow reattachment and leads to a strong overshoot in the normal force and pitching moment, see deep stall example in Fig. 1.2, [1].

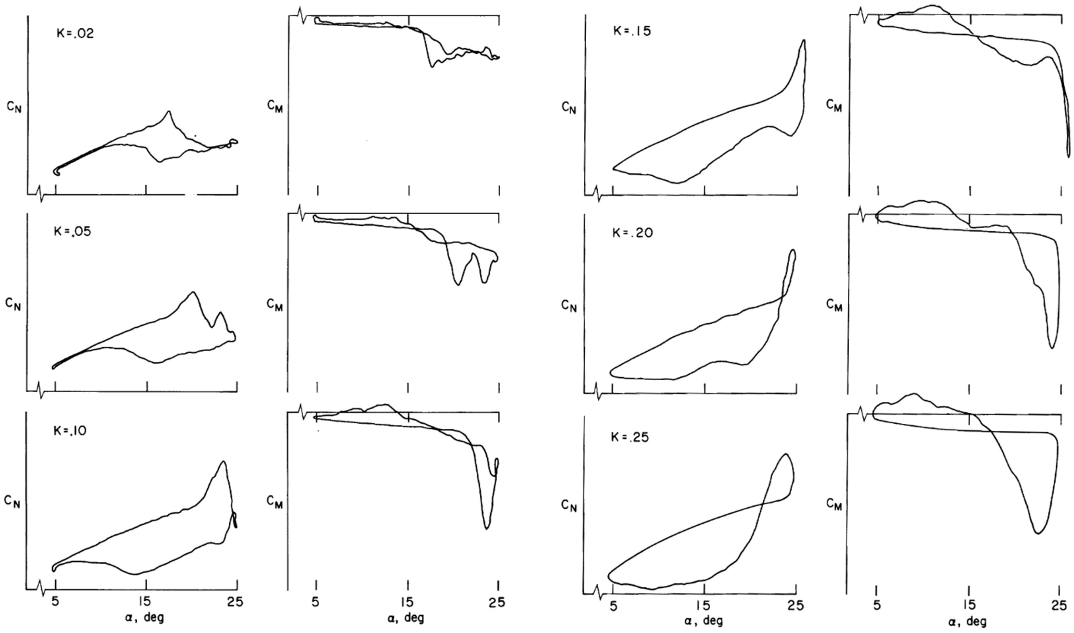

Figure 1.2: Normal force and pitching moment on the NACA 0012 airfoil at $\alpha = 15° \pm 10°$ and $Re = 2.5 \times 10^6$ for varying reduced frequencies $k = 0.02, 0.05, 0.10, 0.15, 0.20, 0.25$ [1], equal scales

At lower frequencies (k = 0.02 - 0.05), the vortex sheds before the maximum angle of attack, whereas at higher frequencies, vortex interactions at higher angles of attack occur even to the extent that lift still increases for a short decreasing angle of attack period (observed at $k \geq 0.2$).

Measurements at higher Mach number show that the reduced frequency has an upper limit to the time rate of change of circulation on the airfoil [52], because sudden stalling, that appears at lower frequency, does not occur at the high frequency. Nevertheless, significant stall onset delay can be observed.

More recent pitching airfoil tests by Wei et al. [4] were performed on the NACA 0012 airfoil at a Reynolds number of $Re = 1.5 \cdot 10^6$ using experimental and numerical methods for reduced frequencies of $k = 0.035, 0.05, 0.1$ and at $\alpha = 15 \pm 10^\circ$, see Fig. 1.3. Increasing reduced frequency increases the strength of the dynamic stall vortex. This stronger vortex increases load peaks and delays stall onset and flow reattachment. These results confirm the experimental findings of Carr et al. [1].

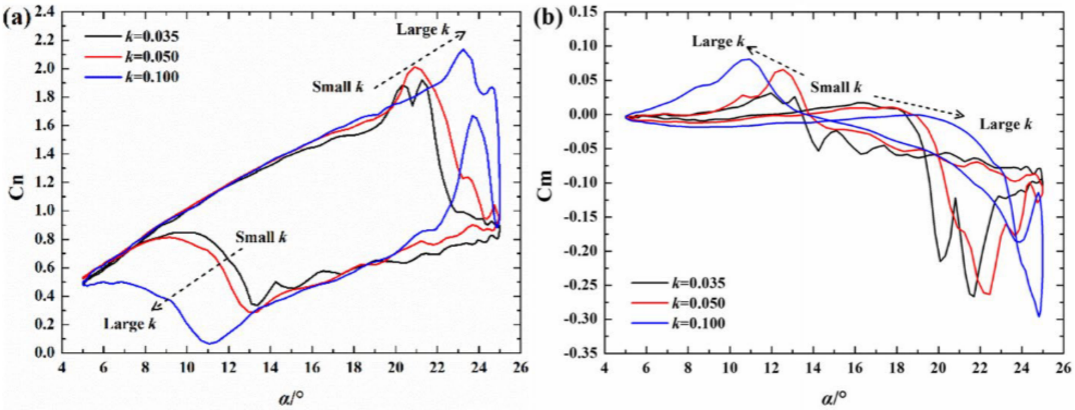

Figure 1.3: Experimental aerodynamic normal force and moment coefficient during dynamic stall on a pitching NACA 0012 airfoil at $Re = 1.5 \cdot 10^6$, $\alpha = 15 \pm 10^\circ$ and for reduced frequencies of $k = 0.035, 0.03, 0.1$ [4]

Influence of Mach Number Dynamic stall in high-speed flow conditions ($Ma > 0.3$) is often characterized by shock-induced stall with a shedding of several vortices instead of a single large vortex. Liiva [54] observed a possible prevention of vortex-shedding due to the formation of shock waves on the airfoil's upper surface at $Ma = 0.6$. It is noted that even at relatively low free-stream Mach numbers, supersonic flow can develop near the leading edge of an airfoil at high angles of attack. Nevertheless, transonic shock-wave formation seems to play no major role up to $Ma = 0.35$. However, the impact of shock-induced separation on vortex-shedding during dynamic stall is a topic that is not extensively investigated. Fig. 1.4 shows that the dynamic stall vortex location is moved aft with increasing Mach number, although the effect is minor for low-speed conditions ($Ma \leq 0.3$).
Chandrasekhara showed in [58] that compressibility effects on dynamic stall set in at a free stream Mach number of $Ma = 0.3$. Beyond this value, the dynamic stall process is initiated at lower angles of attack and the maximum attainable lift coefficient decreases with increasing Mach number, as shown in [5, 76], see Fig. 1.4. Moreover, studies by Carr and Chandrasekhara conclude that

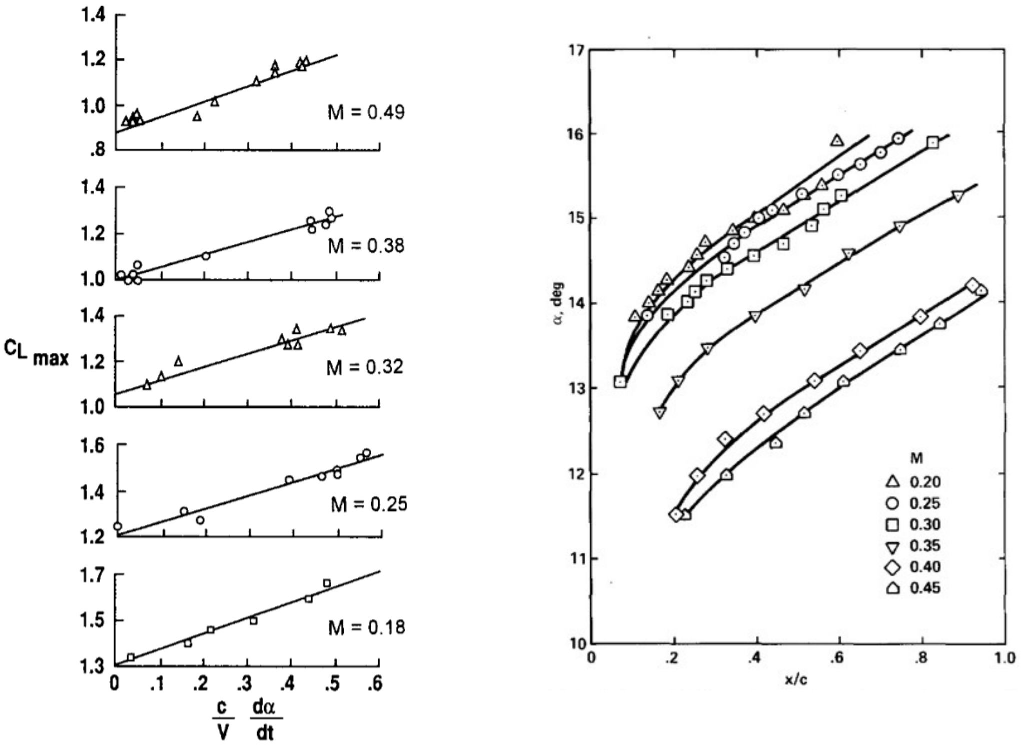

(a) Maximum attainable lift coefficient as a function of non-dimensional pitch rate at various Ma numbers [5]

(b) Effect of Ma number on the position of the dynamic stall vortex with varying angle of attack at $k = 0.05$ [6]

Figure 1.4: Effect of Ma number on dynamic stall vortex location and maximum attainable lift [5, 6]

compressibility effects have been observed over a wide range of Reynolds numbers [5].
In contrast to the Mach effect, an increase in reduced frequency delays stall onset, even under compressible conditions [58], and increases maximum lift coefficient. Therefore, Mach number and reduced frequency have opposite effects on stall timing and maximum lift.

Influence of Reynolds Number In low-speed conditions, dynamic stall is accompanied by small-scale, upper-surface boundary layer vortices, which roll up into a single large-scale coherent structure known as leading-edge vortex. The LEV introduces leading-edge flow separation, see the aforementioned description of the dynamic stall process, and produces a rapid lift drop and a large hysteresis. In contrast to low-speed stall, studies at higher Reynolds numbers ($Re \gg 500{,}000$), see [77–79], show a transition from trailing-edge stall with slow lift roll-off at low reduced frequencies to leading-edge stall with sharp lift roll-off at higher reduced frequencies [46].

The results of Carr et al. [1], see Fig. 1.5 (b), show a weak dependence of airloads on Reynolds number for low reduced frequency ($k = 0.004$). Observed Reynolds effects are a slight stall overshoot and hysteresis increase – which is mainly caused by a delay in flow reattachment – with

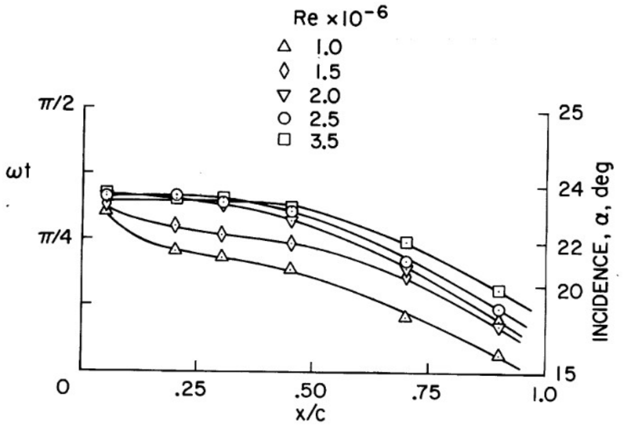

(a) Locus of flow reversal on the NACA 0012 airfoil for varying Reynolds numbers $Re = 1.0,\dots,3.5 \times 10^6$, $\alpha = 15^\circ \pm 10^\circ$, and $k = 0.15$ [1]

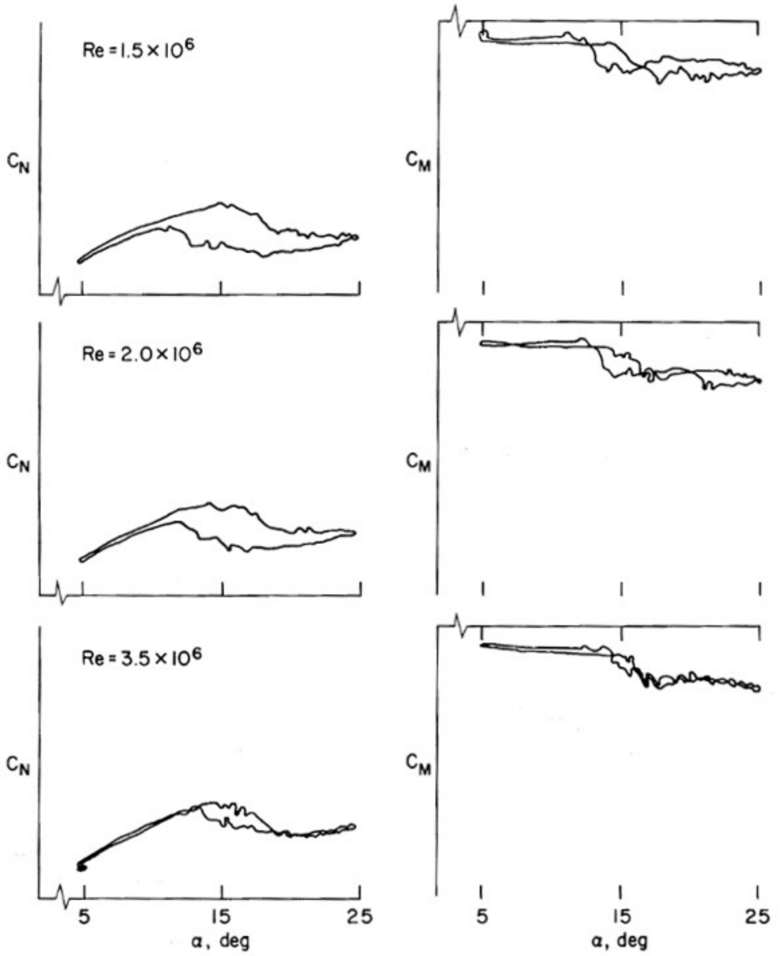

(b) Normal force and pitching moment on the NACA 0012 airfoil at $k = 0.004$ and $\alpha = 15^\circ \pm 10^\circ$ for varying Reynolds numbers $Re = 1.5, 2.0, 3.5 \times 10^6$ [1]

Figure 1.5: Influence of Reynolds number on normal force and pitching moment as well as flow reversal locus on the NACA 0012 airfoil

increasing Re numbers. The effects of Reynolds number on flow reversal position at $k = 0.15$ are shown in Fig. 1.5 (a). For higher Reynolds numbers, flow reversal on the rear of the airfoil is delayed as a function of Reynolds number [1].

Influence of Mean Angle of Attack and Pitch Range According to the experimental investigations of Carr et al. [1], normal force and pitching moment show the characteristic elliptical shapes predicted by unsteady airfoil theory in the pre-stall region, i.e. for low mean angles of attack. As the mean angle of attack increases into the stall onset region, a substantial increase in hysteresis and maximum normal force are observed.

Besides the mean angle of attack, the pitch amplitude has a significant impact on dynamic stall, because it directly influences the time derivative of the angle of attack $\dot{\alpha}$ and is therefore another parameter that describes the unsteadiness of the phenomenon. Fig. 1.6 shows three dynamic stall cases with the same mean angle of attack but increasing pitch amplitude at the same reduced frequency $k = 0.15$ and Reynolds number $Re = 2.5 \times 10^6$. A change in oscillation amplitude can be seen in strength and timing of the dynamic stall vortex. The vortex sheds at the maximum angle of oscillation and causes a milder stall due to early shedding of the weaker vortex at 6° pitch range. Therefore, a change in pitch direction precipitates the stall [1]. For 10° and 14° pitch range, no stall delay was observed for the given reduced frequency. The magnitude of damping at stall is highly influenced by the oscillation amplitude. In the deep stall case ($\Delta\alpha = 14^\circ$), the pitching moment shows areas of positive and negative damping.

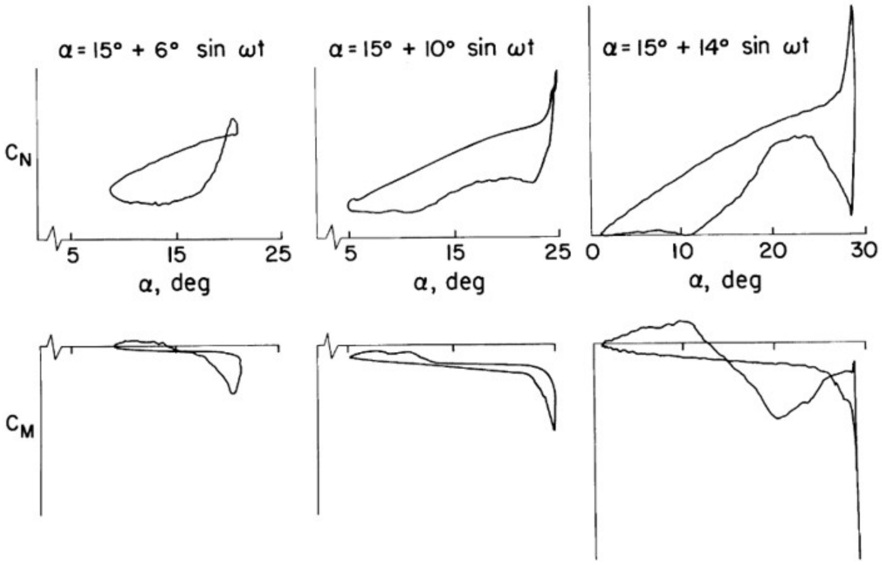

Figure 1.6: Normal force and pitching moment on the NACA 0012 airfoil at $k = 0.15$ and $Re = 2.5 \times 10^6$ for varying pitch amplitude $\alpha = 15^\circ \pm 6, 10, 14^\circ$ [1]

Pitching Finite Wing

In general, stall mechanisms resulting from two-dimensional pitching airfoil tests show different behavior than under three-dimensional effects. With regard to rotor environments, 3D effects, such as radial flow, vortex interaction, and Coriolis effects, play a major role in flow separation mechanisms and dynamic stall airloads. Since measurement techniques have improved significantly within the last two decades, an increasing number of high-resolution validation data has been obtained to experimentally analyze three-dimensional effects. Furthermore, the increase in computational potential beginning in the 1990s facilitated the application of high-fidelity CFD computations on three-dimensional rotor dynamic stall.
A first step to introduce three-dimensional effects to dynamic stall was to investigate pitching finite wings. These experiments were particularly interesting for initial CFD code validation, because they included three-dimensional flow and unsteady effects, which emerge from wing tip interactions, but have a lower level of complexity when compared to a rotating blade.

Lorber et al. [7, 80–82], Coton et al. [83–85], and Piziali [68] experimentally investigated pitching finite wings and compared their data to the extensively pursued, classic two-dimensional dynamic stall experiments. Some of their findings were consistent with pitching two-dimensional airfoil tests. The results of Lorber et al. in [65, 80] provided the first known database of three-dimensional aerodynamic information on a pitching finite wing at realistic combinations of Reynolds and Mach numbers as they occur on helicopters. They observed that despite of three-dimensional flow conditions, the dynamic stall vortex is qualitatively similar to the one observed in two-dimensional flow conditions on the inboard side of the wing. The vortex itself gains strength by increasing pitch rate and loses strength by increasing Mach number and by starting the motion close to the static stall angle. They concluded that unsteady load increments and stall delay increase with increasing pitch rate and decrease with increasing Mach number. Thus, the dynamic stall phenomenon on the inboard portion of the 3D wing is qualitatively similar to the one observed in Two-Dimensional (2D) conditions. [80]

An additional study of compressibility effects on a swept, pitching finite wing [7, 80], see Fig. 1.7, showed that at $Ma = 0.2$, local velocities remain subsonic with an abrupt separation of the turbulent boundary layer starting near 10% chord. The observed blade sweep effects are stall delay and maximum lift increase for static and dynamic conditions.

For the unswept wing, the tip vortex reduces the effective angle of attack and delays stall. At $Ma < 0.3$, the tip vortex interacts with the dynamic stall vortex and enhances unsteady airloads near the tip [80]. This effect decreases with increasing Mach number. At $Ma = 0.3$, a small region of supersonic flow occurs at the leading edge and results in an earlier, but less abrupt stall. At and above $Ma = 0.4$ a significant shock develops and initiates flow separation at the shock position, causing stall to occur at considerably lower angles of attack. The stall is more gradual, and results in a more diffuse stall vortex [7].

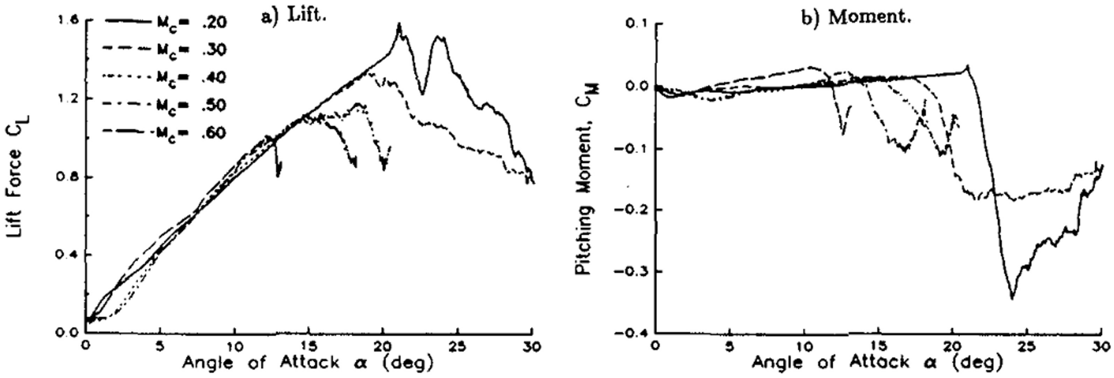

Figure 1.7: Mach number effects on normal force and pitching moment on the NACA 0012 airfoil 0.59c, for non-dimensional pitch rate $\dot{\alpha}c/2V = 0.01$ pitch ramps at $\Lambda = 30°$ sweep angle [7]

Rotor Tests

Dynamic stall on rotating blades is influenced by strong radial flows and pressure gradients, vortex interaction, inertial effects, and aeroelastic effects. To investigate realistic conditions, as they are encountered on helicopters, rotor tests are necessary, which capture all essential aerodynamic and multibody physics on a rotor system. Rotor dynamic stall can be triggered and influenced by many effects, such as vortex interaction, supersonic flow, or reverse flow, in the advancing as well as retreating blade regions. These interactions and initiation processes are most complex in fast forward and maneuvering flight. Exemplary dynamic stall rotor tests can be found in [10–13, 16, 18, 86–88].
Rotor test rigs offer the advantage of deep stall investigation capability and the use of high-resolution measurement equipment in controlled environmental conditions. However, they face the challenge of matching full-scale flight parameters, especially Mach and Reynolds numbers [37]. Commonly known rotor test rigs, which among others have been used for dynamic stall investigations, are listed in Fig. 1.8.

Dynamic stall tests on a hingeless rotor have been performed on the Rotor Test Stand Göttingen (RTG) of the German Aerospace Center (DLR) [8,9,89]. It is a Mach-scaled rotor with a diameter of 1.3 m, that is operated in a wind tunnel under slow axial flow conditions ($< 5m/s$), a reduced frequency of $k = 0.07$, and a chord based Reynolds number of 350,000 and a Mach number of 0.21, both at 75% radius. The high rotor stiffness reduces the dynamic stall phenomenon to an aerodynamic problem and removes uncertainties that are associated with aeroelasticity. The flow and blade deformation were analyzed by means of unsteady blade pressure transducers, particle image velocimetry, and tip deflection measurements covering the whole rotor disk [47, 90].
Müller et al. [18, 91, 92] investigated dynamic stall on a four-bladed Mach-scaled semi-elastic rotor with a double-swept blade planform applied at the RTG. Their investigations focused on aeroelastic behavior at tip Mach and Reynolds numbers of $Ma = 0.285$ and $Re = 5.95 \cdot 10^5$ and varying pitch angles $\Theta_1 = 17° \pm 8°, \Theta_2 = 27° \pm 6°, \Theta_3 = 32° \pm 6°$. They observed a nonlinear behavior in the down-stroke flapping movement, see Fig. 1.9, which they ascribed to a radially

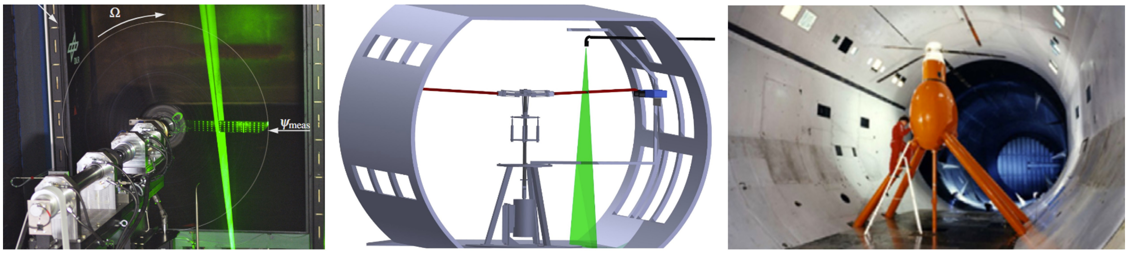

(a) RTG (DLR) (b) HARF (Georgia Tech) (c) 7A Rotor (ONERA)

(d) Onera 7AD Rotor (GOAHEAD) (e) UH-60A Rotor (NASA) (f) UMD rotor (GLMWT)

Figure 1.8: Rotor test stands used for dynamic stall experiments: (a) RTG axial flow facility, DLR Göttingen [8, 9] (b) HARF rotor, Georgia Tech [10] (c) ONERA 7A rotor in the S1MA wind tunnel [11] (d) ONERA 7AD rotor, GoAHEAD [12–14] (e) UH-60A full-scale rotor on the LRTA in the NFAC 40-by 80-Foot wind tunnel [15, 16] (f) UMD rotor setup in GLMWT [17]

phase-shifted dynamic stall process at the forward and backward swept parts of the blade.

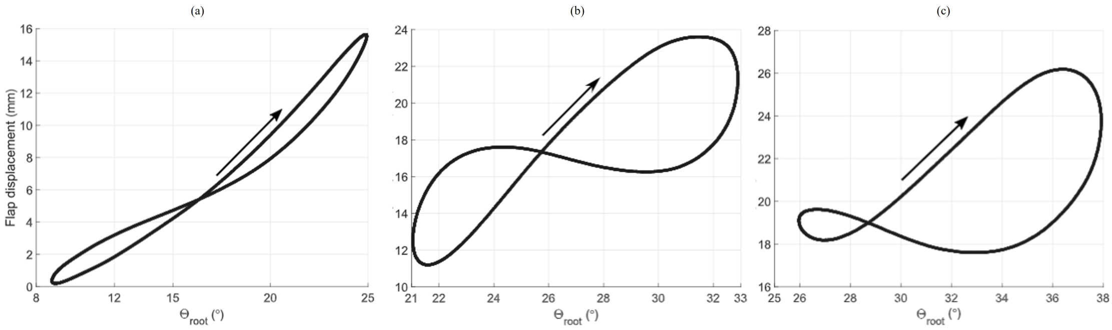

Figure 1.9: Flapping displacement as a function of blade root pitch angle at different pitch variations (a) $\Theta_1 = 17° \pm 8°$, (b) $\Theta_2 = 27° \pm 6°$, (c) $\Theta_3 = 32° \pm 6°$ [18]

Rhagav [10] investigated radial flow effects on dynamic stall in reverse flow conditions on a rigid, two-bladed teetering rotor at high advance ratios on the High Advance Ratio Facility (HARF). Tufts and Particle Image Velocimetry (PIV) were used for flow visualization, while a six-component load cell acquired rotor loads. Rhagav showed that the shear layer instability introduced by centrifugal forces is a fundamental behavior of the radial flow, which allows for analogies to be made between the flow over a rotating disk and a rotating blade. [10]

Three-dimensional dynamic stall on a 40 % Mach-scaled 7AD main rotor model ($R = 2.1\ m$, $c = 0.14\ m$) of the French National Office for Aerospace Studies and Research (ONERA) in a wind tunnel was observed by Kindler et al. [12] using stereoscopic PIV within the framework of the EU project Generation of Advanced Helicopter Experimental Aerodynamic Database (GoAHEAD) [14, 93]. They detected a compact large-scale vortex at 50 % and 60 % blade radius as well as blade tip vortex interaction with the outboard dynamic stall vortex segment, which causes an increase in complexity and 3D effects within the flow field.

A 1.7 m diameter rotor was investigated at advance ratios up to $\mu = 0.9$ and three shaft tilt angles $-4°, 0°, 4°$ by Lind et al. [17] in the Glenn L. Martin Wind Tunnel (GLMWT) at the University of Maryland (UMD). Time-resolved PIV measurements revealed various flow structures in the reverse flow region: among others, the reverse flow starting vortex, the reverse flow dynamic stall vortex, and the tip vortex. Increasing advance ratio increased exposition time to reverse flow conditions, which affected strength, trajectory, and predicted vortex-induced pitching moment of the reverse flow dynamic stall vortex. Moreover, a forward shaft tilt angle had a dramatically significant impact on evolution, strength, and size of the reverse flow dynamic stall vortex [17].

Petot et al. as part of the Action Group for Aeronautical Research and Technology in EURope (GARTEUR) have studied the predictability of stall effects with a total of seven different computational tools [94]. Using experimental data, the numerical models were tuned to the OA213 airfoil. They compared their numerical results with wind tunnel experiments on the 4.2 m diameter four-bladed 7A rotor of the ONERA in the S1MA wind tunnel in Avrieux, France. The blades were instrumented with strain gauges and pressure sensors at different radial stations. Their computational studies with rigid and flexible blades, as well as with and without rotation, led to the following conclusions with respect to blade elasticity and rotational effects: Blade elasticity had a minor lift and power decreasing effect. This was ascribed to the reduction of the local aerodynamic angles of incidence because of the blade's pitch-down twist and elastic flapping [94]. Rotation, on the other hand, had the effect of stall delay and lift increase. The reason for that was derived from 3D boundary layer equations, which showed that with the onset of separation, the 2D boundary layer develops into a 3D boundary layer. The embedded radial flow led to a balancing of the adverse pressure gradient, thus delaying stall [94].

In-Flight Measurements

Dynamic stall flight test data are invaluable, since they depict the full complexity of the rotor aerodynamics and dynamics for various flight maneuvers and environmental conditions, including vortex interactions, hub and fuselage interaction, multi-body dynamics, and aeroelastic effects. However, they most often manifest data of lower quality than experiments in a lab or wind tunnel environment.

The UH60-A flight program [15] offers a comprehensive set of flight data in various flight states including dynamic stall. Radially distributed pressure sensors on the rotor blades allowed for the detection of dynamic stall in level flight (counter 9017) and during a pull-up maneuver (counter

11029). Fig. 1.10 shows a rotor disk mapping of indicators that characterize dynamic stall in both flight states: moment stall, lift stall, and trailing edge separation [19]. Up to three different stall cycles in the third, fourth, and first quadrants were observed during one revolution; all of them show the expected pattern of lift stall occurring after moment stall. These data confirm results from flexible rotor wind tunnel tests and their corresponding computations (e.g. on the 7A [11] and UH-60A [95] rotors) [47].

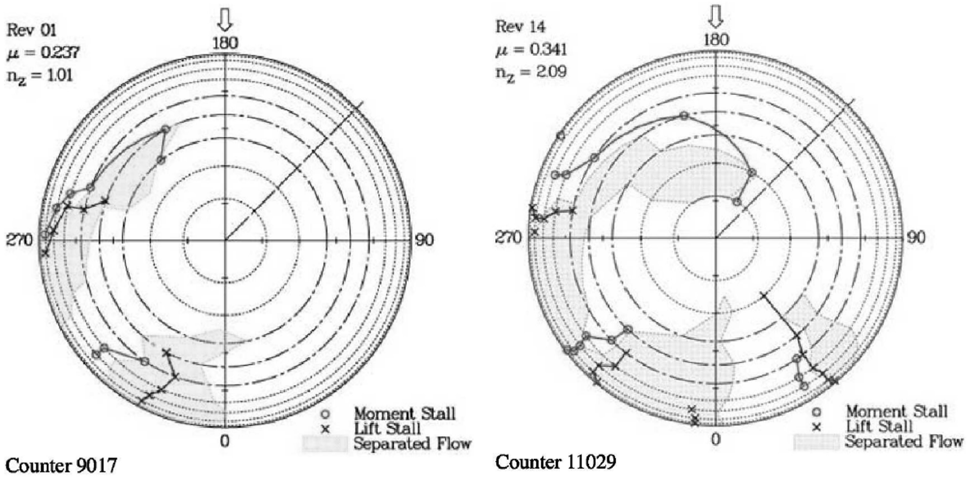

Figure 1.10: Moment stall, lift stall, and separated flow areas on the UH60-A airloads rotor identified in flight tests for level flight (left) and the UTTAS pull-up maneuver (right) [19]

Another flight test campaign that included dynamic stall measurements was performed on the Airbus Helicopters Bluecopter demonstrator during strong left turning flight [96]. The helicopter's instrumentation system measured control settings, flight speed, attitude, pitch link loads, and rotor thrust. Dynamic stall flow measurements are not available to the public. Letzgus et al. [96] simulated the Bluecopter dynamic stall case with a loose CFD/Computational Structural Dynamics (CSD) coupling. The flow field in this flight condition was found to be highly unsteady and complex, featuring massively separated flow, blade–vortex interaction, multiple dynamic stall events, and shock-induced separation. The numerical simulation showed that all CFD/CSD cases underestimated the amplitudes of the flight test and yielded phase shifts. However, overall trends agreed reasonably. The consideration of the rotor hub and fuselage improved the correlation with flight test data, whereas the elastic twist played only a minor role in the dynamic stall events. [96]

Measurement Techniques

Dynamic stall measurement techniques continue to improve in spatial and temporal resolution and provide insight into the physics of the phenomenon. Emerging technologies and the ever-increasing accessibility of data storage and processing capabilities are beginning to make it possible to acquire and process the large datasets needed for computational validation. These developments make complex three-dimensional experiments more accessible through experimental/numerical collaborations [37]. Surface and flow-field measurements are necessary in stall detection [97, 98] and the study of the unsteady flow's boundary layer transition and the cause and sequence of dynamic stall events. Flow visualization has been made possible by time-resolved two- and three-component PIV – including micro-PIV and volumetric PIV in the standard tomographic cross-correlation variant (Tomo-PIV) and the Lagrangian particle-tracking variant Shake the Box – 3D Lagrangian Particle Tracking at High Particle Densities (STB) – and the Background Oriented Schlieren (BOS) method, to analyze off-body flow topology, especially when PIV is not possible [47]. Surface integrated unsteady pressure sensors [99] and infrared cameras [100] are useful tools to study boundary layer transition. Additionally, Differential Infrared Thermography (DIT) and luminescent paints for Pressure Sensitive Paint (PSP)/Temperature Sensitive Paint (TSP) measurements on the airfoil surface are commonly used and reviewed in [101]. Gardner et al. provide a comprehensive review of measurement techniques for unsteady helicopter rotor flows in [101].

Statistical Post-Processing Techniques

Experimental investigations have shown that statistical techniques are necessary for the analysis and understanding of turbulent and separated flow during dynamic stall [37]. Modal approaches [30, 102–105], machine learning algorithms, and data driven approaches [28, 106, 107], are promising tools for the analysis of cycle-to-cycle variations as well as the identification of triggering effects and the system's sensitivity and complex response to these. Proper Orthogonal Decomposition (POD) methods can be used to group cycles of similar aerodynamic behavior [30, 108, 109], which show common force and moment peak heights. They are necessary tools in accurate data processing and evaluation, since mere load phase-averaging of different cycle groups can lead to 30% errors in load estimation [37].

High-Fidelity Dynamic Stall Simulations

Within the last decade, high-fidelity Navier-Stokes simulations have proven the rising capability of modeling dynamic-stall related physical phenomena, see [110, 111]. Klein et al. [112] numerically investigated 2D and 3D pitching airfoil tests, while Nilifard et al. [113] analyzed three-dimensional effects on pitching airfoils. Spentzos et al. [114] and Kaufmann et al. [115] computed three-dimensional dynamic stall cases on a pitching wing and rotational influence was investigated numerically by Gardner et al. [116]. Three-dimensional CFD computations on a rotating pitching airfoil section and blade were also performed by Ruan et al. [117, 118] and Letzgus et al. [20, 119, 120].

Letzgus et al. performed CFD simulations of dynamic stall on a two-bladed Mach-scaled rotor model ($R = 0.65$ m, $Ma_{tip} = 0.6$, $Re_{tip} \approx 1 \times 10^6$) at the RTG with and without axial flow at 14 m/s [20]. The investigated dynamic stall cases were tested at 50 Hz rotor speed with cyclic pitch settings of $9.2° \pm 10°$ and $17.2° \pm 10°$. One of their main findings was that axial flow weakened the dynamic stall event and slightly changes the vortex pattern. Moreover, the simulations predicted an asymmetric omega-shaped vortex resulting from the interaction with the blade tip vortex and the varying Mach number along the span [20], see Fig. 1.11. The tip vortex limits the outboard spreading In addition, they stated that the flow ”around the radial station of r/R = 0.85 – where load and surface pressure distribution revealed to be a crucial contribution to the point of integral lift and moment stall – [...] is quite comparable to the one of two-dimensional dynamic stall” [20]. Further CFD computations with experimental validation using the four-blade RTG rotor tests (with swept blade tip geometry) are published in [96, 121].

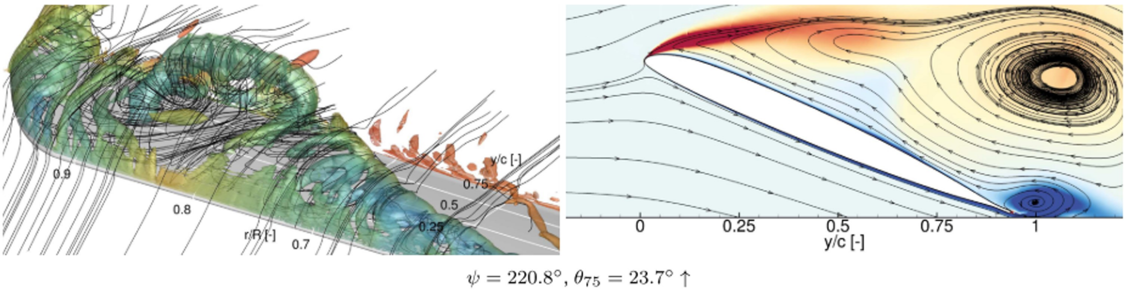

Figure 1.11: Visualization of dynamic stall on a pitching rotor blade with $\Theta_{0.75} = 17.2° \pm 10°$ pitch angle; Left: Instantaneous isosurfaces of the λ2-criterion colored with $\frac{p}{p_\infty}$; Right: Instantaneous vorticity contours and in-plane streamlines at $r = 0.84$ R [20]

Conclusions from State of the Art

The last decades of experimental dynamic stall research have shown that two-dimensional studies were extensively analyzed. They provided a seminal understanding of the stall events, causes, and sensitivities to various parameters. However, three-dimensional and rotational effects have a major influence on dynamic stall mechanisms and disclose a much larger parameter portfolio. Flight tests have identified new locations of dynamic stall occurrence in various maneuvers and flight states under actual conditions. However, tracing the root of their causes is almost impossible in a non-laboratory environment. Rotor lab experiments seem to provide the best conditions for high-resolution measurements at this stage because of their capability to isolate and observe unsteady phenomena associated with dynamic stall in a controlled environment. Facility-based differences (flow circulation, ground effect, wall interferences, flow variations) and differences in rotor configurations (pitch control, blade elasticity, multibody degrees of freedom) have a major impact on the test results. Moreover, previous three-dimensional rotor experiments have shown significant variations in data quality (sensor discretization, signal-to-noise ratio, number of analyzed cycles, amplitude and time resolution), airfoil quality (contour precision, surface roughness) and post-processing algorithms (phase-averaging vs. modal approaches). Smith et al. [37] stated, that comparisons of different conditions tested in a single facility may provide more insight than comparisons of results among facilities. In conclusion, dynamic stall experiments must be performed according to a minimum level of data quality standard and in close interaction with numerical computations to efficiently analyze, validate, and predict dynamic stall mechanisms and loads. This justifies the need for another type of experiment which extends the current knowledge of dynamic stall beyond the state of the art.

1.4 Objective of Work and Scientific Approach

The previous section clarified that there are several questions concerning development, sensitivity, and three-dimensional rotary effects on the dynamic stall phenomenon, that have not yet been answered completely. This underlines the need for three-dimensional pitching and rotating blade experiments. In this regard, the community needs documented large sets of high-quality and high-resolution experimental studies on aerodynamics and structural dynamics during deep dynamic stall tests in hover, climb, and forward flight conditions.

The main objective of this thesis is to experimentally analyze the effect of rotor control parameters – rotor speed, collective pitch, and cyclic pitch – on the structural loads of a rotating pitching blade during dynamic stall. The goal is to identify load trends and reveal correlations and differences with existing pitching airfoil experiments. The results should provide an initial assessment of relevant dynamic stall cases and the influence of control parameters, while indicating directions for future investigations.

The approach to answer the research questions stated in section 1.1 is predominantly experimental in this thesis. Experiments depict real-life physics and account for several effects that are easily neglected in numerical computations. The kind of experiments chosen are tests on a hingeless rotor with geometrically simple and structurally rigid blades in hover. Hence, the blade is not only exposed to pitching, but also to rotational effects and three-dimensional flow conditions during dynamic stall. The blade's rotation accounts for the variation of critical flow parameters, such as Mach number, Reynolds number, and reduced frequency, along the blade radius and the interaction of the omega-shaped vortex on the upper blade surface with the tip vortex and rotor wake. Moreover, preventing further blade motion – such as heaving or lagging – allows for a comparison of the test results with pitching airfoil tests in free-stream conditions and a corresponding identification of three-dimensional rotational effects only. In addition, the experimental analysis mainly focuses on the structural blade root moments and pitch link forces, see Fig. 1.12. Recent studies focused on flow visualization and pressure measurements to understand stall events and provide most accurate aerodynamic data for validation of numerical computations. The analysis of the influence of various parameters on the structural load dynamics during dynamic stall allows the consideration of the phenomenon's sensitivity to relevant flow unsteadiness parameters. However, local flow analysis includes the risk of over-interpretation of local flow conditions, that may have a minor effect on resulting structural loads.

The following steps are taken as a part of the experimental approach:

- Design, instrumentation, and operation of a rotor test rig for cyclic pitch induced dynamic stall investigations in hover, including sensor calibration, data acquisition and processing (chapter 2).
- Elastic rotor modeling for static load prediction and experimental data validation (chapter 3).

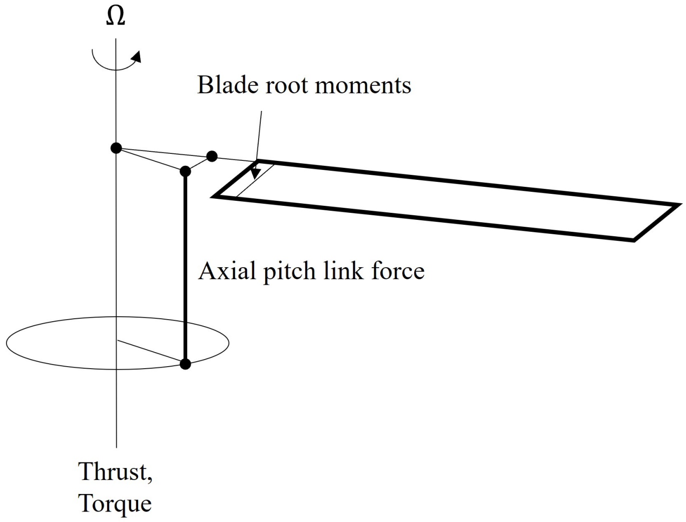

Figure 1.12: Sketch of the measurement entities for the investigation of the effect of dynamic stall on structural loads

- Rotor performance and thrust polar measurements at different rotor speeds into static stall and correlation analysis by comparing measured loads to predicted loads (chapter 4).
- Structural load analyses of ten selected light and deep dynamic stall cases at three different rotor speeds with sensitivity studies and discussion of trends due to varying speed, collective and cyclic pitch control (chapter 4).

This thesis is an initial step towards a deeper understanding of the load dynamics during pitch induced dynamic stall and the sensitivity of the phenomenon to varying control inputs and compressibility effects. The presented results provide a basic understanding of the structural rotor behavior in hover during dynamic stall. Furthermore, it provides an investigation platform for future deep stall analyses by means of different blade geometries, more elastic blade structures, and further measurement techniques in and out of wind tunnel environments to get a comprehensive understanding of the flow physics and structural load dynamics including aeroelastic effects during dynamic stall.

2 Test Rig and Experimental Setup

The Munich Experimental Rotor Investigation Testbed (MERIT) test rig is built for experimental dynamic stall investigations for the present thesis and therefore has to fulfill specific technical requirements. The majority of requirements are derived from the main requirement, that the test rig shall sustain dynamic stall loads and vibrations in hover and forward flight. Beside this most restrictive application, the rotor test rig should also be a testing tool for small-size propellers in inclined flow or large-scale rotors in the near and far future. Therefore, the test rig's minimum requirement list – which would satisfy this thesis's aim – is extended with the specifications long-term applicability, flexibility, and modularity, which significantly influence the overall test rig design.[†]

2.1 Technical Requirements and Design Specifications

Technical requirements describe the functions a system shall perform and can be refined by how well they need to be performed. According to the National Aeronautics and Space Administration (NASA) Requirements Process [122], they can be categorized into functional, performance, interface, environmental, reliability, and safety requirements. All can be subject to technical constraints. Design Specifications, on the other hand, describe how the system fulfills the required functions, i.e. how it is built and how it works.

Within the scope of this thesis, the test rig requirement definitions and design specifications focus on the most important functional and performance requirements as well as design solutions for mechanical and electronic parts under specific technical constraints.

2.1.1 Technical Requirements

As mentioned above, the main test rig requirement is dynamic stall capability. Since this phenomenon predominantly occurs in forward flight conditions on real helicopters, it shall be investigatable in a wind tunnel to simulate asymmetric flow and expose the rotor to high-load conditions. Availability and accessibility of large-scale wind tunnels are critical factors for the utility of a forward flight test rig. The faculty of Aerospace and Geodesy at the Technical University of Munich (TUM) has such equipment at its disposal for the necessary investigations. Therefore, the test rig's dimension and rotor position needs to be designed accordingly to fit into the working section's center of the available wind tunnel A of the Chair of Aerodynamics and Fluid Mechanics, TUM.

[†] Parts of this chapter were previously published in [22, 24].

Compressibility is proven to be determinant for dynamic stall development. Due to the fact that a full-scale rotor cannot be operated in the available wind tunnel, the rotor shall be Mach scaled to account for compressibility effects.

In summary, the primary requirements, that determine the rotor test rig's design and main features, are the following:

1. The test rig shall be sized to sustain dynamic stall loads, in hover and in forward flight.
2. The test rig shall be compliant with installation requirements and test section dimensions of TUM's wind tunnel A [*].
3. The test rig rotor shall be Mach-scaled.

The test rig's secondary requirements are partly derived from the primary requirements and partly an extension from them. These requirements for mechanical components, sensors, and Data Acquisition (DAQ) systems are summarized in Tab. 2.1.

Cyclic blade pitch excitability is needed for dynamic stall investigations in hover and forward flight conditions to create unsteady angle of attack variations on the rotating blade with at least a 1/rev frequency. As initial hover investigations offer valuable pre-analyses in less complex airflow conditions, the pitch range shall be high enough to allow dynamic stall excitation in hover experiments.

The shaft driving engine shall provide constant load-independent speed to prevent unwanted influence of torque induced rotor slowdown during dynamic stall, which would correspond to a lead-lag motion of the blade. For the analyses in this thesis, any form of lead-lag motion should be prevented as it would further increase flow complexity and complicate the backtracking of flow phenomena to their cause. The same reason demands a hingeless rotor and a rigid blade root to prevent flapping and lead-lag motions superimposed with rotating and pitching movements.

A hingeless rotor is subject to very high hub loads under cyclic pitch conditions and can lead to noticeable displacements at the lower shaft end. Thus, the interface between drive and rotor shaft shall compensate radial, axial and angular displacements during operation, but simultaneously offer torsion-stiff torque transmission to prevent speed variations. The rotor blades shall be statically balanceable and offer space for sensor integration into the blade, such as strain gauges, instationary pressure sensors, or fiber-optical sensors. The pitch control shall be vibration-resistant at zero clearance to accommodate the expected dynamic pitch link loads during dynamic stall.

Due to variable operational locations inside and outside the wind tunnel, the test rig frame shall enable quick dismountable handlings to facilitate smooth and secure relocations. Low eigenfrequencies of the rotor-carrying components are desirable because of their excitation during rotor

---

[*] Chair of Aerodynamics and Fluid Mechanics

run-up. At lower rotor speeds, less energy is transferred into the mechanical system, and eigenmode excitation can be avoided due to slow mode amplitude growth.

Primary and secondary requirements, as well as DAQ and performance constraints are summarized in Tab. 2.1. The design specifications for drive train, steel frame, actuation system, rotor and blades are derived from the technical requirements above. These specifications are described in section 2.3, where the main mechanical components are introduced. However, principal constraints and design specifications of the rotor, being the main compound system, need to be explained beforehand. They are needed for first load calculations and further component designs.

2.1.2 Rotor Constraints

Rotor Size and Height

The proposed wind tunnel for forward flight measurements has a working section with a width of 2.4 m, a height of 1.8 m, and a maximum operational speed of 65 m/s for an open and 75 m/s for a closed working section. Interaction of rotor aerodynamics with side shear layers of an open working section, on the one hand, and with the wall of a closed working section, on the other hand, can lead to unwanted influences on the rotor's dynamic stall vortex. Although initial wind tunnel acceptance tests have shown that the required velocity tolerance was satisfied for almost the whole width of the test section, the rotor diameter is set to a maximum of 1.8 m to provide a buffer wall distance of 300 mm to each side of the test section.

The commonly known ”Seiferth wings” at the lateral and upper edges of the air inlet reduce pressure and velocity variations in the open test section and thus improve measurement conditions. Nevertheless, they have to be considered for vertical positioning of the rotor in the wind tunnel's test section, see Fig. 2.1. CFD simulations of the wind tunnel without rotor have shown that at the center of the test section, there are almost constant flow conditions up to 1.5 m from the test section ground [21]. A trade-off between the upper shear layer influence and ground interaction lead to the decision to place the rotor in the vertical middle of the test section, at 900 mm respectively. With another 1.7 m vertical space underneath the wind tunnel ground, the total rotor height results in 2.6 m.

Rotor Speed and Advance Ratio

Mach scaling of the test rig rotor requires the blade tip speed of a representative full scale helicopter. A commonly known reference is the tip speed $v_{tip} = 220$ m/s of the 2-2.5 ton helicopter class representative Bo105, which has a blade tip radius of $R = 4.91$ m, [123]. Given the reference tip speed and the fixed rotor radius, Mach scaling in hover demands a rotor speed of

$$\Omega = 244.4\ rad/s = 38.9\ Hz = 2335\ RPM \tag{2.1}$$

Depending on the effect of wind tunnel blocking with the rotor in open working section configuration, a maximum effective wind tunnel speed of around 45 m/s can be regarded as realistic, resulting in the respective advance ratio of $\mu = 0.2$.

Primary Requirements			
	Operation in dynamic stall		
	Operation in hover and in TUM's wind tunnel A		
	Mach-scaled rotor		
Secondary Requirements			
Drive train	Load independent drive		
	Displacement tolerant coupling		
	Speed control accuracy	±1	RPM
Steel frame	Divisibility, easy (dis-)assembly		
	Low vibrations at and below nominal rotor speed		
Rotor	Hingeless, pitch-variable		
	Number of blades	2,4	
	Stiff blade root		
	Balanceable		
	Blade sensor integrability		
	Max. rotor speed	3000	RPM
Pitch control	Vibration resistant		
	Free of play		
	Collective and cyclic		
	Control accuracy	< 0.1	°
	Pitch angle range	±30	°
Safety	Fail-safe blade loss		
	Redundant engine control		
	Redundant actuator control		
Durability	Rotor shaft bearings	$> 10{,}000$	h
	Critical rotor components	$> 1 \cdot 10^6$	cycles
Rotating sensors	Pitch angle, accuracy	< 0.1	°
	Rotor azimuth, accuracy	< 0.5	°
	Rotor speed, accuracy	1	RPM
	Strain gauges		
	Pressure sensors		
Rotating DAQ	Number of channels	> 30	
	Resolution	≥ 16	bit
	Sampling rate	> 18	kHz
Stationary sensors	Integrated rotor forces and moments, accuracy	0.1	%
	Drive torque, accuracy	1	%
Stationary DAQ	Resolution	> 16	bit
	Sampling rate	> 5	kHz
	Synchronization with rotating data		

Table 2.1: Functional and performance requirements, and technical constraints

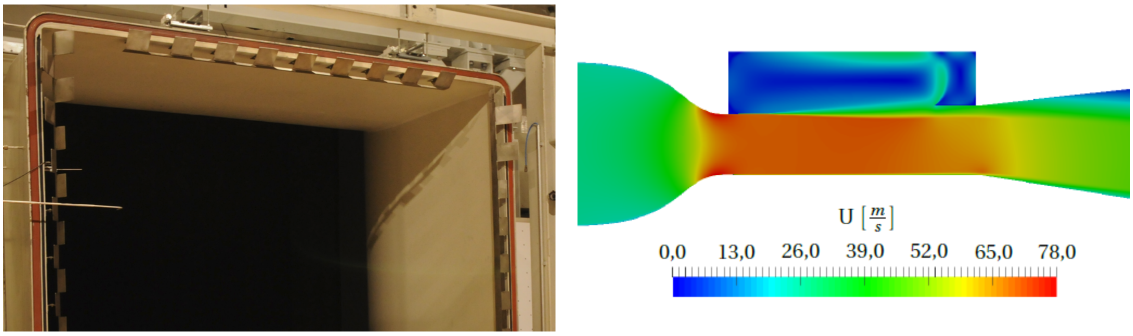

Figure 2.1: Seiferth wings and simulated velocity profile in TUM's wind tunnel A without rotor (side view) [21]

Number of Blades and Blade Attachment

The rotor used for initial operation and hover dynamic stall tests shall have two blades and be extendable to four blades, which shall be accomplished with the same rotor head.

The blade attachment should offer a pitch bearing with collective and cyclic pitch control and a pitch range of $\pm 30^\circ$. With an estimated static stall pitch angle of 20°, this ensures a 10° margin for cyclic pitch induced dynamic stall in hover at high collective pitch settings. The blade attachment should be hingeless to facilitate the sole investigation of the rotational speed influence on a pitching airfoil during dynamic stall without a flapping or lead-lag motion. This restriction to a pitching and rotating movement reduces model complexity and simplifies future simulation validation.

Blade Airfoil and Geometry

The rotational speed influence on dynamic stall in hover should be examined on an airfoil which has been undergoing intensive testing and which provides enough pitching airfoil wind tunnel data to compare rotating pitching blade tests with. The well-proven symmetric NACA 0012 airfoil fulfills these requirements and is therefore chosen for the investigated rotor blade.

The blade geometry is rectangular and has no twist, which ensures best comparability with 2D and 3D pitching airfoil section results. Moreover, the maximum pitch angle to evoke dynamic stall is reduced due to zero twist. Manufacturing purposes demand a trailing edge tab, which is set to 0° (see [23]) to maintain the airfoil's symmetry. The blade chord cannot be scaled geometrically, because future applications demand sensor integrability into the blade, e.g. for instationary pressure sensors and Fiber Bragg Grating (FBG) sensors. A chord of 0.13 m is chosen as a feasible size to run first sensor integration tests. Moreover, a higher chord results in a higher Reynolds number, which provides more realistic Reynolds numbers as on real helicopters.

The main rotor design specifications are summarized in Tab. 2.2.

Rotor Design Specifications	
Rotor height	2.60 m
Rotor diameter	1.80 m
Airfoil	NACA 0012 0° tab
Blade tip speed	$220\frac{m}{s}$
Blade chord	0.13 m
Blade twist	0°

Table 2.2: Design specifications of the MERIT rotor

2.2 Design Loads

Three basic scenarios are regarded to determine the test rigs limit loads:

1. Dynamic stall on a trimmed two-bladed rotor in wind tunnel
2. Trimmed four-blade rotor in wind tunnel
3. Blade loss at highest rotor speed

Based on the given rotor requirements and constraints, a rigid blade model is used to calculate scenario one and two on an isolated single rotor in wind tunnel with the aeromechanic code Comprehensive Analytical Model of Rotorcraft Aerodynamics and Dynamics (CAMRAD II) [124]. Dynamic stall simulation is performed with the semi-empirical Leishman-Beddoes model. The inflow is modeled with the Differential Momentum Theory (DMT) – a combination of blade element and momentum theory – including the Prandtl tip loss correction factor. The rotor is trimmed in wind tunnel at a wind speed of 45 m/s and a rotor speed of 2335 RPM ($v_{tip} = 220$ m/s), with zero revolution averaged hub moments and predefined thrust. The blades are modeled with a rectangular geometry, no twist, and a NACA 0012 airfoil. Aerodynamic load calculation is based on the available NACA 0012 airfoil tables in CAMRAD II. Twenty aerodynamic panels define the blade's aerodynamically efficient region from 0.24 R to 1 R and the blade mass is distributed homogeneously from 0.19 to 1 R with 1.4 kg/m.

The usage of rigid blades and DMT inflow delivers conservative load estimations. However, some components are not included in this estimating calculation, such as blade trim masses, blade instrumentation, blade holder, or pitch links. These include uncertainties considered in the respective safety factors for each component´s design calculations. Blade loss is an extreme scenario with maximum short time rotor imbalance at 3000 RPM.

Table 2.3 summarizes the rounded-up, maximum loads from all scenarios. These loads are used for the design of all mechanical test rig components.

Radial blade attachment force	F_y	33000	N
Short time lateral hub force	$F_{y,short}$	60000	N
Rotor thrust	F_z	3000	N
Hub moment	M_x	900	Nm
Rotor torque	M_T	260	Nm
Blade torsion	M_θ	30	Nm

Table 2.3: Main limit loads in rotating hub axes as maxima from three scenarios including blade loss

2.3 Test Rig Design

The construction and design of mechanical components is based on the calculated loads in Tab. 2.3. The following sections confine themselves to the description of the mechanical components' functions, conceptual design, assembly, material choice, and surface treatments. Component materials and surface treatments are summarized in Tab. A.2, section 2.3.7, off-the-shelf standard parts are shown in Tab. A.1, section 2.3.7.

2.3.1 Steel Frame

The mechanical design of the test rig's frame structure is mainly determined by the following requirements, which are derived from those in Tab. 2.1 and specified into more detail here:

1. The rotor plane height shall be 2.60 m from the ground.
2. The frame structure shall be mountable on TUM's wind tunnel adapter pads and be divisible for transport and mounting purposes.
3. The frame structure shall support the drive train and offer minimum surface, which generates vortices and drag in the wind tunnel's test section.
4. The frame structure shall account for the estimated dynamic loads and vibrations. Moreover, safety precaution requires ability to account for imbalance loads in case of blade loss.
5. The main steel frame eigenfrequencies shall be lower than nominal rotor frequency.
6. Integrated rotor forces and moments shall be measurable for trim purposes.

Given these requirements, a respective test rig structure with the following four welded steel frames is designed, see Fig. 2.2:

- The wind tunnel adaptor welded on clamping pads,
- the middle frame bolted to the wind tunnel adaptor,
- the engine cradle bolted to the middle frame, and
- the bearing frame connected to the middle frame by four three component load cells.

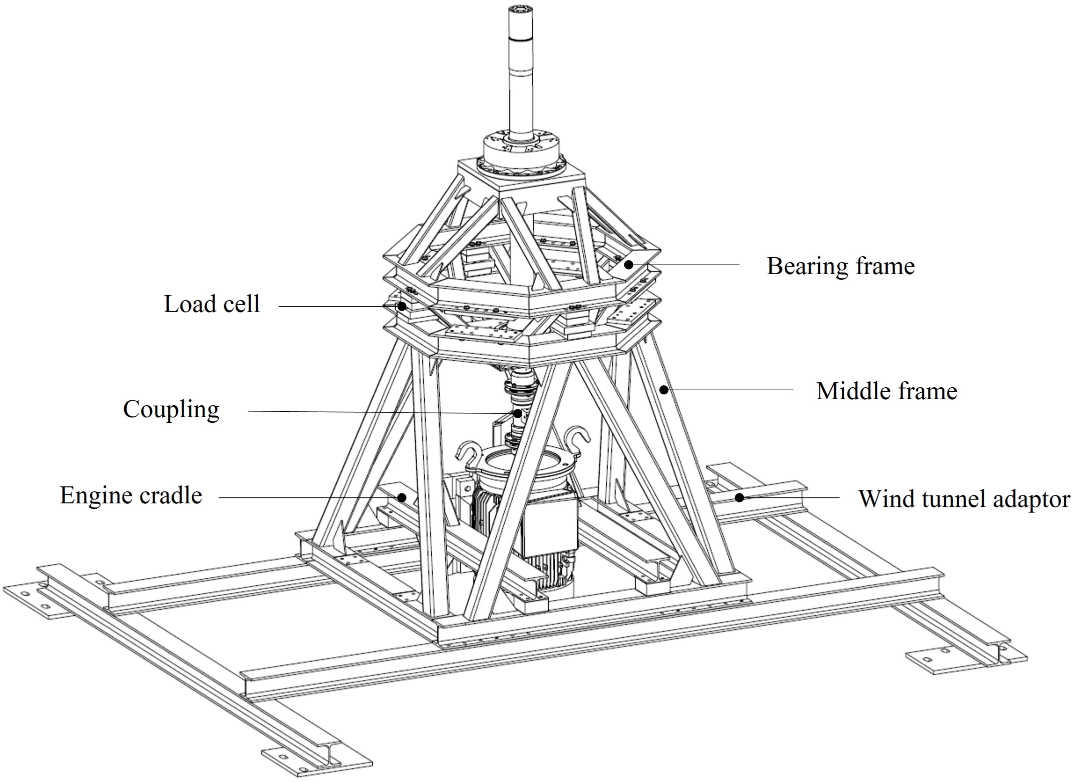

Figure 2.2: MERIT steel frame structure with drive train, bearings, and rotor shaft [22]

The wind tunnel adaptor is the test rig carrying structure including clamping pads which provide a solid mounting in TUM's wind tunnel. Due to its long and heavy beams, the eigenfreqencies are far below the test rig's nominal rotor speeds. For hover investigations outside the wind tunnel, the adaptor is used as a carrier clamped to the concrete fundament. The middle frame carries engine cradle and the upper bearing frame. Four three-component strain gauge load cells of the type $K3D120 \pm 2kN/VA$, *ME-Meßsysteme GmbH*, are mounted between middle and upper frame to measure integrated rotor forces and moments. Each load cell allows for a deformation of 0.06 mm at a nominal force of ± 2 kN in all three axes. The bearing frame containing rotor shaft and bearings offers an attachment surface for swashplate actuation components and the rotor itself. [22]

All frame components are aligned to each other by dowel pins and milled contact surfaces. Pin holes, bearing bore holes, and contact surfaces are machined after the welding process and in the same clamping operation to guarantee highest precision for the alignment of drive and output shaft, perpendicularity between shaft axis and load cell plane of measurement, and shaft centricity in relation to the surrounding load cells, see [125]. Thin metal shims with various thicknesses are used to balance load distribution between the four load cells.

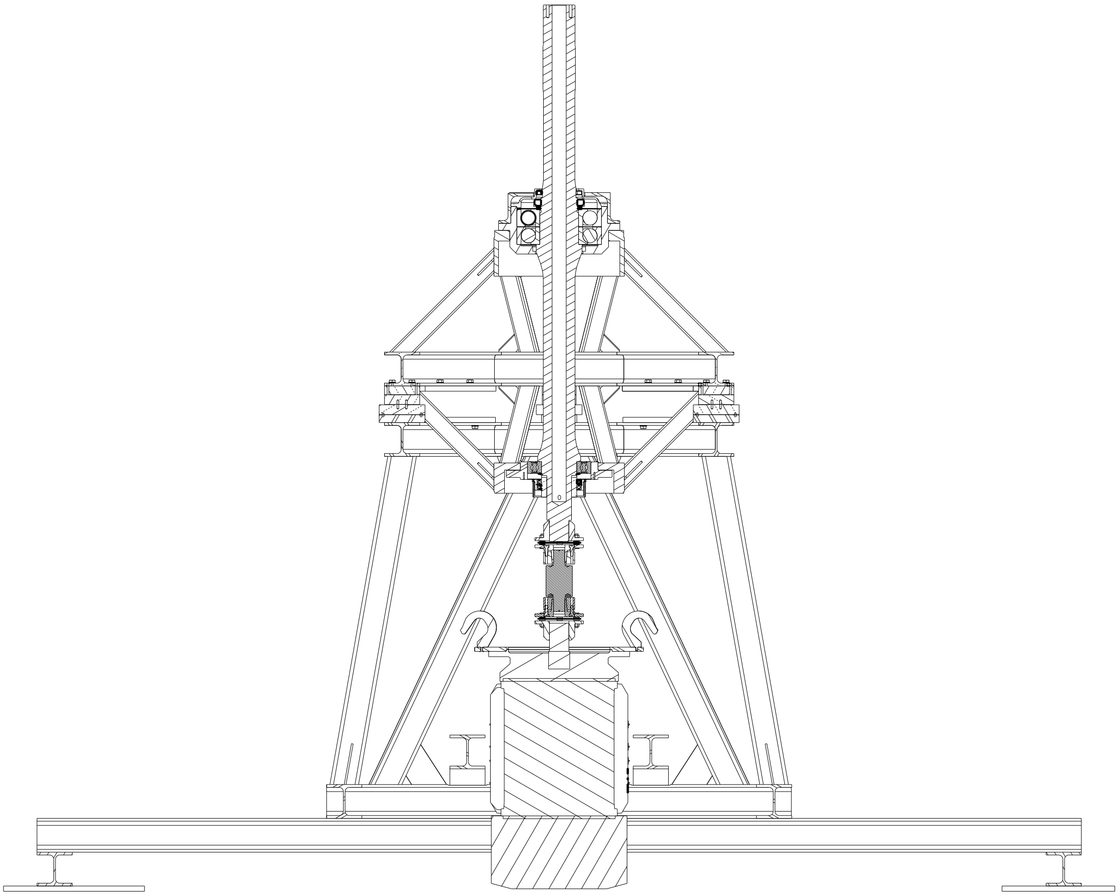

Figure 2.3: Cross-section of the MERIT steel frame and drive train structure

2.3.2 Rotor Shaft and Bearings

Rotor Shaft

The rotor shaft is specifically designed to withstand excessively high short-term imbalance in the unlikely event of blade loss (Tab. 2.3). The following components are attached to the rotor shaft and predetermine shape and surface treatment of the respective contact areas: coupling and torque unit, telemetry data and energy coupler, rotating speed encoder, fixed and floating shaft bearings, swashplate, rotating driver, and clamping set for the rotor head attachment, see Fig. 2.4.

The rotor shaft's borehole provides space for telemetry data and power cables from the rotor head to the coupler. The shaft is made of hardened and tempered steel 42CrMo4+QT, thus providing high ductility and tensile strength. Its surface is gas-nitrided, which yields corrosion protection and a surface hardness of 650 HV necessary for the bearing surfaces. These surfaces are ground after surface treatment to guarantee required bearing fit tolerances. The rotor shaft is balanced according to G 2.5 balancing quality, as defined in the ISO 21940-11:2016 norm [126]. Shaft balancing is accomplished by additional screws at the front end of the upper shaft side and boreholes at the lower shaft end above the ball bearing position.

Rotor Shaft Bearing

The shaft bearing consists of the upper fixed bearing (angular contact ball bearings in O-arrangement) and the lower floating bearing (grooved ball bearing). More details on bearings used for the test rig are listed in Tab. A.1. Bearing distance and dimension are designed according to the initial load estimations shown in Tab. 2.3, including blade loss scenario.

The upper fixed bearing contains two angular contact ball bearings in an O-arrangement to provide maximum clamp stiffness for the shaft. The lower floating bearing is a lifetime lubricated, sealed groove ball bearing, see Fig. 2.3 and 2.4. The bearing positions minimize bearing loads and provide sufficient space for the swashplate actuation components. The bearings in O-arrangement are preloaded by shim rings between the two bearings' outer and inner rings. These thin metal shim rings are lapped to obtain a thickness difference of 0.012 mm with a +/- 0.002 mm tolerance. Bracing the inner rings with a grooved nut up to solid contact provides the desired preload for optimum shaft stabilization. Angular ball bearings and groove ball bearing have an interference fit on the shaft (P5/j6 and P6/h6), and interference and transition fits in their respective bearing container (P7/h6 and J6/h6). In case of temperature change and subsequent shaft elongation, the groove ball bearing can move axially in the lower bearing container.

2.3.3 Motor, Coupling, and Control

Motor

The permanent magnet synchronous motor (85 kW, 170 A) of the type *3000 LSRPM200L1 85kW V6 400V*, *EMERSON Industrial Automation*, has a variable frequency drive (400 V, 250 A), is speed-controlled, and provides a nominal speed and torque up to 3000 RPM and 270 Nm. It is used with a vertical drive axis and side-mounted to the engine cradle. The advantage of the synchronous motor is the torque-independent speed control. It guarantees constant speed despite torque variations, which occur during dynamic stall.

Coupling

A torsion-stiff double gimbal coupling from *KTR Systems GmbH* transfers the motor torque to the rotor shaft with a feather key connection. The direct torque transmission satisfies minimum space and constant speed requirements. The coupling allows for small radial, axial, and angular displacements (up to 3.7 mm, 2.0 mm, and 1.0°). It contains a rotor speed and torque measurement unit, whose stationary component is supported by a holder bolted to the motor carrier.

Control

The rotor speed can be controlled redundantly from the workstation or an entirely independent Human Machine Interface (HMI) touch panel and hand wheel. The workstation and touch panel

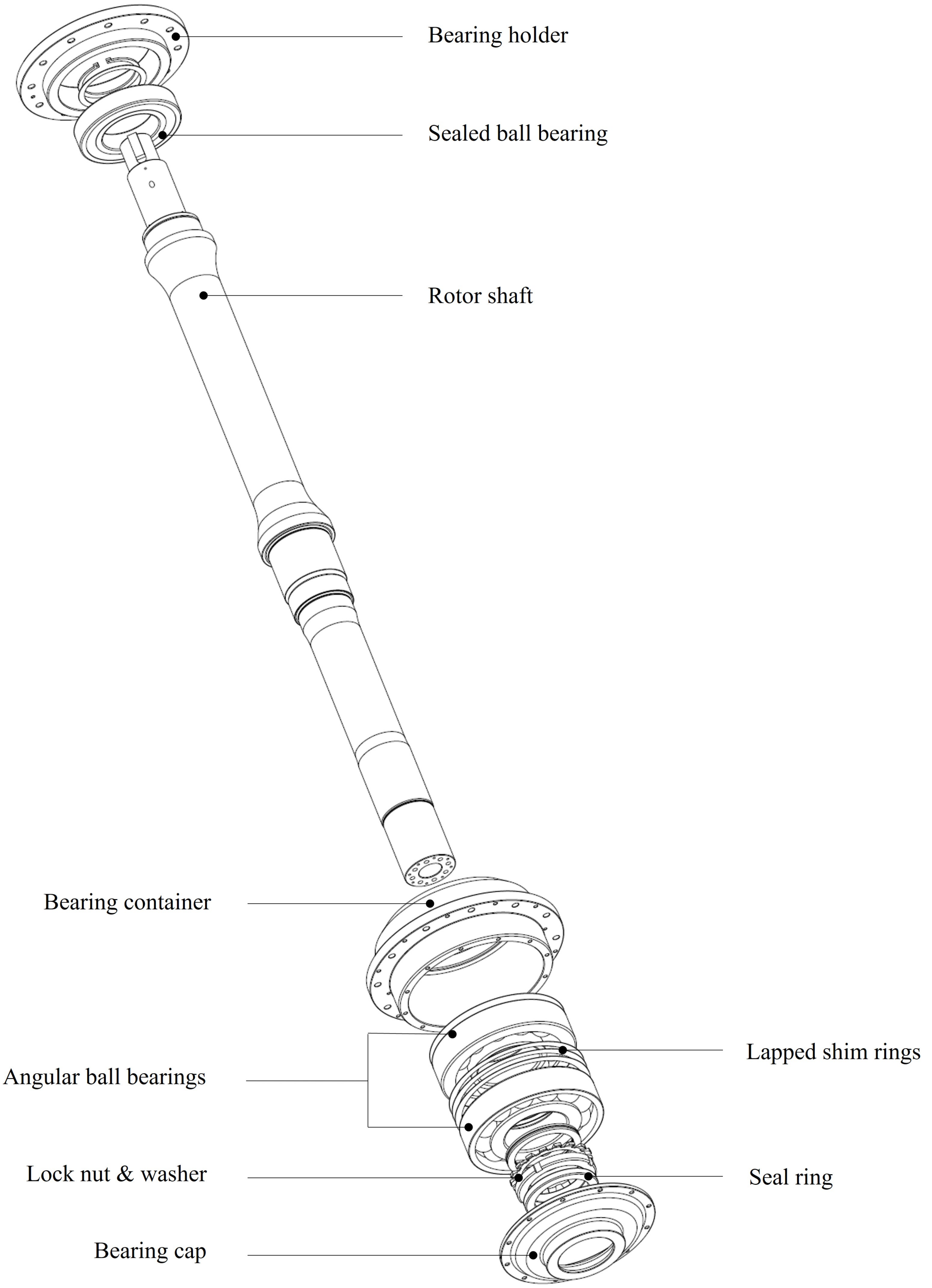

Figure 2.4: MERIT rotor shaft and associated mechanical components

have a direct Ethernet connection to the frequency inverter's control unit. This architecture provides redundancy and full control authority in case one system fails.

2.3.4 Rotor Head and Blade Attachment

Rotor Head

The rotor head is designed to attach four, two, or one rotor blade with a counterweight. A clamping set provides the frictionally engaged connection between the rotor head and the shaft. The rotor head carries a telemetry encoder to amplify and digitalize rotating sensor data. The blade attachment is hingeless to minimize blade flapping and lead-lag motion. A pitch bearing allows for the blade's pitching movement. Fig. 2.5 shows the rotor head with two blade attachments.

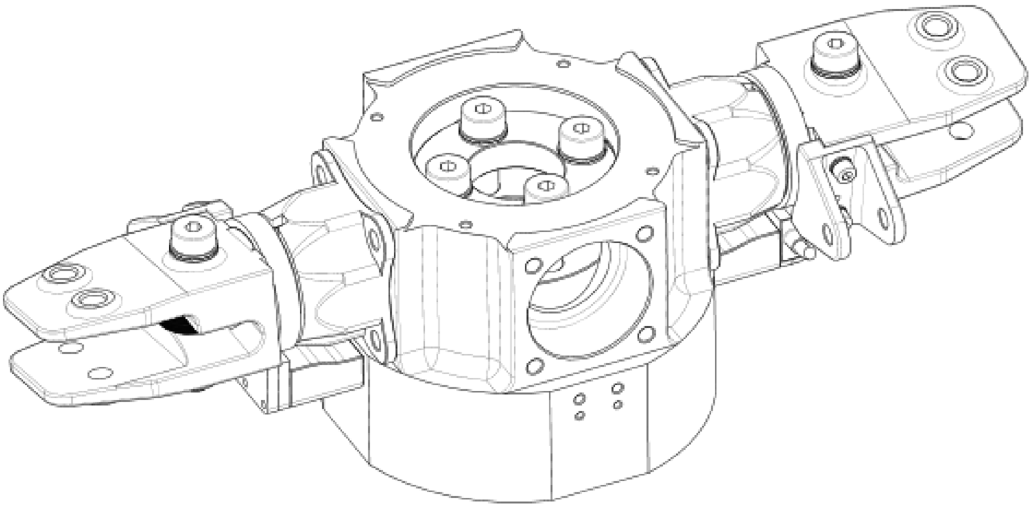

Figure 2.5: Rotor head with two MERIT blade attachments in isometric view [22]

Blade Attachment

The blade holder is a steel component bolted to the rotor head by a tension-torsion strap, which provides centrifugal force suspension. Its geometry causes a negative 10° pre-twist of the tension-torsion strap at $\Theta_0 = 0°$ collective pitch. The blade holder offers a cylindrical running surface for a pair of needle-roller bearings pressed into a sleeve, which is side-mounted to the rotor head (Fig. 2.6). To measure the blade pitch angle, it carries a magnet ring of the type *PMIR7-20-90-M-50*, *ASM Automation Sensorik Messtechnik GmbH*. The respective hall sensor *PMIS4-20-20-120KHZ-TTL-Z1-2M-S*, *ASM Automation Sensorik Messtechnik GmbH*, is bolted to the rotor head below the magnet ring with a vertical gap of approximately 0.1 mm. Manufacturing tolerances of the ground running surface and the needle bearings cause a bearing free-play with a resulting

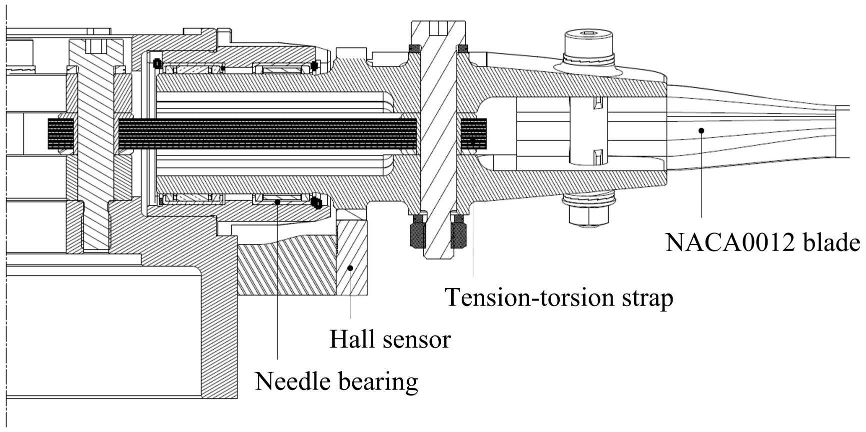

Figure 2.6: Cross-section of the hingeless MERIT blade attachment [22]

blade tip offset of 0.8 and 0.9 mm in the flapping direction. The free-play is one reason for stiffness nonlinearity in the blade attachment; see [127].

Tension-Torsion Strap

The tension-torsion strap consists of 34 cold-rolled, 0.3 mm thick feather steel (1.4310) sheets, see Fig. 2.7. In contrast to axial bearings, this sheet stack has a very high loading capacity, as shown by component tests in section 2.4. This component is one of the most critical rotor parts and, therefore, designed with a conservative limit load assumption of 60 kN axial force resulting from the centrifugal force of the rotor blade, the blade holder, and its own mass at the nominal rotor speed. The tension-torsion strap's outer contour and bolt holes are milled out of a clamped metal sheet stack to minimize manufacturing inaccuracies. The shoulder sleeve and washer are assembled with a slight interference fit (N7/m6).

2.3.5 Rotor Blade

The rotor investigated in this thesis is a two-bladed rotor. Applicability in TUM's wind tunnel A for dynamic stall experiments in forward flight conditions restricted the rotor diameter to 1.8 m to prevent wind tunnel shear layer interactions with the dynamic stall vortex. The rotor blades' design is specific for dynamic stall research on a rotating pitching airfoil. The blades have a simple geometry, an airfoil with a well-published database for pitching airfoil dynamic stall, and high rigidity. The planform is rectangular with a 0.13 m chord and no twist. The chosen airfoil is a NACA 0012 profile with a 0° tab, see Fig. 2.8. The blades are attached to the blade holder by two 10 mm bolts to prevent lead-lag motion. The full carbon blades have a monolithic root and tip section. The homogeneous airfoil section and aerodynamic efficiency begin at 0.3 R.

The rotor blade's carbon composite layup consists of the pre-impregnated, unidirectional and fabric carbon fibers *SIGRAPREG® U600-0/SD-E501/33%* and *SIGRAPREG® C W200 TW2/2*

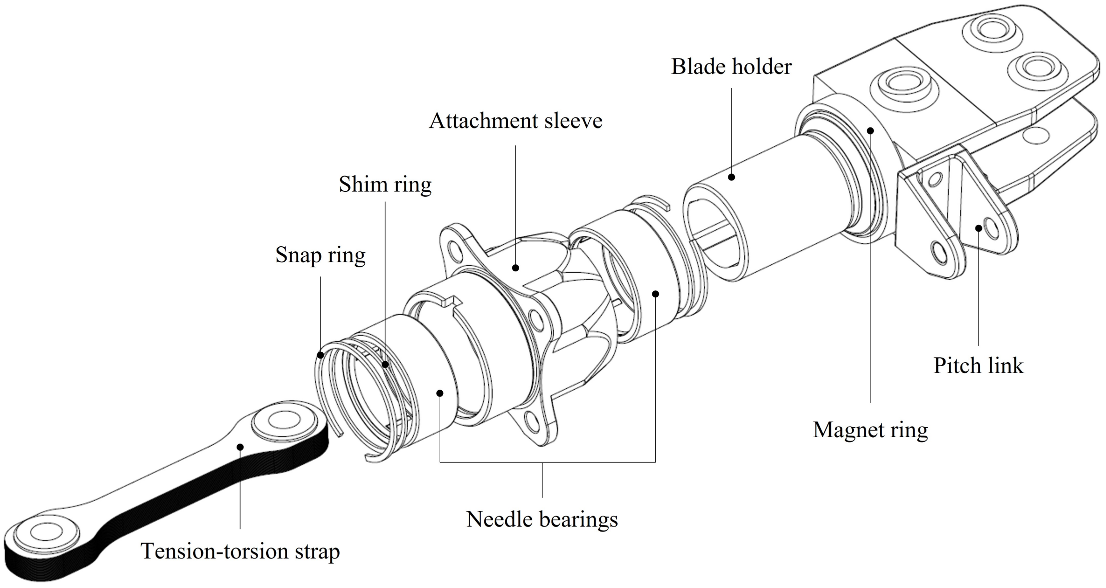

Figure 2.7: Assembly view of the hingeless MERIT blade attachment

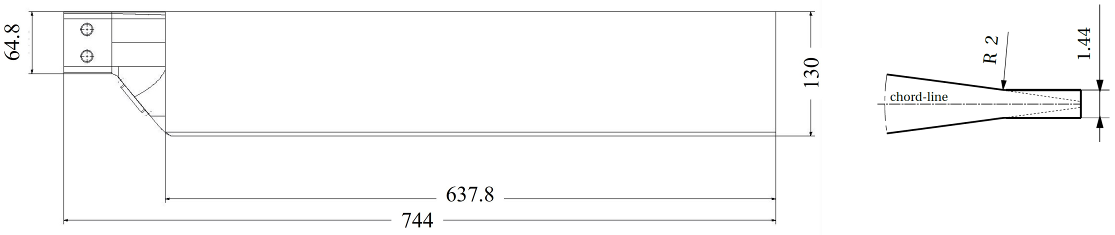

Figure 2.8: MERIT rotor blade sketch and profile tab geometry in mm [22]

E503/45% by *SGL Carbon*. The material properties are derived from coupon tests [31, 128]. The homogeneous section has a divided C-spar with two high-dense *Rohacell® R51 RIMA* foam core halves and a nose lead to shift the cross-sectional center of gravity close to the quarter chord for aeroelastic stability. The ply structure is designed symmetrically to the profile chord to prevent undesirable normal force, bending, or torsional couplings. The cross-section's structure and the location of its structurally characteristic points – mass center, neutral axes, and generalized shear center – are shown in Fig. 2.9.

A titanium balance cell is integrated into the blade tip at the quarter cord to facilitate static rotor balancing up to the quality of G2.5. The holes for the balance cell and the attachment bushings are drilled utilizing positioning devices to provide a position accuracy of at least 0.01 mm. Balance cell and bushing bonding is achieved by small fitting surfaces, which ensure the right adhesive

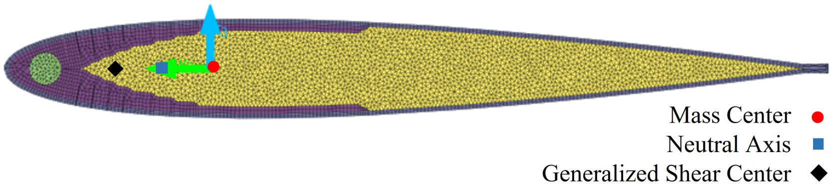

Figure 2.9: Homogeneous NACA 0012 airfoil section of MERIT blade with mass center, neutral axis, and generalized shear center [23]

gap size in addition to accurate positioning. A specifically designed connector plug of the type *GLENAIR Micro-D MWDM 100* can be used as a robust interface for in-blade instrumentation, such as strain gauges, fiber-optical sensors, or pressure sensors. The rotor blades used in this thesis are not instrumented on the inside and use connector surrogates instead. Details on the design and manufacturing process of the rotor blade are given in [23, 129]. Given the presented blade geometry and attachment, the two-bladed MERIT rotor is characterized by the parameters listed in Tab. 2.4.

r_i	r_{CG}	R	c	A	σ	m_{Bl}	γ
$0.276\ m$	$0.513\ m$	$0.9\ m$	$0.13\ m$	$2.54\ m^2$	0.0638	$0.85\ kg$	1.45

Table 2.4: MERIT blade and rotor parameters

Rotor Blade Balancing

The two blades with the Serial Numbers (SNs) *S/N MERIT-A-008-2021-04* and *S/N MERIT-A-007-2021-04* (SN format: rotor system - design version - prototype number - manufacturing year - manufacturing month) are operated in the presented rotor tests. Their respective masses are 833.3 kg and 839.5 kg without balance weights. These blades are statically balanced by storing masses in the tip balance cell, see Fig. 2.10. More details on the static balancing process are shown in [22] and [130]. The rotor is dynamically balanced by small weights, such as washers, at the rotor head and blade attachments as needed.

Figure 2.10: MERIT rotor blade balancing setup [22]

2.3.6 Swashplate and Pitch Control

According to the rotor head, the designed swashplate can actuate four, two, or one rotor blade with counterweight by offering four attachment forks. It contains a spherical brass bearing sliding vertically on the rotor shaft, granting one translational and two rotational degrees of freedom needed for collective and cyclic pitch control, see Fig. 2.11. The swashplate system consists of a rotating component mounted in a non-rotating component by two thin ring ball bearings. It carries two steel sleeves, which can rotate around an inner spherical brass slider on the rotor shaft. A ground steel ring between the steel sleeves provides a fitting gap between the steel and brass components. The steel-brass contact is greased and sealed with two o-rings at its edges. A labyrinth sealing below the thin ring ball bearings prevents grease from leaking and is an ideal contact-free solution for high rotor speeds.

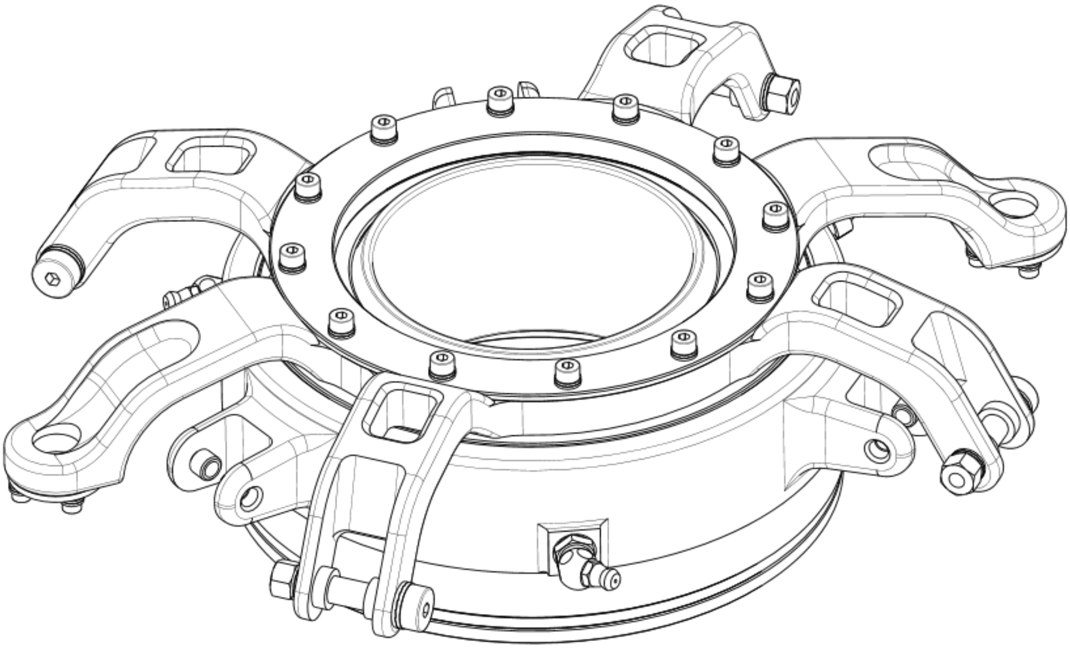

Figure 2.11: Isometric view of the spherical swashplate [22]

Rotating Driver and Swashplate Retainer

The rotating driver transfers the rotor shaft speed to the rotating swashplate components. Its attachment to the shaft is frictional and implemented by a divided clamping sleeve. A pair of hinges and spherical attachments to the rotating swashplate provide the degrees of freedom needed to tilt the swashplate. The swashplate retainer prevents the stationary swashplate components

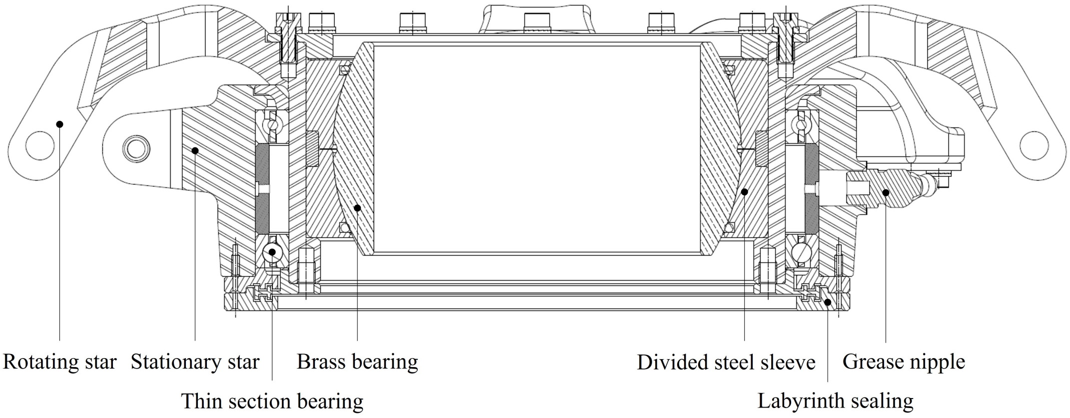

Figure 2.12: Cross-sectional view of the spherical swashplate [22]

from spinning. In addition, it allows the swashplate's tilting movement by a spherical linkage and the vertical translational movement by a respective hinge.

Swashplate Actuation

The spherical swashplate mechanism is needed to pitch the rotor blades collectively and cyclically with a 1/rev motion. The swashplate itself is actuated by three self-contained, linear, electromechanical roller screw actuators with integrated motors of the type *DA67-22-75*, *Diakont*. They are mounted on the shaft bearing cover with a 120° angular offset to each other. Their rod ends are connected to the swashplate with pitch links, which have joint heads at both ends to facilitate swashplate tilting. The roller screw mechanism provides a large contact surface and, thus, a very high accuracy and rigidity. Although roller screw actuators have a very high retention force, they are susceptible to lateral forces. Therefore, a transverse force suspender is installed to reduce side forces on the actuator rod, Fig. 2.13. Detailed actuator parameters are listed in Tab. 2.5.

Max. continuous force	2670	N
Peak force	5560	N
Max. dynamic load	25270	N
Max. speed	208	mm/s
Lead accuracy	0.025/0.3	mm/m
Nominal backlash	0.1	mm
Max. sinus frequency at ± 1 *mm* amplitude	3	Hz

Table 2.5: DA67-22-75 linear roller screw actuator parameters

Each actuator has a maximum lead accuracy of 0.025 mm, which results in an overall maximum pitch angle control accuracy of about 0.025°. The actuated pitch angles range from -30° to +30°. They are indicated with magnetized rings and measured by hall sensors at a maximum accuracy of 0.025°, depending on the resolution of the respective hall sensor.

Actuator Control

Each of the three programmable servo drives of the type *AKD-P00606-NBCC*, *KOLLMORGEN Europe GmbH*, controls one actuator. The three servo drives are controlled by a Programmable Controller Multi-Axis Master (PCMM) of the type *AKC-PCM-M1-120*, *KOLLMORGEN Europe GmbH*, in an EtherCAT cycle. This configuration facilitates the synchronous movement of the actuators to tilt and vertically translate the swashplate. Analogous to the rotor speed control, the actuators can be controlled via the workstation or a fully independent HMI touch panel directly communicating with the PCMM.

The controllable parameters are:

- z_1, z_2, z_3 being the respective actuator rod positions
- $\Theta_0, \Theta_c, \Theta_s$ being the collective and longitudinal and lateral cyclic blade control angles
- $\Theta_{x,SP}, \Theta_{y,SP}, h_{SP}$ being the swashplate tilt angles and the height of the spherical center

Swashplate Kinematics

The equations for the relation between the actuator rod positions z_1, z_2, z_3, the swashplate's tilt angles $\Theta_{x,SP}, \Theta_{y,SP}$ and vertical position h_{SP}, and the blade control angles $\Theta_0, \Theta_S, \Theta_C$ are:

$$\begin{bmatrix} \frac{1}{3} & \frac{1}{3} & \frac{1}{3} \\ 0 & \frac{1}{2r_{SP,i}\cos 30^\circ} & -\frac{1}{2r_{SP,i}\cos 30^\circ} \\ \frac{2}{3r_{SP,i}} & -\frac{1}{3r_{SP,i}} & -\frac{1}{3r_{SP,i}} \end{bmatrix} \begin{bmatrix} z_3 \\ z_1 \\ z_2 \end{bmatrix} = \begin{bmatrix} h_{SP} - l \\ \Theta_{x,SP} \\ \Theta_{y,SP} \end{bmatrix} \tag{2.2}$$

$$\begin{bmatrix} \frac{1}{x_{PH}} & 0 & 0 \\ 0 & -\frac{r_{SP,o}}{x_{PH}} & 0 \\ 0 & 0 & -\frac{r_{SP,o}}{x_{PH}} \end{bmatrix} \underline{\underline{R}} \begin{bmatrix} h_{SP} - l \\ \Theta_{x,SP} \\ \Theta_{y,SP} \end{bmatrix} = \begin{bmatrix} \Theta_0 \\ \Theta_{1C} \\ \Theta_{1S} \end{bmatrix} \tag{2.3}$$

with the rotation matrix

$$\underline{\underline{R}} = \begin{bmatrix} 1 & 0 & 0 \\ 0 & \cos\Delta\Psi & \sin\Delta\Psi \\ 0 & -\sin\Delta\Psi & \cos\Delta\Psi \end{bmatrix} \tag{2.4}$$

and the azimuth dependent blade pitch angle

$$\Theta(\Psi) = \Theta_0 + \Theta_{1C}\cos\Psi + \Theta_{1S}\sin\Psi \tag{2.5}$$

The parameters $l, r_{SP,i}, r_{SP,o}, x_{PH}, \Delta\Psi$ are constants and are dependent on the mechanical components' geometries, see Tab. 2.6.

Short pitch link length	l	74	mm
Radius of stationary (inner) pitch link attachment point	$r_{SP,i}$	113	mm
Radius of rotating (outer) pitch link attachment point	$r_{SP,o}$	140	mm
Radius of pitch horn attachment point from pitch axis	x_{PH}	59.17	mm
Azimuth delta between pitch axis and pitch horn attachment point	$\Delta\Psi$	25	°

Table 2.6: Geometric values for swashplate kinematics

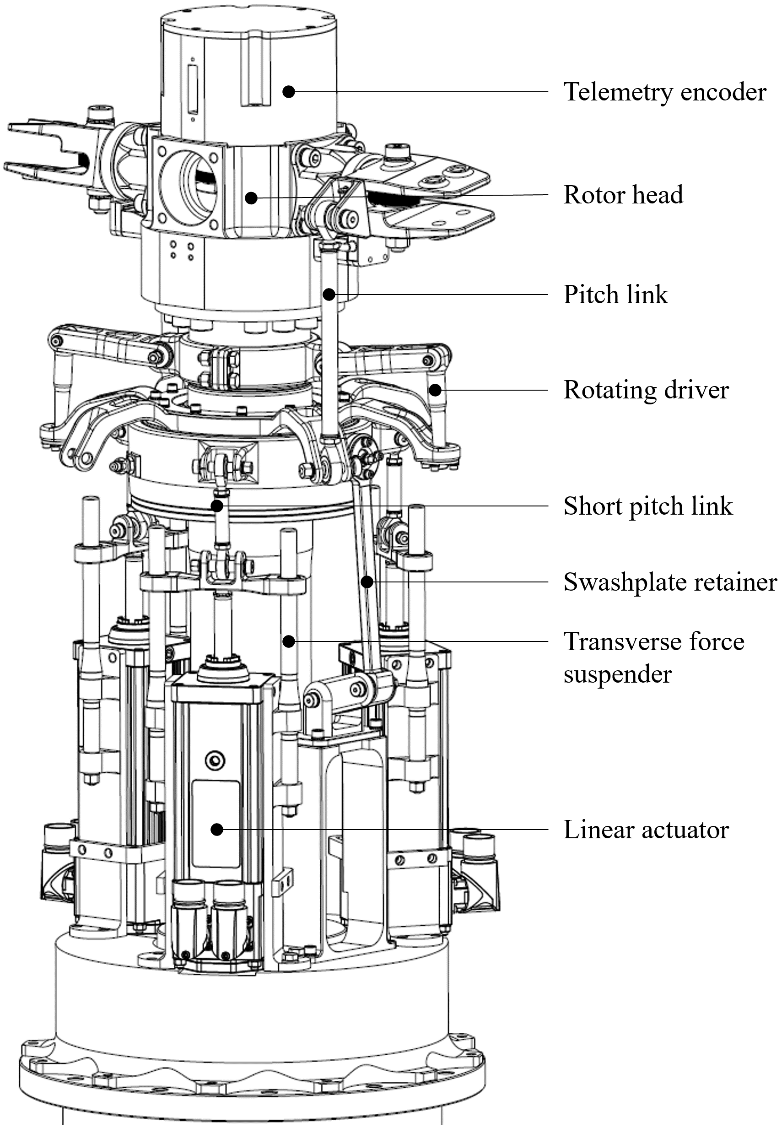

Figure 2.13: MERIT actuation system and blade attachment for a two-bladed rotor

2.3.7 Materials and Surface Treatments

Aluminum

All aluminum parts are made of high-modulus aluminum EN AW 7075. Their surface is hard-anodized with a wall thickening of 25-50 μm, which provides wear and corrosion resistance. To not exceed bearing fit tolerances, the estimated thickening involved in the electrolytic oxidation process is compensated by removing surface material uniformly from each aluminum part in advance.

Steel

The pre-hardened and tempered steel 42CrMo4+QT is used mainly for highly loaded rotating parts. Operation area and load spectra define the needed heat and surface treatments, such as nickel plating, nitriding, and oxidizing. Nickel plating is an effective surface treatment for basic corrosion protection. It is employed on the following rotor components: rotor head, bearing sleeves, pitch links, mounting rings, and hall sensor holders. The thickening of about 10 μm was considered during the manufacturing process. The rotor shaft and blade holders are likewise made of pre-hardened and tempered steel 42CrMo4+QT. They undergo highly dynamic bending and surface loads due to the bearing running surfaces. Therefore, a special surface hardening is necessary, achieved by nitriding. The blade holder is oxidized in addition to nitration to maximize corrosion resistance. Tab. A.2 gives an overview of used materials and surface treatments for the various rotor components.

2.4 Component Tests

Testing the most critical test rig components is necessary for a safe operation. The performed component tests are tensile strength tests of the rotor blade, its bonded balance cell, and the tension-torsion strap. In addition, an experimental modal analysis provides knowledge of eigenfrequencies and mode shapes to identify safe nominal operation speeds. The following sections summarize the most important results.

2.4.1 Steel Frame Experimental Modal Analysis

The Experimental Modal Analysis (EMA) is performed on the steel frame structure, including rotor shaft and bearings, to identify natural frequencies, mode shapes, and damping characteristics of eigenmodes within the operational speed range of up to 3000 RPM (50 Hz). The frame structure is excited with an impact hammer, and its response is measured with accelerometers in a roving accelerometer procedure. The resulting eigenfrequencies and mode shapes are shown in Fig. 2.14.

The main eigenmodes below 50 Hz emerge from the wind tunnel adaptor's long beams and the load cell interface between the bearing frame and the middle frame [24], [131]. Table 2.7 shows

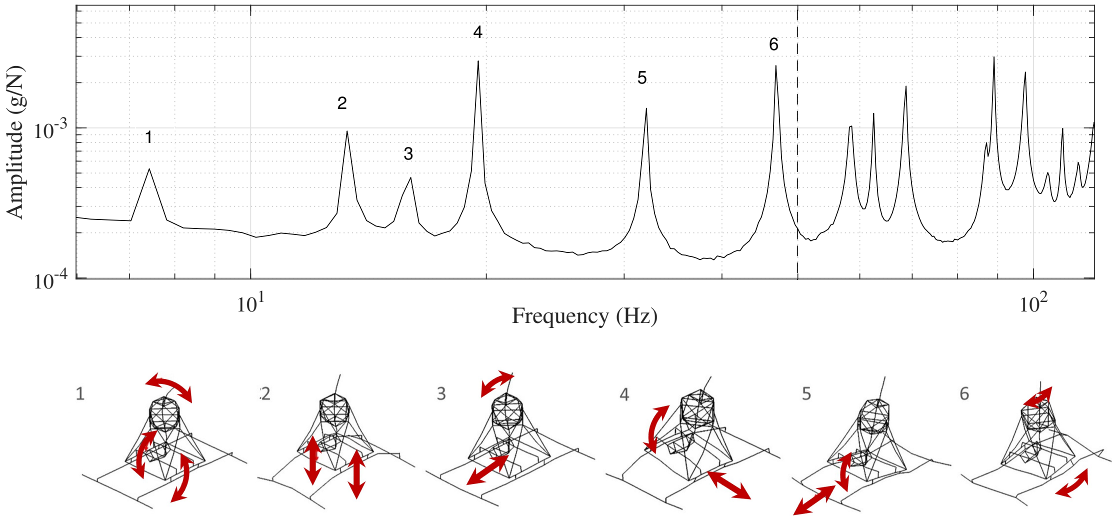

Figure 2.14: EMA eigenfrequencies and mode shapes for the main steel frame eigenmodes up to 100 Hz [24]

the eigenfrequencies identified with the EMA and Finite Element Method (FEM) simulation in Dymore, [132]. The frequencies are allocated using the Modal Assurance Criterion (MAC).

Mode	1	2	3	4	5	6
EMA (Hz)	7.45	13.34	15.81	19.48	31.88	46.97
FEM (Hz)	6.00	11.58	13.31	23.20	44.21	54.98
MAC (-)	0.88	0.96	0.86	0.87	0.89	0.71

Table 2.7: EMA and FEM frequencies, and MAC values for the first six eigenmodes of the steel frame with drive train [24]

2.4.2 Tensile Strength Tests

The tensile strengths of the tension-torsion strap, blade root, and bonded balance cell are complex to predict accurately. However, they are critical because they are liable to very high load cycle numbers within a short time ($1.8 \cdot 10^5$ 1/rev load changes in one hour at 3000 RPM); their failing would cause severe damage. Tab. 2.8 shows each tested component's expected and achieved ultimate loads, see Fig. B.1.

Rotor Blade

The rotor blade's tensile strength is determined by applying axial force at the blade tip*. The weakest section of the rotor blade is expected in the attachment and transition areas, marked

---

*Tests performed at the Institute of Materials Science and Mechanics of Materials, TUM white in Fig. 2.15 left. For a successful axial force introduction at the blade tip without risking premature damage there, the blade tip is modified by adding scarved carbon layers for a smooth stiffness distribution toward the homogeneous profile section. Unexpectedly, the initial failure occurs at the transition between the homogeneous profile section and the section with additional carbon layers at more than twice the expected ultimate load. The observed failure mode is an inter-laminar shear failure of the C-spar, see Fig. 2.15 left.

Balance Cell

Fig. 2.15 on the right shows the setup for the static tensile test[*]. The balance cell's adhesive connection[†] with the monolithic section of the blade tip is tested by applying a tensile force using a threaded pin. In addition to the tensile test machine's integral load cell, a more accurate six-component load cell measures applied forces. As Fig. B.1 shows, the expected ultimate load for the detachment of the balance cell could be exceeded by more than factor eight.

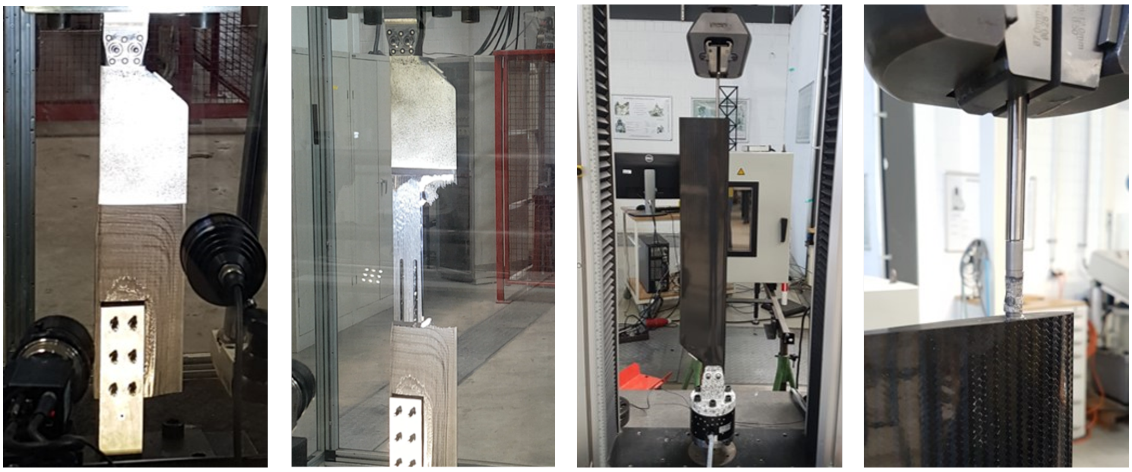

Figure 2.15: Centrifugal force tensile strength test of the MERIT rotor blade (left) and its balance cell (right), [22]

Tension-Torsion Strap

The metal sheet stack carries centrifugal forces from its mass, the mass of the blade holder, and the mass of the blade, see Fig. 2.6. A FEM analysis of the tension-torsion strap under an exemplary axial load of 53 kN by Pfanner [25] shows that the maximum stress values occur at each inner side of the bolt attachment holes suggesting plastic deformation and component failure in these areas, see Fig. 2.16. Nevertheless, these regions underlie singularity problems, so an additional component failure investigation is needed. An experimental reassessment can clarify the reliability of stress prediction in the suspected critical areas. For this purpose, the tension-torsion

---

[*] Tests performed at the Institute of Laboratory for Product Development and Lightweight Design, TUM

[†] Two-component adhesive *3M SCOTCH-WELD EC-9323 B/A*

strap was tested for static tension load failure at zero torsion. Fig. 2.17 shows the 12 mm attachment bolt and tension-torsion strap conditions after the tensile strength test. This test did not provoke a failure of the sheet stack but a ductile shear failure of the bolt instead. The failure load far exceeds the FEM-predicted and expected Ultimate Load (UL) (Fig. B.1).

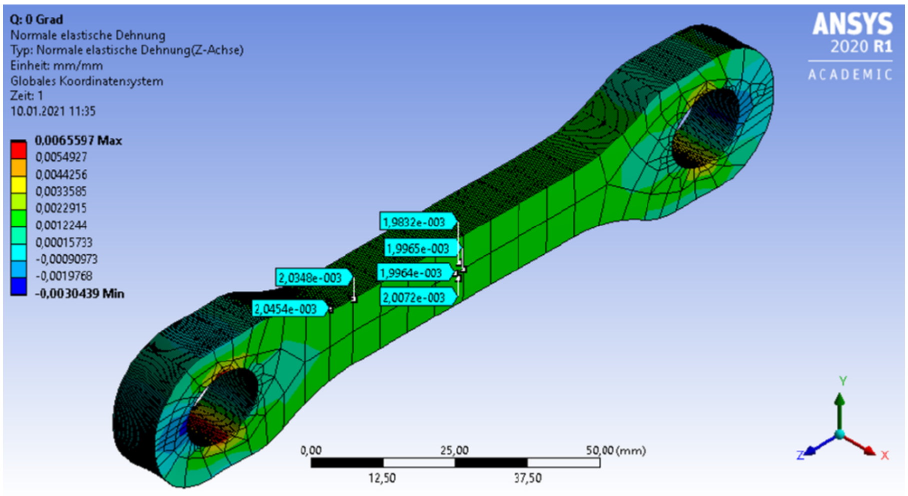

Figure 2.16: FEM simulation of the tension-torsion strap under 53 kN axial load without twist [25]

Figure 2.17: Tension-torsion strap and 12 mm attachment bolt after tensile strength test, actual UL 180 kN

Component	Expected UL (kN)	Actual UL (kN)
Balance cell	1.33	11
Blade	80.69	180
Tension-torsion strap	105.20	180

Table 2.8: Expected and actual ultimate loads of the tensile test components [22]

2.5 Test Rig Instrumentation and Data Acquisition

The following section explains the kind, purpose, and challenges of rotating and stationary sensor data used in this thesis. Available data besides rotor speed are: pitch angles, blade root moments, and pitch link forces in the rotating frame; integrated rotor forces, rotor moments, and rotor torque in the stationary system. Detailed sensor and data acquisition equipment information is summarized in Tab. 2.9.

Rotor Speed and Azimuth Position

The incremental encoder acquires rotor speed and azimuth position, which uses two 90° phase-shifted Transistor-Transistor Logic (TTL) signals and a 0° azimuth impulse once per revolution. Both the rotating and stationary DAQ systems process the rotor's azimuth angle, which is used for data synchronization of rotating and stationary data in post-processing. The incremental encoder generates 1024 pulses per revolution for each of the two TTL signals. Processing the TTL signals' high and low edges provides an azimuth angle accuracy of 0.088°.

2.5.1 Rotating Sensors

Pitch Angles

Two hall sensors of the type *PMIS4-20-20* by *ASM* measure the blade pitch angles indicated by magnet rings of the type *PMIR7-20-90*, which are bonded to the blade grip.

Each hall sensor generates two TTL signals with a ±90° phase shift; the sign depends on the direction of rotation. The processing of high and low slopes of both TTL signals achieves an angular resolution of 0.05° – four times the accuracy shown in the sensor's datasheet. Sosa shows the detailed signal processing in [133] at the example of sensor *PMIS4-40-20*, which provides double resolution compared to sensor *PMIS4-20-20*.

Since the telemetry encoder does not have an integrated counter, the TTL signals have to be sampled with the telemetry's Analog/Digital (A/D) converter. At a specific pitch rate, the telemetry's 20 kHz sampling rate is insufficient to sample each signal edge, leading to a miscount of the pitch angle signal. This problem occurs at high rotor speeds and high cyclic pitch angles. Depending on the measurement task, more or less accurate sensor types should be used to gain maximum accuracy. The experiments in this thesis use sensor *PMIS4-20-20* to provide optimum results with high accuracy for static polar measurements and at high $\dot{\Theta}$ dynamic stall tests simultaneously. A reconstruction of $\Theta(t)$ signals in post-processing provides data for plotting reasons where needed.

Blade Root Moments

Measuring blade loads in the rotating system is challenging for high rotor speeds. An integrated load cell in the blade attachment must account for high centrifugal loads while providing maximum accuracy for blade root forces and moments. These requirements are most often contradictory. Even if they were compliable, off-the-shelf sensors would involve too large dimensions to

integrate into the rotor design. Therefore, blade root moments are attained from strain measurements at the blade root utilizing strain gauge full bridges with pre-calibration to expected loads. The advantage of this load-measuring solution is that load nonlinearities emerging from the free-play in the pitch bearing do not influence measured loads.
Blade root moment data is used for model validation and evaluation of dynamic stall loads in this thesis. In addition, blade torsion in particular serves as complementary data to the measured pitch link forces.

Pitch Link Forces

The rotating pitch links are subject to high bending moments due to centrifugal forces and high dynamic axial loads during dynamic stall due to aerodynamic moments. The initial pitch link design proved too stiff to encounter measurable strain in the axial direction. Therefore, an omega-shaped load cell with high bending stiffness and axial flexibility is designed to measure strain in the axial direction at the expected loads. Each load cell has a pair of linear strain gauge full bridges, which are wired in such a way as to compensate centrifugal load-induced bending, see section 2.6.2.

The measured pitch link forces of the given rotor design are a superposition of various loads: the rotor blade's torsion emerging from aerodynamic and inertia loads and the tension-torsion strap's torsion emerging from its twist and friction between the metal sheets. The tension-torsion strap's torsional load shows a pitch-dependent and speed-dependent hysteresis. A calibration helps to experimentally determine and separate these loads from the blade loads as shown in 2.6.2.

2.5.2 Non-Rotating Sensors

The instrumentation in the non-rotating frame consists of four three component load cells between the bearing frame and the middle frame, measuring the global rotor forces and moments, and the drive coupling unit, measuring torque and rotor speed.

Integrated Rotor Forces and Moments

The four three-component load cells of the type *K3D120-2kN/VA* ±*2kN* by *ME Meßsysteme* measure the global rotor forces and moments and are mounted between the upper bearing frame and the middle frame, see Fig. 2.2. Each load cell has a nominal full-scale force range of ±2 kN in each of the three measuring axes with a reported accuracy of 0.5 %.

The set of load cells is calibrated by applying an axial and transverse force in an interval of 45° azimuthal angle at the rotor head. The force is applied using steel ropes, deflection pulleys, and weights to simulate a calibration load of up to 378 N. More details on the calibration process and results are explained in [133] and [22].

The load cells are used for polar measurements in hover and rotor trim in forward flight conditions. They are susceptible to coupling forces and steel frame dynamics. These loads are superimposed on the rotor loads and should not be relied on solely when analyzing rotor dynamics.

Rotor Torque

The torque sensor *Radex-N 60* is part of the coupling unit of the type *DATAFLEX 32/500*, *KTR*, and uses strain gauges for torsional strain measurement. It is designed for a maximum torque of 500 Nm and has an accuracy of 0.1 % Full Scale (FS). An integrated hardware filter of 1000 Hz is applied to the analog signals before sampling in the DAQ system to diminish electromagnetic disturbance by the synchronous motor. Torque data is used for the calculation of power consumption and investigations of rotor drag, especially during dynamic stall.

2.5.3 Data Acquisition

Two different DAQ systems are used for the rotating and non-rotating sensor data. Rotating sensor data is sampled with 20 kHz, and non-rotating data is sampled with 5 kHz. Table 2.9 summarizes the most significant sensor and DAQ equipment information. Live data processing and monitoring of stationary and rotating sensor data are done with *Labview*, see [133].

Rotating Data Acquisition - Inductive Telemetry

The rotating sensor data is acquired by a 16-bit, 32-channel[*], inductive telemetry system with a sampling rate of 20 kHz per channel by *MANNER Sensortelemetrie GmbH*. Two additional channels process the incremental encoder signal to obtain rotor speed (0-3000 digits) and azimuth position (0-4096 digits). The respective encoder contains an amplifier and A/D converter for each channel and is mounted on top of the rotor head. The availability of the encoder in the rotor system has the advantage of short analog sensor cabling and, therefore, little susceptibility to electromagnetic noise. The digital data cables lead to the power and data coupler (below the lower shaft ball bearing) within the hollow rotor shaft. The coupler is a component that transfers energy and data between stationary and rotating systems. This inductive telemetry data transmission technology is contact-free, space-saving, and maintenance-free. A processing unit assesses digital data and provides the power and voltage needed for the encoder and sensors. The telemetry encoder can acquire any resistance-based sensor data.

Non-Rotating Data Acquisition - CompactRIO

The non-rotating sensor data is acquired and processed with the real-time controller *CompactRIO*, *National Instruments*. The chassis uses an onboard processor and a Linux-based operating system to digitalize and synchronize incoming data. In the scope of this thesis, four *NI9237* Modules (AI 24 Bit, 50 kS/s/ch) for the four three-component load cells, two *NI9401* Modules (5V TTL, 100 ns) for the rotating encoder's TTL signals, and one *NI9205* Module (AI 16 bit, 250 kS/s) for the coupling's torque signal are used.

---

[*] extensible up to 128 channels with the same coupler and high-frequency generator infrastructure

Hall sensors and magnetic rings		
Manufacturer	*ASM*	
Type name of sensor	*PMIS4-20-20*	
Type name of magnet ring	*PMIR7-20-90*	
Max. impulse frequency	120	kHz
Signal periods	1800	
Accuracy	0.05	°
3-Component load cells		
Manufacturer	*ME*	
Type name	*K3D120*	
Nominal force x,y,z	± 2000	N
Max. load	150	%FS
Accuracy class	±0.5	%FS
Crosstalk	1	%
Nominal deformation	0.06	mm
Rotating encoder		
Manufacturer	*Globalencoder*	
Type name	*IH150*	
Pulses	1024	1/rev
Azimuth resolution	0.088	°
Max. speed	4000	RPM
Coupling unit		
Manufacturer	*KTR*	
Type name	*DATAFLEX32*	
Max. torque	500	Nm
Accuracy	±0.1	%FS
Pulses	720	1/rev
Azimuth resolution	0.125	°
Max. speed	7500	RPM
Inductive telemetry		
Manufacturer	*MANNER*	
Number of channels	32	
Sampling rate	20	kS/s
Resolution	16	bit
CompactRIO		
Manufacturer	*NI*	
Type name	*cRIO 9047*	
Timing resolution	12.5	ns
Sample clock frequency max.	10	MHz
Internal storage SSD & RAM	4	GB

Table 2.9: MERIT sensor and data acquisition system information [22]

2.5.4 Data Synchronization

The rotating encoder mounted to the rotor shaft is used by the Telemetry Processing Unit (TPU) to sample data once per revolution at $\Psi = 0^\circ$ azimuth. In addition to the enforced sampling point at $\Psi = 0^\circ$, all data is sampled with a constant time delta of $\Delta t_T = 1/20,000\ s$. The same encoder signal is acquired by the *CompactRIO* controller for synchronization purposes but with a different sampling technique: mere constant time sampling with $\Delta t_A = 1/5,000\ s$.

Initial data synchronization between stationary and rotating data is achieved using the initial $\Psi = 0^\circ$ azimuth position to trigger data acquisition and recording of the *CompactRIO*. The trigger synchronization accuracy depends on the sampling rate and the trigger's minimal impulse width. With a sampling rate of 20 kHz and a minimum impulse width of $3 \cdot 10^{-5}\ s$, the latency lies at maximum 80 μs [133]. The rotating encoder's position signal fed into stationary and rotating DAQ systems provides necessary information for synchronization during data post-processing with a maximum accuracy of 360/4096 deg azimuth in case of rotor speed variations.

An overview of the equipment used for actuator and motor control, sensing, and data acquisition and processing is shown in [22]. The measurement system's architecture with the flow of information is sketched in Fig. 2.18. Note that pressure sensors in these figures are mentioned as examples and not used in this thesis.

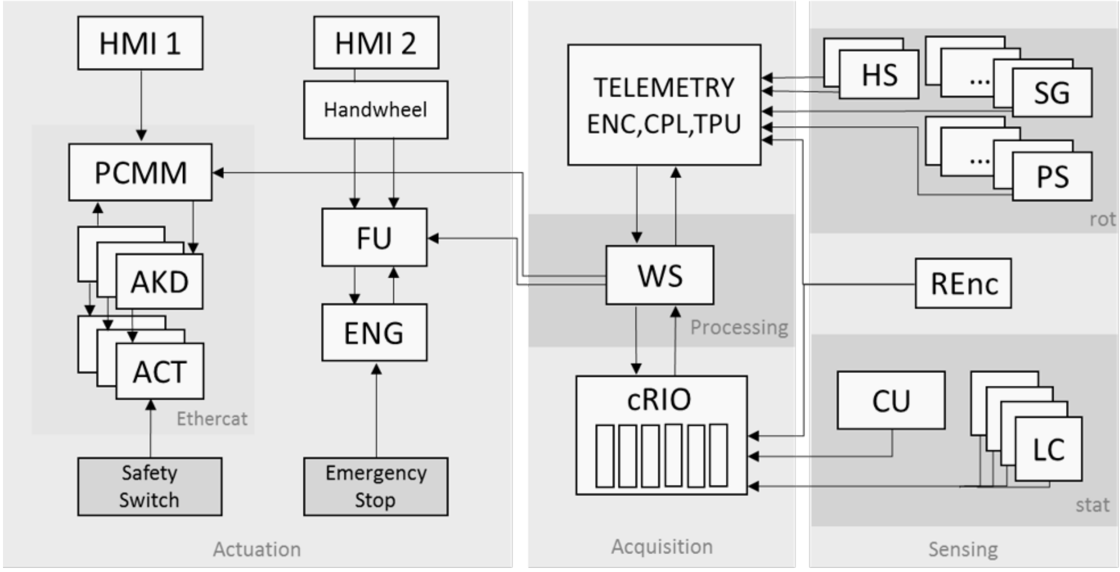

Figure 2.18: MERIT's actuation, sensing, and data acquisition hardware system architecture [22]

2.6 Blade Load Measurement and Calibration

Characterizing the effects of dynamic stall on structural rotor loads emphasizes the need for rotor load measurements. For this purpose, one blade's root and both pitch links were instrumented with strain gauges to measure blade root moments (torsion, flapping, and lead-lag moments) and axial pitch link forces. This section explains how these strain-measuring sensors were applied, wired, and calibrated to provide reliable forces and moments.

2.6.1 Blade Root Moments

Three sets of strain gauge full bridges measure surface strains and provide blade moments at a specific radial station near the blade root.

2.6.1.1 Sensor Choice and Arrangement

The blade root moment sensors are metal-foil strain gauges particularly suitable for alternating load tests with the following requirements mainly relevant for applications on carbon composite materials:

- High resistance ($R_{1,2,3,4} = 1000\ \Omega$) to prevent excessive sensor heating due to carbon's low thermal conductivity
- High measuring grid length (more than five times the fiber distance) to average strain and prevent overloading by stress peaks (empirical grid length for composites $> 6\ mm$ [134]
- Temperature compensation for quartz ($\alpha_T = 0.5\ [10^{-6}/K]$) to prevent temperature-induced strain measurements

The strain gauges of the M series by *Hottinger Brüel & Kjaer GmbH (HBK)* offer maximum fatigue strength using a Modco measuring grid and a high-emperature carrier. Due to their very high stiffness, they are suitable for transducers with high accuracy requirements [134].

To reduce the overall number of sensor channels and prevent temperature influence, Four strain gauges wired into one full bridge are used to measure each blade root moment. Equation 2.6 shows the correlation between full-bridge detuning and strains for equal gauge factor k and $\varepsilon_1 = \varepsilon_3 = -\varepsilon_2 = -\varepsilon_4$ [26]. If wired correctly, the influence of transversal bending, axial elongation, and shear deformations on bending and torsional full bridges is reduced, although not fully nihilated. Placing the strain gauges close and symmetrically to the neutral axis helps minimize cross-coupling effects between the strain gauge measuring values, which is predominantly effective on homogeneous components. However, full compensation is hardly possible on anisotropic materials, such as a composite layup. Fig. 2.19 shows respective wiring and sensor arrangements for bending moments and torsion [26].

$$\frac{\Delta U_{SG}}{U_e} = \frac{1}{4}\left(\frac{\Delta R_1}{R_1} - \frac{\Delta R_2}{R_2} + \frac{\Delta R_3}{R_3} - \frac{\Delta R_4}{R_4}\right) = \frac{k}{4}(\varepsilon_1 - \varepsilon_2 + \varepsilon_3 - \varepsilon_4) = k\,\varepsilon \qquad (2.6)$$

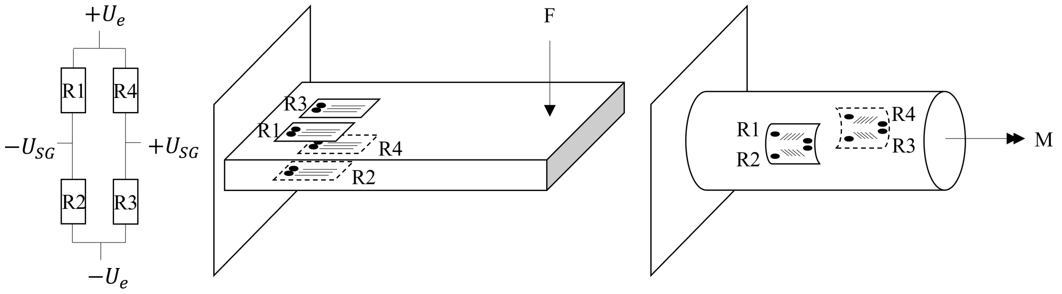

Figure 2.19: Strain gauge sensor arrangement for bending moment and torsion with compensation of unwanted forces and moments [26]

Four linear strain gauges of the type *1-LM16-6/1K0GE*, *HBK*, are used to measure flapping and lead-lag bending moments each. Torsion is obtained by two torsional strain gauges of the type *1-XM46-6/1K0GE*, *HBK*, with two integrated measuring grids each. The upper and lower blade side instrumentation is symmetrical to the chord. Linear and torsional strain gauge sensor properties are given in Tab. A.4.

2.6.1.2 Sensor Positions

Radial and chordwise sensor positions have to be chosen with the goal of gaining maximum strain signals, but minimally disturbing the air flow in the aerodynamic efficient section, at the same time. An experimental strain analysis helps for identifying the most suitable sensor positions in terms of maximum strain values.

Strain Analysis of Static Blade Deformation

Static deformation of the first blade prototype SN001 is measured with the Digital Image Correlation (DIC) system *ARAMIS SRX* by *Carl Zeiss GOM Metrology GmbH*, see Fig. 2.20. The tests aim to validate sectional stiffness properties and identify surface strains for different load cases. A random speckle pattern distributed over the blade defines unique facets that are optically recognized, analyzed in their deformed state, and compared to the undeformed one. Torsion, bending moments, axial and shear forces are applied at the blade tip and measured by a six-component load cell at the blade attachment. The experimentally derived sectional stiffness properties are shown in [23, 129, 135].

The deformation tests show superficial strain distributions along the blade chord and radius. Analyses of various cross-sections at different load cases (flapping shear force, lead-lag shear force, torsion) support a practical position choice for the strain gauges. Fig. 2.21 shows the normal and torsional surface strains ε_Y, ε_{XY} over each section's arc length. The sections are chosen at three radial stations in the inner homogeneous blade area with the radial stations r_1, r_2, r_3. The nomenclature of these radial stations in the test setup coordinate system is Y + 200, 230, 260 mm, which corresponds to the following fraction radii when mounted on the test rig: $r_1 = 0.329\ R$, $r_2 = 0.362\ R$, $r_3 = 0.396\ R$. The shown arc length is approximately 20 mm shorter than the

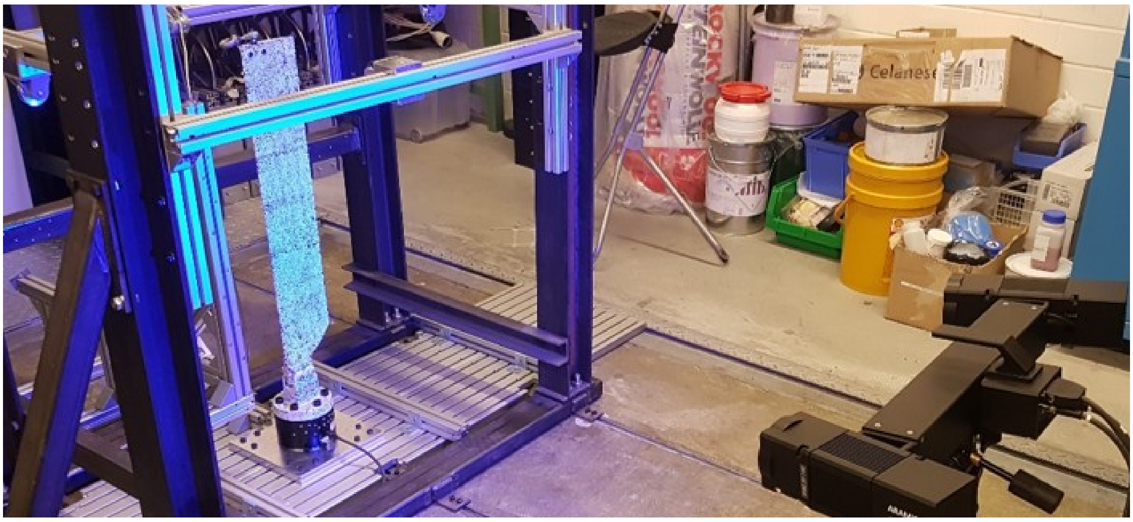

Figure 2.20: Static deformation measurement setup of the first MERIT blade prototype SN001 using DIC [22]

design chord because the analysis surface begins behind the leading edge and ends before the profile tab.

Radial Sensor Position

The most decisive criteria for the radial sensor position are:

1. Homogeneity of the radial section
2. Minimal disturbing effect on aerodynamic efficiency
3. Minimal inertial effects from sensor and cabling masses
4. No influence of stiffening effects by the blade clamping and sensor connector

The graphs in Fig. 2.21 show that the strains' absolute values at r_1 are disproportionally higher than those at r_2 and r_3, especially for the flapping case. This disproportion is probably ascribed to the transition of the homogeneous section to the monolithic section at the blade root. For the most inner section r_1, there is a beginning connector influence, showing a stiffening of the area around it. Concerning the torsional load, the highest absolute strain values occur more outward, although the values vary strongly along the chord, which impedes trend recognition.

All sections offer measurable strains. Given the pre-investigations, the radial sensor position is selected between r_1 and r_2 to reduce connector influence and minimize airflow disturbance. All blade root strain gauges are aligned at radius Y + 208 or $r = 0.338$ R respectively, see Fig. 2.22.

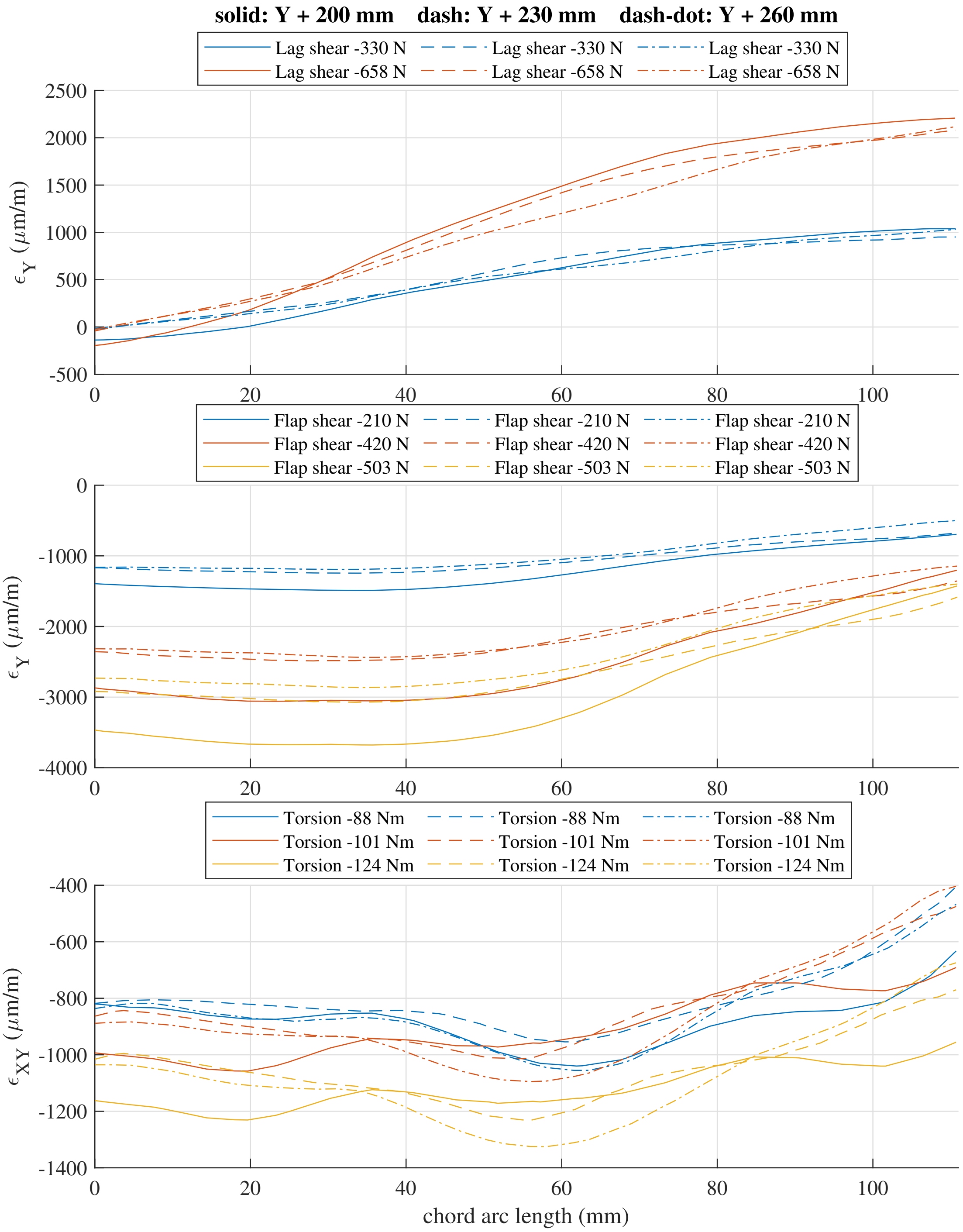

Figure 2.21: Normal and torsional strain distributions along the chord arc length from DIC measurements at three different radial stations and different load cases (flap shear force, lead-lag shear force, torsion)

Chordwise Sensor Position

The chordwise position is a trade-off between space restrictions and strain measurability. The experimental strain analyses for the sections r_1 and r_2 at different loads are used to identify suitable areas for each sensor group.

The flapping moment causes maximal strains at the highest profile thickness, as the data in Fig. 2.21 confirms. Therefore, 0-50 mm arc length ($\approx 8-46$ % design chord) is appropriate for applying flapping-moment strain gauges.
The lead-lag moment is most reliable when using strains with a maximum chordwise distance from each other. The steepest, almost linear axial strain slope is observable from 0 to 80 mm arc length ($\approx 8-69$ %). The slope decreases significantly beyond this range. Therefore, the optimal positions for lead-lag moment strain gauges are close to the leading edge and 80 mm arc length.
The torsional strains show up to three local minima along the chord. Nonregarding local strain fluctuations, a trend to lower strains towards the trailing edge is visible, predominantly decreasing after 80 mm arc length but still leaving enough measurable strain at 100 mm arc length (≈ 85 % chord).

Fig. 2.22 shows the final radial and chordwise sensor positions. The strain gauges are applied at blade SN007. Note that the torsional strain gauges were installed at 80 % for initial feasibility studies and left at their position, although higher strains could have been measurable at 50 or 60 % chord.

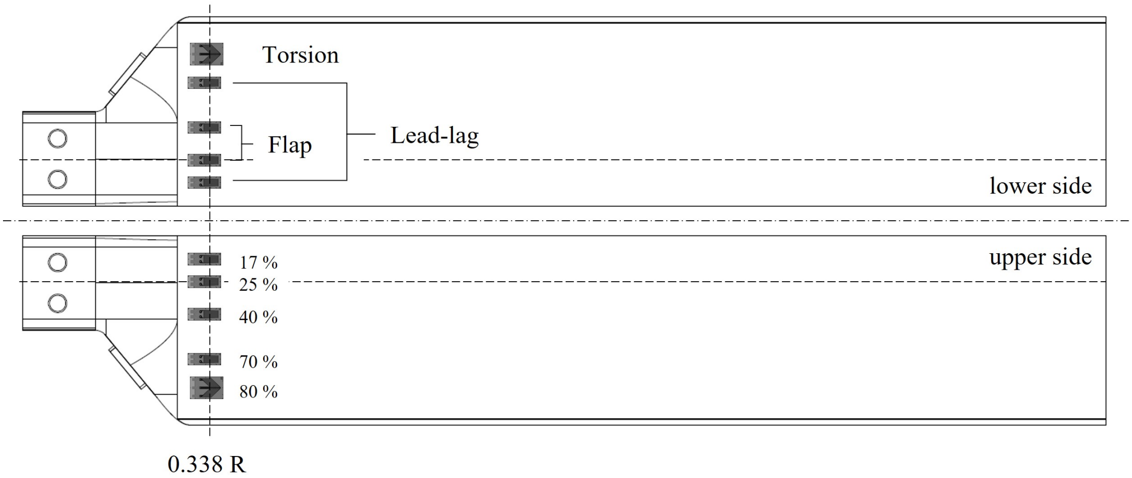

Figure 2.22: Radial and chordwise blade root strain gauge positions on SN007

All pairs of sensors are mounted on the blade surface and symmetrically to the profile chord. The full bridge cabling is symmetrical to the profile chord as shown in Fig. 2.19 to measure the resulting bending and torsional strains and to compensate for other influences such as temperature changes or axial forces. However, the anisotropic properties of composites limit the compensation possibilities due to inhomogeneous stress distribution and structural couplings. Therefore, the blade root moment sensors must be calibrated.

2.6.1.3 Calibration

Calibration Setup

Strain gauge sensors are calibrated in a setup with a six-component load cell at the blade attachment to measure applied forces and moments. To apply axial force at the blade tip, the first prototype blade, SN001, is modified. It has an extended monolithic blade tip with integral bushings for two-bolt mounting designed for a maximum axial force of $30,000\ N$. Torsional twist is applied to the blade tip using a test setup with rollers and steel cables as described in [135], while combined axial and shear forces are applied using the laboratory crane at a maximum axial force of $20,000\ N$, see Fig. 2.23.

The root of the SN001 blade is instrumented with the same sensors at the same positions as the SN007 blade. The calibration blade is attached to the load cell by means of an adapter whose blade attachment geometry is similar to that of the blade holder used for the rotational tests. The reference moments $M_\beta, M_\zeta, M_\theta$ at the strain gauge radial station r_{SG} can be calculated by knowing the load position and using all the forces and moments measured with the six component load cell.

Calibration matrix

Calibration of strain gauges, which is a procedure to gain physical load entities in Nm from bridge detuning values in Volts, is a challenging task, when they are applied on anisotropic materials, due to non-uniform stress distribution and nonlinear coupling effects. The following calibration process assumes that cross-coupling effects and axial force influences on bending moments are linear within the expected operational range.

To calculate the calibration matrix K, positive and negative flapping, lead-lag, and torsional moments are used independently and in combination. The sensor data are measured with a digital amplifier of the type *GSV8-DS*, *ME-Meßsysteme GmbH*, at a sampling rate of 100 Hz with an excitation voltage of $U_e = 5V$ and an input sensitivity of $3.5\frac{mV}{V}$. With n sampling points, the measured full-bridge detuning ΔU_{SG} in volts results in the corresponding strain ε_{SG} calculated as follows:

$$\frac{\Delta U_{SG}}{U_e} = k\ \varepsilon_{SG} \tag{2.7}$$

With the respective gauge factors k_{LM} for the flapping and lead-lag moments, and k_{XM} for the torsional moment:

$$\varepsilon_{SG} = \begin{bmatrix} \varepsilon_{\beta,SG} \\ \varepsilon_{\zeta,SG} \\ \varepsilon_{\theta,SG} \\ F_{z,6LC} \end{bmatrix} = \begin{bmatrix} \frac{\Delta U_{\beta,SG}}{U_e\ k_{LM}} \\ \frac{\Delta U_{\zeta,SG}}{U_e\ k_{LM}} \\ \frac{\Delta U_{\theta,SG}}{U_e\ k_{XM}} \\ F_{z,6LC} \end{bmatrix}, \quad dim(\varepsilon_{SG}) = 4\ x\ n \tag{2.8}$$

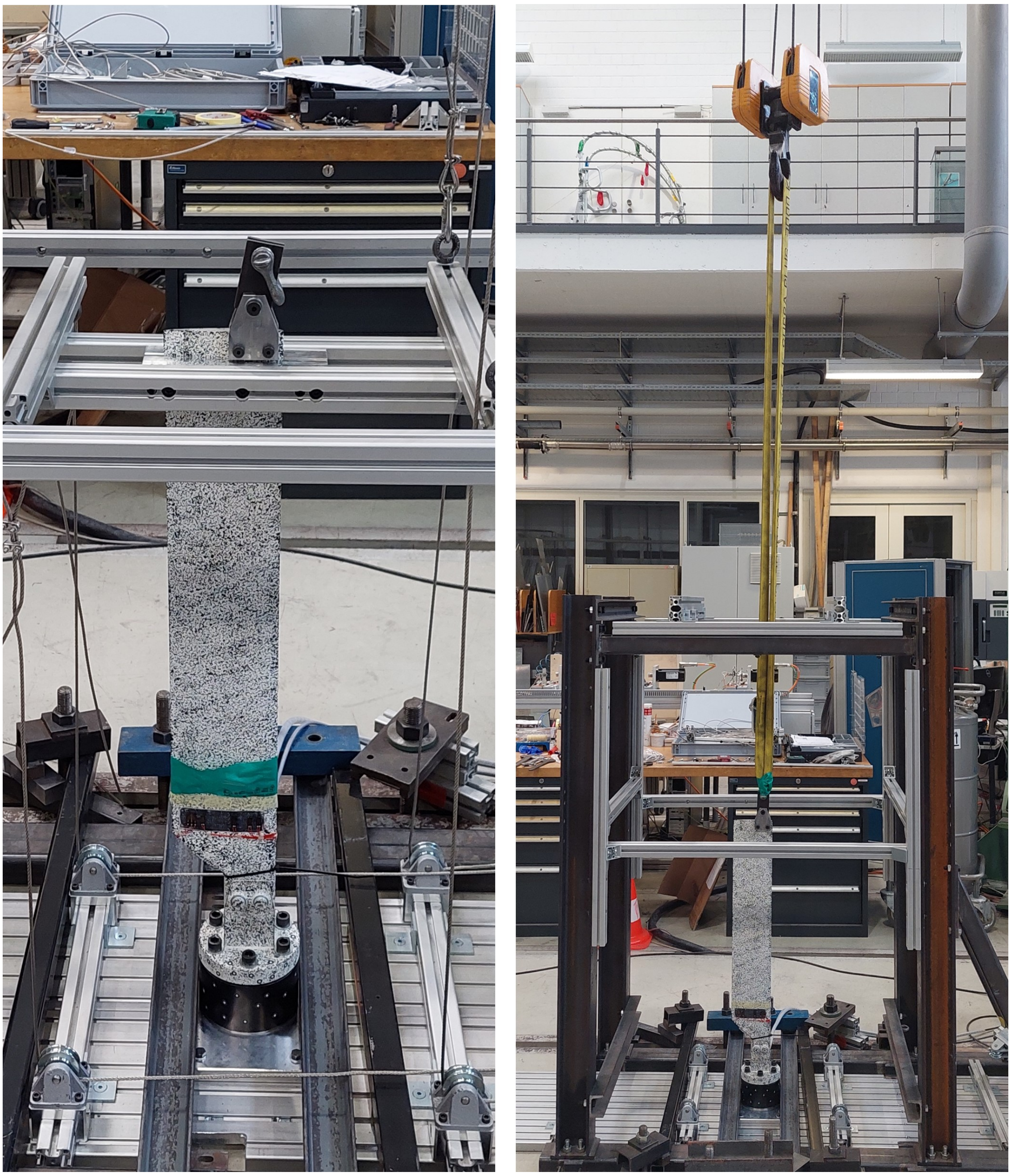

Figure 2.23: Calibration setup for rotor blade SN001 with blade tip load application and lab crane connection tools for gaining calibration matrices K_{001} and K_{001,F_z}

$F_{z,6LC}$ is the measured axial load cell force in. The reference moments at the radial strain gauge station are calculated from the load cell forces and moments and the distance of the radial strain gauge station from the six-component load cell coordinate origin $a_3 = 0.208\ m$:

$$M_{ref} = \begin{bmatrix} M_{x,6LC} + a_3 F_{y,6LC} \\ M_{y,6LC} - a_3\ F_{x,6LC} \\ M_{z,6LC} \\ F_{z,6LC} \end{bmatrix}, \quad dim(M_{ref}) = 4\ x\ n \tag{2.9}$$

The inverse of the desired calibration matrix K with $dim(K) = 4\ x\ 4$ is obtained by:

$$A = \varepsilon_{SG}\, M_{ref}^{-1} \quad \wedge \quad K = A^{-1} \tag{2.10}$$

Calibration Application

The identified calibration matrix can now be applied to the strains, calculated from the measured full bridge detunings, and the underlying axial force $F_{z,i}$.

$$M_{SG} = K \begin{bmatrix} \varepsilon_{\beta,SG} \\ \varepsilon_{\zeta,SG} \\ \varepsilon_{\theta,SG} \\ F_{z,i} \end{bmatrix} \tag{2.11}$$

As the axial forces are not measured, they are replaced by the calculated axial sectional force (at the radial strain gauge position of $r = 0.338\ R$) resulting from the centrifugal acceleration as a function of speed (900, 1200, 1500 RPM) and give:

$$\begin{aligned} F_{z,900} &= 3300\ N \\ F_{z,1200} &= 5872\ N \\ F_{z,1500} &= 9178\ N \end{aligned}$$

These forces assume perfect mass distribution within the blade and do not include additional mass from blade instrumentation or trim mass in the balance cell.

Calibration Results

Different calibration matrices are identified for different blades and configurations. Axial force is shown to have a non-compensable influence on the measured strains and their couplings. To estimate the amount of influence, the calibration matrices of blade SN001 with and without axial load are compared. As SN001 is the only blade capable of absorbing high axial forces, the transferability to the rotating blade SN007 must also be investigated. Therefore, three calibration matrices are analyzed and compared.

1. K_{001} for blade SN001 without axial load influence

2. K_{001,F_z} for blade SN001 with axial load influence

3. K_{007} for blade SN007 without axial load influence

Matrices 2.12 and 2.13 show that the axial load changes the coupling values slightly, while the diagonal entries remain almost the same. However, the axial force has a non-negligible influence on the flapping and lead-lag strains.

$$K_{001} = \begin{bmatrix} 0.1246 & -0.0027 & -0.0051 & 0 \\ -0.0062 & 0.4405 & 0.0177 & 0 \\ 0.0012 & 0.0076 & 0.0951 & 0 \\ 0 & 0 & 0 & 1 \end{bmatrix} \tag{2.12}$$

$$K_{001,Fz} = \begin{bmatrix} 0.1225 & -0.0049 & -0.0024 & -0.0013 \\ -0.0055 & 0.4311 & 0.0175 & 0.0053 \\ 0.0073 & 0.0070 & 0.0960 & -0.0001 \\ 0 & 0 & 0 & 1 \end{bmatrix} \tag{2.13}$$

However, the calibration matrices identified by the scheme described above are not unique. In particular, the coupling terms vary depending on the load level and load combination considered for calibration. Therefore, loads and load combinations, which are similar to the estimated loads, are selected for calibration. The calibration load data set is shown in Fig. 2.25, where the reference moments are compared with the calibrated moments for the example of blade SN007.

Blade SN007 cannot be calibrated under axial load, but its influence is not negligible as shown for blade SN001. The influence of the axial load must therefore be applied to blade SN007. To do this, blade SN007 is first calibrated without axial load, see Fig. 2.24. For this purpose, a data set of different load cases was used to identify the calibration matrix. 80% of the data points are randomly chosen and used to train the matrix, while the remaining 20% are used to test the calibration matrix in a single run.

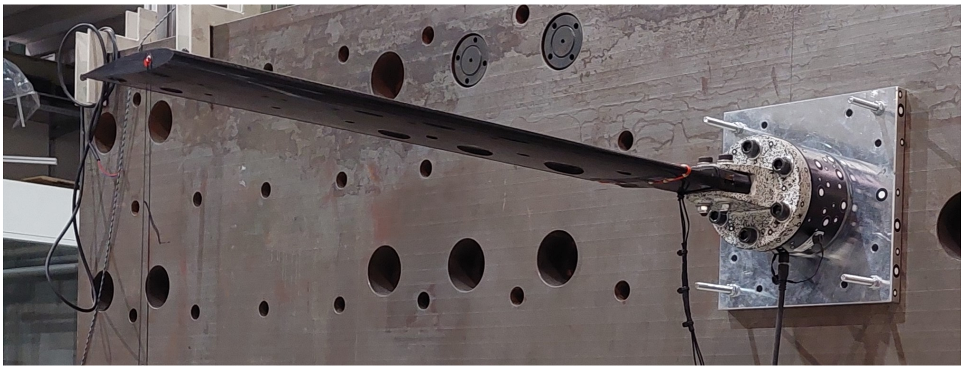

Figure 2.24: Calibration setup with SN007 and six-component load cell for gaining calibration matrix K_{007}

After one hundred runs in total, the mean of the resulting calibration matrix is:

$$K_{007,\mu} = \begin{bmatrix} 0.1132 & -0.0007 & -0.0019 & 0 \\ 0.0102 & 0.4375 & 0.0013 & 0 \\ 0.0030 & -0.0021 & 0.0957 & 0 \\ 0 & 0 & 0 & 1 \end{bmatrix} \tag{2.14}$$

with a standard deviation of

$$K_{007,\sigma} = \begin{bmatrix} 1.4\cdot10^{-6} & 5.9\cdot10^{-6} & 8.5\cdot10^{-6} & 0 \\ 2.5\cdot10^{-6} & 1.9\cdot10^{-5} & 2.8\cdot10^{-5} & 0 \\ 2.9\cdot10^{-6} & 4.6\cdot10^{-6} & 1.7\cdot10^{-5} & 0 \\ 0 & 0 & 0 & 1 \end{bmatrix} \tag{2.15}$$

A comparison between K_{007} and K_{001} shows that there are noticeable differences in the diagonal entries and especially in the coupling terms. This may be due to the additional stiffening of the blade at the extended tip, but also to manufacturing inaccuracies. Nevertheless, Fig. 2.25 and 2.26 show very satisfactory agreements between the reference moments and the calibrated moments.

In addition, to account for the axial force, the last column in $K_{001,Fz}$ is superimposed on K_{007}. Tab. 2.10 shows, that there is no significant difference in the Root Mean Square Error (RMSE) between $K_{001,Fz}$ and K_{001} superimposed on the last column of $K_{001,Fz}$.

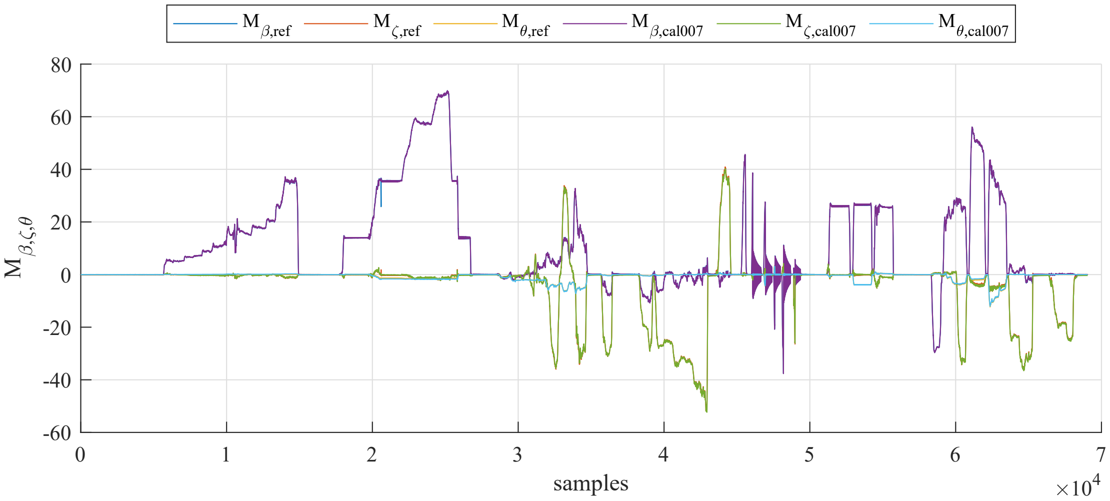

Figure 2.25: Calibration load data; reference moments compared to calibrated moments of SN007 using K_{007}; RMSE: $e_{M_\beta} = 0.30\,Nm$, $e_{M_\zeta} = 0.19\,Nm$, $e_{M_\theta} = 0.12\,Nm$, see Tab. 2.10

In order to obtain a quantitative evaluation of the calibration differences between SN007 and SN001, and with or without axial force influence, the RMSE of the blade moments $M_\zeta, M_\beta, M_\theta$

	SN001, with Fz			SN001, no Fz			SN007, no Fz		
RMSE	M_β	M_ζ	M_θ	M_β	M_ζ	M_θ	M_β	M_ζ	M_θ
K001-Ref	10.10	41.38	1.17	0.25	0.29	0.17	2.03	3.08	0.46
K001+KFz - Ref	0.49	0.65	0.39	-	-	-	-	-	-
K001Fz - Ref	0.49	0.65	0.39	0.25	0.29	0.17	2.03	3.08	0.46
K007 - Ref	-	-	-	-	-	-	0.30	0.19	0.12

Table 2.10: Root mean square errors between blade moments $M_\zeta, M_\beta, M_\theta$ with different calibration matrix applications and their respective reference moments

with different calibration matrix applications and their respective reference moments are calculated and listed in Tab. 2.10.

The main observations are:

1. Adding the axial force influence has a significant influence on the RMSE.
2. There is a noticeable difference between SN001 and SN007 calibration results.
3. There is no difference between calibration matrix identification with axial force and adding axial force components to the calibration identified for $Fz = 0$.

The following conclusions are drawn from these observations:

1. Calibration matrix K_{007} renders the most accurate results with the influence of F_z in the calibration matrix, that can not be neglected.
2. Calibration matrix K_{007} can be superposed with the last column of $K_{001,Fz}$ assuming, that F_z is known and that the axial force influence on both blades is identical and linear.

Note that the axial load is applied at two attachment points on the blade tip, while the blade experiences centrifugal acceleration at each differential mass element as it rotates. This is approximated by using the calculated axial blade section load as the acting force.
The matrix used this thesis is given in the equation 2.16.

$$K_{007+F_z} = \begin{bmatrix} 0.1132 & -0.0007 & -0.0019 & \mathit{-0.0013} \\ 0.0102 & 0.4375 & 0.0013 & \mathit{0.0053} \\ 0.0030 & -0.0021 & 0.0957 & \mathit{-0.0001} \\ \mathit{0} & \mathit{0} & \mathit{0} & \mathit{1} \end{bmatrix} \tag{2.16}$$

Table 2.11 shows the condition numbers of the obtained calibration matrices. The condition number of a matrix is a measure of how close the matrix is to being singular; a matrix with a large condition number is nearly singular, whereas a matrix with a condition number close to 1 is far from being singular [136]. The condition number is therefore a very useful quantity in assessing the accuracy of solutions to linear systems [136].

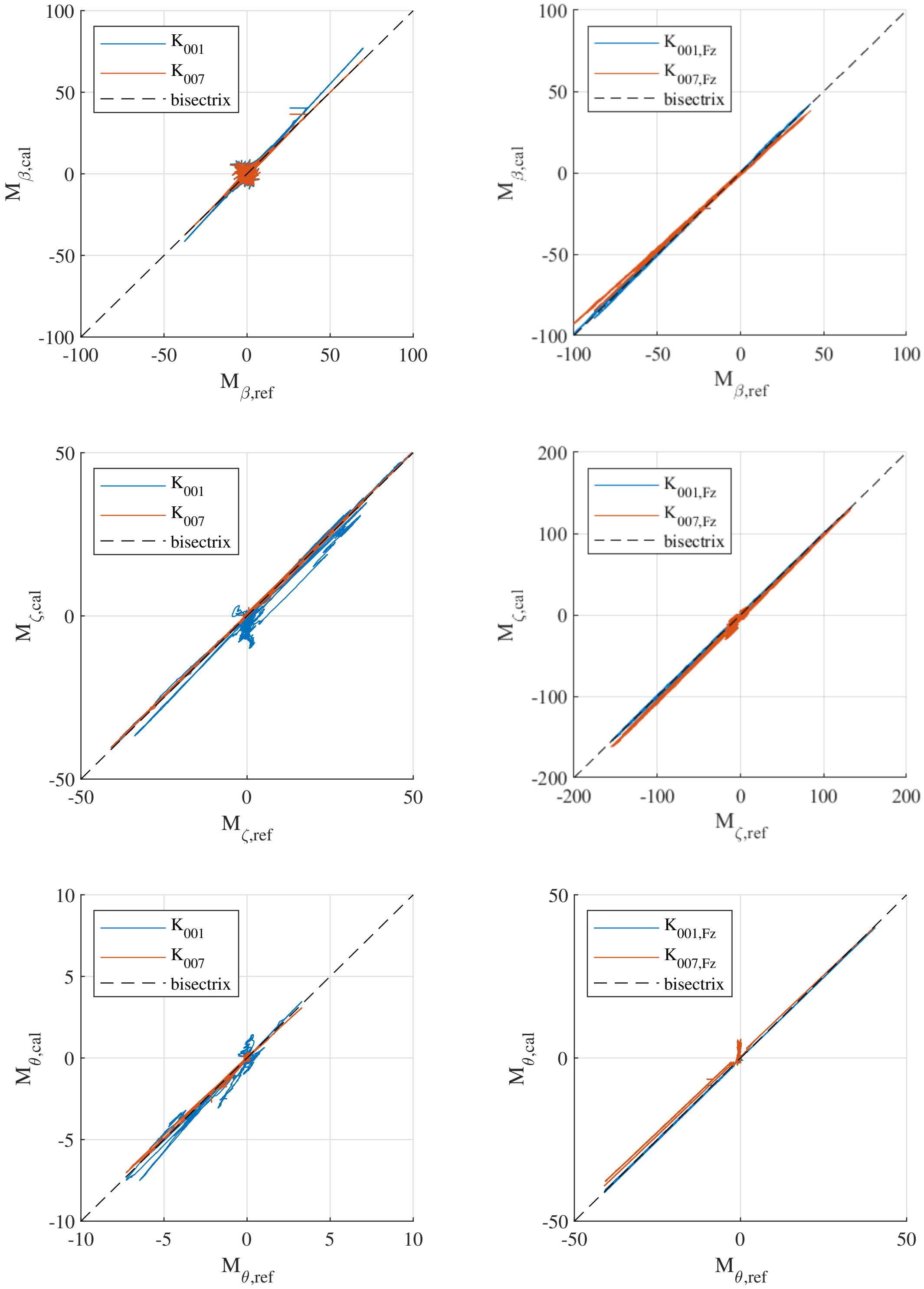

Figure 2.26: Calibrated moment correlation with reference moments and calibration matrices K_{001} and K_{007} applied on blade SN007 without axial force correction (left column), and blade SN001 with axial force correction (right column)

K_{001}	K_{001,F_z}	K_{007}	K_{007+F_z}
4.66	10.47	4.57	10.45

Table 2.11: Condition numbers of the various calibration matrices

2.6.2 Axial Pitch Link Forces

The main function of the pitch links is to provide a backlash-free connection between the swashplate and the pitch horn with minimal deformation to maintain a constant pitch angle even at high vibration levels during dynamic stall and rotor speeds up to 3000 RPM.

At the 140 mm radial position, the pitch links experience much higher strains due to centrifugal bending moments than the axial force strains due to aerodynamic moments. The ratio of bending moment strains at 1500 RPM to the smallest measurable axial force, 0.5 N, is in the order of 10^5. The pitch link itself is designed to withstand bending moments up to 3000 RPM. A 12 mm diameter hollow steel rod is used for this purpose. However, this steel rod is too stiff to detect strains induced by axial forces with acceptable accuracy. In this thesis, maximum axial pitch link forces of 500 N are expected. With a 0.1% FS accuracy, at least 0.5 N should be detectable, which corresponds to a calculated minimum strain of 0.01 $\frac{\mu m}{m}$. This value is too small to be accurately measured with strain gauges applied directly to the pre-designed steel pitch links.

Consequently, a load cell is designed that is resistant to bending but sensitive to axial force. An omega-shaped aluminum component, as shown in Fig. 2.27, based on the design in [137], meets these requirements, as the finite element calculation shows, see Fig. 2.27 left.

2.6.2.1 Instrumentation

Each omega-shaped load cell is instrumented with two full bridges of linear strain gauges of the type *1-LA13K3/350_E*, *HBK*, with temperature compensation for aluminum ($\alpha_T = 23 \cdot 10^{-6}/K$), see Tab. A.4. Referring to section 2.6.1, Fig. 2.19, each leg is instrumented with four linear strain gauges like a bending beam. In this way, the full bridges compensate for transverse bending due to centrifugal acceleration. However, perfect alignment of the omega region perpendicular to its centrifugal force cannot be guaranteed. In addition, the orientation changes slightly with the pitch angle. Therefore, the resulting axial pitch link force is obtained by averaging the full-bridge detunings of the left and right legs and a static load calibration factor. Fig. 2.27 on the right summarizes the initial design, the subsequent design development with integrated omega-shaped

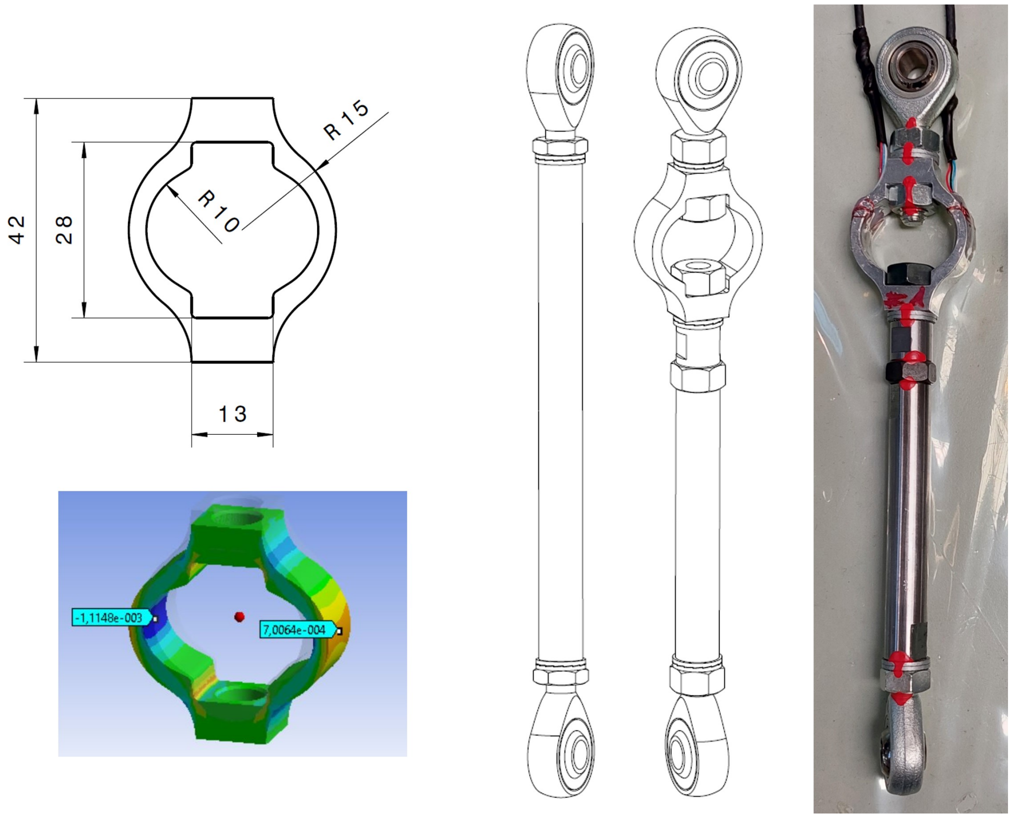

Figure 2.27: Omega-shaped load cell geometry and its elastic strain simulation in ANSYS Mechanical at 500 N compression force (left); pitch link design with and without load cell (middle); fully instrumented pitch link as used in rotating tests (right)

load cell, and the final instrumented version.

2.6.2.2 Calibration

Each load cell must be calibrated to determine load cell stiffness. This must be done statically and dynamically while rotating on the test stand to account for any tension-torsion strap influence.

Static Calibration

Static calibration is performed in two different ways: by applying a tensile force in the tensile testing machine and by applying a compressive force to the highly sensitive three-component load cell of the type *K3R70, ME Meßsysteme GmbH* by applying weights (Fig. 2.28).

The strain gauge averages of both load cells are shown in Fig. 2.29 as a function of axial tension/-compression force. A linear regression fit through both load cell calibration data points yields the following equation:

$$\varepsilon = -1.76\, F_{PL,1/2} - 2.24 \tag{2.17}$$

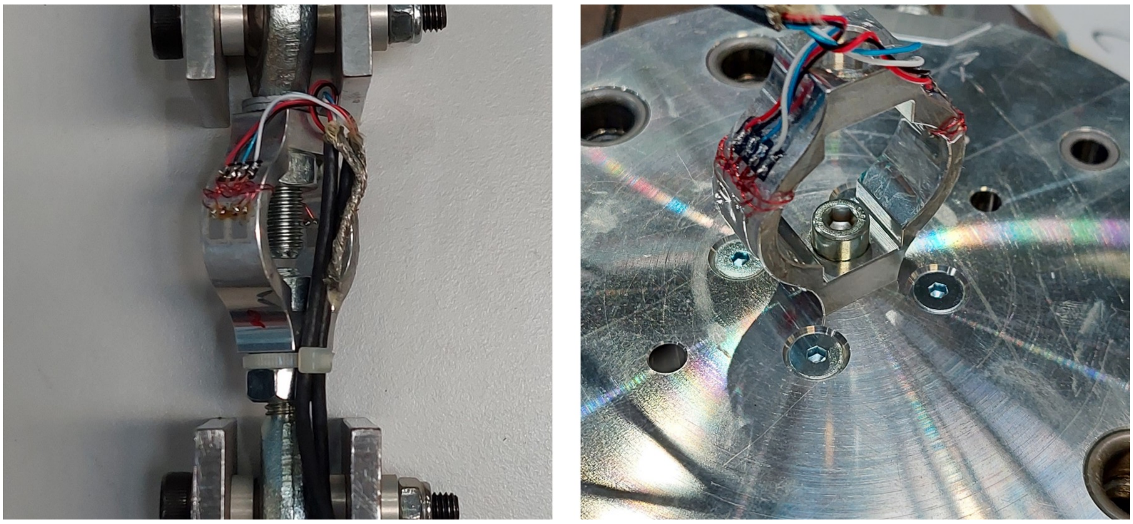

Figure 2.28: Omega-shaped load cell calibration in tension (left) and push force (right) setup

Mind that positive pitch link forces indicate axial pressure.

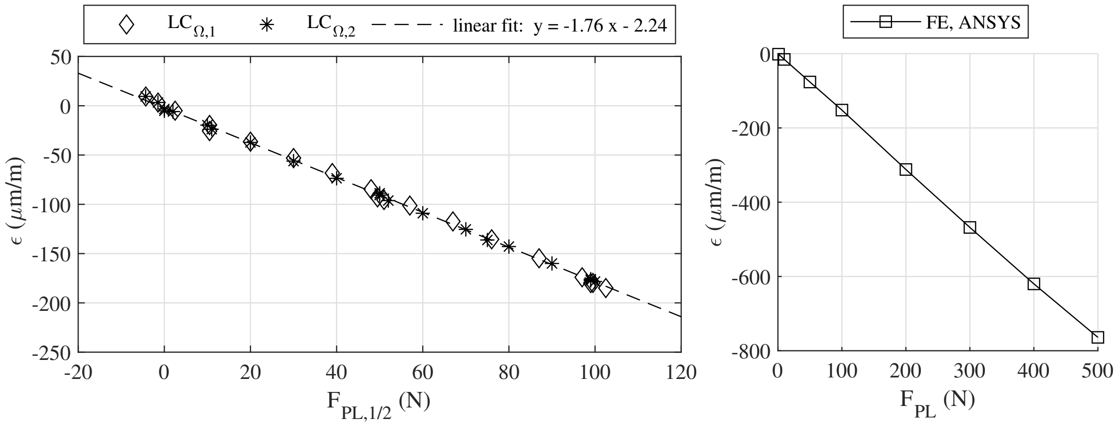

Figure 2.29: Calibration results of the pitch link load cells under axial load and FEM analysis results in ANSYS Mechanical

Dynamic Calibration

The pitch link load cells are introduced to measure axial loads resulting from aerodynamic blade moments. However, the torsional blade load is partially suspended by the tension-torsion strap, which accounts for the centrifugal blade load. Due to the friction between the metal sheets in the tension-torsion strap, this effect increases with higher rotor speeds and twist angles.

To quantify and analyze the load flow, a dynamic calibration test is required to simulate the centrifugal force without aerodynamic loads. For this purpose, steel blade weights (Fig. 2.30) are designed to have the same resulting centrifugal force as a blade at the same rotor speed. In addition, the torsional moment of inertia of the calibration weight is designed to be the same as that of the blade: $I_{\Theta,weight} = I_{\Theta,blade} = 8.4 \cdot 10^{-4}\ kgm^2$. With these, the pitch link forces are measured at the three relevant speeds of 900, 1200, and 1500 RPM, as well as the collective pitch Θ_0 from -4° to +24°. Each pitch angle is held constant for about 10 seconds, and the pitch link loads are biased at 0° pitch and 0 RPM.

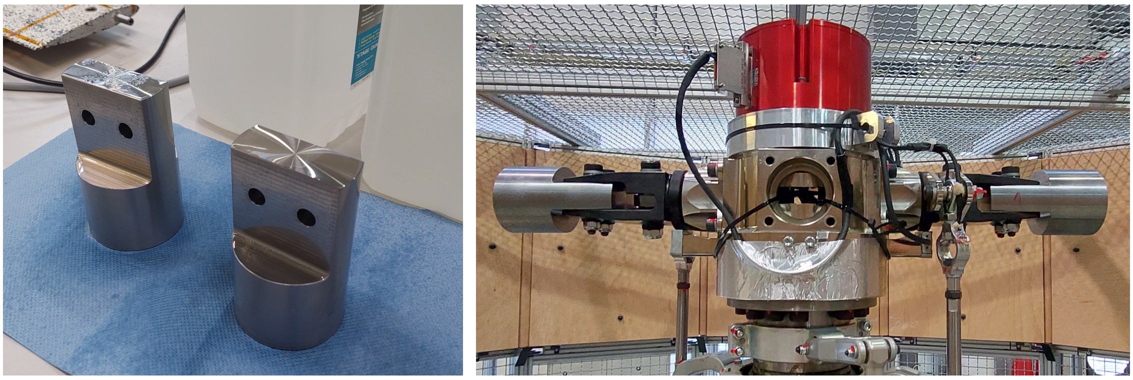

Figure 2.30: Pitch link calibration weights and setup on the rotor to identify the nonlinear structural load influence of the tension-torsion straps without aerodynamic blade loads

The calibration results for the pitch link forces as a function of collective pitch for all three rotor speeds are shown in Fig. 2.31.

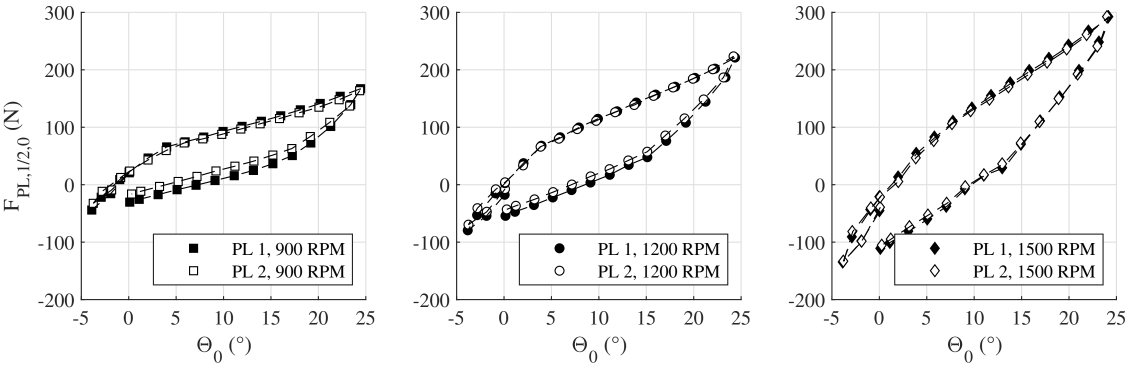

Figure 2.31: Pitch link forces from tension-torsion strap measured at 900, 1200, 1500 RPM with calibration weights simulating centrifugal forces

The following observations can be drawn from these measurements:

- The pitch link forces are in the same order of magnitude as the calculated pitch link forces resulting from aerodynamic moments and are therefore not to be neglected.

- The pitch link forces show a strong hysteresis for pitch angle variations.
- The torsional stiffness of the tension-torsion strap increases with rotor speed.
- Hystereses increase with rotor speed and are symmetrical to 10° pitch.
- Pitch link forces vary between the two blade attachments.
- The pitch link loads for 0° are not reproducible.

Increasing stiffness and hysteresis are ascribed to increasing friction between the metal sheets at higher rotor speeds. The hysteresis symmetry around 10° pitch is due to the -10° pre-twist of the tension-torsion strap at $\Theta_0 = 0^\circ$ collective pitch.

The following conclusions are drawn from the calibration results, which are critical for accurate measurements in this work:

1. The force flow through the tension-torsion strap cannot be neglected and must be reduced from the measured pitch link forces during operation.
2. Each tension-torsion strap has a unique load hysteresis and must be measured once prior to initial use.
3. The controlled pitch angle sequence appears to have an effect on the load hysteresis. Therefore, polar measurements follow the same pitch order as during calibration.

In addition to the static pitch calibration, the dynamic calibration is considered with respect to the performed dynamic stall cases, see section 4.3.1. The pitch link loads with calibration weight for collective pitch variation are shown in Fig. 2.32, those for cyclic pitch variation in Fig. 2.33.

Both figures show very small cycle-to-cycle variations for each pitch link. Both pitch links show similar dynamic behavior with acceptable dynamic load variations. For each dynamic stall case, the revolution-averaged calibration loads are subtracted for the corresponding pitch link load.

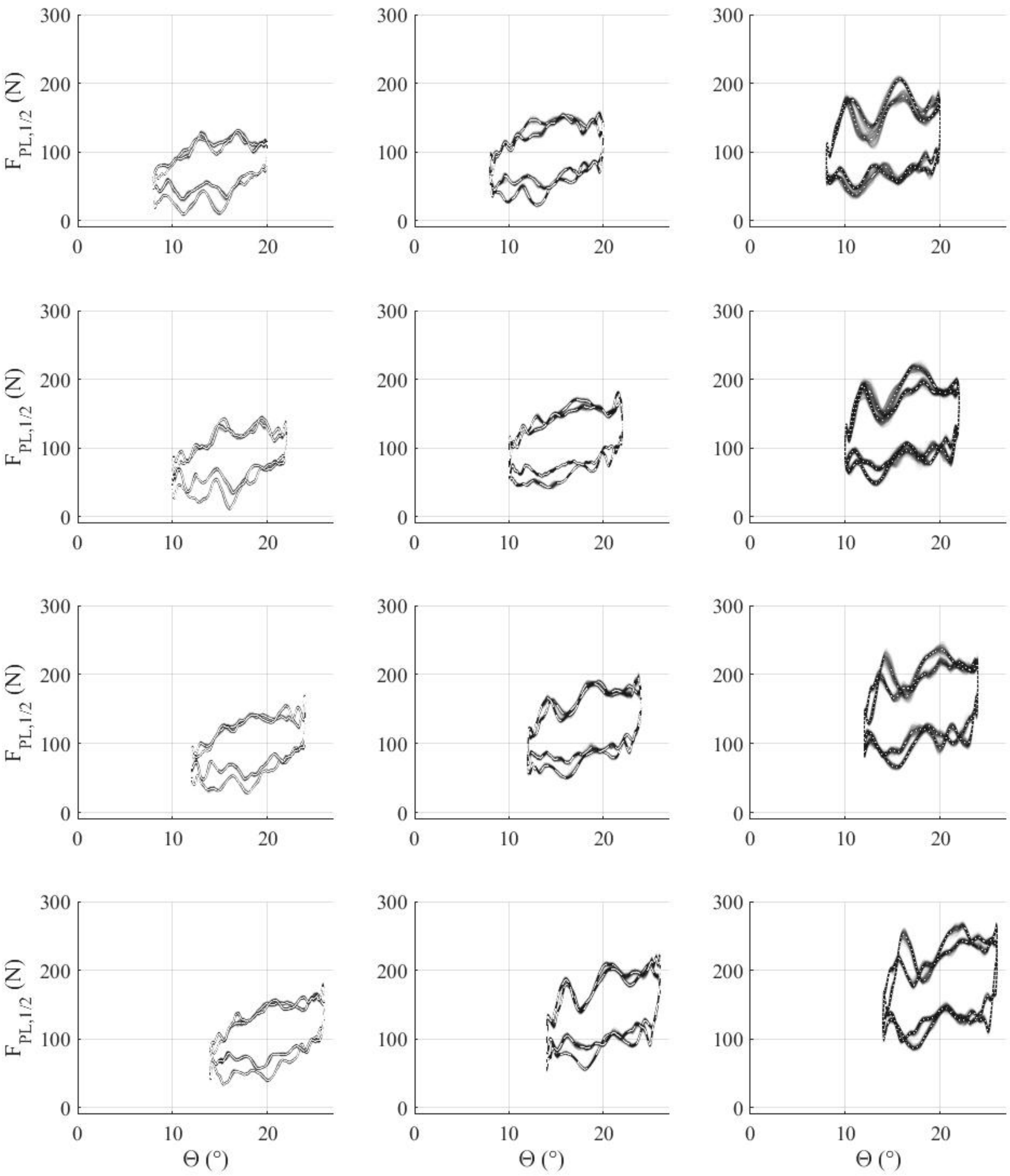

Figure 2.32: Pitch link loads for dynamic calibration on rotor with surrogate weights; collective pitch variation from top to bottom $14, 16, 18, 20 \pm 6°$; at 900, 1200, 1500 RPM from left to right; multiple revolutions of $F_{PL,1}$ and $F_{PL,2}$ shown in one axis each, revolution average plotted in white

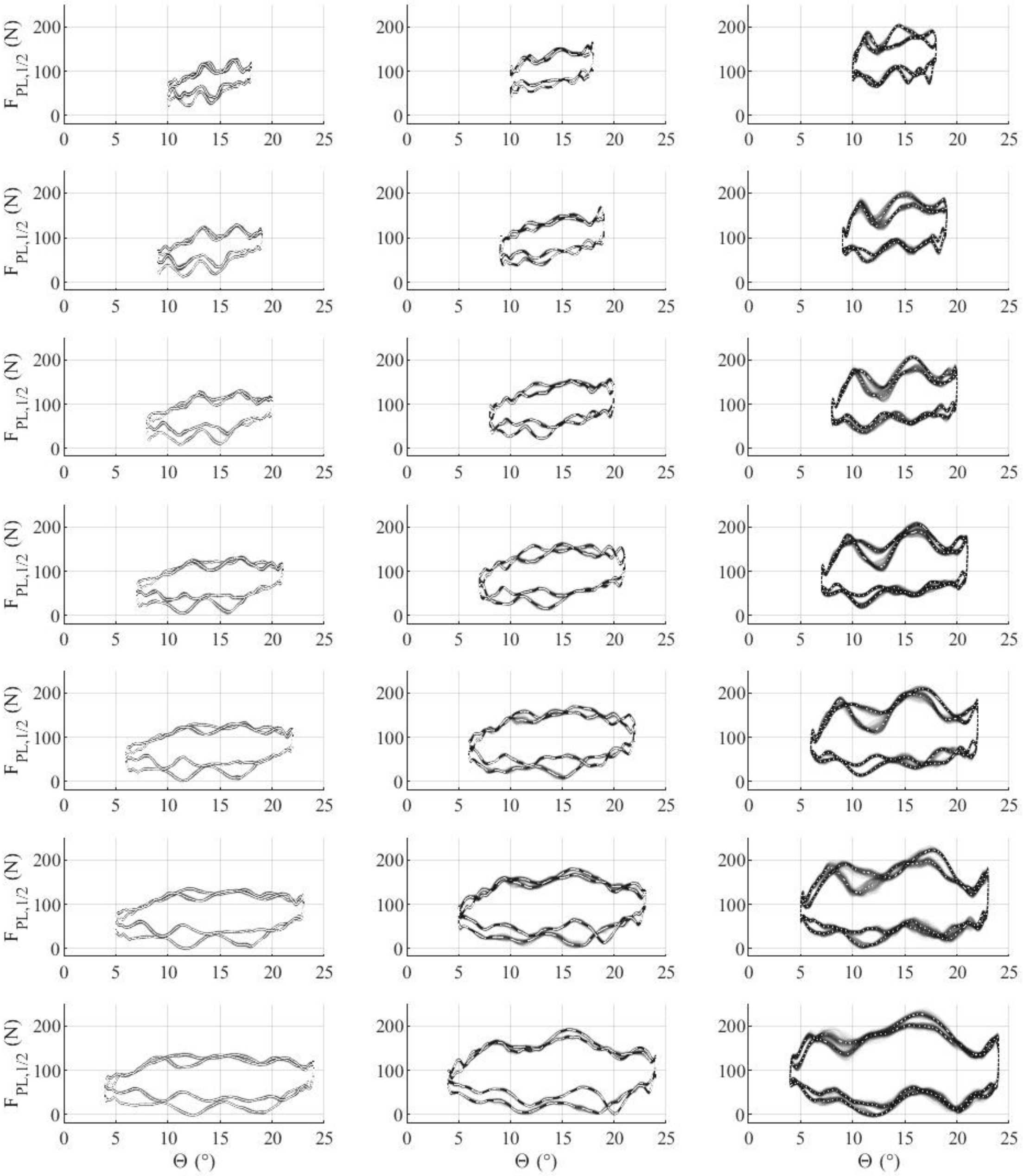

Figure 2.33: Pitch link loads for dynamic calibration on rotor with surrogate weights; cyclic pitch variation from top to bottom $14 \pm 4, 5, 6, 7, 8, 9, 10°$; at 900, 1200, 1500 RPM from left to right; multiple revolutions of $F_{PL,1}$ and $F_{PL,2}$ shown in one axis each, revolution average plotted in white

2.6.3 Scaling Factors

In order to correctly apply the identified calibration slopes and matrices to all strains measured in the rotating environment and acquired with the telemetry system, some telemetry-specific calibration factors must be considered. They must be applied to convert the digital, unamplified bridge detuning voltage x_d to strains ε before applying calibration factors. The telemetry system provides each channel with a supply voltage of 3.3 V and uses 16-bit resolution A/D conversion. Taking into account the manually adjusted telemetry amplifier offset O_T and sensitivity S_T for each channel, as well as a given, constant reduction factor R_T for strain gauges with resistances other than 350 Ω (telemetry-specific), the resulting strain reads

$$\varepsilon = \frac{x_a}{3.3V\ k} 10^3 \tag{2.18}$$

with

$$x_a = \left(\frac{x_d - 32.768}{29.491} 10V - O_T \right) \frac{S_T}{3.03(1 - R_T)} \tag{2.19}$$

The respective units are

$$[x_a] = V \quad \wedge \quad [\varepsilon] = \frac{\mu m}{m} \tag{2.20}$$

The constants k, R_T, S_T are listed in Tab. 2.12, with the exception of offset O_T. It is automatically adjusted before each test to compensate for sensor drift errors.

Description	Entity	Unit	M_β	M_ζ	M_θ	F_{PL1}	F_{PL2}
Gauge factor	k	-	2.19	2.19	2.26	2	2
Reduction factor	R_T	-	0.031	0.031	0.031	0	0
Sensitivity	S_T	-	2	0.5	0.5	3	3

Table 2.12: Telemetry and strain gauge specific constants for the scaling of measured voltage in order to obtain strain values the calibration matrix can be applied to

2.7 Coordinate Systems and Definitions

The three main coordinate systems used in the scope of this work are the body system B, the hub system H, and the sectional blade system S. They are outlined in Fig. 2.34 and described below.

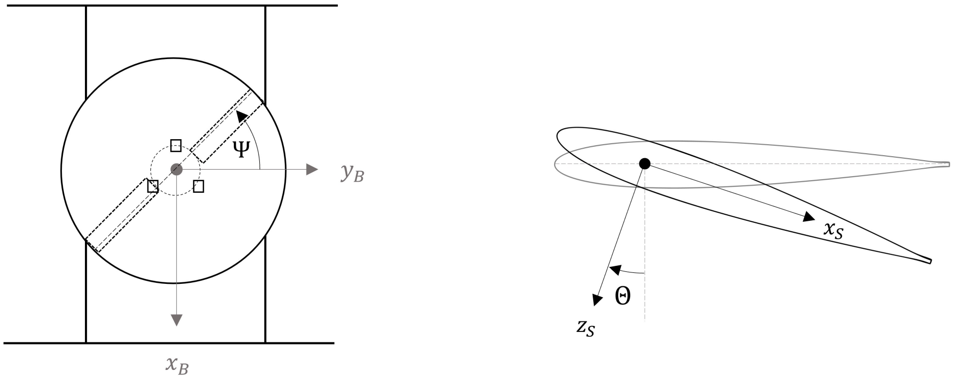

Figure 2.34: Body, hub, and sectional blade coordinate systems

The Frame Body System B is a nonrotating, frame-fixed system with its

- z-axis collinear to the rotor shaft axis and positive upwards,
- y-axis in the rotor plane and at $\Psi = 0°$,
- x-axis in the rotor plane and perpendicular according to right-hand rule.

Thrust, torque, and swashplate tilt angles are primarily given in the body system.

The Sectional Blade System S rotating and fixed to the instrumented blade SN007 with its

- y-axis aligned with the blade beam axis, pointing to the hub center
- x-axis aligned with the blade chord, pointing to the trailing edge and rotating with the control pitch angle $\Theta(\Psi) = \Theta_0 + \Theta_{1C} \cos\Psi + \Theta_{1S} \sin\Psi$
- z-axis perpendicular according to right-hand rule.

The blade root moments are given in the sectional blade system. Positive blade root moments indicate flapping upwards ($M_\beta > 0$), lead-lag backwards to the trailing edge ($M_\zeta > 0$), and torsion with leading edge down ($M_\theta > 0$). Due to the absence of geometric blade twist, $\Theta_{TW} = 0°$, the orientation of the sectional blade system does not change along the blade radius in the undeformed state. However, blade deformation causes the sectional blade system to tilt along the radius in the flap, lead-lag, and twist directions as defined above.

2.8 Measurement Uncertainty and Propagation of Uncertainty

Systematic and Random Errors

Measurement uncertainty describes the amount of deviation from an estimated value. It covers an interval (estimator ± uncertainty) within which an actual value is to be found. It is a critical value for evaluating the reliability of a measurement.

According to [138], errors can be categorized into two groups: Gauss's "irregular or random errors" and "regular or constant errors", which are referred to as systematic errors.

Accuracy is the average difference between a measured value and the actual value and thus describes the closeness to the true value. It is quantified by a systematic error e_{sys} and depends on the capability of the sensor. Calibration can help to improve the accuracy of a sensor. In this work, it is assumed that measurement devices are non-drifting and that the systematic errors are known and constant. They are taken from the manufacturer's calibration and data sheet. Sampling inaccuracies and temperature effects are neglected. Thus, the systematic error consists only of the sensor uncertainties.

Precision describes the range or spread of values around the true value. It is also called random error, temporal noise, or measurement repeatability e_{rand}. This error is best captured by repeating a given experiment often enough to achieve statistical stationarity, assuming that the experiment is not subject to any other systematic environmental influence or source of error.

The total error is calculated by:

$$e = \sqrt{e_{sys}^2 + e_{rand}^2} \tag{2.21}$$

Reproducibility can be demonstrated by measuring data samples from the same experiment on different days, as long as the environmental conditions are the same or accounted for if they affect the experiment.

Standard Deviation of the Means

To calculate the random error e_{rand}, first the mean $\bar{x}$ of a group of samples is needed. In the case of revolutional data, a group consists of M samples per revolution. The local mean is calculated with:

$$\bar{x} = \sum_{i=1}^{M} \frac{x_i}{M} \tag{2.22}$$

The total mean is the average of the individual means of the N revolutions:

$$\mu_{\bar{x}} = \frac{\sum_{j=1}^{N} \bar{x}_j}{N} \tag{2.23}$$

The standard deviation of data samples over multiple revolutions is calculated as standard error of each revolution's mean from the total mean for N revolutions:

$$\sigma_{\bar{x}} = \sqrt{\frac{\sum_{i=1}^{N}(\bar{x}_i - \mu_{\bar{x}})^2}{N}} \tag{2.24}$$

The random error considers the 95% confidence interval I_c around the phase average using the standard error of the means. The confidence interval is given by

$$I_c = \mu_{\bar{x}} \pm e_{rand}; \quad e_{rand} = 1.96\,\sigma_{\bar{x}} \tag{2.25}$$

Propagation of Uncertainty

With x_i being the mean value and e_{x_i} being the corresponding error, data uncertainty is propagated into the function y with the following calculation rules for addition/subtraction and multiplication/division [139, 140]:

$$y = ax_1 + bx_2 - cx_3 \quad \rightarrow \quad e_y = \sqrt{(ae_{x_1})^2 + (be_{x_2})^2 + (ce_{x_3})^2} \tag{2.26}$$

$$y = \frac{x_1 x_2}{x_3} \quad \rightarrow \quad e_y = |\,y\,| \sqrt{\left(\frac{e_{x_1}}{x_1}\right)^2 + \left(\frac{e_{x_2}}{x_2}\right)^2 + \left(\frac{e_{x_3}}{x_3}\right)^2} \tag{2.27}$$

3 Rotor Model

This thesis focuses primarily on experimental dynamic stall investigation on a Mach-scaled rotor test rig. However, a numerical model is required for design load calculations and for validation of power and thrust polars, and structural blade loads. Although a numerical model may have limited validity, it is a powerful tool for verifying trends and rotor performance.[†]

A rigid rotor modeled in CAMRAD II is used for conservative load calculations for rotor and test rig design, see section 2.2. The rigid blade model is also adequate for thrust and power polar calculations, especially due to the low torsional deformation. However, for validation of blade deformation and blade root moments, an elastic blade model is required. At high rotor speeds, even small blade deformations have a strong influence on the structural blade loads. For example, the centrifugal force acting on the deformed blade results in a reduction of the blade root moment. This effect cannot be neglected.

In this thesis, the elastic blade model is used for the following purposes:

- Calculation of axial force at the radial station of strain gauges
- Calculation of blade root moments for measurement validation
- Verification of thrust and power polars

This elastic rotor model focuses on the rotor with its pitch links connected to the swashplate. The modeled half view of the rotor is shown in Fig. 3.1.

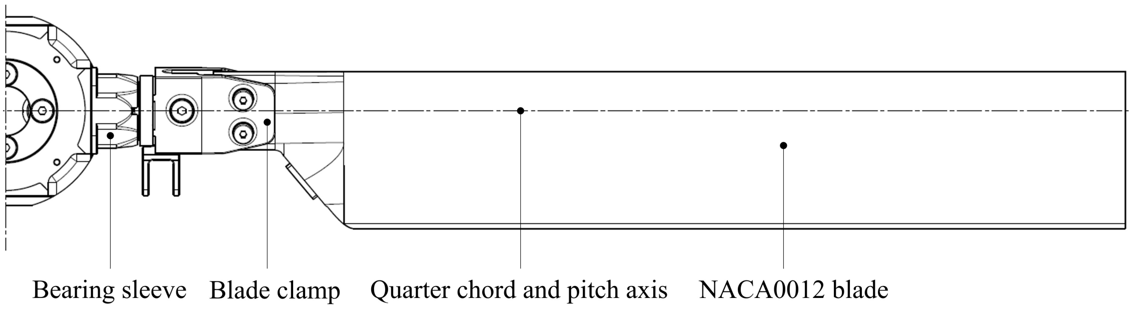

Figure 3.1: MERIT rotor half-view

[†] Parts of this chapter were previously published in [127].

3.1 Aerodynamic Rotor Model

3.1.1 Airfoil Polars

The c81 airfoil tables for the aerodynamic coefficients C_l, C_d, C_m of the NACA 0012 0° tab airfoil are calculated with the TAU compressible CFD solver [141] for Mach numbers $Ma = 0.2, 0.3, \ldots, 0.7$ and angles of attack $-10^\circ \leq \alpha \leq +20^\circ$ on a 2D airfoil section. The flow is assumed to be fully turbulent and the Reynolds-Averaged Navier-Stokes (RANS) simulations are performed using the Spalart-Allmaras One-Equation Model (SA) turbulence model [142] for turbulence closure. Near to the stall region, an Unsteady Reynolds-Averaged Navier-Stokes (URANS) solver is applied in order to capture unsteady effects.

A fully structured O-grid is used to discretize the computational domain. The far-field boundary is placed at radius $R = 50c$ from the quarter chord of the airfoil. The surface of the airfoil is resolved using 200 cells each along the upper and lower surfaces, with a cell size of 0.05 % of the chord length at the leading edge and 0.01 % at the trailing edge. The first layer of the grid is generated such that the dimensionless wall distance of $y+ < 1$ is applied for each CFD simulation performed. Furthermore, a growth factor of 1.1 is chosen between the cells for the region around the airfoil ($R = 0.75c$). Outside this region, the growth factor is increased to 1.15. Fig. 3.2 shows the computed aerodynamic coefficients of the NACA 0012 0° tab airfoil used for the airfoil tables.

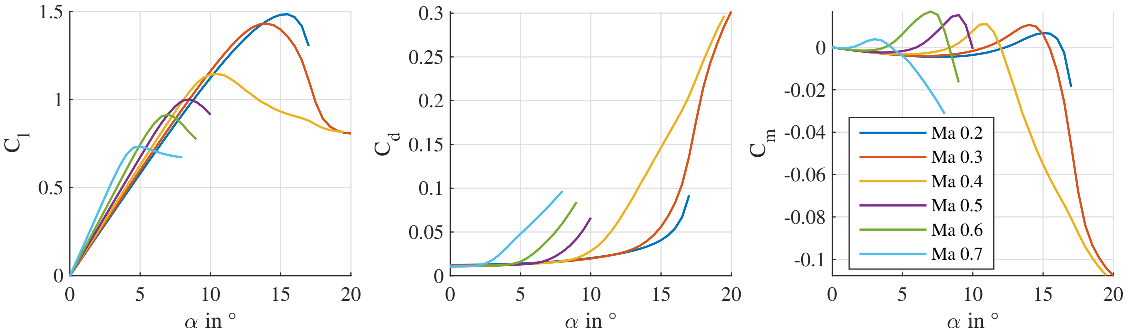

Figure 3.2: Aerodynamic coefficients for the NACA 0012 0° tab airfoil calculated in TAU and used for the NACA 0012 airfoil table in CAMRAD II

The numerical setup used for the NACA 0012 0° tab airfoil is validated by similar experimental studies provided in [27] with the same numerical setup, turbulence model and mesh in advance. The validation case is shown in Fig. 3.3 for $Ma = 0.4$. The parameters used for the CFD calculations of the MERIT airfoil and a validation case on a NACA 0012 airfoil are shown in Tab. A.3.

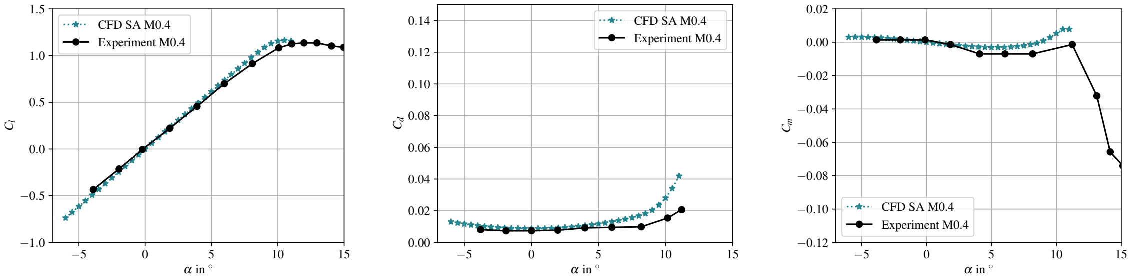

Figure 3.3: CFD polar validation for $Ma = 0.4$ with experimental results given in [27]

3.1.2 Aerodynamic Panel Distribution

The aerodynamic force calculation in CAMRAD II uses the lifting-line theory and evaluates 2D airfoil characteristics at discrete radial stations using airfoil tables [124]. In this work, these are obtained from CFD calculations, as described in the last section. The blade is discretized into n = 10 aerodynamic panels in the spanwise direction. They are distributed radially with the constraint of equal circular area. The radial stations, which define the edges of the aerodynamic panels, are calculated according to the following equations with the boundary conditions $R_1 = 0.276$ m and $R_{n+1} = 0.9$ m:

$$R_i^2 - 2R_{i+1}^2 + R_{i+2}^3 = 0 \quad \forall \ i = 1, ..., n-1 \tag{3.1}$$

$$\begin{array}{ccccccc} R_1^2 & - & 2R_2^2 & + & R_3^3 & = & 0 \\ R_2^2 & - & 2R_3^2 & + & R_4^3 & = & 0 \\ & & & \vdots & & & \\ R_9^2 & - & 2R_{10}^2 & + & R_{11}^3 & = & 0 \end{array} \tag{3.2}$$

$$\begin{pmatrix} 0.276^2 \\ 0 \\ 0 \\ \vdots \\ 0 \\ 0.9^2 \end{pmatrix} \begin{pmatrix} 1 & 0 & 0 & 0 & \underline{\underline{0}} \\ 1 & -2 & 1 & 0 & \underline{\underline{0}} \\ 0 & 1 & -2 & 1 & \underline{\underline{0}} \\ & & \ddots & & \\ \underline{\underline{0}} & 0 & 1 & -2 & 1 \\ \underline{\underline{0}} & 0 & 0 & 0 & 1 \end{pmatrix} = \begin{pmatrix} R_1^2 \\ R_2^2 \\ R_3^2 \\ \vdots \\ R_{10}^2 \\ R_{11}^2 \end{pmatrix} \tag{3.3}$$

The resulting radial stations are:

$$R_i = 0.276, 0.387, 0.472, 0.544, 0.608, 0.666, 0.719, 0.768, 0.814, 0.858, 0.900\ m$$

3.1.3 Inflow Model

The rotor wake is calculated using a three-trailer free vortex wake analysis at the radial stations 0.25 R, 0.7 R, 1 R. A full wake distortion is calculated and vortex roll-up is modeled without trailer consolidation. The wake geometry is truncated after three rotations. A single-peak model is used to determine the bound vorticity at the rotor blade [143].

A comparison between uniform inflow, differential momentum theory with Prandtl tip loss factor, and a free wake model for the thrust polar calculation is shown in Fig. 3.4. It shows that the free wake calculations agree very well with the experimental thrust, while the uniform inflow and DMT overestimate the thrust by about 17 %.

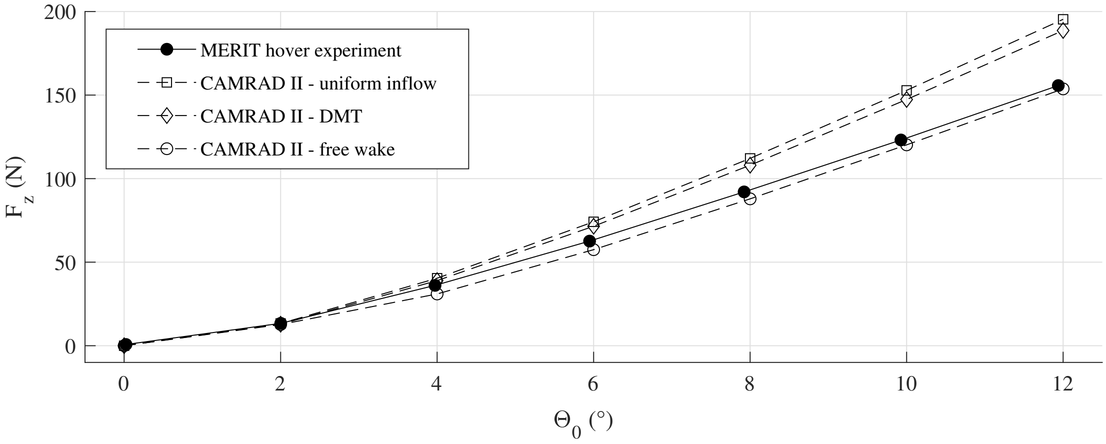

Figure 3.4: Thrust polars for $\Theta_0 = 0, 2, ..., 12^\circ$ collective pitch and 900 RPM, experiment compared to different inflow models in CAMRAD II

Since the free wake calculations show thrust results very close to the measured MERIT polar, the free wake model is considered for further investigation.

3.2 Elastic Rotor Model

The hingeless rotor is modeled in CAMRAD II [124] as an isolated single rotor with two elastic blades and an equivalent attachment stiffness in a surrogate flapping hinge.[*]

3.2.1 Swashplate and Pitch Link

The pitch link is modeled as a linear spring with the stiffness $k_{PL} = 8 \cdot 10^6 \frac{N}{m}$. This stiffness is derived from FE calculations on the pitch link load cell. Since this part is the most flexible part of the swashplate attachment to the pitch horn, all other parts are assumed to be ideally stiff.

---

[*] Parts of this chapter are published in [127].

The nonlinear torsional stiffness of the tension-torsion strap is not modeled here, but must be considered in post-processing of the experimental data. The geometry of the pitch link attachment between the swashplate and the pitch horn is shown in Fig. 3.5. The geometrical parameters used are listed in Tab. 3.1.

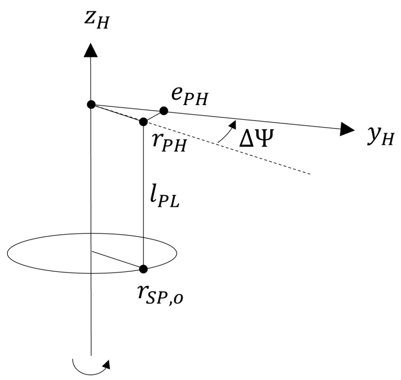

Figure 3.5: Swashplate and pitch link model scheme in the $\Theta = 0°$ position

Description	Entity	Value
Radial pitch horn station	e_{PH}	0.141 R
Pitch horn attachment angle relative to pitch axis	$\Delta\Psi$	25°
Pitch link length	l_{PL}	0.211 R
Radial swashplate attachment point	$r_{SP,o}$	0.156 R
Radial pitch horn attachment point	r_{PH}	0.156 R

Table 3.1: Geometric parameters of the pitch link model in CAMRAD II

3.2.2 Blade Beam

Blade Material Properties

The rotor blades used on MERIT are C-spar, carbon skin blades with a foam core. They contain preimpregnated carbon fibers (prepregs) from *SGL Carbon SE*, in particular the Unidirectional Fiber (UD) *SIGRAPREG® U600-0/SD-E501/33%* and the fabric *SIGRAPREG® C W200 TW2/2 E503/45%*. The unidirectional fibers contribute primarily to the flapping stiffness, while the twill weave used in a ±45° arrangement provides high torsional stiffness. Fiber composites must be tested in different layup combinations at the coupon level to obtain elastic material properties. For the carbon prepreg material used in this thesis, the properties are derived from coupon tests published in [31, 128]. Their mean values and Standard Deviation (STD) are summarized in Tab. 3.2.

		UD		Fabric	
	Unit	Mean	STD	Mean	STD
E_1	GPa	134.6	5.2	65.3	1.16
E_2	GPa	9.02	0.41	65.3	1.16
E_3	GPa	9.02	0.41	11.7	
ν_{12}	-	0.336	0.051	0.077	0.037
ν_{13}	-	0.336	0.051	0.34	
ν_{23}	-	0.388		0.34	
G_{12}	GPa	4.75	0.1	4.58	0.12
G_{13}	GPa	4.75	0.1	4.34	
G_{23}	GPa	3.02		4.34	

Table 3.2: SGL carbon prepreg elastic material properties of the SGL preimpregnated unidirectional (UD) and fabric carbon fibers *SIGRAPREG® U600-0/SD-E501/33%* and *SIGRAPREG® C W200 TW2/2 E503/45%* derived from coupon tests [31]

Blade Sections

The MERIT rotor blade model is divided into five different sections, Fig. 3.6, which are extracted from the carbon layup design:

1. A monolithic blade attachment that supports the two attachment bushings,
2. the scarf transition between the blade attachment and the homogeneous airfoil section with a sensor connector,
3. the NACA 0012 homogeneous airfoil section with a 0° tab and a C spar,
4. a scarf transition between the homogeneous airfoil section and the blade tip, and
5. the monolithic blade tip.

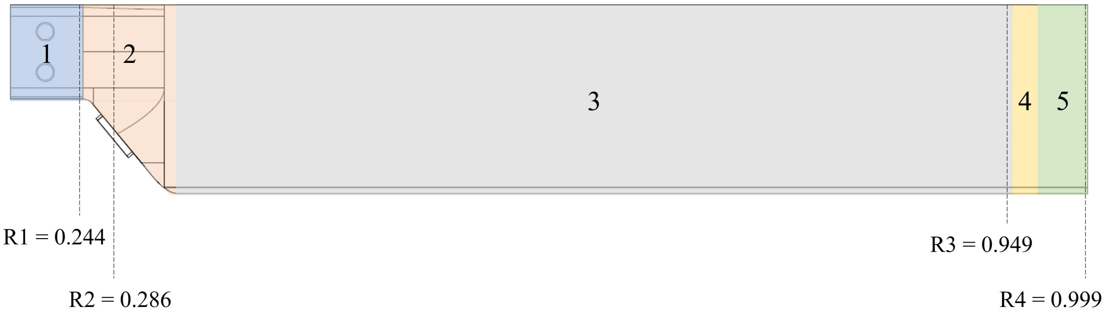

Figure 3.6: MERIT rotor blade with normalized radial stations of the five different sectional beam properties

The mass and stiffness properties of these sections are used to define an anisotropic beam.

Sectional Mass and Stiffness Properties

The structural stiffness and mass properties for the anisotropic beam model are calculated at the four different 2D cross-sections R1, R2, R3, R4 (see Fig. 3.6) using the preprocessor SONATA for the 2D cross-section mesh generation [144] and VABS for the calculation of sectional beam properties [145], such as section mass and stiffness.

Fig. 3.7 shows the 2D finite element model of the four sections generated in SONATA at the respective radial station. The monolithic blade root section is modeled with a layup of unidirectional and twill fibers, while for the tip section homogeneous material properties are assumed and calculated in ELAMX^2 using classical laminate theory for a layup design of 50 % twill and 50 % unidirectional fibers. The beam properties for section 4 are calculated by a linear property interpolation between sections 3 and 5. The diagonal entries of the stiffness matrix and their distribution over the blade radius are shown in Fig. 3.8.

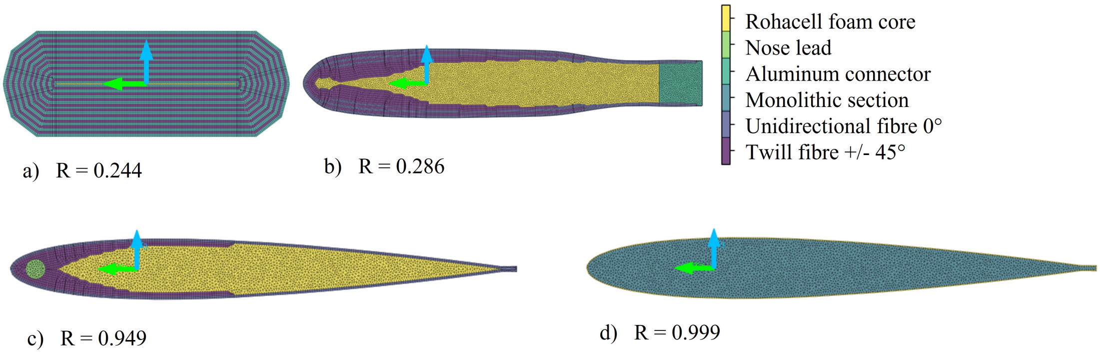

Figure 3.7: MERIT SGL blade sections modeled with SONATA and used for sectional stiffness and mass properties calculations with VABS

The calculated total mass of the blade is 0.8154 kg, not including the balance cell, attachment bushings, and blade instrumentation. The calculated blade center of gravity is 0.5707 R. The average of the measured weights of the two blades (SN007 and SN008) without balance weights is 0.8364 kg. The measured radial center of gravity of the uninstrumented SN008 blade with the balance cell is 0.57 R.

Beam Properties

A beam theory for anisotropic materials including transverse shear deformation is used for each rotor blade [146]. Five additional beam nodes at the radial stations 0.1,0.2,0.5,0.7,0.9 R discretize the beam into six elastic beam elements. Each of these has 2 axial, 2 flapping bending, 2 lead-lag bending, and 2 torsional degrees of freedom. Thus, the elastic motion of each beam component is described by the axial, bending, and torsional deflection of a beam.

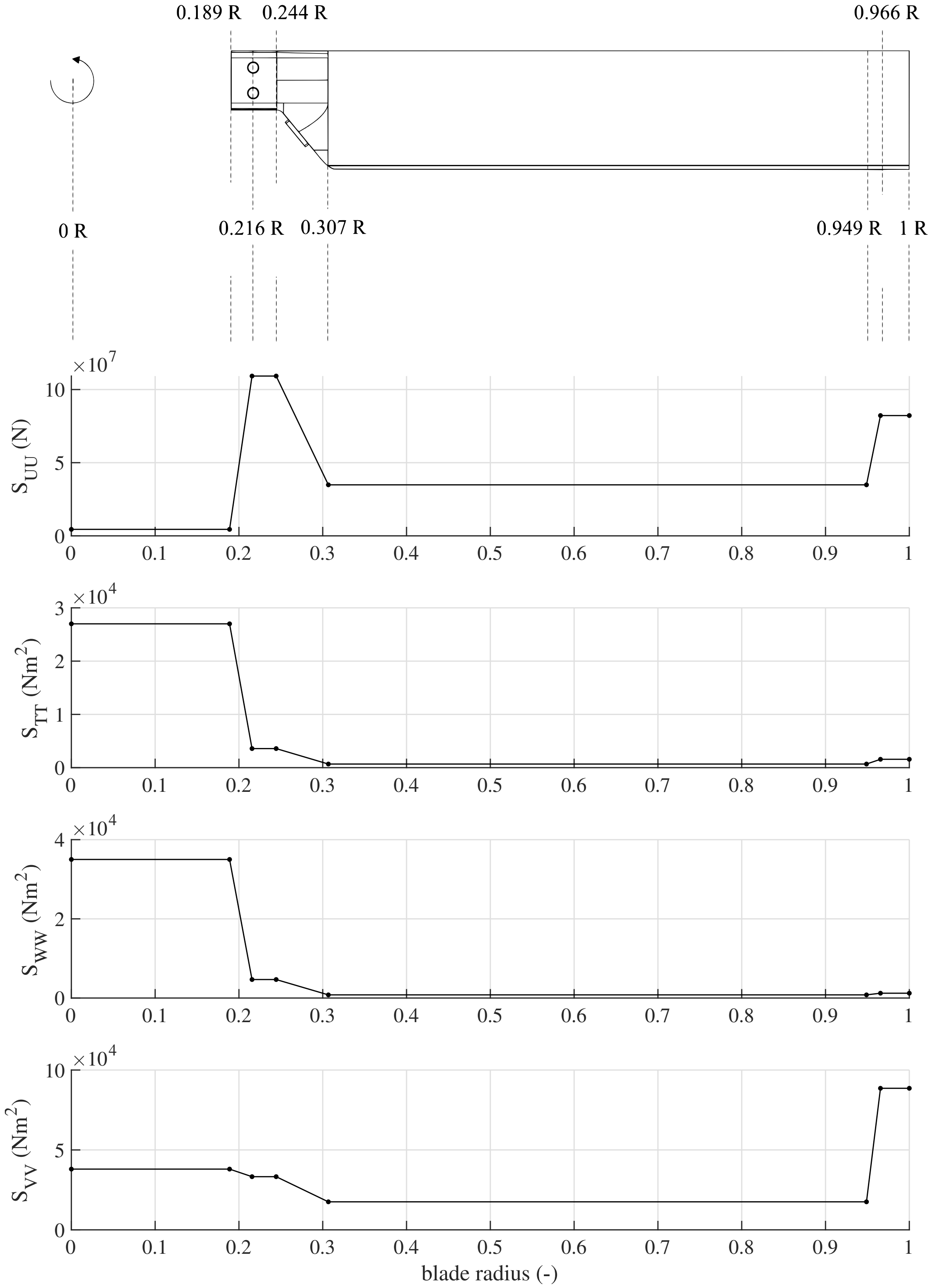

Figure 3.8: Main sectional blade stiffness properties in CAMRAD II, S_{UU}: axial stiffness, S_{TT}: torsional stiffness, S_{WW}: flap bending stiffness, S_{VV}: lead-lag bending stiffness

3.2.3 Static Blade Deformation

The beam model in CAMRAD II is experimentally validated by static deformation measurements on the first blade prototype SN001 using DIC, as described in [135] and [23]. The results show that the experimentally derived stiffness properties are in good agreement with the calculated ones [129]. The shear flapping load case (501.75 N tip flap shear force) is used to validate the flapping deflection, see Fig. 3.9. The upper and lower deflections, measured with DIC, are compared to the beam deflections in CAMRAD II.

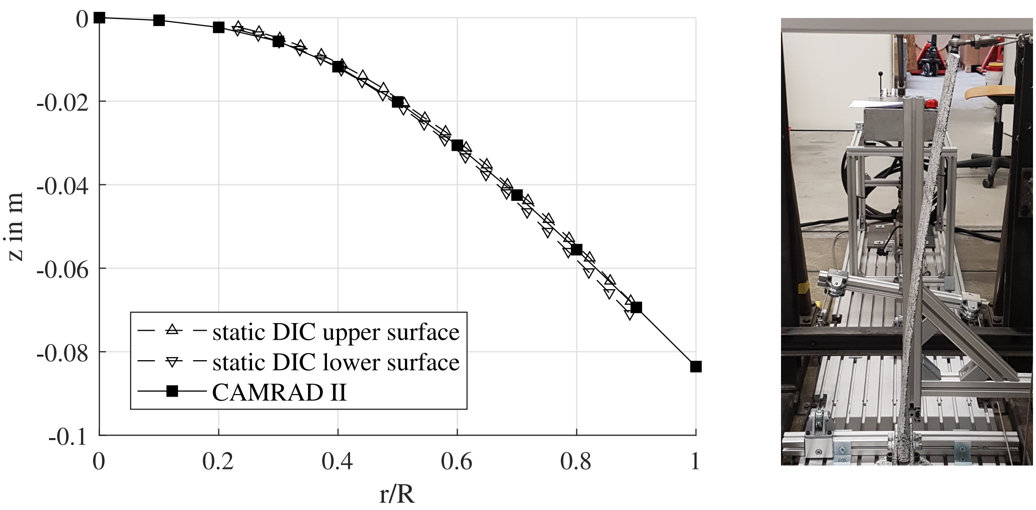

Figure 3.9: Calculated (CAMRAD II) and measured (DIC) z-displacement (flap) of blade prototype SN001 at zero pitch and for a static tip load (flap shear force) [23]

The model deformation lies between the two measured curves, but closer to the upper side for an attachment stiffness of $EI_\beta = 10,000\ Nm^2$ for the blade clamp adaptor (see section 3.3).

3.3 Blade Attachment Flapping Hinge

3.3.1 Attachment Stiffness Identification and Model Validation

The displacements of the two-bladed MERIT rotor are measured with a photogrammetry setup at the rotational speeds of 20, 900 and 1800 RPM, each with a collective pitch of 0°-12°, see Fig. 3.10 and Tab. 3.3, to determine the attachment stiffness and validate the model in CAMRAD II.[*]

Rotor Speed	Collective Pitch	FPS	FPR
20 RPM	$0,1,\ldots,6,8,\ldots,20,25,30^\circ$	12	36
900 RPM	$0,1,\ldots,6,8,10,12^\circ$	540	36
1800 RPM	$0,1,\ldots,6,8,10,12^\circ$	1000	33

Table 3.3: Photogrammetry test setup parameters: rotor speed, collective pitch angles, frames per second (FPS), and frames per revolution (FPR)

The sensors used are two *ARAMIS SRX 1600 MV4200 HD* cameras from *Carl Zeiss GOM Metrology GmbH*. They offer a powerful, robust, and flexible setup with easy handling, and fast assembly and disassembly. They are rigidly connected to a 1600 mm beam with integrated Light Emitting Diode (LED) lights and span a maximum measurement volume of 4200 *x* 2350 *x* 2350 mm^3. The sensors are mounted on the laboratory crane at a vertical distance of 4.365 *m* above the rotor plane in order to cover the entire rotor area as well as the reference frame below, see Fig. 3.10.

The accuracy of the 3D deformation measurement is in the range of about ±0.08 *mm*. The blade is discretized with 21 retroreflective markers (size $d = 18$ *mm*) on each blade, which allows a good reflector detection even at high pitch angles. Applying a frame rate of 540 Hz at 900 RPM, and 1000 Hz at 1800 RPM provides an image for every 10° and 10.8° azimuth.

A 2 x 2 m aluminum frame, rigidly attached to the pyramidal bearing frame, serves as the reference frame for rigid body motion correction in the case of steel frame vibrations and oscillations, and in the case of ARAMIS SRX sensor movements.

For meaningful and efficient post-processing, a 3D touch probe is used to create reference geometries and a global coordinate system. It is a calibrated, reflector-carrying, pen-like tool for capturing surfaces or points that cannot be captured by the cameras in direct line of sight. It provides an accuracy of ±0.15 *mm*.

The measurements at 20 RPM and 0° to 30° pitch serve as reference stages. All deformations at higher speeds are compared to their respective reference pitch stage. Further details on test setup and preparation of geometric references are given in [127].

---

[*] Parts of this chapter are published in [127].

Figure 3.10: Photogrammetry measurement setup of the *ARAMIS SRX 1600 MV4200 HD* sensor attached to the lab crane 4.365 m above the MERIT rotor plane

An accurate and efficient comparison of experimental and model deformation requires a carefully considered choice of coordinate systems (frames), which turned out to be the following: two rotating hub frames originating from the global frame with their respective y-axis pointing to each blade tip, and seven successive frames for each blade along the pitch axis from root to tip, Fig. 3.11. These are generated at the radial station extracted from the area centroid of a set of three reflectors projected onto the pitch axis, and oriented parallel to the pitch and rotor shaft axes. The attachment of each spanwise frame to the three-point component causes the frames to move and deform with the blade. Therefore, the resulting radial stations for the two blades are not identical.

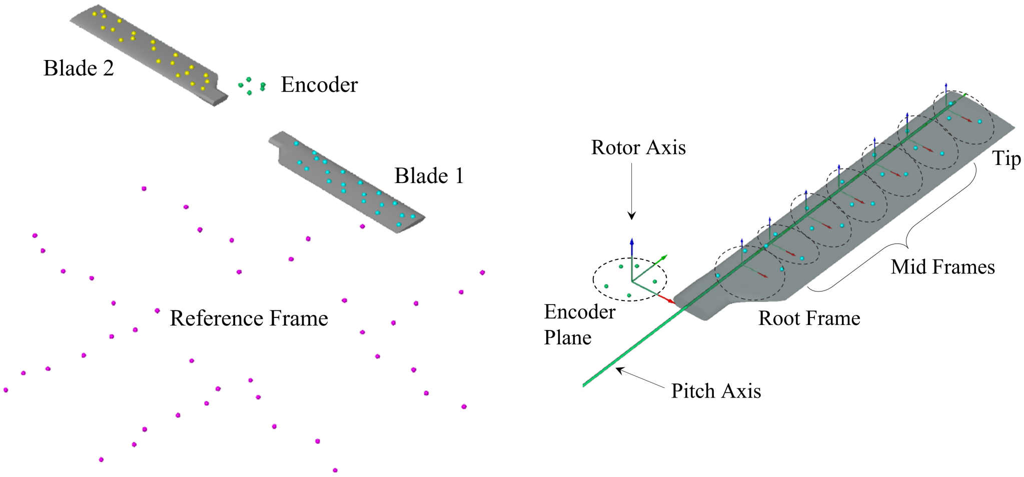

Figure 3.11: Reference geometries, point components, and rotor blade frames generated in *GOM Correlate Pro* for the reference frame, telemetry encoder, and the two blades

Blade flap, lead-lag, and axial displacements are calculated at the radial station of each coordinate system by considering the translational shift of the origin with respect to its corresponding reference position. Blade twist deformation is calculated by measuring the local coordinate rotation along the y-axis.

All calculated deformations are corrected for the rigid body motion of the reference frame. Movements of the rotor head relative to the reference frame are small (amplitude of deflection from center less than 1 mm), but should not be seen in the deformation measurements. Therefore, all deformation data are given in the encoder coordinate system. Its origin moves with the rotor head, but its z-axis remains parallel to the virtual shaft axis, since the encoder plane is not satisfactorily perpendicular to the shaft axis due to manufacturing intolerances.

The photogrammetry data analysis shows that more than 95 % of the recorded stages can be successfully processed in *GOM Correlate Pro 2021* using the shown reflector clustering. During the test campaign, a total of three reflector points were lost, mainly due to their proximity to the leading edge. These points are not included in the post-processing.

In the following, blade tip displacements are shown in the rotating hub coordinate system, while radial blade displacements are shown in the blade section axes.

3.3.2 Blade Tip Displacement Analysis

The blade tip flap, lead-lag, axial and torsional displacements are shown in Fig. 3.12 for both blades as well as 900 and 1800 RPM as a function of collective pitch Θ_0. The data points indicate the mean value over all revolutions of a test case, the bars show the standard deviation.

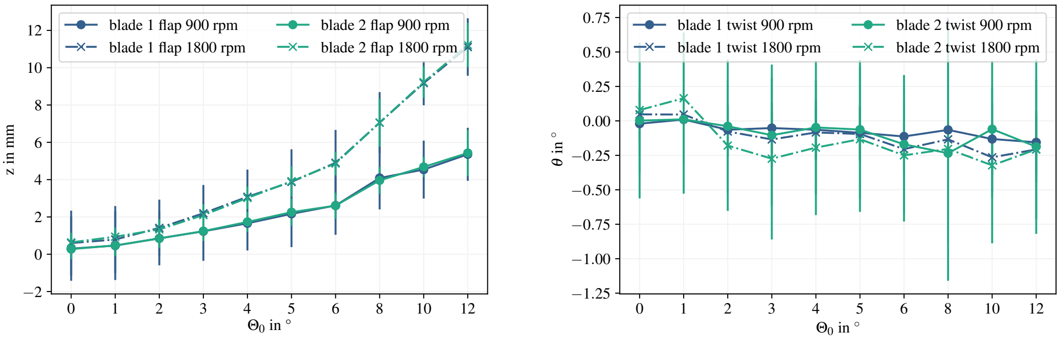

Figure 3.12: Blade tip flap and torsional displacements in rotating hub axes as a function of collective pitch Θ_0 at 900 RPM and 1800 RPM

Flap

Both blades show almost no difference in tip flapping deformation. The graphs show nearly linear behavior from 2° pitch onward. Note that the scaling of the x-axis changes at 6°. The amplitudes double at twice the speed.

Torsion

The torsional deformation shows a small negative trend (leading edge down) with increasing pitch. This can be explained by the location of the shear center in front of the quarter chord, which was intentionally designed for aeroelastic stability.

The standard deviation shows very high values for axial and torsional deflections compared to their absolute values. This is due to the measurement noise, which is most noticeable at small displacements. The standard deviation for the lead-lag displacement is within the noise amplitudes of the reference stage, while the flapping motion shows much higher error bars. This indicates a high vibration level, probably increased by flow recirculation.

3.3.3 Radial Displacement Analysis

The radial displacements as a function of fractional radius for flapping z, and lead-lag x can be seen in Fig. 3.13 and 3.14. Blades 1 and 2 have slightly different radial stations at which the displacements are given due to different point clustering.

Flap

Both blades show similar deformation at all stages. A noticeable result in the radial flapping deformation is the positive z-deflection for 900 and 1800 RPM at 0° pitch. The flapping deformations at 8° and 900 RPM are a special case. They are unusually high but visible for both blades. The cause of this effect needs further investigation.

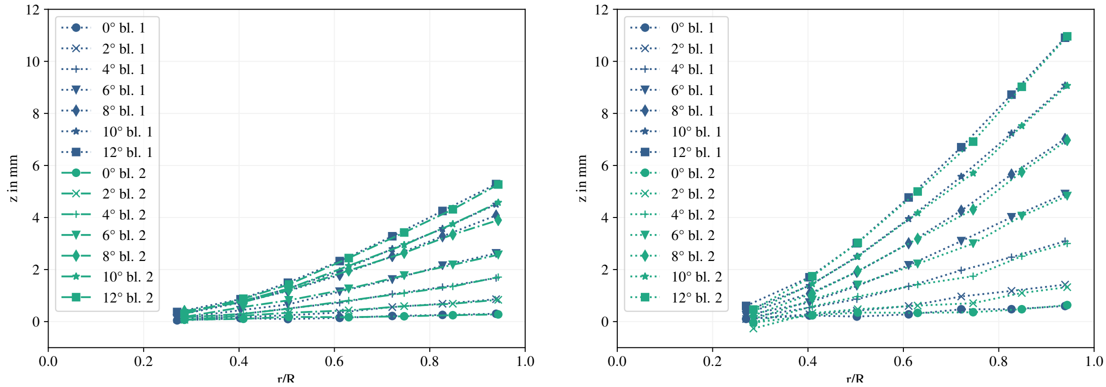

Figure 3.13: Radial blade flapping displacements at 900 RPM (left) and 1800 RPM (right) in blade section axes

Lead-Lag

The lead-lag deflections are shown in Fig. 3.14.

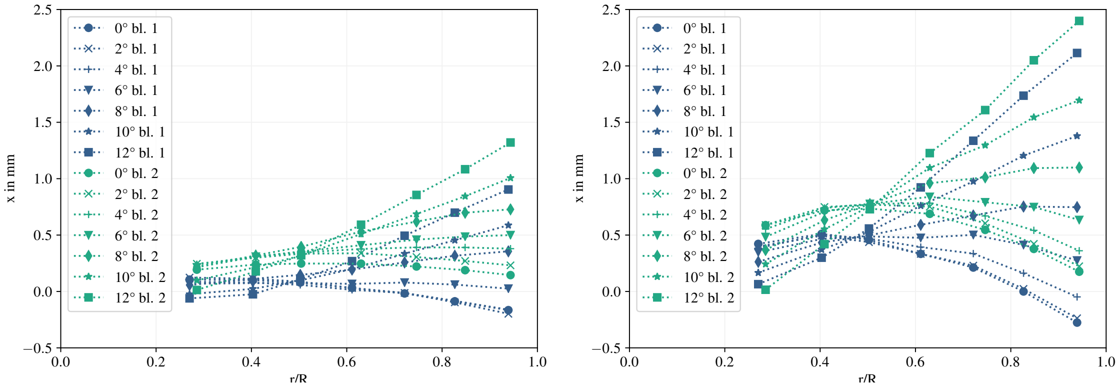

Figure 3.14: Radial blade lead-lag displacements at 900 RPM (left) and 1800 RPM (right) in section axes

The displacements of both blades show a continuous offset to each other, which can be explained by different bearing clearances and slightly different chordwise mass distributions. However, both blades show similar trends with increasing pitch. For small pitch angles (0-6°) the blade moves towards the leading edge. This is due to the fact that the center of gravity of the homogeneous section is located slightly behind the quarter chord or pitch axis. For increasing pitch, this trend is reversed as the drag increases and dominates the deflections. This trend can also be seen in the simulation results, see Fig. 3.15.

3.3.4 Rotor Simulation Validation

Rotor simulations are performed with a surrogate flapping hinge set to match the static flapping deflection. It has a radial offset of 0.2 R and a linear stiffness of 15,000 Nm/rad. The comparison between simulated and measured radial displacements for 900 RPM and selected pitch angles $\Theta_0 = 4, 8, 12°$ is shown in Fig. 3.15.

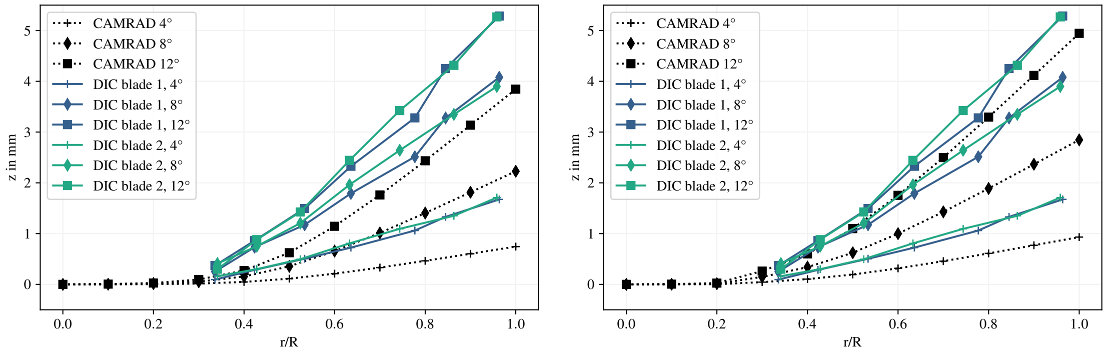

Figure 3.15: Radial blade flapping displacements in section axes for $\Theta_0 = 4,\ 8,\ 12°$ collective pitch and 900 RPM without (left) and with (right) flapping hinge

Without the flapping hinge, the tip displacements differ on average by about 1.5 mm between simulation and experiment. Also, the measured deflections and curvature at the blade root do not perfectly match the simulation displacements.

With the virtual flapping hinge, the blade tip displacements are much closer to the measured ones. However, the tip deflection is still 1 mm off but is considered constant due to the bearing clearance.

4 Static and Dynamic Stall in Hover

The research questions posed in section 1.1 are answered by an experimental approach within the scope of this thesis. For this purpose, the designed Mach-scaled rotor, described in section 2, see Fig. 4.1, performs hover investigations at different rotor speeds.

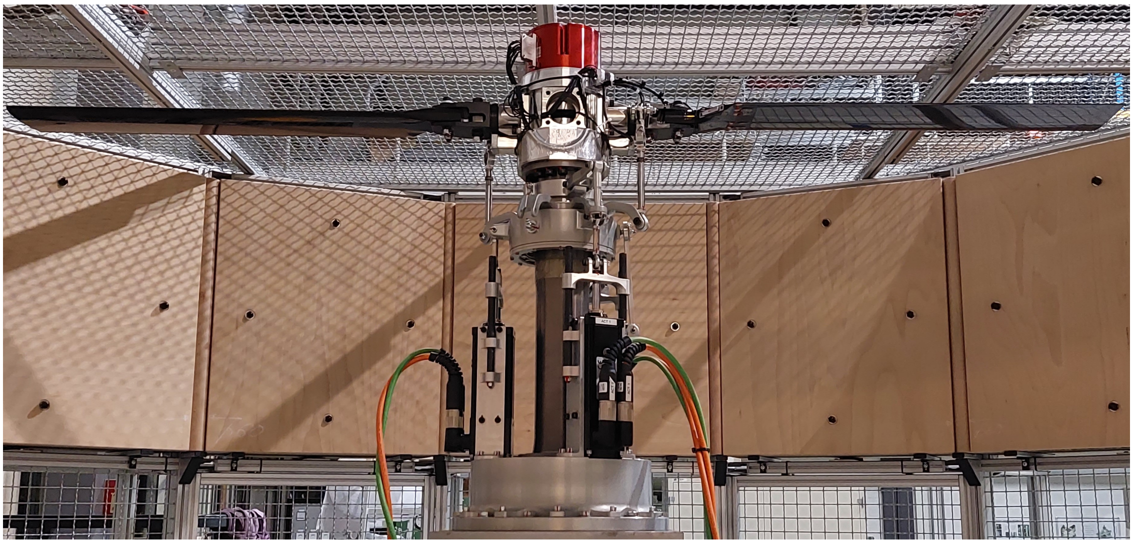

Figure 4.1: MERIT rotor configuration for static stall and dynamic stall measurements

The measurement campaigns performed are divided into two sections:

1. Rotor performance measurements up to static stall angles at different rotor speeds (section 4.2).
2. Cyclic pitch induced dynamic stall tests with different control parameter settings at different rotor speeds (section 4.3).

Section 4.2 contains rotor performance and polar measurements, including blade root moments, pitch link forces, integral rotor thrust, and drive power at three selected rotor speeds. Experimental data are compared with simulation results and analyzed with an emphasis on polar symmetry, repeatability, and static stall detection. The comparison of experimental and numerical load data for the stiff and elastic rotor model, see chapter 3, supports the verification of measurement and calibration procedures for ongoing experimental load analyses.

Section 4.3 builds on the previous static stall polar measurements. It analyzes light and deep dynamic stall cases at the same rotor speeds as in section 4.2. The dynamic stall cases are excited by various combinations of collective and cyclic control pitch angles in hover conditions. A comparison of the structural loads with the static polars assists in the detection and classification of dynamic stall. Finally, the experimental analysis focuses on the influence of compressibility effects, mean pitch angle, and pitch range on structural load dynamics such as blade root moments and pitch link forces during dynamic stall.

4.1 Experimental Approach

This section clarifies the experimental approach and initial conditions that apply to all experiments conducted in this thesis. It introduces the rotor and measurement configuration, the experimental procedure and environment, the data preparation, and the power and thrust validation with the Autonomous Rotorcraft for Extreme Altitudes (AREA) rotor [147] before proceeding with the static and dynamic stall results.

4.1.1 Rotor Configuration and Sensor Equipment

The investigated rotor comprises two blades with the serial numbers SN007 and SN008 and pitch links, each with integrated load cells. Blade SN007 is instrumented with strain gauges at the blade root and is attached to attachment two. Blade SN008 is not instrumented and is attached to attachment one. Blade pitch angles are measured with hall sensors of the type *PMIS4-20-20, ASM,* to achieve a final pitch angle accuracy of 0.05°. The rotor configuration is the same for all measurements shown in this thesis, see Fig. 4.1.

Table 4.1 summarizes all measured sensor data used for the experimental analysis. Stationary sensor data is sampled at 5 kHz, while rotating data is sampled at 20 kHz. Sensor calibration and data synchronization are performed as described in chapter 2.

	Attachment 1 SN008	Attachment 2 SN007	Symbol	Sampling
Rotating				
Pitch angle	Hall sensor 1	Hall sensor 2	$\Theta_{1/2}$	20 kS/s
Blade root moments	-	Strain gauges	$M_{\beta/\zeta/\theta}$	20 kS/s
Pitch link forces	Load cell 1	Load cell 2	$F_{PL,1/2}$	20 kS/s
Rotor speed	Rotating encoder		Ω	20 kS/s
Rotor azimuth	Rotating encoder		Ψ	20 kS/s
Stationary				
Rotor forces	4 x 3-axes load cell		$F_{x/y/z,1/2/3/4}$	5 kS/s
Shaft torque	Coupling unit		M_T	5 kS/s
Rotor azimuth	Rotating encoder		Ψ	5 kS/s

Table 4.1: Rotating and stationary sensor equipment

4.1.2 Testing Procedure and Environment

Environmental conditions, such as air temperature and local pressure, affect rotor performance and can be easily accounted for by non-dimensionalization of physical parameters. Conversely, parameters that change over time and depend on rotor run time and load, such as the temperature of mechanical components or displacement effects, can be a source of time-dependent data variation and complicate repeatability analyses and model validation.

The sequence of control parameters has been shown to be a source of systematic error in rotor experiments on MERIT. Several factors affect the structural loads in different ways. Some of these effects are due to high energy dissipation and non-linear dependence of structural loads on time and deflection or displacement. These factors can include:

- Displacement effects that occur when a preload is applied, e.g., by initial spin-up,
- Load cell creep, which develops gradually due to the permanent presence of a load, such as the predominant upper frame weight on the four stationary load cells,
- Load hysteresis due to high contact friction, as shown for the tension-torsion strap,
- Temperature rise in the bearings, resulting in material expansion and changes in preload and friction, and
- Inertia of the mechanical rotor components as well as the rotor wake system circulating around the rotor casing.

Most of these factors are complex and challenging to account for with simple models. For example, measurable and repeatable load hystereses can be experimentally determined and accounted for, as shown for the tension-torsion strap. Time-dependent equilibrium states, on the other hand, can be achieved by applying a specific preload or simply by allowing the system to settle over time. These effects highlight the need for procedures that create conditions for successful comparability between different test cases. Overall, these effects must be considered in the analysis and in the assessment of data reliability.

Air Pressure and Temperature

All experiments are performed at 482 m above sea level. The local pressure is taken from a local weather station on the campus[*]. The indoor temperature is recorded and averaged for each test period and is used to calculate air density and non-dimensionalization of loads. The local air density ρ is calculated according to the ideal gas law.

$$\rho = \frac{p}{R_s T}, \quad R_s = 287.1 \, \frac{J}{kgK} \tag{4.1}$$

---

[*] Weather Station Garching, Dr. Reinhold Dorn, D-85748 Garching

Pitch Range and Sequence

Testing experience has shown that stationary load cell data quality is subject to displacement effects. The four load cells are constantly subjected to the weight of the top frame, shaft, rotor, and control system. This prevailing preload can cause the load cells to creep. A load sweep in different directions around the preload can enforce the settling effects to obtain reproducible data. Three consecutive load sweeps within ±4° collective pitch at 900 RPM are used to determine if the thrust polar is symmetrical and reproducible, see Fig. 4.2. Each point of the sweep contains a steady collective pitch state for 10-15 seconds before moving on to the next point.

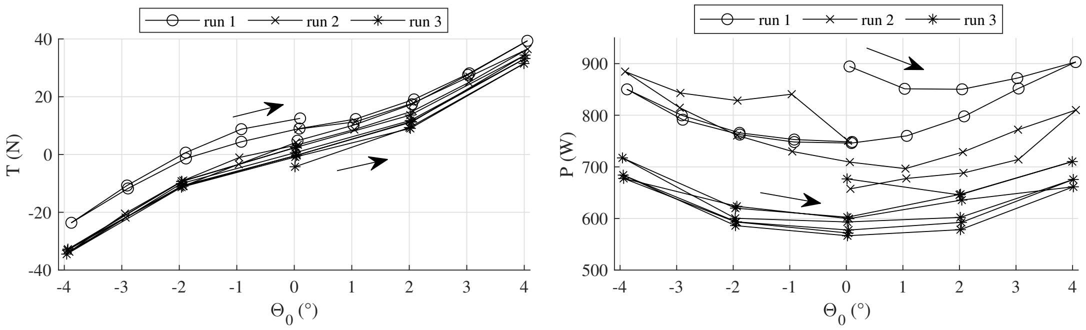

Figure 4.2: Rotor thrust and power for three successive pitch sweeps within the range of $\Theta_0 = \pm 4°$ at 900 RPM; average standard deviations of $\sigma_T = 12.8\ N$ and $\sigma_P = 74\ W$ for the shown measurement range

The thrust data shows an initial offset decrease after the first sweep around $\Theta_0 = \pm 0°$. After that, the thrust data moves within sensor accuracy around the expected averages. On the other hand, the power data shows that the initial power consumption is very high compared to the values that level off during the third run. This decrease in power is due to the increasing rotation time and the associated temperature rise in the shaft bearings since the first run started with a cold rotor and drive system.

Based on these results, the following pitch sequence is chosen for each polar measurement: $0, -2, -4, -3, -1, 0, 2, 4, ..., 24, 23, 21, ..., 1, 0°$. This initial negative pitch sweep procedure is used to adjust and verify zero thrust at $\Theta_0 = \pm 0°$. At the same time, this procedure allows the rotor components, especially the shaft and bearings, to reach operating temperature for repeatable power measurements, as shown in Fig. 4.2. The maximum pitch angle $\Theta_{0,max} = 24°$ for static polar measurements is chosen to represent stall onset and development for all selected rotor speeds.

Recording Time

Inflow perturbations in the present test case can occur due to blade vortex interaction, asymmetric inflow, wake recirculation, and interaction with the casing walls, etc. These perturbations can induce various aerodynamic effects and lead to cycle-to-cycle load variations during dynamic stall.

Therefore, significant hover data is obtained by phase averaging over several rotor revolutions. To determine the minimum recording time for a negligible remaining average change, a convergence study is performed for different speeds and pitch angles using the example of rotor thrust and torque.

Figures 4.3 and 4.4 show the RMSE between the average of the current revolution at a given time and the average of the past revolutions up to that time, for static pitch settings and zero cyclic pitch. Thrust and torque RMSE are shown in percentage of the measured thrust and torque mean values. All shown RMSE graphs show an exponential decrease with increasing recording time and number of revolutions. Accordingly, the phase average for all three speeds does not change significantly after 15 seconds. Therefore, the resulting recording time for each data point is set to at least 20 seconds, which includes a 5-second margin for flow adjustment after a new rotor control setting.

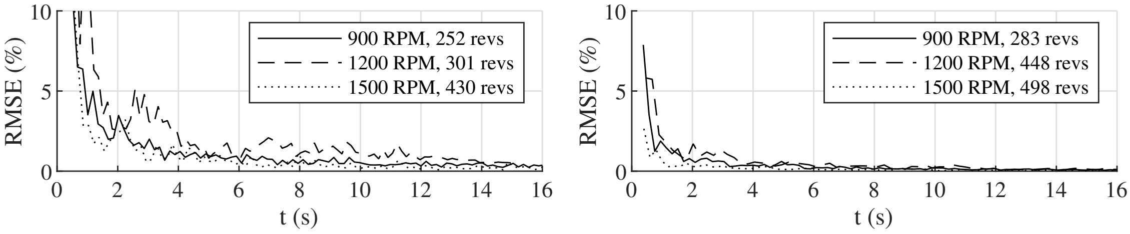

Figure 4.3: Relative thrust RMSE convergence as function of recording time for $\Theta_0 = 0°$ (left) and $\Theta_0 = 15°$ (right)

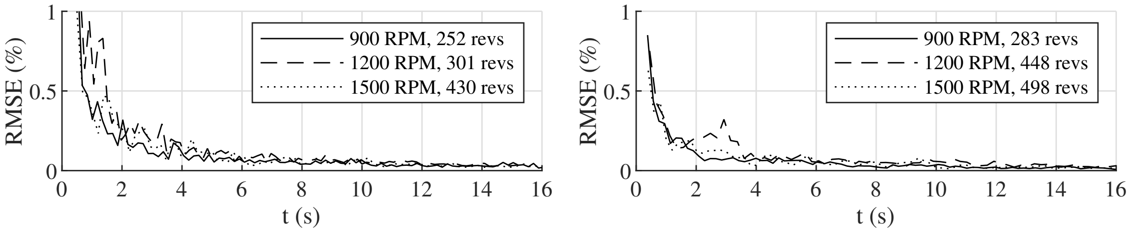

Figure 4.4: Relative torque RMSE convergence as function of recording time for $\Theta_0 = 0°$ (left) and $\Theta_0 = 15°$ (right)

Rotor Speeds

As Chandrasekhara showed in [58], compressibility effects on dynamic stall set in at a free stream Mach number of $Ma = 0.3$. Beyond this value, the dynamic stall process is initiated at lower angles of attack. Since the location of the omega-shaped dynamic stall vortex is estimated to be between 70% and 90% radius [83], the rotor speeds should be in a range where this area of the blade experiences Mach numbers of at least $Ma = 0.3$ to account for compressibility effects. The rotor speeds chosen to analyze compressibility effects and control parameter influences are 900, 1200, and 1500 RPM. All parameter studies for the static pitch polar and dynamic stall measurements are performed at these three rotor speeds. They cover blade tip Mach numbers from 0.25 to 0.41, tip Reynolds numbers from 7×10^5 to 1.2×10^6, and tip speeds from 85 m/s to 141 m/s, see Tab. 4.2.

Ω (RPM)	$v_{0.75R}$ (m/s)	v_{tip} (m/s)	$M_{0.75R}$ (-)	M_{tip} (-)	$Re_{0.75R}$ (-)	Re_{tip} (-)	$k_{0.75R}$ (-)	k_{tip} (-)
900	63.63	84.82	0.18	0.25	534,998	713,331	0.096	0.072
1,200	84.83	113.10	0.25	0.33	713,373	951,165	0.096	0.072
1,500	106.03	141.37	0.30	0.41	891,685	1,188,913	0.096	0.072

Table 4.2: Speed dependent rotor parameters for dry air at 1 bar and 20° C

The variables in Tab. 4.2 are calculated according to the following equations:

$$v = \Omega r, \qquad M = \frac{v}{a}, \qquad Re = \frac{\rho c v}{\eta}, \qquad k = \frac{c}{2r},$$

Sutherland's formula [148] is used to calculate of dynamic viscosity η and the ideal gas law to determine air density ρ

$$\eta = \eta_0 \frac{T_0 + C}{T + C} \left(\frac{T}{T_0}\right)^{3/2} = 1.84 \cdot 10^{-5}\ Pa\ s, \qquad \rho = \frac{p}{R_s T} = 1.19\ \frac{kg}{m^3} \tag{4.2}$$

with the Sutherland constants for air η_0, T_0, C and the ideal gas constant for dry air R_s:

$$\eta_0 = 18.27 \cdot 10^{-6}\ Pa\ s, \quad T_0 = 291.15\ K, \quad C = 120\ K, \quad R_s = 287.058\ \frac{J}{kgK}, \quad a = 343.2\ \frac{m}{s}$$

Due to the operating altitude of the test site – 482 m above Mean Sea Level (MSL) – the pressure is slightly less than 1 bar, which has a reducing effect on the Reynolds number but is not considered here. The pressure dependence of the dynamic viscosity is negligible and is not included in the Sutherland model.

4.1.3 Data Preparation

Data Filtering

The torque measuring unit uses a pre-installed hardware low-pass filter with a cut-off frequency of 1000 Hz. Filtering is necessary because the torque sensor is close to the synchronous motor, and its analog data is susceptible to high-amplitude electromagnetic noise, resulting in an unsatisfactory signal-to-noise ratio. All other data is unfiltered.

Mean Calculation

Each polar point describes the phase-averaged mean $\bar{x}$ for M recorded revolutions and N samples per revolution. The standard error is calculated as the deviation of each revolution's average $\bar{x}_i$ from the total mean $\bar{x}$ to avoid a misinterpretation of harmonic oscillations as a deviation from the total mean, see equations 2.23 and 2.24 in section 2.8.

Power Offset Correction

The dissipated energy in the pre-loaded upper shaft bearings leads to high power consumption compared to the overall power needed for rotation with blades. This power can be numerically estimated or experimentally determined for the selected rotor speeds and needs to be subtracted from the overall measured power to provide comparability between measured and computed rotor power. In addition, drive power is dependent on bearing grease level and bearing temperature. Therefore, it can still vary during one test campaign. The drive power is measured as 970, 1300, and 1700 W without blades at 900, 1200, and 1500 RPM, respectively.

4.1.4 Power and Thrust Measurement Validation

The initial operation of the MERIT test rig is performed with the two left-rotating blades of the AREA drone [149], see Fig. 4.5. The drone uses two intermeshing two-bladed rotors are used in a Flettner configuration for high-altitude applications. Power and thrust data for one rotor is measured on the test rig and compared to simulation and flight test data to determine data quality and provide validation with another test rig.[*]

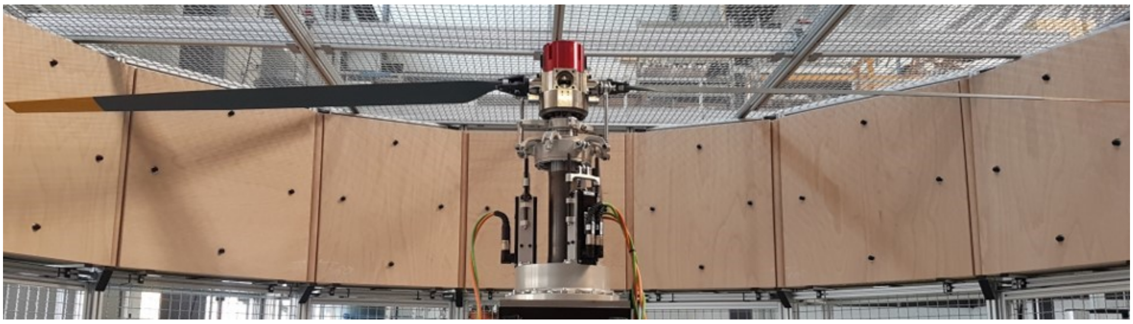

Figure 4.5: Left-rotating AREA rotor on the MERIT test rig

The thrust and power polars of the AREA rotor are measured at rotor speeds of $\Omega = 550, 600, \ldots, 800$ RPM to obtain tip speeds that are similar to the AREA rotor on the drone. These speeds must be adjusted because the AREA blades [150] on the MERIT rotor have a slightly different rotor radius than the AREA drone due to differences in blade attachment radii. A comparison of thrust and power values for single operating points, defined by collective pitch and tip speed, shows a very satisfactory agreement of AREA-on-MERIT with AREA-on-drone data from [147, 149].

As mentioned above, the power required to compensate for the energy dissipated in the bearings is not negligible. It must be determined in order to compare the rotor power consumption for the relevant rotor speeds. For the tests with the AREA blade attachments, this power was measured without blades and is between 514 W at 550 RPM and 922 W at 800 RPM [22].

---

[*] Parts of this section were previously published in [22].

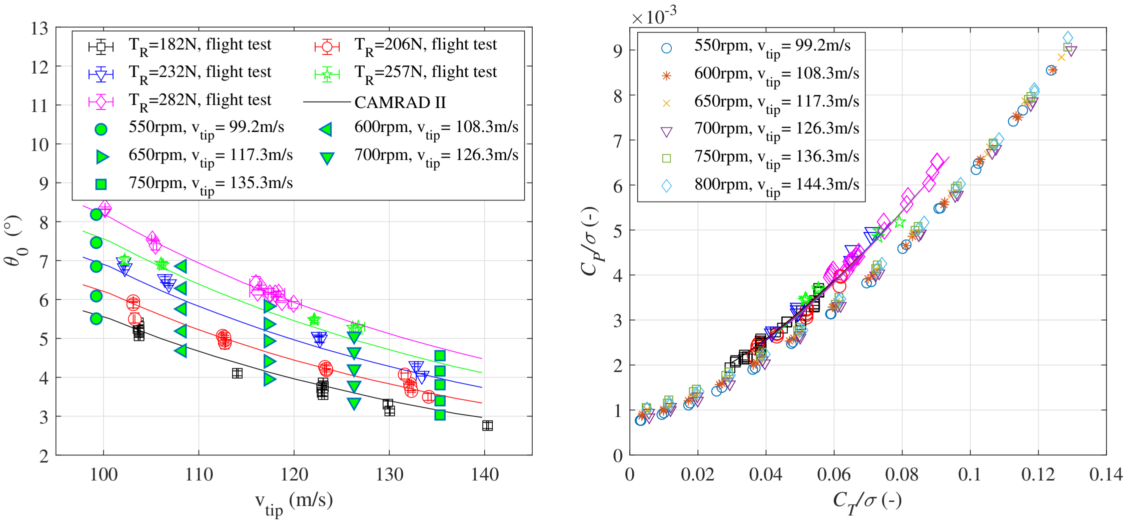

Figure 4.6: Comparison of AREA flight test data (intermeshing rotors), CAMRAD II calculations, and whirl tower data (single rotor) for various rotor thrusts; flight test at 500 m above MSL [22]

The slightly higher power consumption in the flight tests is ascribed to intermeshing rotors and the smaller rotor diameter. Further details on the experimental setup, data analysis, and discussion are published in [22]. The comparison between the power and thrust data of the AREA rotor on the drone and on the MERIT test rig shows satisfactory results. Minor differences are due to differences in the rotor diameter and drive system.

4.2 Rotor Performance and Static Stall

Rotor performance is analyzed at the speeds of 900, 1200, and 1500 RPM. This analysis includes thrust and power, blade root moments, and pitch link forces from -4° to 24°, which is well beyond the static stall limit. The investigated rotor is a two-bladed rotor with the MERIT blades SN007 and SN008, as described in section 4.1.1.[*]

4.2.1 Thrust and Power Polars

The thrust and power polars for the three selected rotor speeds are measured on the same day. The mean and standard deviation for each data point are shown in Fig. 4.7 compared to the simulation results for the rigid blade and free wake model in CAMRAD II. Power and thrust are non-dimensionalized according to:

$$c_P = \frac{P}{\rho A(\Omega R)^3}, \quad c_T = \frac{T}{\rho A(\Omega R)^2} \tag{4.3}$$

The thrust and power data show symmetry around $\Theta_0 = 0°$ up to $\Theta_0 = \pm 4°$, as expected for a symmetrical airfoil. Thrust increases nonlinearly up to about $\Theta_0 = 4°$, as the rotor downwash is not yet fully developed, and the rotor interacts with its rotor wake and tip vortices. Beyond this value, thrust increases linearly with collective pitch until static stall occurs. This behavior is observed at all three rotor speeds. A decrease in the thrust gradient indicates the stall onset region. The static stall pitch angle is observed between 19° and 21° for the different rotor speeds and can vary even at the same speed, depending on environmental conditions and flow recirculation, see section 4.2.5.

The power consumption in the whirl tower tests is consistently higher than in the simulation. The relative deviation is between 6% and 10% within 3°-19° collective pitch. Deviations are higher at very low pitch angles and in the stall region due to the high level of flow perturbation and vortex interaction. Low-fidelity models cannot accurately represent the aerodynamic loads in these regions.

Overall, the comparison of thrust and power from the experiment with the rigid-blade free wake model shows very satisfactory data agreement in the out-of-stall region. The numerical model estimates stall at much higher pitch angles, between 23° for 1500 RPM and 26° for 900 RPM, while the experiment shows a premature static stall between 19° and 21°. Furthermore, the simulation shows a sudden loss of lift in the stall region, while the experiment shows a slight loss of lift with a subsequent increase. In addition, power consumption in the stall region is underestimated in the numerical results. Here, the primary model deficiency lies in the computation of profile drag with CFD. Drag prediction is still a complex task that depends on the right choice and combination of turbulence models. Despite the different absolute value offsets between experiment and simulation, the trends are the same.

---

[*] Parts of this section were published in [151, 152].

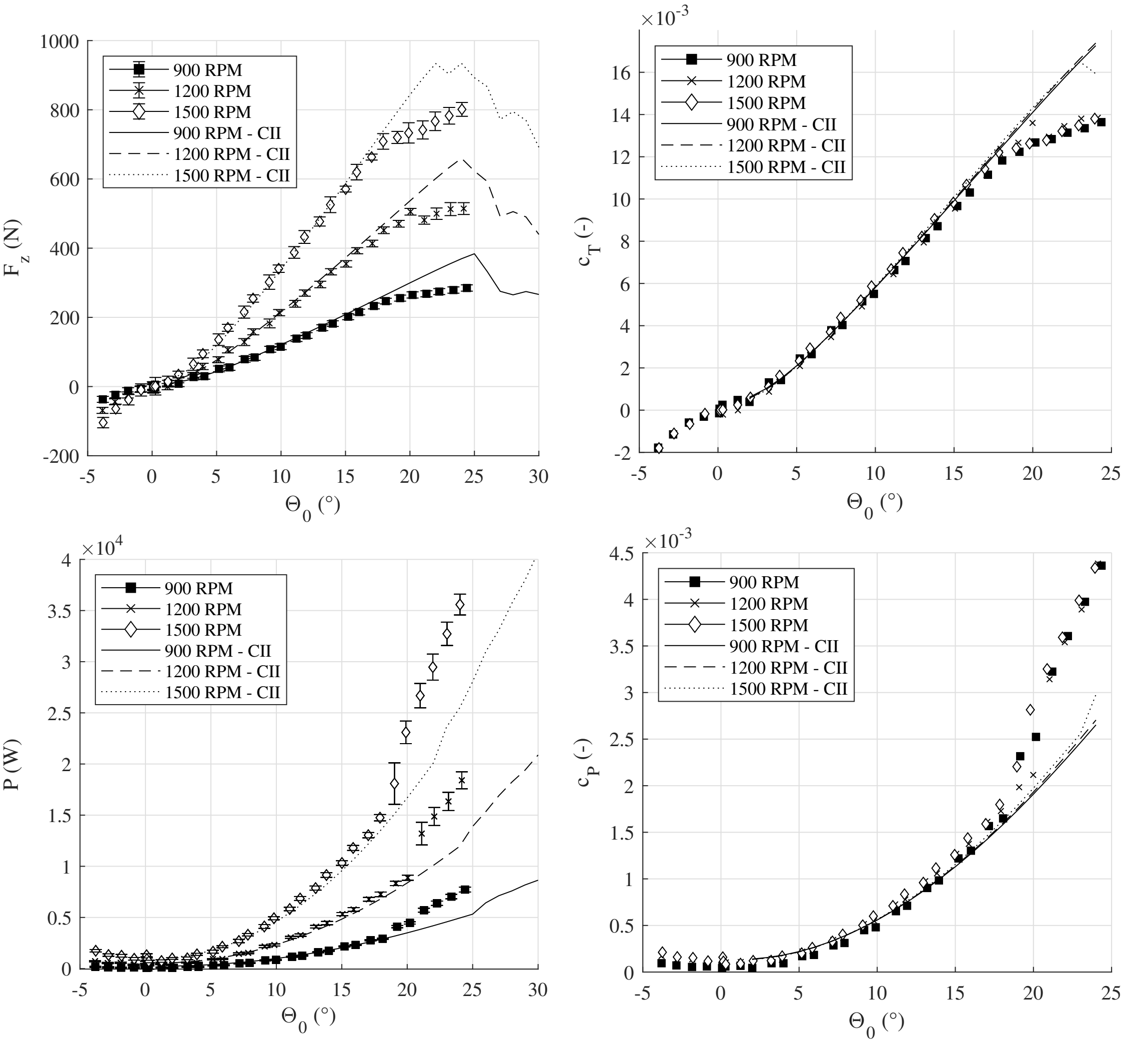

Figure 4.7: Measured and calculated thrust and power as function of Θ_0 at 900, 1200, 1500 RPM

4.2.2 Repeatability Measurements

The polar measurements are repeated on two different days with the same experimental setup but varying environmental conditions, such as local air pressure and laboratory temperature: 16.9° C and 951 hPa on day one, and 21.6° C and 960 hPa on day two. Figure 4.8 shows both days' respective thrust and power polars.

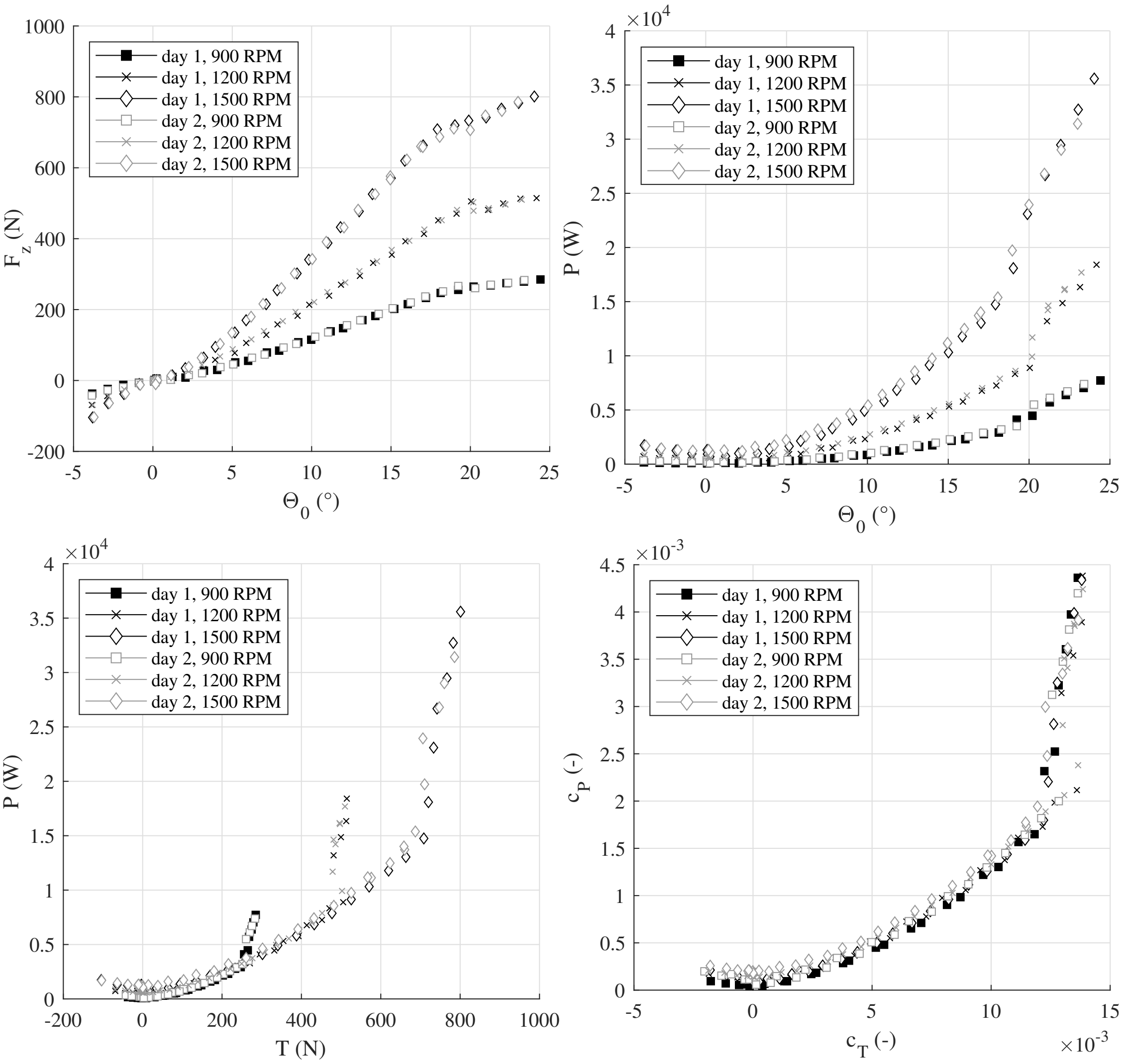

Figure 4.8: Repeatability check for thrust and power as function of Θ_0 on two different days

The two measurements show good agreement with a few slight deviations in the stall onset region. For example, the repeat measurement at $\Theta_0 = 20°$ and 1200 RPM shows stall onset in contrast to the original measurement at that point. Stall onset has been observed to be ambivalent and sensitive to triggers such as recirculation. Therefore, it depends on the time of recording whether the recorded data shows stall or not. Consideration of load amplitudes and standard deviation helps to determine stall occurrence. They are analyzed and discussed in section 4.2.5.

The most considerable discrepancy between the two repeated measurements is the power consumption at 1500 RPM. It is almost 10% higher on day 1 than on day 2 for the same thrust. Experience has shown that this power offset is due to differences in bearing characteristics such as bearing temperature and grease level. Power consumption calculated from drive torque generally includes energy dissipation in the bearings. Lubricating bearings prior to a test may initially result in higher power consumption due to the flexing work on the grease until it is evenly distributed and a constant bearing temperature is reached.

4.2.3 Blade Root Moments and Pitch Link Forces

Blade Root Moments

Fig. 4.9 shows the measured blade root flapping and lead-lag moments for 900, 1200, and 1500 RPM and $\Theta_0 = -4° \ldots +24°$.

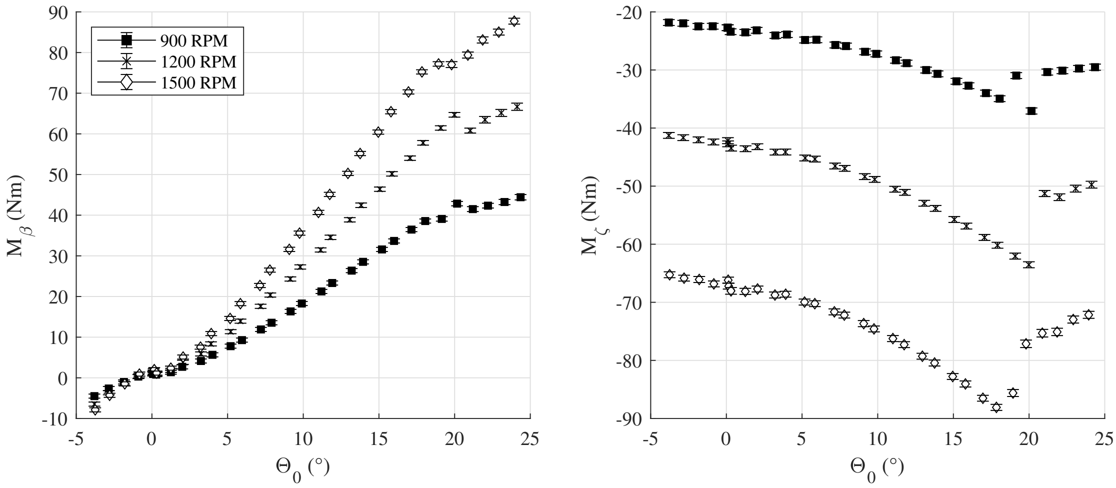

Figure 4.9: Measured blade flapping moment M_β and lead-lag moment M_ζ as a function of collective pitch Θ_0 at 900, 1200, 1500 RPM

The flapping moments show symmetry around zero pitch up to $\Theta_0 = 4°$ and a linear increase with collective pitch up to the stall onset region. As indicated by the thrust data, stall onset occurs at a lower pitch angle at higher rotor speeds, see section 4.2.5. After a slight loss of flapping moment, a clear increase with a smaller slope can be seen. This is partly due to the increase in aerodynamic drag, which contributes to the flapping moment of the blade section, since the flapping direction in this context is defined perpendicular to the blade chord, just as the lead-lag direction is defined parallel to the chord.

The lead-lag moment data shows a static load offset at zero pitch, that consists of resulting moments from centrifugal force and profile drag at the respective rotor speed. After stall onset, the absolute values of the lead-lag moment decreases. As pitch angle increases, the increasing aerodynamic drag gains more influence on blade flapping moment and less influence on lead-lag moment due to the pitch rotation of the blade and its moment sensor axes.

Pitch Link Forces

The measured, uncorrected pitch link forces for pitch links 1 and 2 as a function of collective pitch and rotor speed are shown in Fig. 4.10. They are a superposition of aerodynamic and frictional loads and indicate a load hysteresis symmetrical about $\Theta_0 = 10°$ due to the tension-torsion straps' pre-twist by $-10°$ at $\Theta_0 = 0°$ collective pitch.

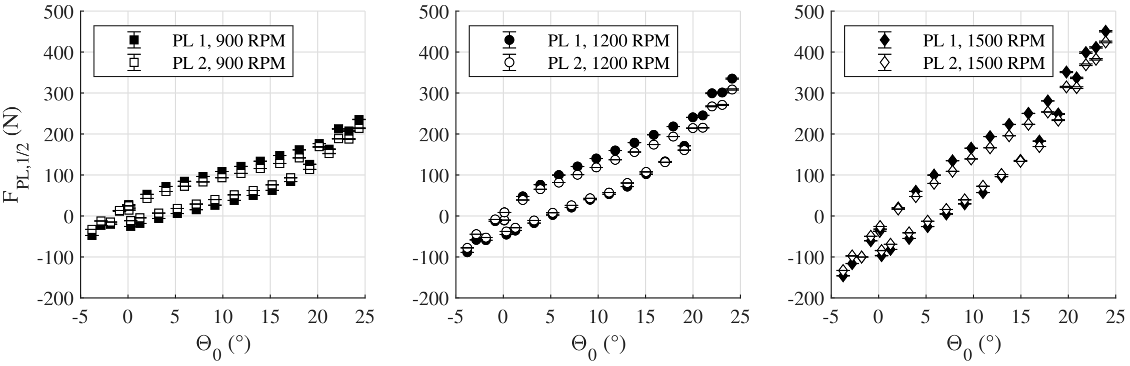

Figure 4.10: Measured, uncorrected pitch link loads for the rotor polars at 900, 1200, 1500 RPM

As explained in section 2.6.2, the measured hysteresis in the pitch link forces is due to the frictional load hysteresis of the tension-torsion strap, see the results of the calibration test with the representative weight in Fig. 2.31. To eliminate the effect of the tension-torsion strap loads on the pitch link forces, the measured total loads must be corrected by subtracting the measured calibration values for each pitch angle and rotor speed, as shown in Fig. 4.10: $F_{PL,1/2,corr} = F_{PL,1/2} - F_{PL,1/2,cal}$ The calibration tests for this correction are described in more detail in section 2.6.2. The results after applying the hysteresis correction are shown in Fig. 4.11.

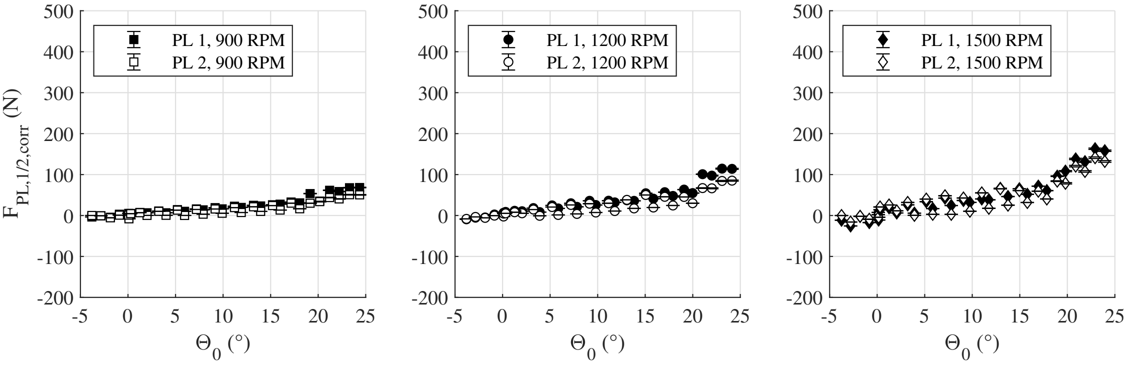

Figure 4.11: Corrected pitch link loads for the rotor polars at 900, 1200, 1500 RPM

Since the aerodynamically induced pitch link loads are in the same order of magnitude as the frictional loads of the tension-torsion straps, the measured load hysteresis strongly influences the resulting loads and cannot be neglected. In addition, pitch link 1 shows different loads than pitch link 2, indicating that the hysteresis is slightly different for each tension-torsion strap. In addition, pitch link force 2 shows more scatter after correction than pitch link force 1. The slightly different mass distributions and, therefore, centrifugal forces between blades 1 and 2, due to manufacturing inaccuracies and blade tip balancing masses, contribute to the observed load differences between pitch links 1 and 2. Nevertheless, the simulated pitch link loads capture the trends and absolute value range of the measured pitch link loads, as shown in the next section, see Fig. 4.16. In the case of future experimental investigation of rotor blades with a positive airfoil camber, higher total aerodynamic moments and, therefore, higher total pitch link loads are expected, in which the loads resulting from the tension-torsion straps will be a less significant proportion.

4.2.4 Rigid and Elastic Blade Model Comparison

The measured structural blade and pitch link loads are subject to aerodynamic and inertial loads. Due to the high rotor speeds, the latter significantly impacts structural loads and cannot be neglected. The inertial influence is analyzed in this section employing the numerical model.

The elastic and rigid blade model results are used for a comparison with the experimental measurement results at the example of 900 RPM to show blade elasticity effects and validate the measured loads. The model variant referred to as the elastic blade model is the model introduced in chapter 3, including the surrogate flapping hinge. In contrast, the model variant referred to as the rigid blade model is a rigid beam model without a hinge. The aerodynamic free wake model is kept the same for both model variants, as described in chapter 3.

Simulations above 1000 RPM with the statically validated elastic beam definition (see chapter 3) show a very high sensitivity of numerical convergence to the initial solution. This initial solution must be found in an iterative process with tiny increments in rotor speed, control angle, or beam discretization. Validating the experimental blade root moment data with the elastic blade model at 900 RPM is considered sufficient regarding this model limit. Given the disproportionate effort required to achieve numerical convergence at higher rotor speeds, an elastic blade model calculation at 1200 and 1500 RPM does not add significant value to the core message of this load validation approach.

Thrust and Power

Numerically predicted and measured thrust and power polars are shown in Fig. 4.12 as a function of collective pitch control angle Θ_0.The elastic and rigid blade models show almost identical thrust and power polar results in the out-of-stall region. The thrust and power predictions differ slightly between the two models in the stall region, where the elastic blade model predicts a consistently 1° lower static stall onset angle than the rigid blade model. The prediction data are within the 95 % confidence interval of the experimental measurement data up to $\Theta_0 = 15^\circ$ for thrust and up to $\Theta_0 = 18^\circ$ for power.

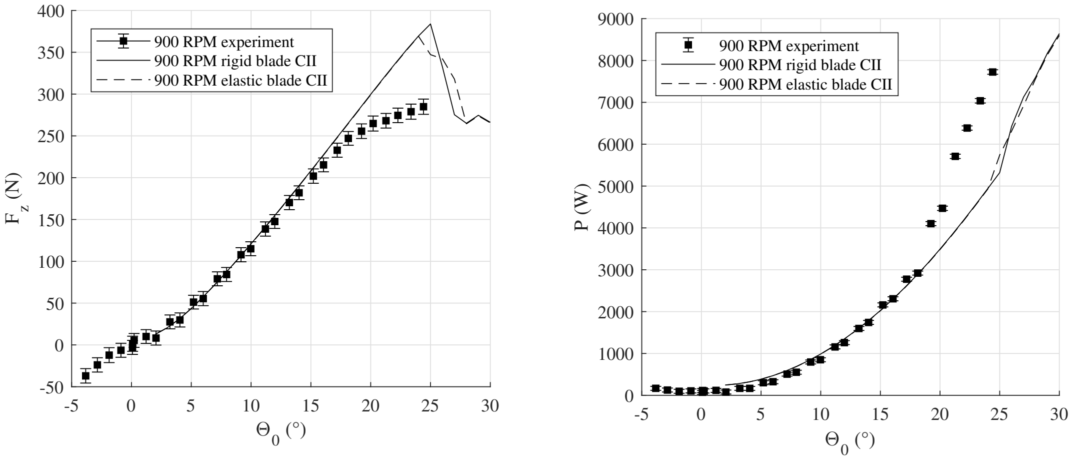

Figure 4.12: Measured and predicted thrust F_z and power P as a function of Θ_0 at 900 RPM, comparison between experiment, elastic, and rigid blade model

Blade Root Moments and Pitch Link Forces

Blade elasticity generally reduces blade root moments. As the aerodynamic lift of the blade deflects the blade in the flapping direction, the centrifugal force is given a lever that results in a relieving blade root moment – a moment opposite to that resulting from the aerodynamic lift. The calculation of blade root moments for a rigid and elastic blade model clearly shows the moment-relieving influence of the centrifugal force once blade deformation is allowed. The corresponding blade root flapping and lead-lag moments M_β, M_ζ, and pitch link forces $F_{PL,1}, F_{PL,2}$ from experiments and rigid and elastic blade calculations in CAMRAD II are shown in Fig. 4.13 and 4.14 at 900 RPM as a function of collective pitch.

The elastic and rigid blade models show the same trends as the experimental results in flapping and lead-lag moments, but a 4° and 5° higher static stall angle. The sectional blade loads differ significantly between the static and elastic blade beam models, especially in the flapping direction. The aforementioned load-relieving effect of the blade elasticity is particularly high for the flapping moment, since the blade experiences its greatest deformation in the flapping direction. Like the flapping moment, the lead-lag moments for the rigid and elastic blade models start at the same values but show increasing differences with increasing pitch angle. The moment-relief effect increases with pitch control, just as the deformation increases with pitch.

A comparison between the elastic blade model and the experimental results shows that the numerical loads are slightly but consistently underestimated in the flapping direction and below stall. For the lead-lag moment, the numerical results show a higher absolute zero pitch offset and a flatter load increase with pitch angle. Thus, the measured lead-lag moments lie between the rigid and elastic blade model results. The lead-lag deformation is much stronger than the flapping deformation. However, inertia has a greater effect on structural loads in the lead-lag direction due to the larger chordwise blade dimension. Manufacturing inaccuracies, such as small variations

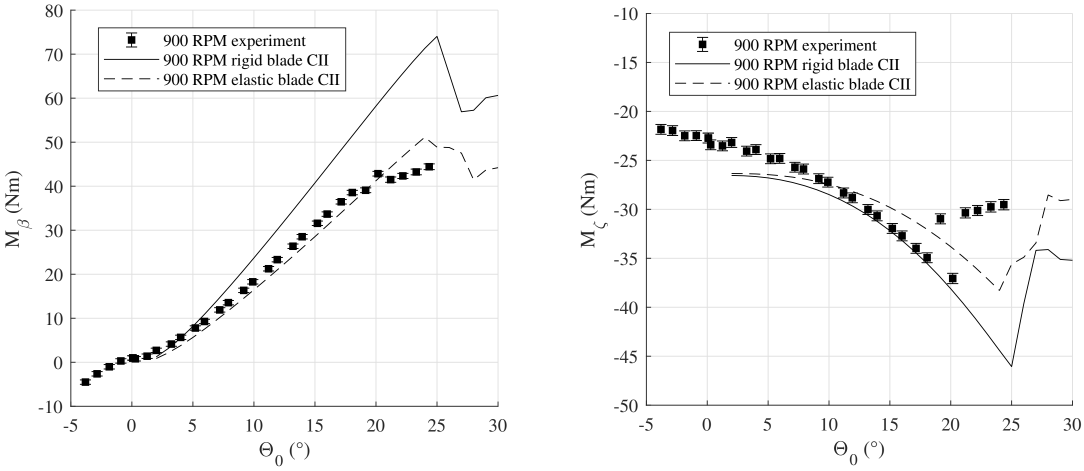

Figure 4.13: Measured and predicted M_β and M_ζ as a function of Θ_0 at 900 RPM, comparison between experiment, elastic and rigid blade model

in the chord-wise position of the nose lead, strongly affect the chordwise mass distribution and thus the inertia moments, which vary with increasing pitch. Nevertheless, the same trends are observed in experiment and simulation.

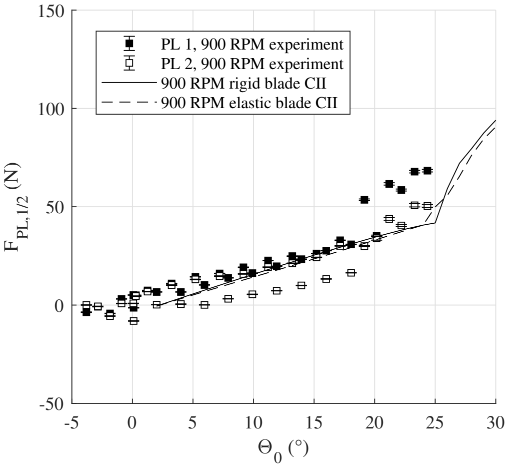

Figure 4.14: Measured and predicted pitch link forces $F_{PL,1}, F_{PL,2}$ as a function of Θ_0 at 900 RPM, comparison between experiment, elastic, and rigid blade model

The pitch link forces show almost no difference between the elastic and rigid blade models, as the blade elasticity has a minor effect on blade torsion. Furthermore, the numerical results correlate well with the measured loads on pitch link 1, although the prediction slightly underestimates the pitch link forces, especially at lower pitch angles. As shown in section 2.6.2, pitch link 2 exhibits a strong hysteresis in the experiment that cannot be corrected consistently.

Rigid Blade Load Trends for Higher Speeds

Finally, load calculations at rotor speeds above 900 RPM were performed with the rigid blade model. The load trends for the rigid blade model at higher rotor speeds follow the same trends as the experiments and show reasonable agreement with the measured data, except for the flapping moment, which shows the highest inertia influence. The rigid blade model and experimental results for all speeds and all considered blade loads are shown in Fig. 4.15 and 4.16.

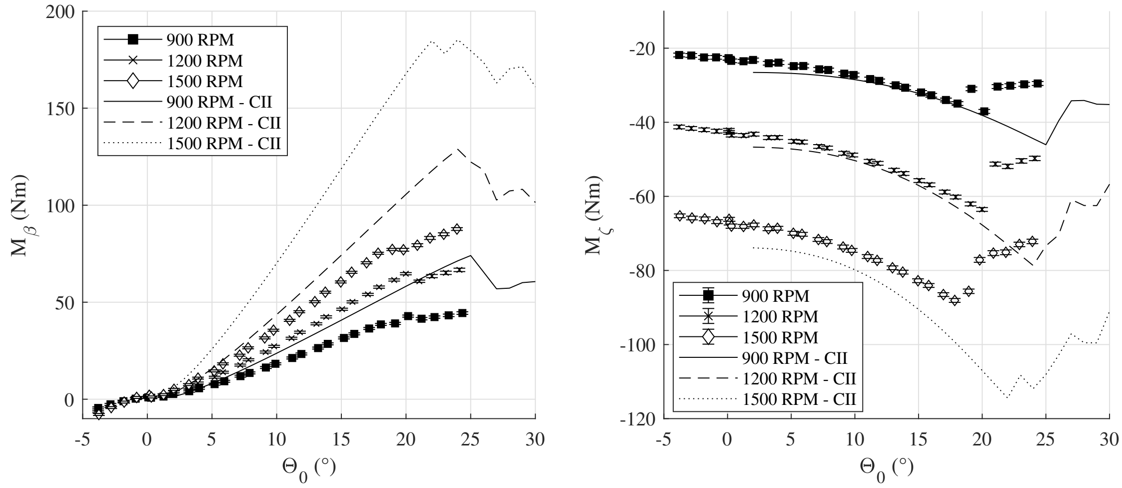

Figure 4.15: Blade flapping and lead-lag moments M_β and M_ζ as a function of Θ_0 at 900, 1200, 1500 RPM; experiment compared to the rigid-blade model

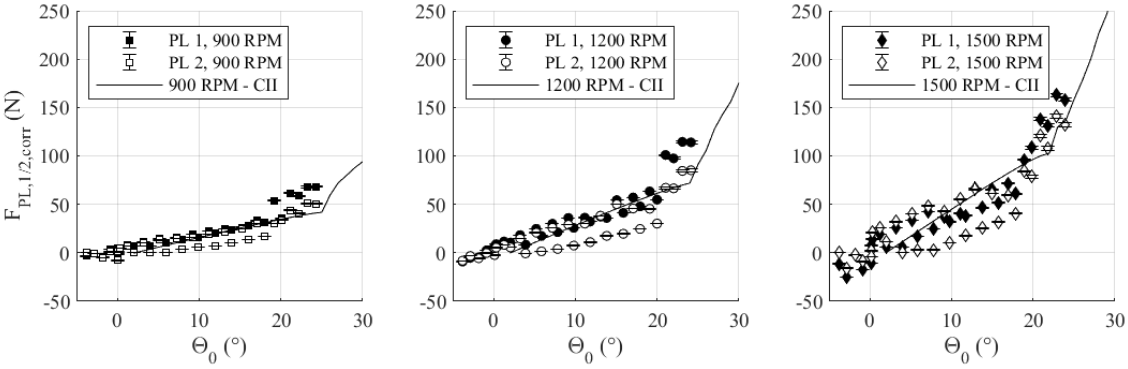

Figure 4.16: Corrected pitch link forces $F_{PL,1,corr}, F_{PL,2,corr}$ for the polars at 900, 1200, 1500 RPM; experiment compared to the rigid-blade model

4.2.5 Static Stall

According to measurements on a rotor under the influence of a given free stream velocity, there are three main indicators of static stall: loss of lift, increase in drag, and increase in load amplitudes and vibration. The polars of the MERIT rotor show that the slopes of the thrust and the blade root flapping moment decrease significantly at a pitch angle between 19° and 22°. The stall onset angle depends on the rotor speed and the ascending or descending pitch branches and can be induced by flow recirculation. For some pitch angles near stall, there is even an ambivalent state where stall and recirculation alternate within seconds without any change in rotor control.

Considering structural load amplitudes confirms the static stall pitch angles for each selected rotor speed, see Fig. 4.17, where the blade root moments are shown as a function of data samples. The sudden disproportionate increase in amplitudes marks the stall regions, consistent with the perceived sudden change in rotor acoustics during a stall.

According to the load amplitudes derived from Fig. 4.17, stall occurs at the following pitch angles:

- 900 RPM: between 22° for ascending pitch, and 19° for descending pitch
- 1200 RPM: between 22° for ascending pitch, and 21° for descending pitch
- 1500 RPM: between 20° for ascending pitch, and 19° for descending pitch

Power and thrust polars show a slight tendency for stall to occur at lower pitch angles for increasing speed. The numerical model supports this tendency. The CFD polars also indicate that lift loss and drag increase occur at a lower collective pitch as the Mach number increases. However, the load amplitudes confirm that stall occurs over a varying range of pitch angles, depending on whether the pitch branches are ascending or descending. The trend shows a lower pitch angle for descending pitch. An influencing factor for this behavior is that the initial flow condition is different in both cases. In addition, the variation of the stall onset angle can be attributed to a partial stall on the rotor blade that develops into a full stall. A smaller pitch angle increment in the stall region would be required to more accurately determine the stall location.

Furthermore, in the expected stall region, stall initiation depends on external triggers such as blade vortex interaction, recirculation, or inflow perturbation due to interaction with the test rig casing. Rotor operation in the stall region has shown that the rotor can be in an ambivalent state between attached and detached flow at a given collective pitch angle. This is the case for 21° at 1200 RPM and 19° at 1500 RPM. These two different states occurring at the same pitch angle can alternate at intervals of several seconds. Rotor acoustics and vibrations observed confirm this behavior. In addition, stall occurrence depends on the ambient conditions and can vary slightly with air density and temperature; see section 4.2.2.

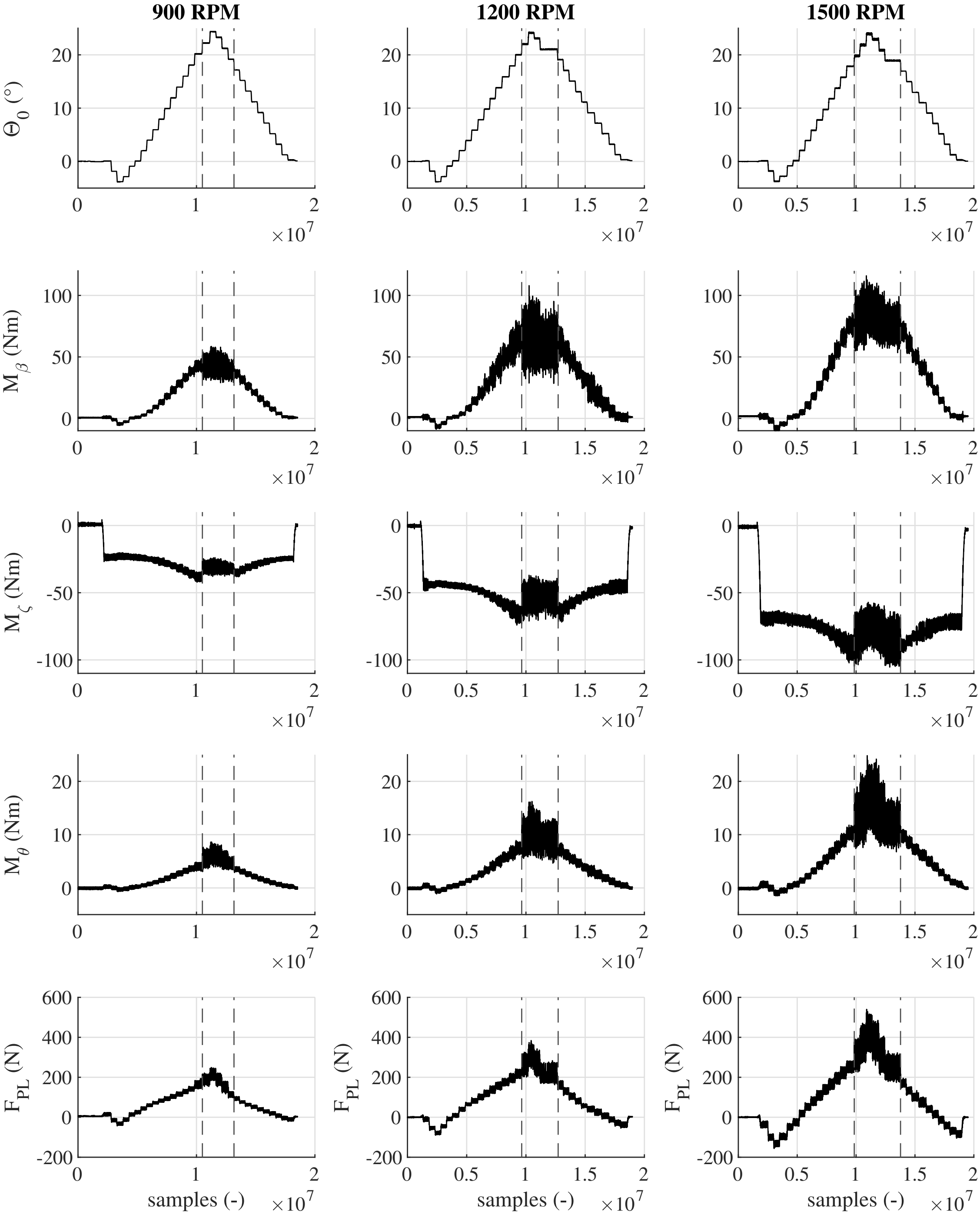

Figure 4.17: Pitch angle, blade root moments, and pitch link force as a function of data samples for the measured polars at 900, 1200, 1500 RPM; dashed lines delimit stall regions

4.3 Dynamic Stall - Structural Load Analysis and Parameter Study

The following sections present the dynamic stall test cases analyzed, a preliminary study of phase averaging convergence, data non-dimensionalization, and measurement repeatability. This is followed by an analysis of the effects of the control parameters – collective pitch, cyclic pitch, rotor speed – on the structural loads flapping moment, lead-lag moment, torsion, and pitch link forces.[*]

4.3.1 Dynamic Stall Test Cases

The number and type of dynamic stall test cases selected should demonstrate the influence of collective pitch, cyclic pitch, and rotor speed on the phenomenon. Collective pitch influence is studied using the pitch angles $14, 16, 18, 20^\circ \pm 6^\circ$ and cyclic pitch effects are analyzed using the pitch settings $14^\circ \pm 4, 5, 6, 7, 8, 9, 10^\circ$ to cover light and deep stall cases, see Tab. 4.3 and Fig. 4.18. All cases are examined at the three rotor speeds of 900, 1200, and 1500 RPM. The dynamic stall load data are compared with the corresponding static polar data shown in section 4.2.

Test	900 RPM			1200 RPM			1500 RPM		
case	Θ_0 (°)	Θ_C (°)	$\dot{\Theta}_m$ (°/s)	Θ_0 (°)	Θ_C (°)	$\dot{\Theta}_m$ (°/s)	Θ_0 (°)	Θ_C (°)	$\dot{\Theta}_m$ (°/s)
1	14	4	377	14	4	503	14	4	628
2	14	5	471	14	5	628	14	5	785
3	14	6	565	14	6	754	14	6	942
4	14	7	660	14	7	880	14	7	1100
5	14	8	754	14	8	1005	14	8	1257
6	14	9	848	14	9	1131	14	9	1414
7	14	10	942	14	10	1257	14	10	1571
8	16	6	565	16	6	754	16	6	942
9	18	6	565	18	6	754	18	6	942
10	20	6	565	20	6	754	20	6	942

Table 4.3: Collective pich, cyclic pitch, and maximum pitch rate $\dot{\Theta}_m$ for the analyzed dynamic stall test cases at different rotor speeds

4.3.2 Pre-Analyses

This section presents initial dynamic stall analyses to verify data reliability and test conditions. It shows how the revolution-averaged data changes with the number of cycles recorded, how repeatable the structural load measurements are during dynamic stall, and how the data is non-dimensionalized to provide data comparability between different rotor speeds.

Non-Dimensionalization

The structural moments and forces are non-dimensionalized according to the equations (4.4) to provide comparability between the three speeds without considering the influence of dynamic

---

[*] Parts of this section were published in [151, 152].

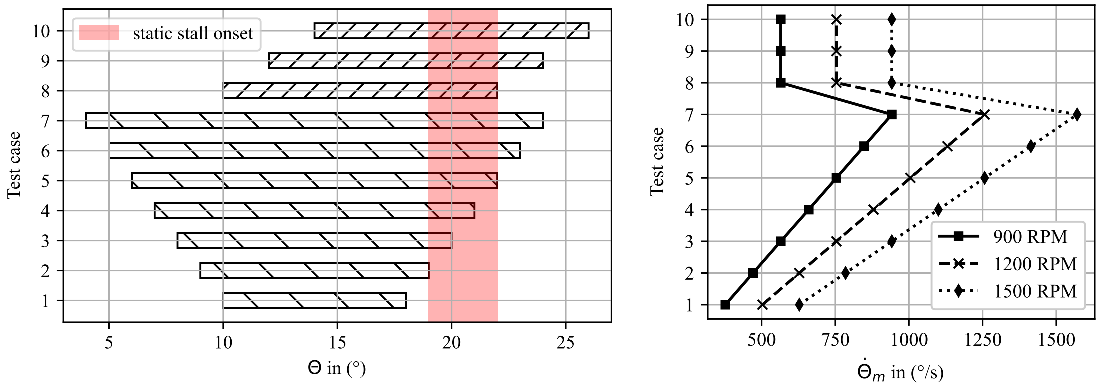

Figure 4.18: Blade root pitch ranges (left) and maximum pitch rates $\dot{\Theta}_m$ (right) for the tested dynamic stall cases at 900, 1200, and 1500 RPM

pressure. Fig. 4.19 shows the non-dimensionalized polars for the blade root flapping and the lead-lag moment at 900, 1200 and 1500 RPM.

$$C_{M_{\beta,\zeta,\theta}} = \frac{M_{\beta,\zeta,\theta}}{\rho A(\Omega R)^2 R}; \qquad C_{F_{PL1/2}} = \frac{F_{PL1/2}}{\rho A(\Omega R)^2} \tag{4.4}$$

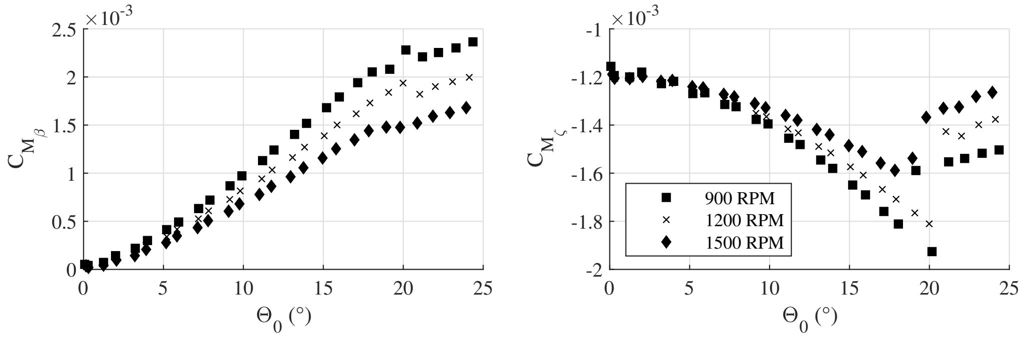

Figure 4.19: Non-dimensionalized polars for blade root flapping and lead-lag moments at 900, 1200, and 1500 RPM

The non-dimensionalized polars show decreasing values with increasing rotor speed because the centrifugal force of an elastically deformed blade has a mitigating effect on the blade root moments, especially in the flapping direction, as shown in 4.2.4. The load evaluation parameters – dynamic load increase, load range, and hysteresis – are evaluated with the corresponding static polar values at the stall angle.

Revolution-Averaged Convergence

Dynamic stall is a highly unsteady phenomenon that is very sensitive to external triggers. Significant cycle-to-cycle variations can occur during dynamic stall that cannot be characterized as experimental uncertainty. Several studies have shown that phase averaging can introduce errors of up to 30 % in aerodynamic loads [28, 30, 33, 108, 109, 153]. A study of the deviation of each revolution's data from the phase average with increasing number of recorded revolutions should show how strong these variations are visible in integral structural loads. In addition, this study should provide information on how many revolutions must be recorded for the phase average not to change significantly. Fig. 4.20 shows that the RMSE between the actual revolution and the mean of the last revolutions decreases with increasing number of revolutions. The cases shown in Fig. 4.20 are the deep stall cases $14^\circ \pm 10^\circ$ and $20^\circ \pm 6^\circ$. The recorded data is plotted as a solid line with 2% transparency to visualize the statistical distribution of the data over the recorded revolutions using different shades of gray.

Both cases show that the RMSE decreases continuously for all three speeds, falling below 1 Nm (0.7 % FS) for the flapping and lead-lag moments and below 0.01 Nm (0.04 % FS) for the torsional moment after 300-400 revolutions. The RMSE trends for the remaining dynamic stall cases are shown in the appendix, section B.2.

Repeatability

The formation and characteristics of dynamic stall are easily perturbed by uncontrollable conditions such as flow recirculation or vortex interactions. Therefore, a repeatability test should verify that the structural load dynamics show repeatable results with the same experimental setup on different days. The deep stall case $20 \pm 4^\circ$ at three rotor speeds of 900, 1200 and 1500 RPM was chosen for this purpose. Temperature and local pressure are 17.5° C and 943.0 hPa on the first day, and 18.2° C and 953.3 hPa on the second day.

Fig. 4.21 shows as an example the non-dimensionalized blade root flapping moments for all speeds on both days. The repeatability results of the remaining structural load data are shown in the appendix, B.3. All load data show very satisfactory agreement in terms of absolute values and load dynamics. In particular, the pitch link forces show surprisingly good repeatability because they are strongly influenced by the nonlinear static and dynamic loads of the tension-torsion strap. As shown in the calibration of the pitch link load cells, both pitch links are influenced by the nonlinear torsional loads in the tension-torsion straps. In addition, minimal mechanical differences (within manufacturing tolerances) between the two tension-torsion straps affect the load differences in the pitch link forces. Overall, all measured structural loads are rated as repeatable for the deep stall case shown.

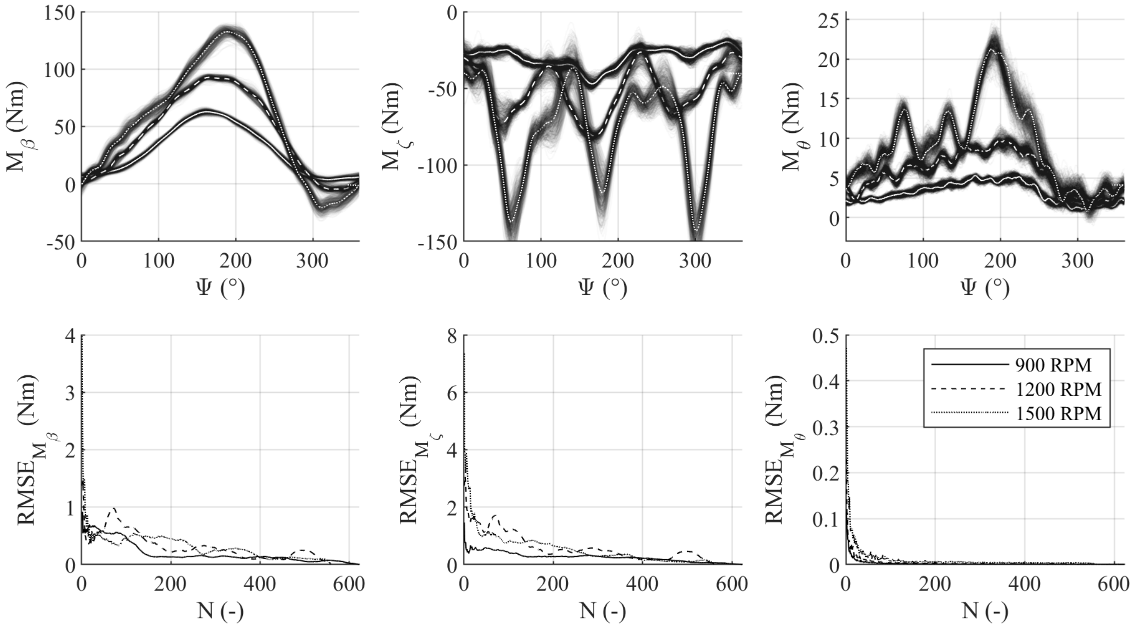

(a) 14° ± 10°

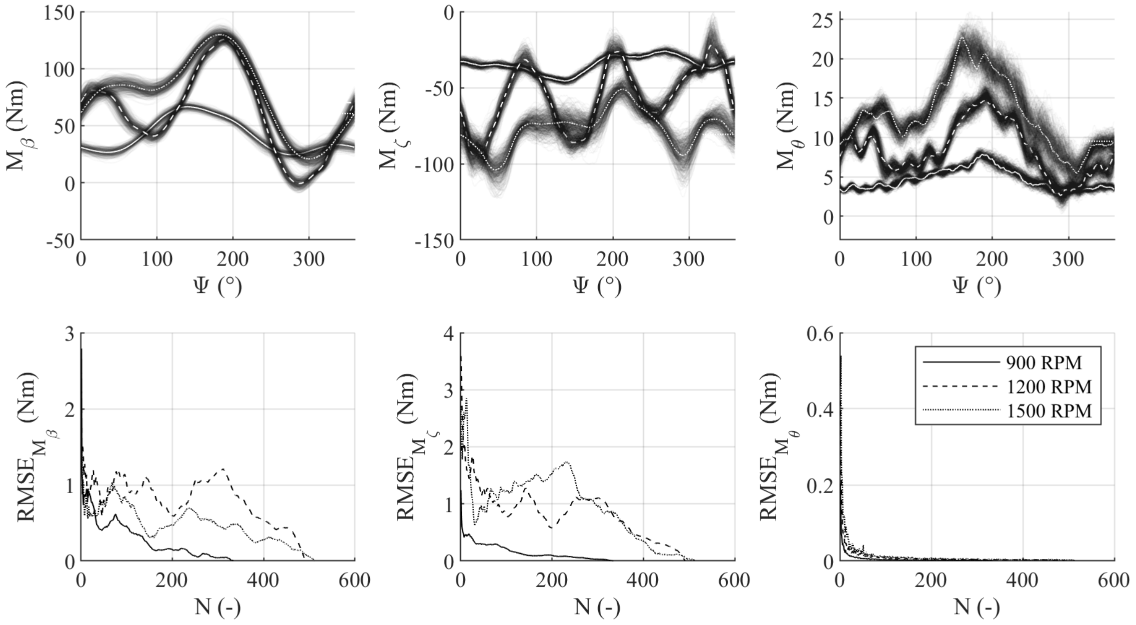

(b) 20° ± 6°

Figure 4.20: Blade root moments as a function of rotor azimuth and root mean square errors thereof as a function of recorded number of revolutions N for the two deep dynamic stall cases 14° ± 10° and 20° ± 6° at 900, 1200, and 1500 RPM

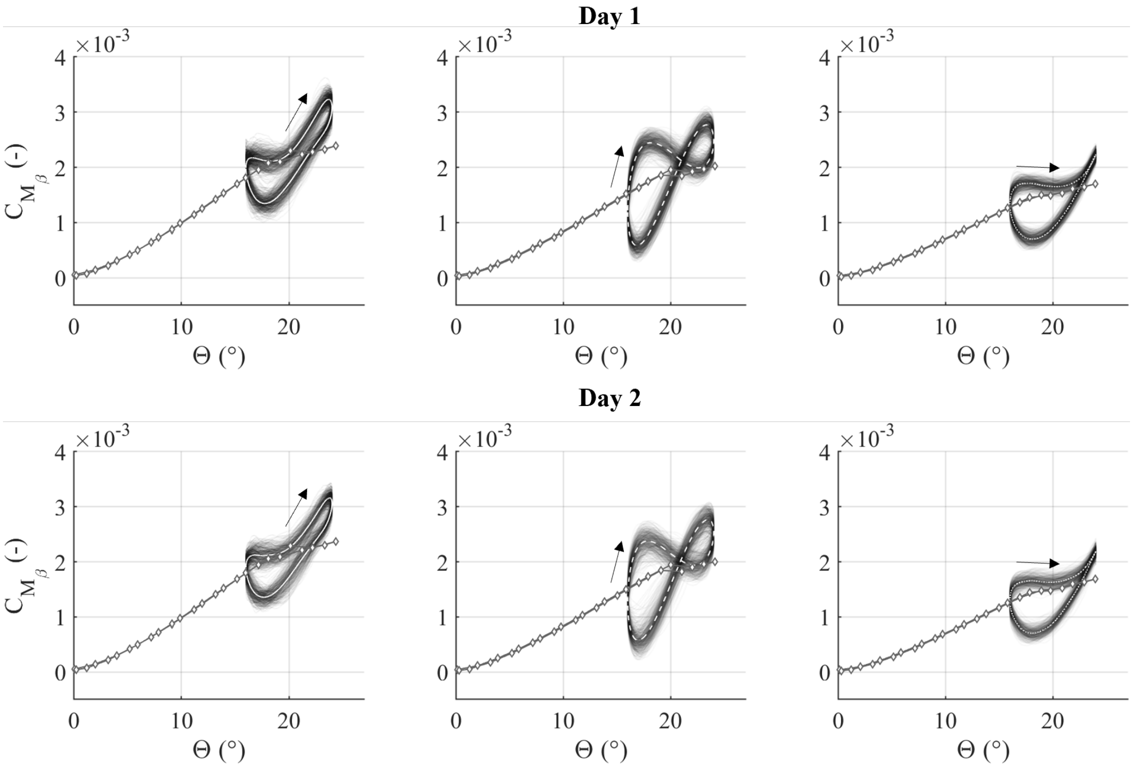

Figure 4.21: Repeatability test for the exemplary deep dynamic stall case 20° ± 4° at 900, 1200, and 1500 RPM and the non-dimensionalized blade root flapping moment as a function of pitch angle; upper graphs recorded on day 1, 17.5°C, 943 hPa; lower graphs recorded on day 2, 18.2°C, 953.3 hPa.

4.3.3 Collective Pitch and Mach Influence

This section examines the effect of collective pitch and rotor speed on structural loads in dynamic stall. For this purpose, the aforementioned dynamic stall cases $14, 16, 18, 20° \pm 6°$ at 900, 1200, and 1500 RPM are selected. McCroskey introduced the terminology of light and deep stall [42]. He characterized the dynamic stall cases according to the magnitude of the viscous-inviscid flow interaction, which is predominantly influenced by the maximum AoA during an airfoil oscillation. McCroskey differentiated between no stall (weak interaction), stall initiation (mild interaction), light stall (strong interaction), and deep dynamic stall (viscous dominated) [61]. The following section uses the three expressions stall onset ($16° \pm 6°$), light ($18° \pm 6°$), and deep ($20° \pm 6°$) stall for the selected cases.

The graphs in the following sections show all recorded revolution data plotted with a preset level of transparency to see the difference between overlapping data and outliers using different shades of gray. The white lines show their phase averages, while the gray lines with diamond markers show the corresponding static stall polar for the selected entity and speed. The three main effects that accompany dynamic stall are high normal forces and negative pitching moments, as well as large load hystereses caused by a delay in stall onset and flow reattachment. Therefore, all data are analyzed using three parameters that describe the shape and magnitude of the load hysteresis according to the following three equations. These parameters are the dynamic load increase relative to the static stall peak load $C_{M_{\beta,\zeta,\theta},max}$ (load overshoot), the dynamic load delta between the maximum and minimum value of the hysteresis $C_{M_{\beta,\zeta,\theta},\Delta}$, and the hysteresis area $C_{M_{\beta,\zeta,\theta},hys}$.

$$C_{M_{\beta,\zeta,\theta},max} = \frac{max(C_{M_{\beta,\zeta,\theta},DS})}{C_{M_{\beta,\zeta,\theta}}(\Theta_{SS})} \tag{4.5}$$

$$C_{M_{\beta,\zeta,\theta},\Delta} = \frac{max(C_{M_{\beta,\zeta,\theta},DS}) - min(C_{M_{\beta,\zeta,\theta},DS})}{C_{M_{\beta,\zeta,\theta}}(\Theta_{SS})} \tag{4.6}$$

$$C_{M_{\beta,\zeta,\theta},hys} = \frac{1}{\Theta_C \, C_{M_{\beta,\zeta,\theta}}(\Theta_{SS})} \left| \int_{\Theta_0-\Theta_C}^{\Theta_0+\Theta_C} C_{M_{\beta,\zeta,\theta},DS}(\Theta)\, d\Theta - \int_{\Theta_0+\Theta_C}^{\Theta_0-\Theta_C} C_{M_{\beta,\zeta,\theta},DS}(\Theta)\, d\Theta \right| \tag{4.7}$$

Although all load data are non-dimensionalized, their absolute values cannot be directly compared between rotor speeds due to the load-decreasing effect of inertia as rotor speed increases. Therefore, the parameters $C_{M_{\beta,\zeta,\theta},max}$ and $C_{M_{\beta,\zeta,\theta},\Delta}$ are set in relation to the maximum static stall load $C_{M_{\beta,\zeta,\theta}}(\theta_{SS})$, and the parameter $C_{M_{\beta,\zeta,\theta},hys}$ is additionally set in relation to the cyclic pitch value Θ_C to allow comparison between different cyclic pitch angles. The static polar peak load is determined at $\Theta_{SS} = 20°$ pitch for all speeds. While the load evaluation parameters are shown for all dynamic stall cases mentioned, three examples are used to demonstrate load shapes as a function of pitch and azimuth angles.

In the following, all data are plotted as a function of pitch and azimuth angles. Fig. 4.22 explains the following dynamic stall graphs including static polar, dynamic stall loop, dynamic load increase factor, and maximum load azimuth position.

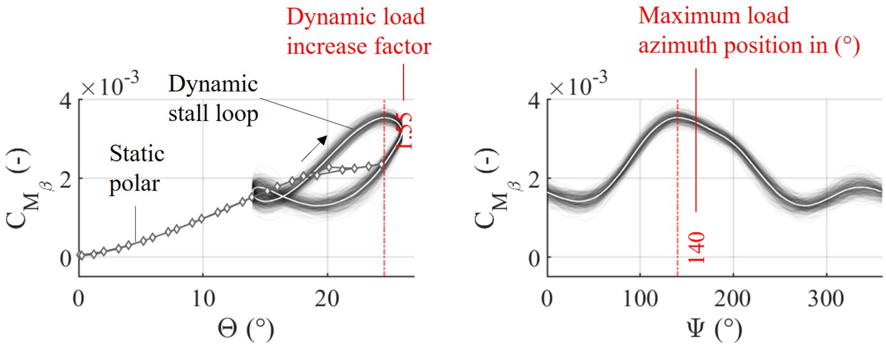

Figure 4.22: Exemplary graph explanation with static polar, dynamic stall loop, dynamic load overshoot $C_{M_{\beta,\zeta,\theta},max}$, and azimuth of maximum load in degrees

Flapping Moment

The non-dimensionalized blade root flapping moments as a function of pitch and azimuth are shown in Fig. 4.23 for the three dynamic stall cases 16, 18, 20° ± 6°.

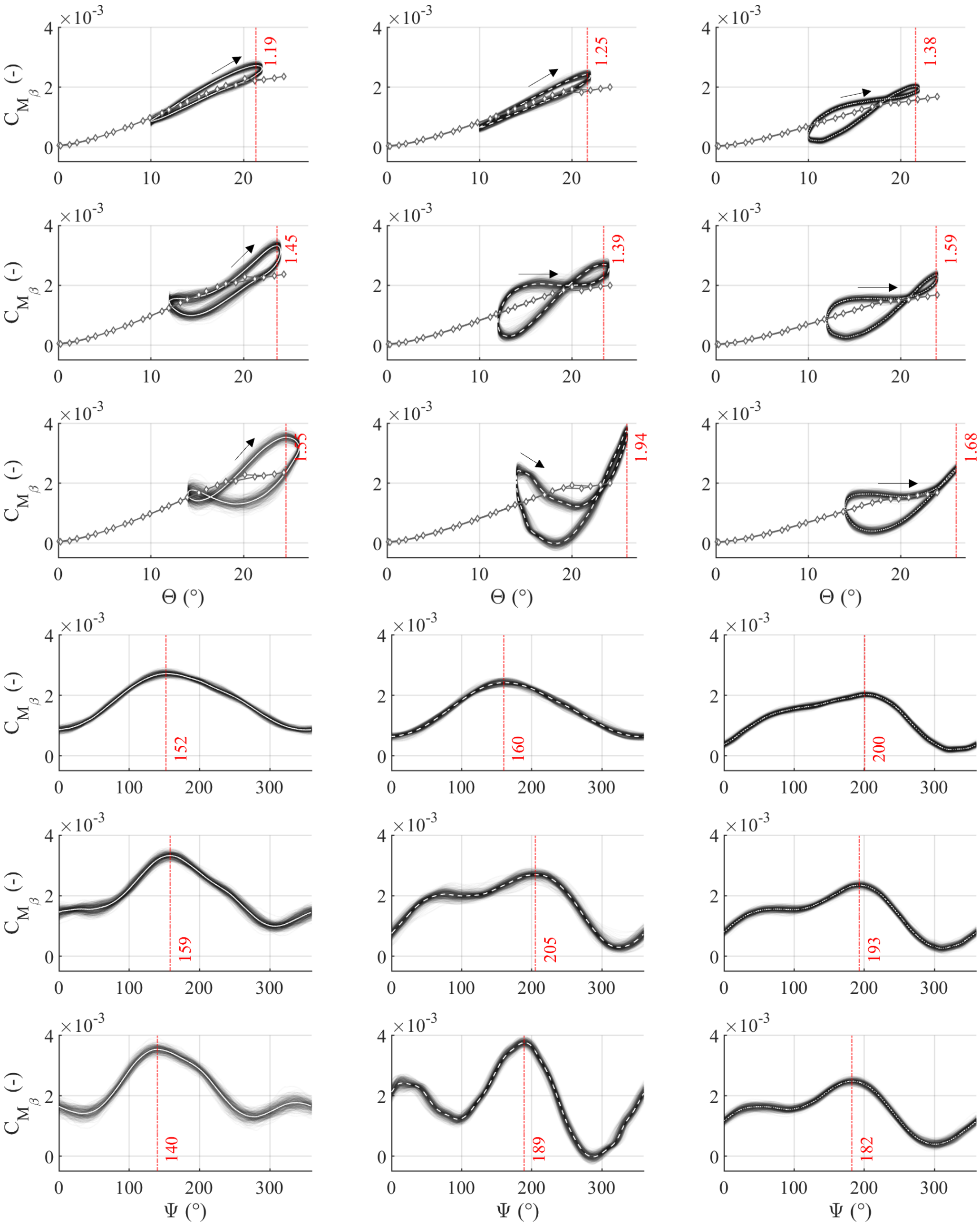

Figure 4.23: Non-dimensionalized blade root flapping moments for the dynamic stall cases 16° ± 6°, 18° ± 6°, 20° ± 6° from top to bottom and 900, 1200, 1500 RPM from left to right; loads shown as a function of pitch (upper three rows) and as a function of azimuth (lower three rows)

The various graphs show different shapes of stall hysteresis, which are divided into four groups: Shape 1 – the elliptical shape – is well known from unsteady airfoil theory (stall onset at 900 and 1200 RPM); it shows stall onset by slightly exceeding the static stall angle with maximum pitch angle; dynamic load increase is minimal. Shape 2 – the early stall shape – is accompanied by maximum load values that are reached before the maximum pitch angle (light and deep stall at 900 RPM); an apparent hysteresis is visible. Shape 3 – the late stall shape – shows maximum load values reached after maximum pitch angle with a load plateau before maximum load and a steep drop after stall onset (stall onset at 1500 RPM, light stall at 1200 and 1500 RPM, deep stall at 1500 RPM). Shape 4 is a special case and an intensified form of shape 3 with extreme maximum and minimum values and a significant overshoot followed by an undershoot of the static stall polar immediately after flow reattachment (deep stall at 1200 RPM).

The three parameters used to describe the load peaks, range, and hysteresis for the flapping moment are shown in Fig. 4.24. They show the load trends for different collective pitch angles and rotor speeds. The load analysis includes the additional measurement point at $14° \pm 6°$ to clarify the trends. The additional dynamic stall case data is presented in the appendix, section B.4.

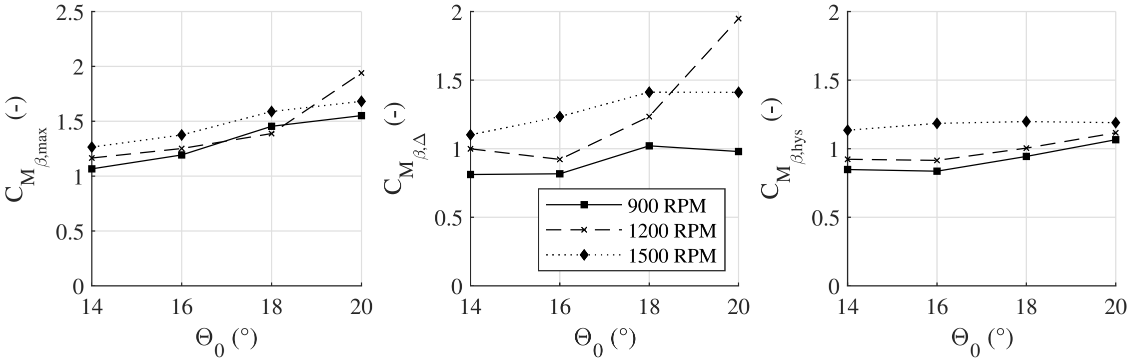

Figure 4.24: Blade root flapping moment increase, load range, and hysteresis area for $14, 16, 18, 20 \pm 6°$ at 900, 1200, 1500 RPM

As the collective pitch increases, there is a moderate increasing tendency in the load peak and range. Load hysteresis shows an increasing tendency at 900 and 1200 RPM, but no significant change with collective pitch at 1500 RPM. As the rotor speed increases, the load peaks, hysteresis magnitudes, and load ranges increase. The amount of increase varies slightly from case to case. The deep stall case – shape 4 – at 1200 RPM falls out of the pattern described. It far exceeds the load peaks and range of the deep stall case at 1500 RPM.

Lead-Lag Moment

The non-dimensionalized blade root lead-lag moments as a function of pitch and azimuth are shown in Fig. 4.25 for the three dynamic stall cases $16, 18, 20° \pm 6°$.

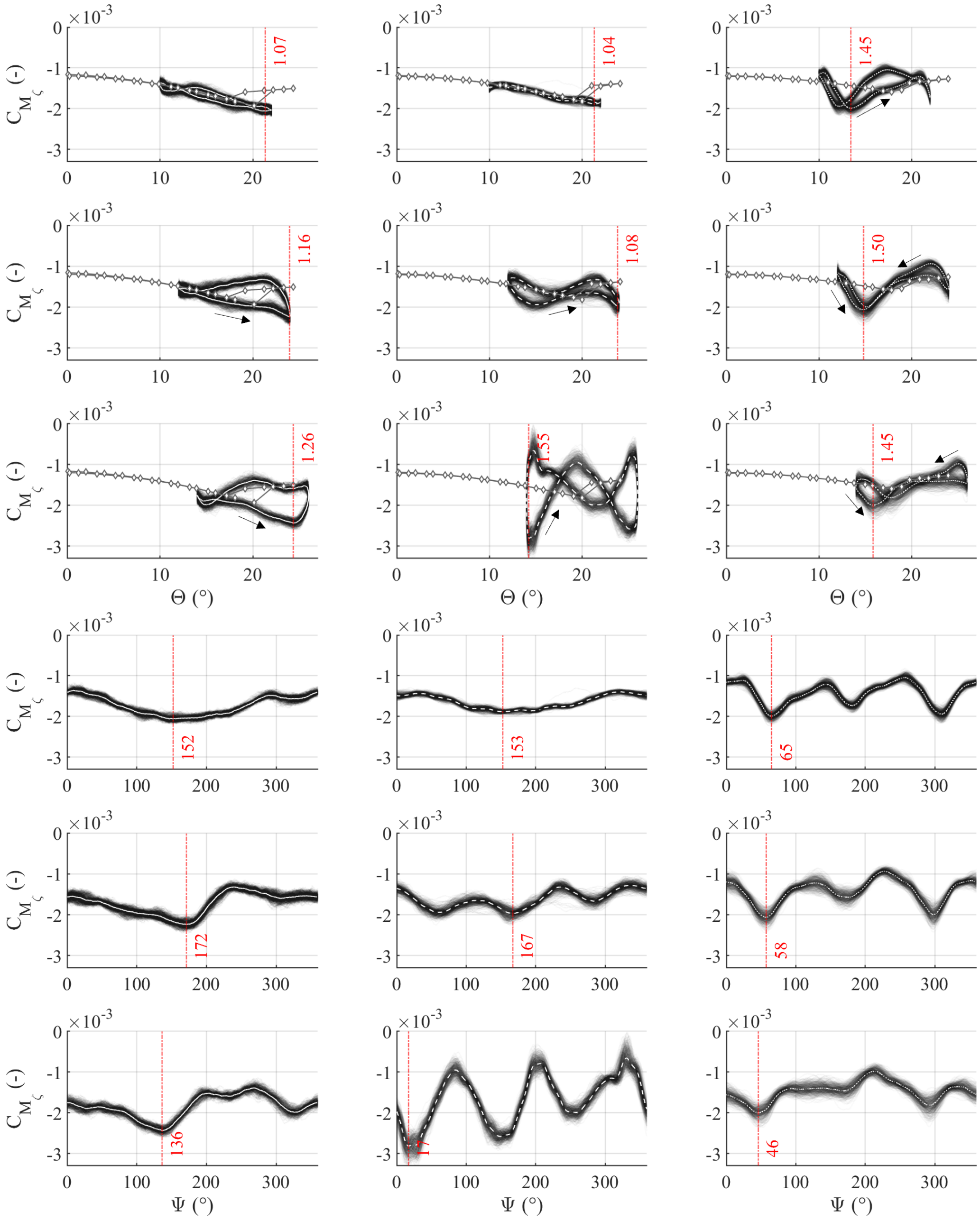

Figure 4.25: Non-dimensionalized blade root lead-lag moments for the dynamic stall cases $16° \pm 6°$, $18° \pm 6°$, $20° \pm 6°$ from top to bottom and 900, 1200, 1500 RPM from left to right; loads shown as a function of pitch (upper three rows) and as a function of azimuth (lower three rows)

The lead-lag moments show four different shape groups similar to the flapping moment: Shape 1 shows a minimal hysteresis with a slight dynamic load increase (stall onset at 900 and 1200 RPM). Shape 2 has a strong hysteresis with a sharp load drop in stall (light and deep stall at 900 RPM). Shape 3 – the S-shape – represents a highly dynamic load behavior with 3/rev oscillations with moderate dynamic load increase and minimal hysteresis (stall onset at 1500 RPM, light stall at 1200 and 1500 RPM, deep stall at 1500 RPM). Shape 4 is the aforementioned particular case with maximal hysteresis and high-amplitude 3/rev oscillations; the load range here is the highest (deep stall at 1200 RPM).

Load peak increase and load range show an increasing tendency with collective pitch for all speeds, except for the decreasing tendency at 1500 RPM and $\Theta_0 = 20^\circ$ collective pitch, see Fig. 4.26. Similar to the flapping moment, the special deep stall case at 1200 RPM shows dynamic load values and a hysteresis that even exceeds its corresponding value at the highest rotor speed of 1500 RPM. The values at 1200 RPM are slightly but consistently lower than those at 900 RPM for $\Theta_0 \leq 18^\circ$. All values at 1500 RPM show an increasing trend with increasing collective pitch. This trend reverses from $\Theta_0 = 18^\circ$ to 20°. Note the location of the peak load for the deep stall at 1200 RPM and all stall cases at 1500 RPM after reattachment right at the beginning of the blade pitch-up motion.

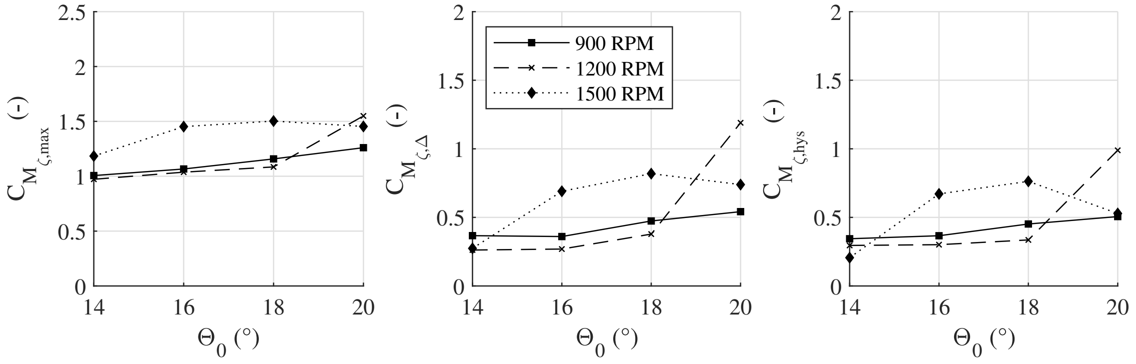

Figure 4.26: Blade root lead-lag moment increase, load range, and hysteresis area for $14, 16, 18, 20 \pm 6^\circ$ at 900, 1200, 1500 RPM

In summary, there are positive load trends for $C_{M_{\zeta,max}}, C_{M_{\zeta,\Delta}}, C_{M_{\zeta,hys}}$ with increasing collective pitch, but not with increasing rotor speed, in contrast to the flapping moment. The load range and hysteresis are generally smaller for the lead-lag moments than for the flapping moments.

Torsion

The non-dimensionalized blade root torsional loads as a function of pitch and azimuth are shown in Fig. 4.27 for the three dynamic stall cases $16, 18, 20° \pm 6°$.

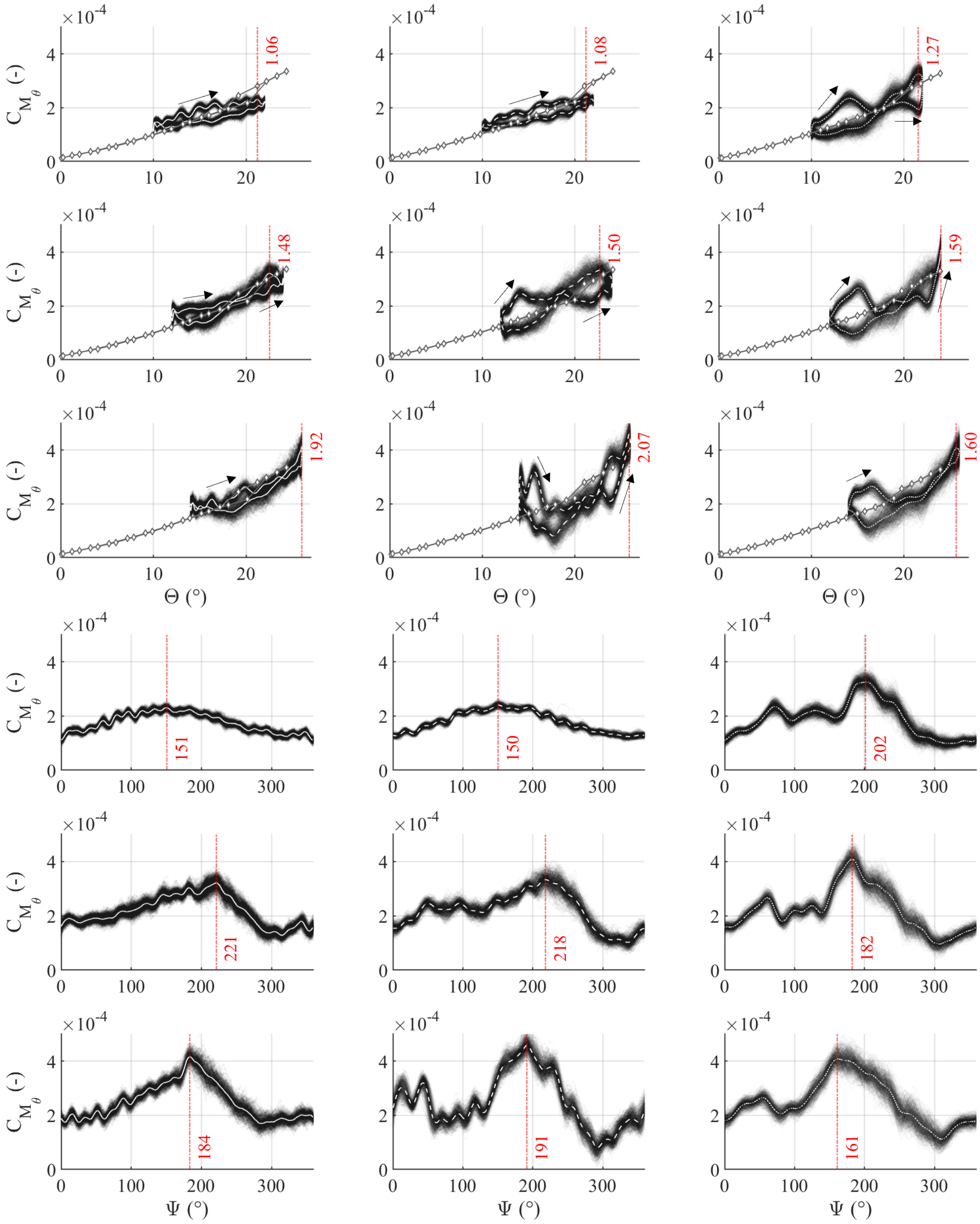

Figure 4.27: Non-dimensionalized blade root torsion for the dynamic stall cases $16° \pm 6°, 18° \pm 6°, 20° \pm 6°$ from top to bottom and 900, 1200, 1500 RPM from left to right; loads shown as a function of pitch (upper three rows) and as a function of azimuth (lower three rows)

The light and deep stall cases at 1200 RPM and all cases at 1500 RPM show a significant load peak in the initial pitch-up motion after flow reattachment. The same observation is made in the flapping moment for the same cases.

The dynamic load increase shows a strong positive trend with increasing collective pitch, see Fig. 4.28, and an increasing tendency with rotor speed, although this trend reverses for 1500 RPM from 18° to 20° pitch. The same trend reversal was observed for the lead-lag moment above. The load hystereses are weak, with almost no difference between 900 and 1200 RPM. The hysteresis at 1500 RPM falls below the lower speed values at 18° and 20° pitch.

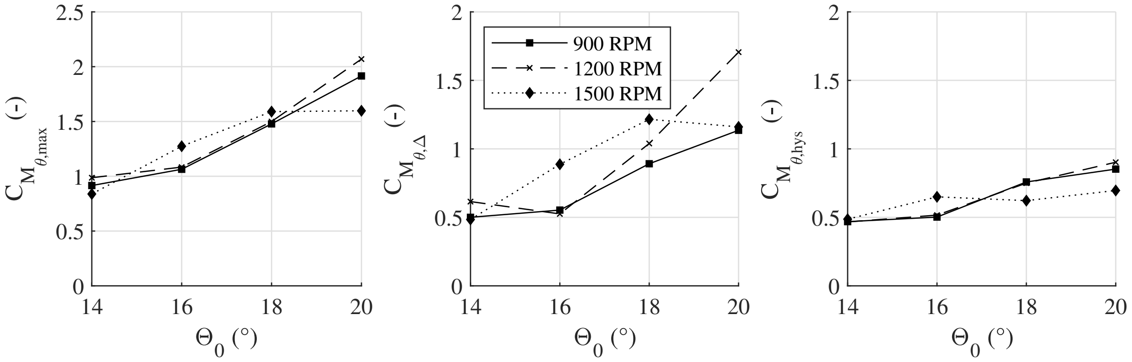

Figure 4.28: Blade root torsion increase, load range, and hysteresis area for $14, 16, 18, 20 \pm 6°$ at 900, 1200, 1500 RPM

The azimuth plots in Fig. 4.27 show how stall is delayed between shape 1 and shapes 2-4. This moment stall delay is a classic sign of dynamic stall. Increasing the collective pitch or rotor speed results in a significant dynamic load increase and hysteresis development, but also in a notable delay of the load peaks. Further increase of the collective pitch results in a continuous reduction of the stall delay.

Pitch Link Forces

The non-dimensionalized pitch link forces for pitch link 2 are shown as a function of pitch and azimuth in Fig. 4.29 for the dynamic stall cases $16, 18, 20° \pm 6°$ (see Fig. B.21 for pitch link 1).

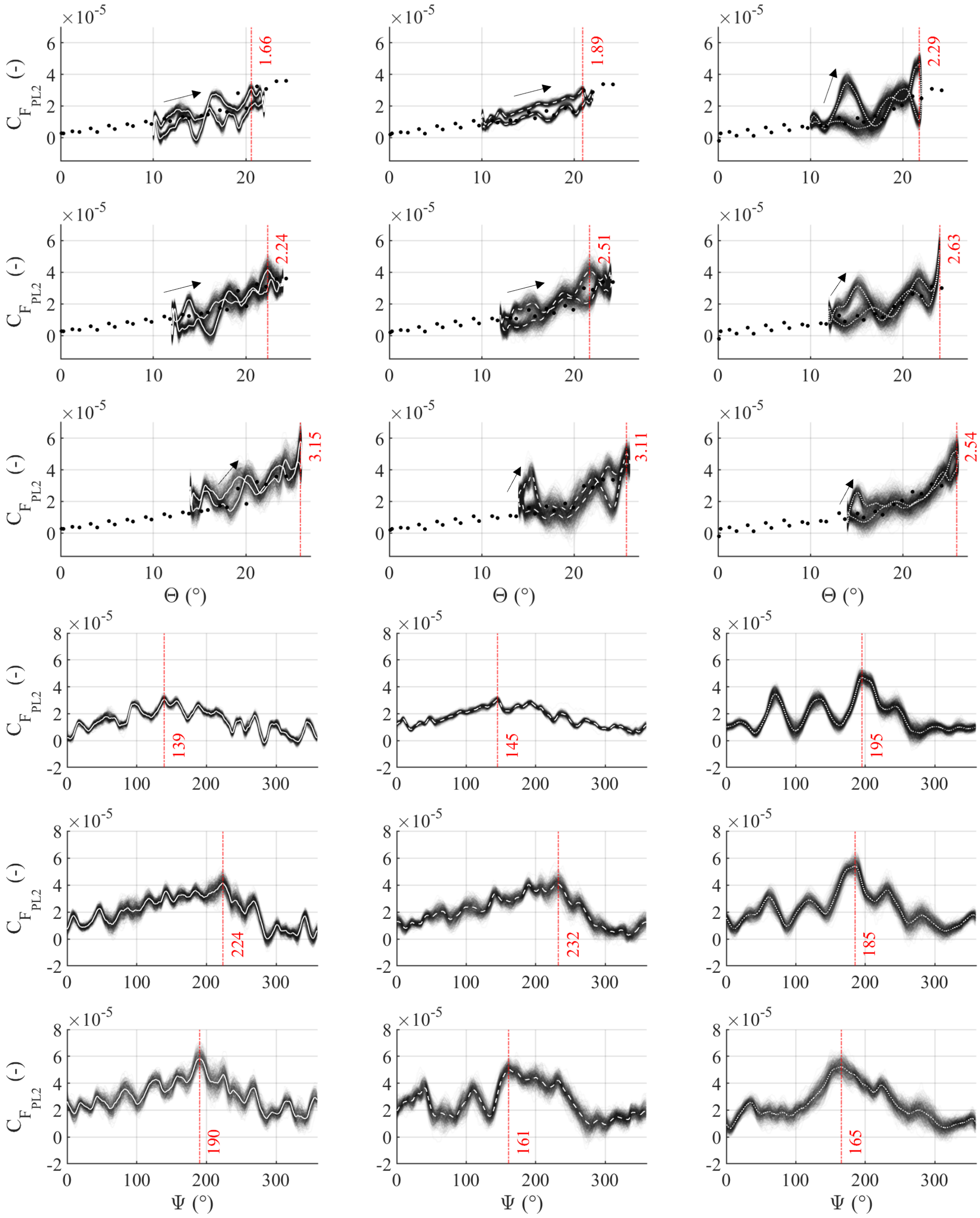

Figure 4.29: Non-dimensionalized pitch link 2 force for the dynamic stall cases $16° \pm 6°, 18° \pm 6°, 20° \pm 6°$ from top to bottom and 900, 1200, 1500 RPM from left to right; loads shown as a function of pitch (upper three rows) and as a function of azimuth (lower three rows)

The pitch link loads are influenced by the aerodynamic blade pitch moment and the frictional load of the tension-torsion strap, which increases with rotor speed (see Fig. 2.32 and 2.33). Especially at 900 and 1200 RPM, high-frequency oscillations are visible in the measured pitch link forces, Fig. 4.29, which are most likely due to the high-frequency oscillations in the tension-torsion strap that cannot be fully compensated by calibration. Fig. 4.29 also shows that the high-frequency oscillation amplitudes are less pronounced at higher rotor speeds. In particular, the high load peaks after reattachment confirm the observations in the torsional dynamics at 1500 RPM. Pitch link 1 shows similar trends, but much higher load peaks and high-frequency oscillation amplitudes. These were also seen in the tension-torsion strap calibration results; both show slightly different behavior.

Fig. 4.30 shows the load evaluation parameters. The dynamic load increase and load delta show a clear positive trend with increasing collective pitch, although the increasing trend weakens for the highest speed of 1500 RPM and between 18° and 20° collective pitch. There is no consistent increase in load as the rotor speed increases. The hystereses indicate an increasing trend at 900 and 1200 RPM, which reverses at 18° pitch. The hysteresis at 1500 RPM is less than or equal to those at all lower speeds. Overall, the pitch link force is consistent with the torsional loads, despite the frictional effects of the tension-torsional strap.

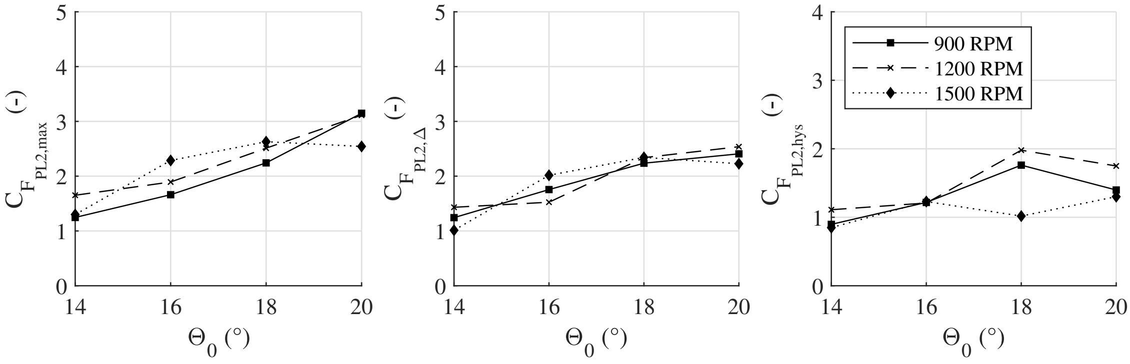

Figure 4.30: Pitch link 2 force increase, load range, and hysteresis area for $14, 16, 18, 20 \pm 6°$ at 900, 1200, 1500 RPM

4.3.4 Cyclic Pitch and Mach Influence

This section focuses on the influence of cyclic pitch angle and rotor speed on structural loads in dynamic stall. Load trends are shown for the stall cases $14° \pm 4, 5, 6, 7, 8, 9, 10°$ at 900, 1200, and 1500 RPM. The same evaluation parameters as for the collective pitch study are used to describe dynamic load increase, load range, and hysteresis. The azimuth and pitch load graphs are limited to the three example cases $14° \pm 6°$ (stall onset), $14° \pm 8°$ (light stall), and $14° \pm 10°$ (deep stall).

Flapping Moment

The non-dimensionalized blade root flapping moments as a function of pitch and azimuth are shown in Fig. 4.31 for the three dynamic stall cases 14° ± 6, 8, 10°.

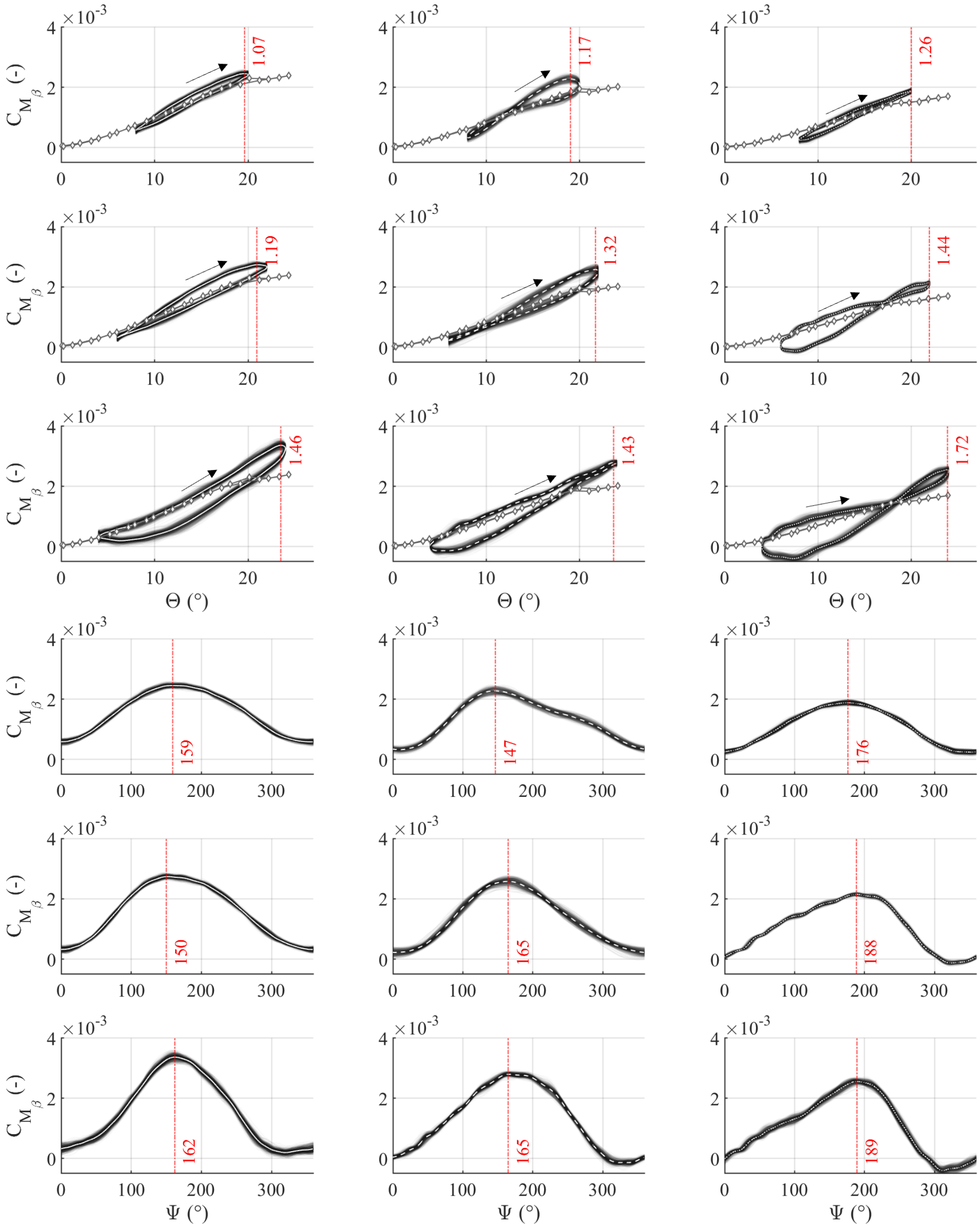

Figure 4.31: Non-dimensionalized blade root flapping moments for the dynamic stall cases 14° ± 6°, 14° ± 8°, 14° ± 10° from top to bottom and 900, 1200, 1500 RPM from left to right; loads shown as a function of pitch (upper three rows) and as a function of azimuth (lower three rows)

The various graphs show different shapes of stall hysteresis, which are divided into three groups: Shape 1 – the elliptical shape – has a minimum dynamic load increase (stall onset, 900 RPM). Shape 2 – late stall shape – has maximum load values that are reached after maximum pitch angle with moderate signs of a load plateau before load peak and a steep drop after stall onset (light and deep stall at 1500 RPM). Shape 3 – early stall shape – has maximum load values reached before maximum pitch angle (stall onset at 1200 and 1500 RPM, light and deep stall at 900 and 1200 RPM).

The load evaluation parameters provide insight into the load trends that occur with varying cyclic pitch and rotor speed; see Fig. 4.32. The dynamic load increase, load range and hysteresis increase almost linearly and in parallel, as the cyclic pitch and rotor speed increase. The only exception to this trend is the steeper slope between 9° and 10° cyclic pitch at 900 RPM. The load range shows a slightly lower slope at 1200 RPM compared to 900 and 1500 RPM. The hysteresis slope is the same and constant for all three rotor speeds. The absolute hysteresis magnitude increases significantly from 1200 RPM to 1500 RPM. All three load parameters show a distinct increase with rotor speed and stall is delayed with increasing rotor speed.

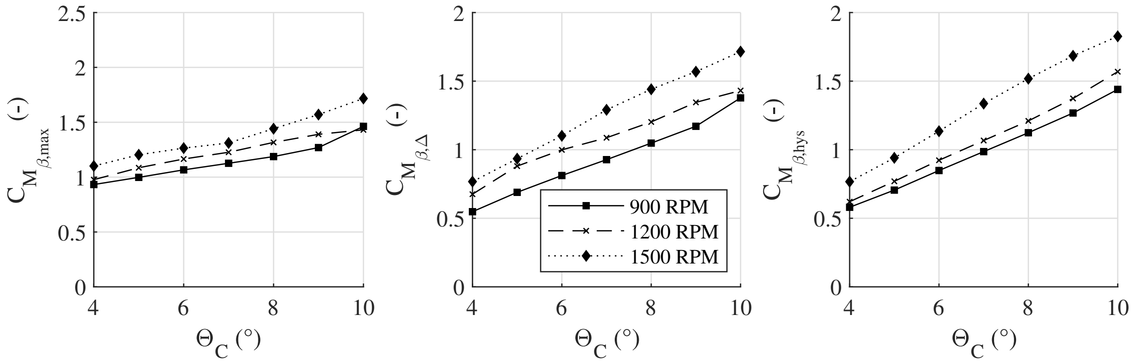

Figure 4.32: Blade root flapping moment increase, load range, and hysteresis area for $14^\circ \pm 4,5,6,7,8,9,10^\circ$ at 900, 1200, 1500 RPM

Lead-Lag Moment

The non-dimensionalized blade root lead-lag moments as a function of pitch and azimuth are shown in Fig. 4.33 for the three dynamic stall cases 14° ± 6, 8, 10°.

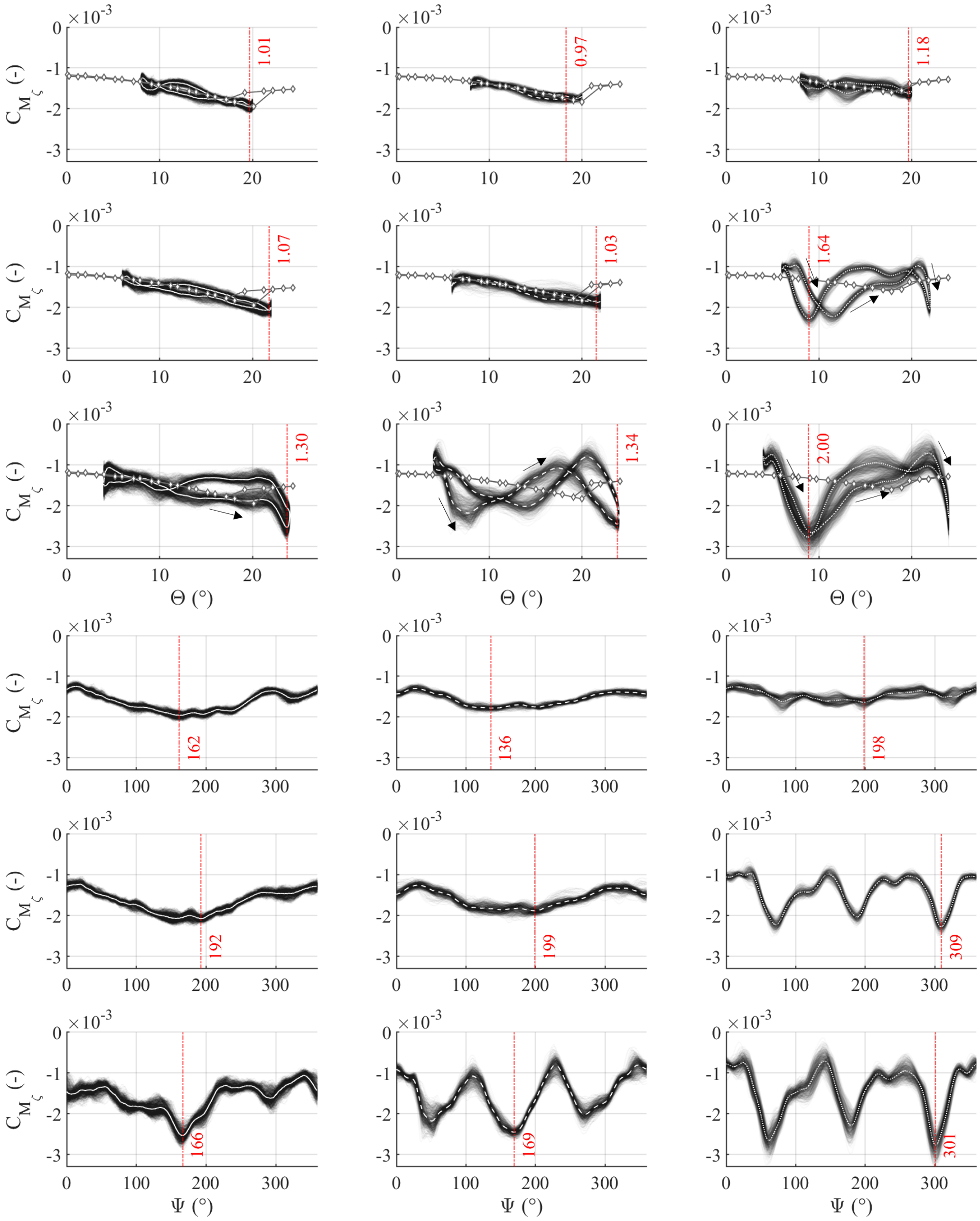

Figure 4.33: Non-dimensionalized blade root lead-lag moments for the dynamic stall cases 14° ± 6°, 14° ± 8°, 14° ± 10° from top to bottom and 900, 1200, 1500 RPM from left to right; loads shown as a function of pitch (upper three rows) and as a function of azimuth (lower three rows)

The lead-lag moment has a 3/rev oscillation with substantially high amplitudes at deep stall and 1200 RPM and light and deep stall at 1500 RPM with a maximum dynamic load increase of factor 2.0. The load peak, load range, and hysteresis show a bilinear increase with increasing cyclic pitch angle from a shallow slope to a significantly steep slope. The slope changes at $\Theta_C = 9°$ for 900 and 1200 RPM, and at $\Theta_C = 6°$ for 1500 RPM, see Fig. 4.34. Below these thresholds, there is no significant load difference between the individual rotor speeds; in particular, the parameters at the lower speeds (900 and 1200 RPM) show similar values. The possible reasons for this behavior are discussed in section 4.3.5.

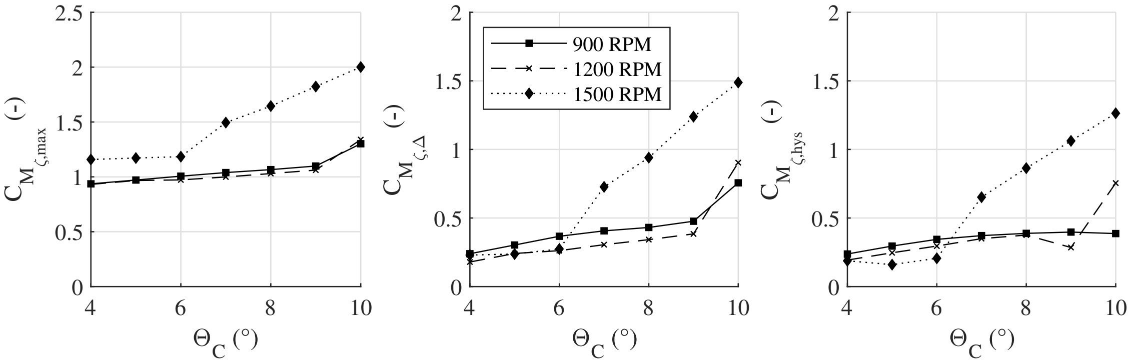

Figure 4.34: Blade root lead-lag increase, load range, and hysteresis area for $14° \pm 4,5,6,7,8,9,10°$ at 900, 1200, 1500 RPM

Torsion

The non-dimensionalized blade root torsional loads as a function of pitch and azimuth are shown in Fig. 4.35 for the three dynamic stall cases 14° $\pm 6, 8, 10°$.

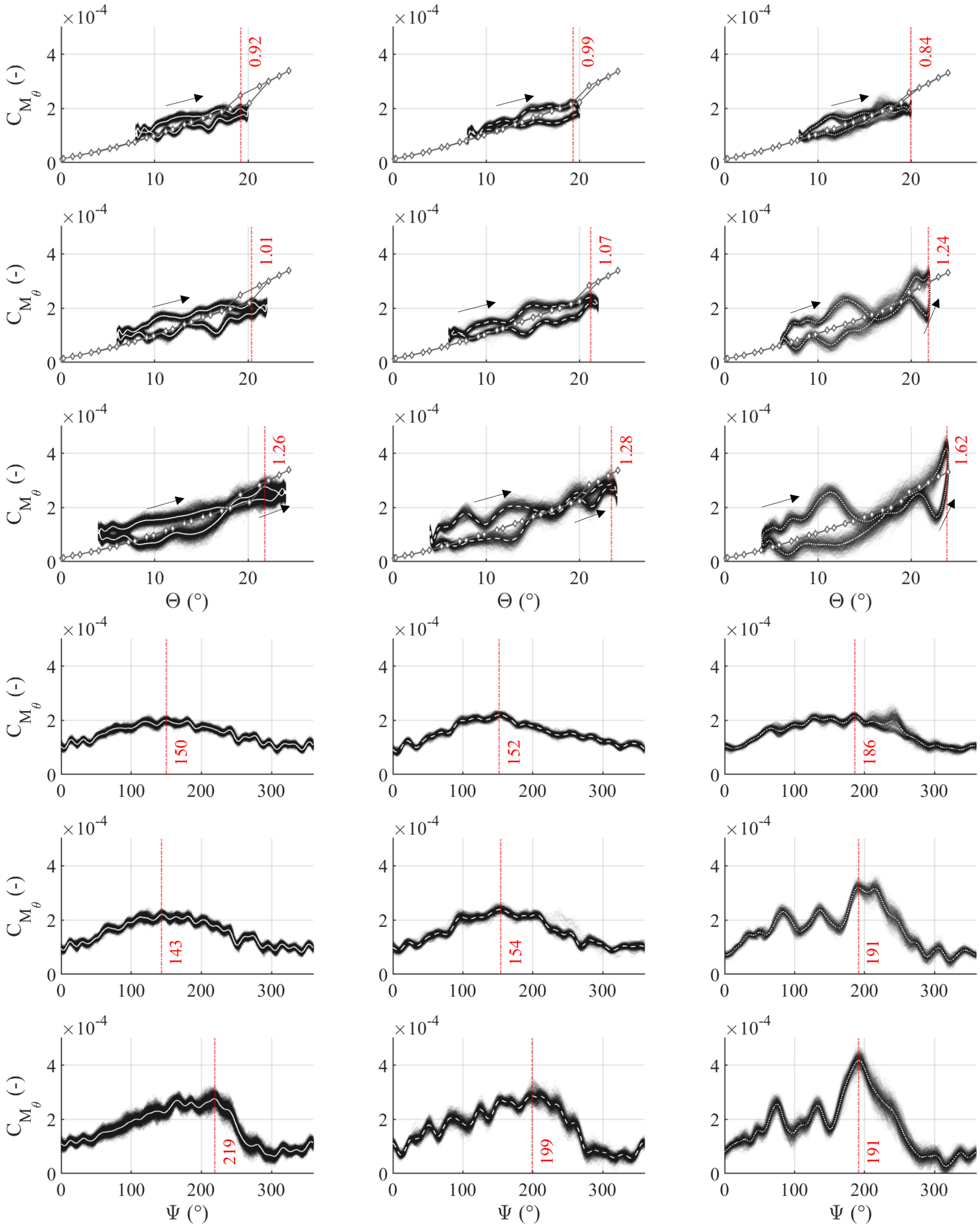

Figure 4.35: Non-dimensionalized blade root torsion for the dynamic stall cases 14° $\pm$ 6°, 14° $\pm$ 8°, 14° $\pm$ 10° from top to bottom and 900, 1200, 1500 RPM from left to right; loads shown as a function of pitch (upper three rows) and as a function of azimuth (lower three rows)

Like the collective pitch variation, torsion shows a strong dynamic load increase immediately after reattachment for light and deep stall at 1500 RPM and deep stall at 1200 RPM. All load evaluation parameters for torsion show an increasing linear trend with increasing cyclic pitch, but with a significant increase in slope from 9° to 10° cyclic pitch at 900 and 1200 RPM, and above 6° cyclic pitch for 1500 RPM, see Fig. 4.36. The same behavior was observed for the lead-lag moment. The values at 900 and 1200 RPM are very close. The hysteresis magnitudes are almost the same for all speeds with the exception of slightly higher values for 1500 RPM at $7^\circ - 9^\circ$ cyclic pitch.

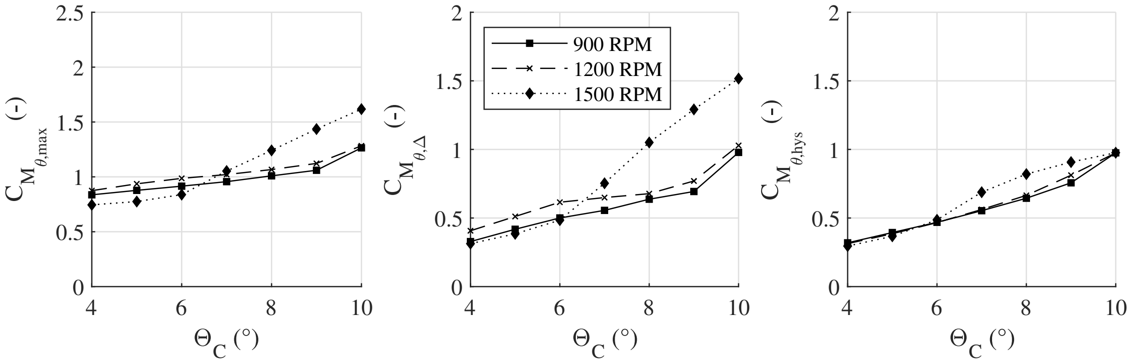

Figure 4.36: Blade root torsion increase, load range, and hysteresis area for $14^\circ \pm 4, 5, 6, 7, 8, 9, 10^\circ$ at 900, 1200, 1500 RPM

Pitch Link Forces

The non-dimensionalized pitch link forces are shown as a function of pitch and azimuth in Fig. 4.37 for the dynamic stall cases 14° ± 6, 8, 10° (see Fig. B.27 for pitch link 1).

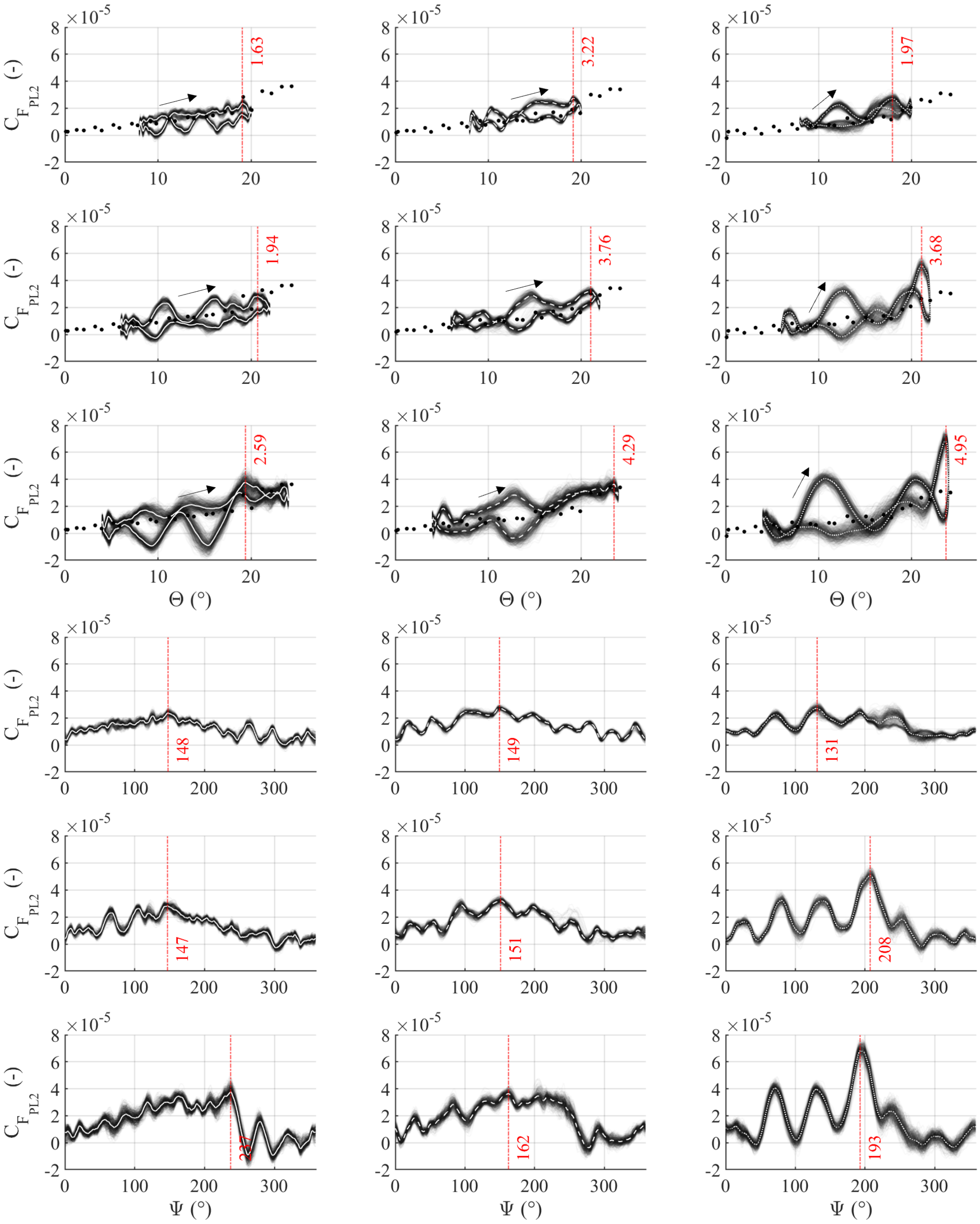

Figure 4.37: Non-dimensionalized pitch link 2 force for the dynamic stall cases 14° ± 6°, 14° ± 8°, 14° ± 10° from top to bottom and 900, 1200, 1500 RPM from left to right; loads shown as a function of pitch (upper three rows) and as a function of azimuth (lower three rows)

The pitch link forces show similar trends to the torsional and lead-lag moments, see Fig. 4.38. However, they are not directly comparable because the pitch link force is superimposed by the nonlinear frictional loads in the tension-torsion strap and changes as a function of pitch angle due to the pitch horn kinematics $M_{\zeta} = M_{TTS}(\Theta(t),\Omega) + F_{PL}dcos(\Theta(t))$. Therefore, the load trends are not bilinear. Nevertheless, the significantly increasing trend in dynamic load increase and load range at 1500 RPM and $\Theta_C \geq 6°$ is visible. Dynamic load increase and hysteresis are slightly higher at 1200 RPM compared to 900 RPM. The hysteresis is similar for all three speeds.

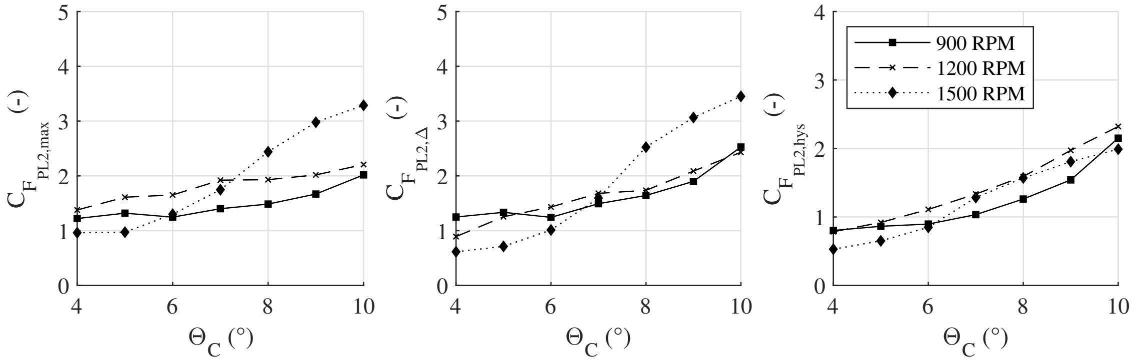

Figure 4.38: Pitch link 2 force increase, load range, and hysteresis area for 14° $\pm 4, 5, 6, 7, 8, 9, 10°$ at 900, 1200, 1500 RPM

4.3.5 Discussion of Parameter Study

The following sections summarize the observations and findings of the control parameter study on structural rotor loads during dynamic stall. In the next step, these results are discussed and compared to state-of-the-art experimental dynamic stall research on pitching airfoils and rotating pitching wings to identify and analyze (dis-)similarities of the results in this thesis with related studies. This step conveys the scientific contribution of this thesis to state-of-the-art dynamic stall research.

Load Peak, Load Range, and Hysteresis

All tested dynamic stall cases have one thing in common: initiating dynamic stall at a combination of collective and cyclic pitch angles, whose resulting maximum pitch value exceeds the static stall angle. This fact confirms the findings of several previous studies on pitching airfoils and wings, and is fundamental for the following discussion.

Cyclic pitch increase has a linear effect on load increase and hysteresis of the flapping moment, see Fig. 4.32. Moreover, dynamic load increase and hysteresis rise with rotor speed. In contrast to the flapping moment, the lead-lag moment and torsion show a bilinear dependency between cyclic pitch and load increase or hysteresis with a trend from a shallow to a steep positive slope, see Fig. 4.34 and 4.36. For the highest analyzed speed, the bilinearity occurs earlier: between $\Theta_C = 6°$

and $\Theta_C = 7°$. This is the cyclic pitch at which the resulting maximum pitch angle exceeds the static stall angle and dynamic stall onset begins. The bilinear load trends at 900 and 1200 RPM show the slope change between $\Theta_C = 9°$ and $\Theta_C = 10°$. These trends are mainly visible in the dynamic load increase and range, whereas hysteresis depicts them with less pronounced strength and only at 1200 and 1500 RPM. Overall, the trends observed at 1500 RPM differ significantly from 900 and 1200 RPM. The bilinearity at 1500 RPM sets in at 3° lower cyclic pitch than at the two lower speeds. So far, it is not clear, what effect causes bilinearity and why it occurs at lower cyclic pitch for higher speed. Increasing rotor speed implies Reynolds and Mach effects. Reynolds number is still below the critical border found in pitching airfoil tests. In addition, its load increasing effect is minimal. On the other hand, Mach effect could play a major role, because the free-stream Mach numbers on the outer blade area $\geq 0.75\,R$ vary between $Ma = 0.3$ and 0.41; $Ma = 0.3$ is the threshold at which the initiation of Mach effects was observed on pitching airfoil and pitching wing tests [5–7, 45, 58, 81, 154]. Carr and Chandrasekhara concluded in [5], that compressibility effects can have a major impact on dynamic stall events and can even completely change the physics of the stall process that occurs at low Mach number. However, Carr et al. [5] also stated that compressibility effects decrease dynamic load increase and cause a premature stall onset on a pitching airfoil. In contrast, the present analysis shows rather the opposite effect rotor speed has on the integral blade root moments and pitch link force: increasing of rotor speed – thus of free-stream Mach number – raises load peaks and delays stall onset, especially for the deep stall cases. Reduced frequency substantially affects dynamic load increase and causes stall delay on pitching airfoils. The exact reason for the load increase with rotor speed is not known yet. The position of the dynamic stall vortex plays a major role because of radially varying parameters (Ma, Re, k). The combination of these will determine strength and development of the vortex.

Another factor that needs consideration is the maximum pitch rate. McCroskey et al. stated that the time history of the AoA – especially in the area of exceeding the static stall angle – strongly affect quantitative airloads [42]. Although a change in rotor speed or cyclic pitch angle does not influence local reduced frequency, it increases the pitch rate and therefore the severity of the structure-fluid interaction. Maximum pitch rate at 1500 RPM and $\Theta_C = 8°$ (test case 5) is the same as the one at 1200 RPM and $\Theta_C = 10°$ (test case 7): 1257 $°/s$, see Tab. 4.3 and Fig. 4.18. Their respective load increase, range, and hysteresis are very close to each other, as well. Thus, the pitch rate of the rotor blade seems to have a significant influence on dynamic load increase and hysteresis and should be considered in load evaluation. Close investigation of the flow physics by means of flow visualization and/or measurement of the airfoil's surface pressure distribution are needed to understand this rotor speed effect and its implications on loads.

Collective pitch variation depicts tendencies that are not as clear as cyclic pitch variation. One reason for that may be the lower number of measuring points. Nevertheless, rising trends of load increase and hysteresis with collective pitch are visible for the blade moments and pitch link force. These trends are less pronounced for 900 and 1200 RPM than for 1500 RPM and cannot be described as linear throughout. The load trends for 1500 RPM are distinctive from those at lower speed, especially for the lead-lag moment, see Fig. 4.26, while the absolute values of load increase, range and hysteresis tend to be higher than those at lower speeds for moderate angles $\Theta_0 = 16°, 18°$. The highest overall dynamic load increase occurs between 16 and 18° for all speeds and most of the loads. Similar to the cyclic pitch trend, the loads increase substantially at 1500 RPM. As mentioned above, flow visualization can help clarify causes for this effect. Moreover, it is unclear why dynamic load increase at the highest speed tends to level off or even decrease for the $20° \pm 6°$ case, see Fig. 4.26 and 4.28. One possible reason is that the collective pitch is greater than the static stall angle, which slightly decreases for increasing rotor speed. Carr et al. stated that hystereses are the highest, when the airfoil pitches in and out of the static stall region [1]. This could explain that dynamic load increase does not increase further as soon as a major part of the pitching movement is within the static stall region.

A special case that was observed in the collective pitch variation analysis is the unproportionally high load increase at 1200 RPM and between 18 and 20° collective pitch, especially for the flapping and lead-lag moment, see Fig. 4.24 and 4.26. As the static stall measurements have shown, the highest load amplitudes occur in stall regime at 1200 RPM, where the excitation of the eigenmode of a rotor component is assumed. This excessive load increase might be triggered by structural vibrations and needs closer investigation.

To conclude, an increase in collective and cyclic pitch shows significant tendencies of increase in structural rotor dynamic load increase and hystereses for the rotor speeds 900, 1200, 1500 RPM.

Collective and Cyclic Pitch Effects

As stated above, dynamic stall on the examined rotor sets in at a combination of collective and cyclic pitch angles, whose total value exceeds the rotor's static stall angle. Nevertheless, the composition of collective and cyclic pitch plays a significant role. The aforementioned load analyses show that cyclic pitch angles have a stronger impact on dynamic load increase than collective pitch. This effect increases with rotor speed. Fig. 4.39 shows the dynamic load increase as a function of rotor speed at the example of the flapping moment using four combinations of collective and cyclic pitch.

Two of these four graphs ($16° \pm 6°$ and $14° \pm 8°$) result in a maximum pitch angle of $\Theta_{max} = 22°$ and the other two ($16° \pm 6°$ and $14° \pm 8°$) result in a maximum pitch angle of $\Theta_{max} = 24°$. The cases with higher maximum pitch have higher load peaks than those with lower maximum pitch. Moreover, there is a significant difference between the load peaks of different collective and cyclic pitch composition. The load peaks at higher cyclic pitch ($14° \pm 8°$ and $14° \pm 10°$) exceed those for higher collective pitch ($16° \pm 6°$ and $18° \pm 6°$), although both combinations lead to the same maximum pitch angle. This trend is not present at 900 RPM, but increases significantly with rotor speed.

Dynamic Stall Location - Pitch and Azimuth

As pitching airfoil and wing experiments have shown, increasing cyclic and collective pitch during dynamic stall leads to a delay in dynamic stall onset for the lift and moment coefficients. The

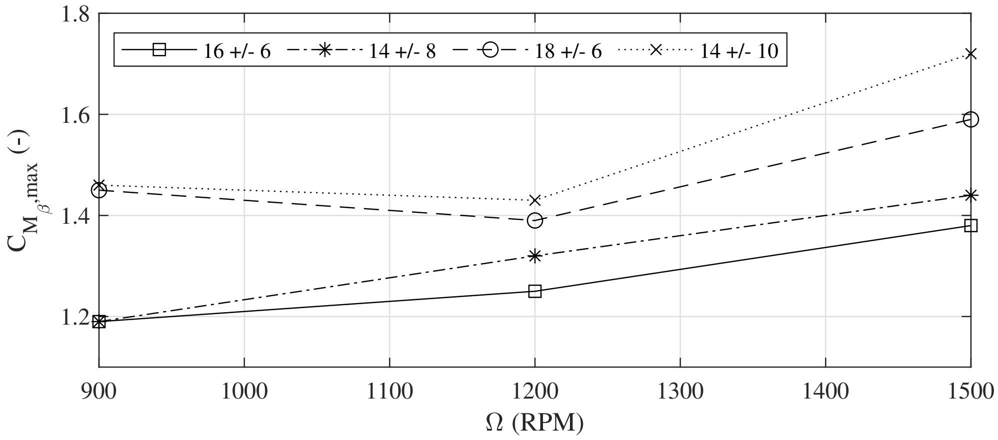

Figure 4.39: Dynamic load overshoot of the blade root flapping moment for four different dynamic stall cases and the rotor speeds 900, 1200, 1500 RPM

timing of dynamic stall onset is a result of a strong interaction of the airfoil's pitching movement with the surrounding fluid. Dynamic stall onset occurs close to its resulting maximum pitch angle and therefore close to the turning point between upward and downward pitching motion. Parameters, such as reduced frequency or Mach number, determine the exact timing of lift and moment stall, which might be at the end of the pitch-up or at the beginning of the pitch-down movement. The same trend, that was observed on pitching airfoils and wings, could be shown on the rotating pitching MERIT blade. Increasing cyclic and collective pitch implies a linear rising trend of dynamic load peak location, with a few exemptions, see Fig. 4.40.

The stall location is positively linear-dependent on the cyclic pitch angle at all rotor speeds, and there are only a few slight deviations in slope or offset between the rotor speeds. The stall location exceeds the static stall angle of $\Theta_{SS} = 20^\circ$ between 6° and 7° cyclic pitch. In most cases, the dynamic stall angle is still smaller than the maximum pitch angle resulting from collective and cyclic pitch. This means that stall occurs before or after (not right at) the directional change between pitch-up and pitch-down movements. To determine the exact stall location, the dynamic stall angle needs to be analyzed as a function of the azimuth angle, see Fig. 4.41.

Significant outliers from the described linear stall location trends are visible for the lead-lag moment at 1500 RPM and $\Theta_C \geq 7^\circ$ or $\Theta_0 \geq 16^\circ$, respectively. For these cases, the load peaks are reached at $\Theta_{max} = 9^\circ$ to 16°, which is about $4^\circ - 11^\circ$ below the static stall angle. The lead-lag moments depict three load peaks per revolution (at around $\Psi = 60^\circ, 170^\circ, 290^\circ \pm 20^\circ$, case-dependent) with similar amplitude. The same lead-lag moment behavior is observed at 1200 RPM and $20^\circ \pm 6^\circ$.

Because of the composition and interaction of the parameters Mach number, Reynolds number, and reduced frequency, the observed outliers cannot be traced back to their cause with the available data. Flow visualization techniques and local pressure measurements are needed to locate

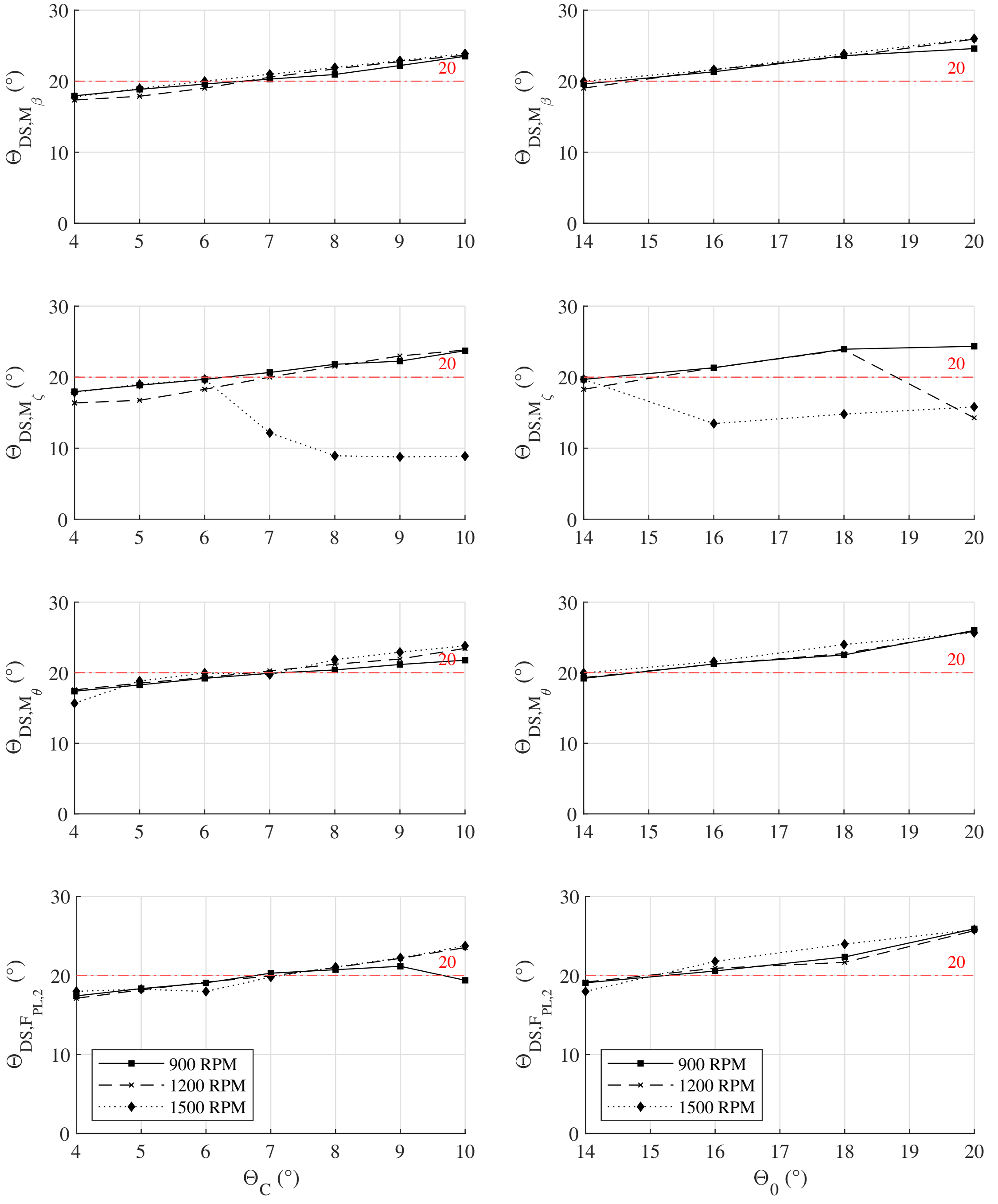

Figure 4.40: Pitch angle at load peaks for all blade root moments and pitch link 2 force as well as for cyclic (left column) and collective (right column) pitch variations

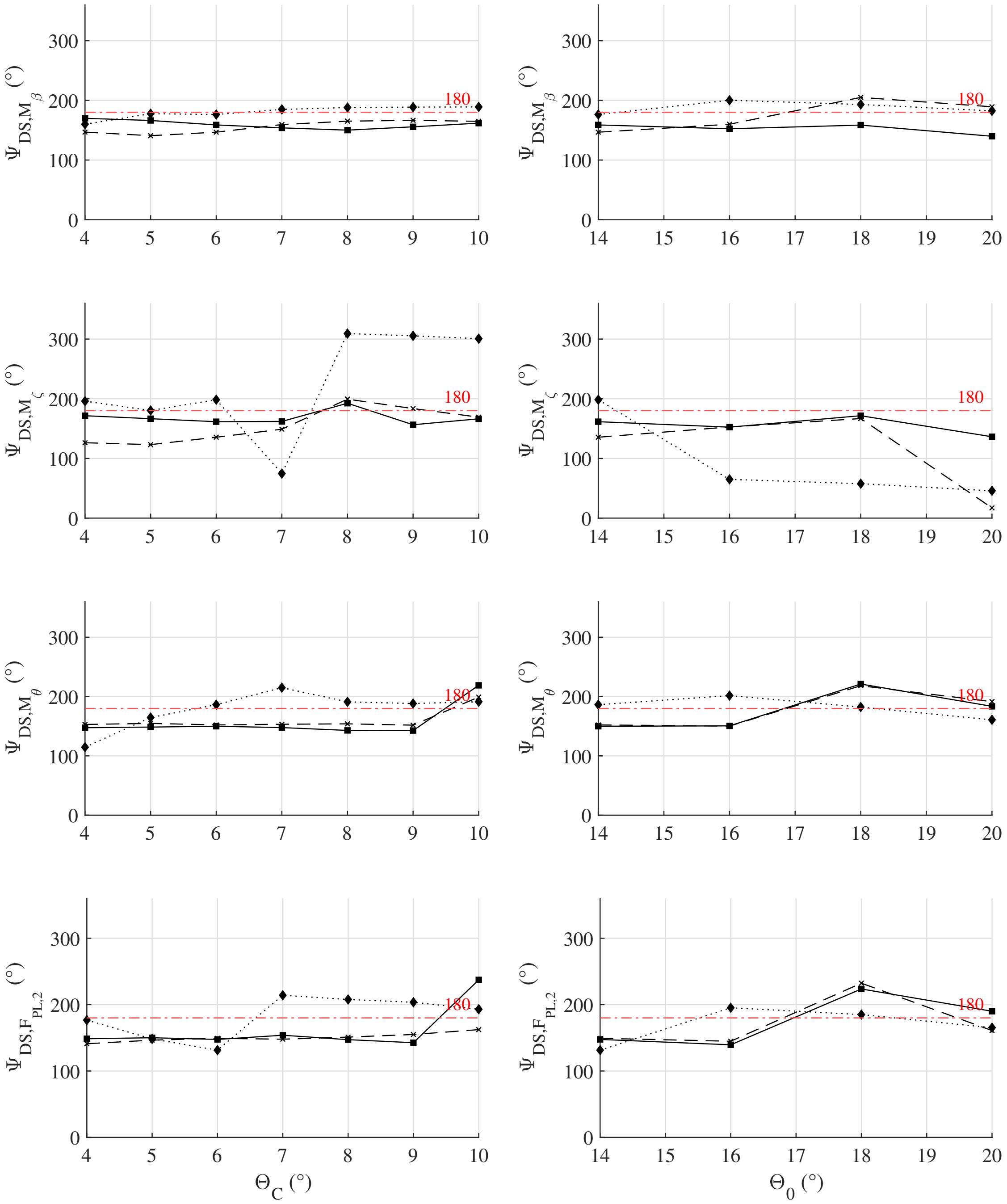

Figure 4.41: Azimuth angle at load peaks for all blade root moments and pitch link 2 force as well as for cyclic (left column) and collective (right column) pitch variations

the dynamic stall vortex and analyze its development and movement in radial and chord-wise directions. This way, the strength and dominant effects of local parameters on the unsteady flow field can be identified and understood better.

Comparison to Pitching Airfoil Tests

The influence of the control parameters rotor speed and pitch angle are discussed in this section through a juxtaposition of pitching airfoil and pitching rotating blade experiments. This juxtaposition focuses on the comparison of the pitching airfoil lift coefficient and the blade root flapping moment on the pitching, rotating blade. The parameters that have the most substantial impact on dynamic stall of a pitching NACA 0012 airfoil are Mach number, Reynolds number, reduced frequency, AoA range, and mean AoA. Their effects were explained in the introductory section 1.3 and are summarized in Tab. 4.4. The influence of these parameters cannot be investigated independently from each other on a rotor. Mach number, Reynolds number, reduced frequency, and AoA vary with the blade radius in hover and forward flight. In hover, rotor speed directly influences Reynolds and Mach numbers, while the reduced frequency is independent of rotor speed or pitch angle. The mean AoA and AoA range are directly affected by collective and cyclic pitch control.

Previous experimental and numerical studies on pitching airfoils identified ranges in which Mach, Reynolds, or flow unsteadiness effects on dynamic stall occur. Compressibility effects on a pitching airfoil were observed at or above $Ma = 0.2 - 0.3$. Beyond $Ma = 0.3$, an increase in Mach number leads to an early stall onset and a decrease in C_l overshoot due to shock wave participation on a pitching airfoil. Rotor speed variation between 900 and 1500 RPM implies Mach numbers between 0.18 and 0.3 at 75% radius on the MERIT rotor. The analysis of the maximum flapping moment on the MERIT rotor blade during dynamic stall showed that increased rotor speed leads to higher load peaks. Mach number has a decreasing effect on C_l load peaks of a pitching airfoil, and rotor speed has an increasing effect on dynamic load increase of M_β on the rotating, pitching MERIT blade. This conflict was described above and needs closer analysis.

Reynolds number slightly influences pitching airfoil dynamics with an increasing effect on load peaks and hystereses, especially for $Re > 1 \cdot 10^6$. The Reynolds numbers on the MERIT rotor cover a medium-low range of $5.3 \cdot 10^5 \leq Re_{0.75R} \leq 8.9 \cdot 10^5$ for rotor speeds varying from 900 to 1500 RPM. Therefore, Reynolds effects should play a minor role in the MERIT load analysis. Detailed information on the radial vortex location would help determine which local parameters (Re, Ma, k) are most dominant.

The reduced frequency has a very strong increasing and delaying effect on dynamic stall loads. It describes the grade of unsteadiness of the flow phenomenon. At the same time, this factor needs to exceed a particular region to allow for visible dependencies of dynamic load increase on other parameters, such as AoA. One example of the importance of reduced frequency in parameter study is shown by Tsang et al. [155]. They analyzed the effect of mean pitch angle and pitch range on the NACA 0012 pitching airfoil during dynamic stall at a Reynolds number of $Re = 7.7 \cdot 10^4$ and varying reduced frequencies of $k = 0.005, 0.01, 0.02, 0.04$ and $\alpha = 5 \pm 5^\circ, 10 \pm 5^\circ, 15 \pm 10^\circ$.

Pitching airfoil, Carr et al. [1, 58]		Pitching & rotating blade, experiments on MERIT	
Studied parameters	Observed trends in C_l	Observed trends in M_β	Control parameters
Mach number Ma	Compressibility effects on dynamic stall set in at a free stream Mach number of $Ma = 0.3$. Beyond this value, an increase in Ma number leads to an early stall onset, thus a decrease in α_{DS} and dynamic load increase.	Mach number at 75% radius covers the following range: $0.18 \leq Ma_{0.75R} \leq 0.3$. Increase in rotor speed shows a trend of rising dynamic load increase and a tendency of stall delay, even into the pitch-down movement of the blade.	Rotor speed Ω
Reynolds number Re	Low Re ($< 5 \cdot 10^5$): TE stall; High Re ($> 1 \cdot 10^6$): LE stall, increasing Re number leads to a delay in flow reversal and a slight increase in load peaks and hysteresis at low k.	Absolute values and range of Re numbers ($5.3 \cdot 10^5 \leq Re_{0.75R} \leq 8.9 \cdot 10^5$) are considered medium low for the tested speeds, its influence is regarded as minor.	
Reduced frequency k	Pre-stall region: no substantial effect on $C_{l,max}$, slight effect on hysteresis. Post-stall region: increased k delays stall onset to higher α_{DS} [58] and increases hysteresis and peak load $C_{l,max}$ significantly.	The reduced frequency k of a rotating pitching blade varies with blade radius and cannot be changed by variation of rotor speed or pitch control. The airflow in the region $r \leqq 0.75\ R$ is considered as unsteady with $k \geq 0.1$.	-
Mean AoA α_0	Post-stall region: Substantial increasing effect on $C_{l,max}$ and lift hysteresis in combination with high k	Pre-stall region: increasing collective pitch leads to stall delay Post-stall region: Strong effect on $M_{\beta,max}$ and marginal effect on hysteresis, especially at high Ma number. Further increase of Θ_0 leads to premature stall onset.	Collective pitch Θ_0
Pitch range $\Delta\alpha$	Strong increasing effect on $C_{l,max}$, hysteresis, and α_{DS}	Strong increasing effect on $M_{\beta,max}$ and hysteresis	Cyclic pitch Θ_C

Table 4.4: Juxtaposition of parameter influences on lift coefficient and blade root flapping moment for the NACA 0012 pitching airfoil (Carr et al. [1]) and the NACA 0012 pitching rotating MERIT blade

Tsang et al. observed that the maximum lift coefficient and dynamic stall angle are significantly affected by k, but only for cases where the maximum angle of attack exceeds the static stall angle (post-stall region). They stated that the increasing of mean pitch angle and pitch range has a very small increasing effect on lift peak, hysteresis, and stall angle at low reduced frequencies of $k = 0.005, 0.01$, and their impact rises significantly at a higher reduced frequency ($k = 0.04$) [155].

Comparing the influence of mean AoA to the effect of AoA range on a pitching airfoil in dynamic stall [5, 155], the results show similar effects as those observed on the MERIT blade for collective and cyclic pitch variation: the mean AoA has a slight effect on load increase and stall delay, whereas pitch range has a more significant effect on dynamic stall angle and maximum lift coefficient.

In summary, the dominant factors for load dynamics on a pitching airfoil are the reduced frequency and AoA range, whereas the highest dynamic load increase and hysteresis on the pitching rotating blade occur at the highest speed (1500 RPM) and a high cyclic pitch setting (14° ± 10°).

4.3.6 Cycle-to-Cycle Variations

Several studies have shown significant scatter in the aerodynamic loads of pitching airfoils and rotating blades near stall angle of attack. For many decades, phase average and standard deviation have been used to evaluate loads and their variation with time. Closer analysis by Ramasamy et al. [28, 30, 33, 108, 153, 156] showed that some of the dynamic stall data scatter is not randomly distributed around the phase average, but contains bifurcations and can be grouped into different data bundles, see Fig. 4.42 [28, 29].

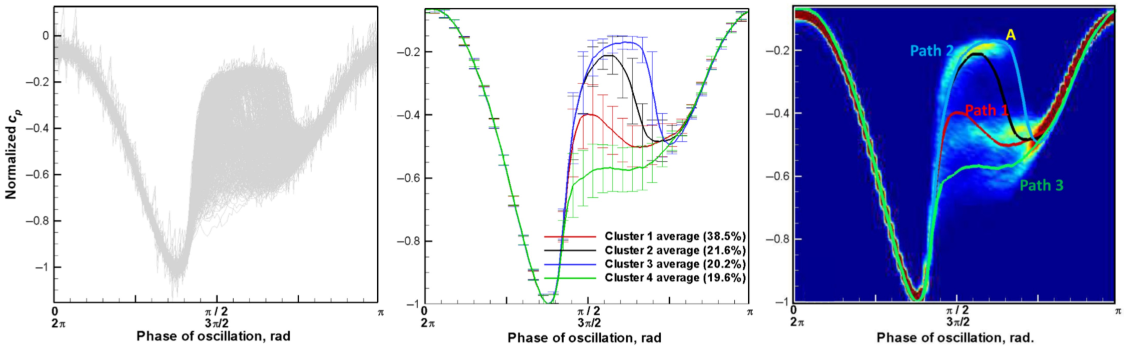

Raw data

RPAC clustering

JPDF with RPAC overlay

Figure 4.42: Conventional (phase-averaged) and clustered dynamic stall load analyses of 97 cycles in total at $Ma = 0.3,\ k = 0.15,\ \alpha = 18^\circ \pm 5^\circ$ [28, 29]

Dynamic stall data bifurcation was mainly found in the separation and reattachment regions of the pitching motion by Ramasamy et al. They attributed it to various different physical processes, such as differences in separation location, boundary layer reattachment, the occurrence of leading-edge or trailing-edge stall, and the presence of a dynamic stall vortex [30]. Moreover, they stated that conventional phase averaging in many cases obscures these physical processes and their effects, which can lead to large deviations of single revolutional data from phase-averaged data [30]. Clustering similar load cycles with model order reduction methods, such as POD, can be an efficient way to individually analyze different dynamic stall mechanisms. Applying different clustering methods can lead to more accurate load analyses and help identify the causes of different stall effects. This has been demonstrated by recent investigations on pressure and structural load data from the UH-60A wind tunnel measurements (pushrod loads, blade surface pressures, section loads, torsional moments) as shown in [156]. Ramasamy et al. used the normal distribution test of the JPDF as an initial check on the need for a clustering algorithm to evaluate the data. Applying a data-driven clustering algorithm [29] showed higher peak loads and lower variance for each cluster compared to conventional phase averaging. Most importantly, the simulation results showed significantly improved correlation with one of the clusters [156].

Up to this point, all analyses in this thesis have focused primarily on phase-averaged structural load data. This section investigates cycle-to-cycle variations of the structural loads on the investigated two-blade MERIT rotor using JPDFs based on a normal kernel function [157]. The maximum measured load deviation from the phase average and the probability density of load data at the load peak azimuth position for selected deep dynamic stall cases are used to determine the degree of bifurcation in structural loads and to quantify possible errors in load evaluation by phase averaging.

The JPDF plots of all structural loads and dynamic stall cases examined are shown in section B.6 of the appendix. Some of these plots show areas of moderate scatter, while strong bifurcation is evident in only two cases: $14 \pm 6^\circ$ at 1500 RPM and $14 \pm 9^\circ$ at 1200 RPM, see Figures 4.43 and 4.44. The highest data scatter in these two cases occurs over all azimuth positions for the lead-lag moment and in the flow reattachment region for the torsion and pitch link forces. The bifurcation in the flapping moment is weak compared to the absolute load range, while the local probability density functions evaluated at the rotor azimuth – where the load peak evaluation for the trend analysis is performed – shows bimodal data scatter in the flapping moment of both cases. All other cases, even the deep dynamic stall cases at $20 \pm 6^\circ$ and $14 \pm 10^\circ$, show data that are mainly normally distributed around the phase average with no visible bifurcation, see blade root moments as a function of azimuth in Figures B.71 and B.50 with the Probability Density Function (PDF) at the corresponding load peaks in section B.7 of the appendix.

The last row in Figures 4.43 and 4.44 as well as the plots in section B.7 show the local maximum relative deviation $e_{M_{\beta,\zeta,\theta},rel,max}$, which describes the maximum deviation of a data point from the phase average at each azimuth position Ψ_i in relation to the difference between the absolute maximum and minimum values of all revolutions. This deviation is calculated according to:

$$e_{M_{\beta,\zeta,\theta},rel,max}(\Psi_i) = \frac{M_{\beta,\zeta,\theta,max}(\Psi_i) - \bar{M}_{\beta,\zeta,\theta}(\Psi_i)}{M_{\beta,\zeta,\theta,max} - M_{\beta,\zeta,\theta,min}} \tag{4.8}$$

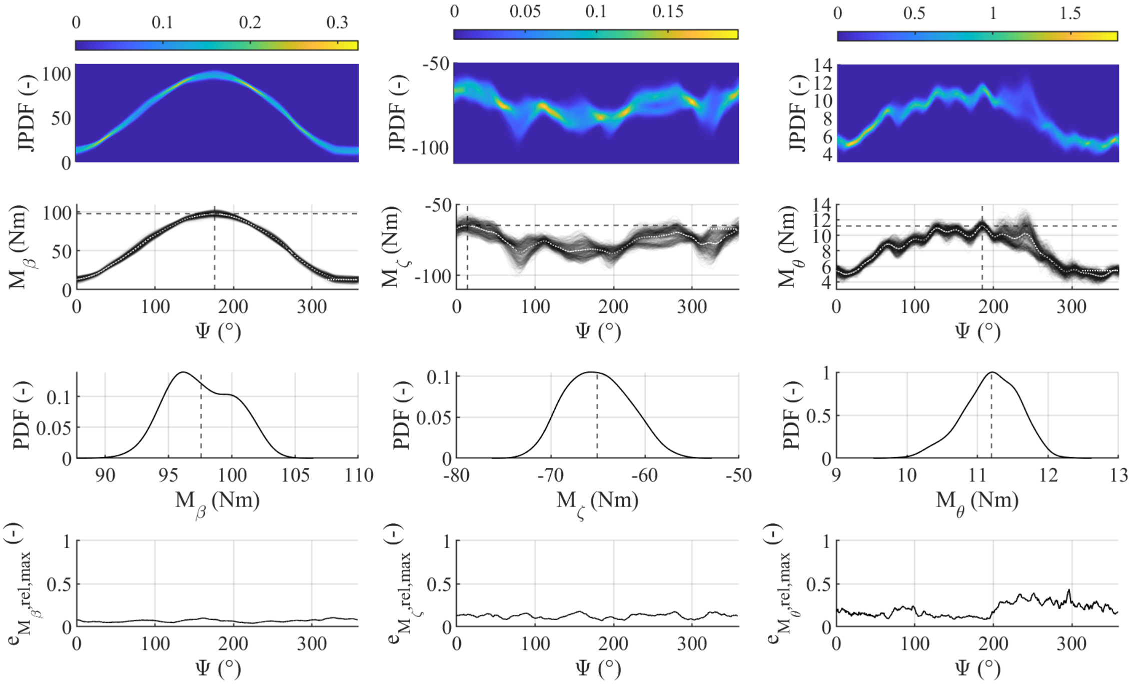

Figure 4.43: Probability density estimates for the blade root moments at 14 ± 6° and 1500 RPM

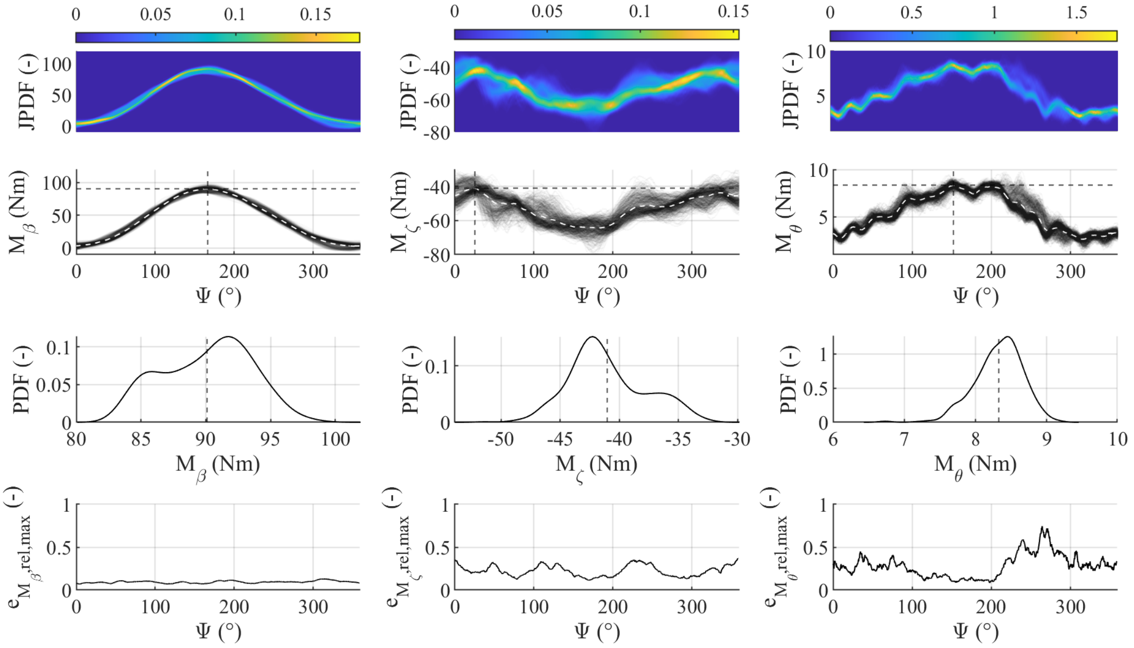

Figure 4.44: Probability density estimates for the blade root moments at 14 ± 9° and 1200 RPM

The maximum relative deviation shows the deviation of the strongest outliers at each point and therefore strong deviation even in cases where no bifurcation is visible in the JPDF plots. It indicates local deviations up to 170% from the phase average for the torsion and 80% for the lead-lag moment in the deep stall case $14 \pm 10^\circ$, while the (joint) probability density plots show a predominantly normal distribution around the phase average at the load peak azimuth for all three moments in this case, see Figures B.71. The deviation of local outliers increases with rotor speed, collective, and cyclic pitch. The advantage of clustering methods in this case would be that single outliers like these are not overestimated, while the grouping of data into different bundles with similar probability allows the identification and separation of different physical flow phenomena and the comparison with computational results.

The data investigated in this thesis shows significant deviations of single outliers from the phase average in many cases, but only two cases with notable bifurcation, where a clustering method could be applied. Since bifurcation mainly occurs in the reattachment areas and the parameter trend analysis is performed predominantly by means of the peak values, data clustering as shown in [33] is not considered necessary for the structural load data investigated. Of course, this does not generally apply to the analysis of local pressure data, where bifurcation analysis of local airflow is highly recommended nevertheless.

The occurrence of only two cases with bifurcation at moderate stall conditions, raises the question of whether this is due to the rotating blade environment or the selection of data examined. The latter is unlikely, because of the study of Ramasamy et al., who found strong bifurcation in structural loads of the UH-60A, such as pitch link forces. To estimate the influence of the rotating environment, the parametric study by Harms et al. on a pitching airfoil provides deeper insight. It reveals the physical mechanisms leading to cycle-to-cycle variations [30] by varying AoA range and pitch frequency. Harms and Ramasamy performed the same dynamic stall experiments on an SC1094R8 airfoil model at different research facilities [28, 30]. Their main findings were that dynamic stall reattachment bifurcation predominantly occurred at lower AoA amplitudes (9° and 11°) and lower reduced frequencies ($k = 0.055$ and $k = 0.067$), as shown in the bifurcation classification matrix, see Fig. 4.45. Moreover, bifurcation seemed to decrease with increasing k, but only weakly compared to its decrease with alpha. All of the other cases showed no significant cycle-to-cycle variation. [30]

The parameter study of Harms et al. [30] shows that bifurcation is not always embedded in dynamic stall reattachment data scatter. It may be confined to certain regions of pitch range and flow unsteadiness. This finding confirms the observations in this thesis, where bifurcation was detected in only two out of ten dynamic stall cases and in regions with lower mean pitch angles. Therefore, the low number of bifurcations found in this thesis cannot be traced back to the rotating environment. Of course, the investigated parameter set is limited and should be extended in order to further investigate dynamic stall data bifurcation. Moreover, extended data such as local pressure should be examined to expand the understanding of changes in flow physics from cycle to cycle at the same control inputs.

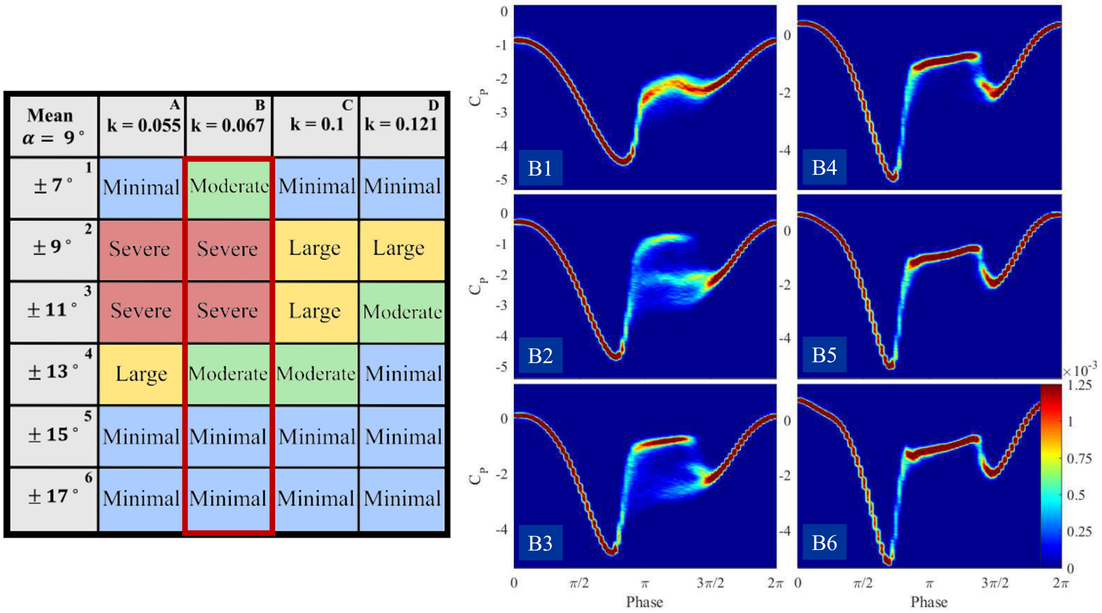

Mean α = 9°	A k = 0.055	B k = 0.067	C k = 0.1	D k = 0.121
1 ± 7°	Minimal	Moderate	Minimal	Minimal
2 ± 9°	Severe	Severe	Large	Large
3 ± 11°	Severe	Severe	Large	Moderate
4 ± 13°	Large	Moderate	Moderate	Minimal
5 ± 15°	Minimal	Minimal	Minimal	Minimal
6 ± 17°	Minimal	Minimal	Minimal	Minimal

Figure 4.45: Graphical matrix with bifurcation classifications for each test case and JPDF of pressure data for all cases at $k = 0.067$ [30]

4.3.7 Frequency Analysis

Experimental frequency analysis was previously performed on the steel frame structure, including the drive train, by hammer impact excitation; see section 2.4.1. The rotor and drive systems were not part of the eigenfrequencies obtained. Knowledge of the frequencies of the entire test rig system, including the operating rotor, is critical for stability and control analysis or system identification. Due to the high stiffness of the rotor and frame structure, identifying a Campbell diagram can be challenging. Substantial energy is required to excite the wide range of high eigenfrequencies of the hingeless MERIT rotor to measurable vibration amplitudes. Various approaches to mode excitation include the excitation of the frame through a shaker, the perturbation of inflow, and high-frequency step or sweep pitch control inputs. Another possibility is the excitation by unsteady aerodynamics as in dynamic stall. In this section, dynamic stall mode excitation is examined and compared to static stall excitation using the example of 900 RPM.

The blade modes depend on the rotor speed and are calculated in CAMRAD II for a two-bladed rotor with and without surrogate flapping hinge at an exemplary rotor speed of 900 RPM; see the eigenfrequencies for the first nine blade modes in Tab. 4.5. The corresponding fan plot for the rotor with rigid blade attachment is shown in Fig. 4.46.

The calculated fan plot assumes perfect mass distribution and perfect sectional stiffness properties. On an experimental rotor, these entities are generally subject to manufacturing tolerances and may differ significantly from the theoretical model. Experiments are more accurate in identifying realistic rotor eigenfrequencies of the test rig system, provided that the modes of interest are

	ω_1	ω_2	ω_3	ω_4	ω_5	ω_6	ω_7	ω_8	ω_9
Without hinge	40.1	109.2	229.2	286.1	584.3	593.0	873.3	879.4	1074.0
With hinge	32.7	109.2	173.1	285.8	476.8	592.9	871.7	879.3	1041.2

Table 4.5: MERIT blade eigenfrequencies in Hz at 900 RPM with and without elastic flapping hinge

excitable and detectable. The amplitude spectrum shows detectable eigenmodes of the measured rotor data after a Fast Fourier Transformation (FFT). The FFT is performed on two exemplary signals in the rotating and stationary frame: the blade flapping moment and the rotor thrust, both under different excitation methods (static stall at $\Theta_0 = 24°$ and dynamic stall at $\Theta = 14° \pm 8°$) at 900 RPM, see Fig. 4.47 and 4.48.

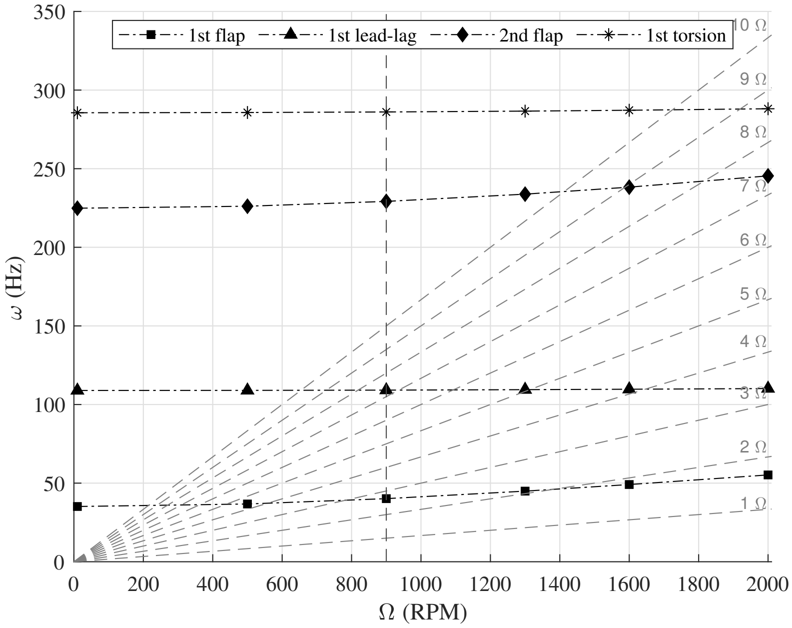

Figure 4.46: Campbell diagram (natural rotor blade eigenfrequencies as a function of rotor speed) for the MERIT rotor blade model in CAMRAD II with ideally stiff blade attachment

A comparison of the amplitude spectrum of the flapping moment for static and dynamic stall excitation shows that the selected dynamic stall case excites many more modes over a wide frequency range, see Fig. 4.47. Amplitude spectrum plots for the remaining blade root moments and pitch link forces are shown in the appendix, B.5. This excitation method excites not only the 1/rev multiples that are most visible due to the cyclic input but also many modes between the n/rev frequencies. In contrast to the dynamic stall excitation, the amplitude spectrum plot for the static stall excitation shows only the integral rotor speed multiples up to about 100 Hz and two weak amplitude peaks at about 35 Hz and 192 Hz. However, in the case of the dynamic stall excitation, it is not possible to unambiguously assign the measured eigenfrequencies to the calculated ones using a single measurement variable on a complex multi-body system that contains eigenfrequencies of different components and their multiples. Radially distributed measurement data along the blade, such as blade deformation, would be required to obtain blade modes for different rotor speeds.

The amplitude spectrum analysis of the rotor thrust data gives similar results, see Fig. 4.48. Amplitude spectrum plots for the in-plane rotor forces are shown in the appendix, B.5. Dynamic stall excitation results in higher mode excitability than static stall excitation. Amplitude peaks are detectable for multiples of the rotor harmonics and eigenmodes. As shown in section 2.4.1, the calculated frame modes are indicated by dash-dotted lines. They are calculated in the Finite Element Based Tool for the Analysis of Nonlinear Flexible Multibody Systems (DYMORE) [158] for the non-rotating shaft without a rotor and are therefore not expected to exactly match the frequencies shown. An operational modal analysis of the entire steel frame with a rotating shaft is necessary to correctly assign the eigenfrequencies by their mode shapes.

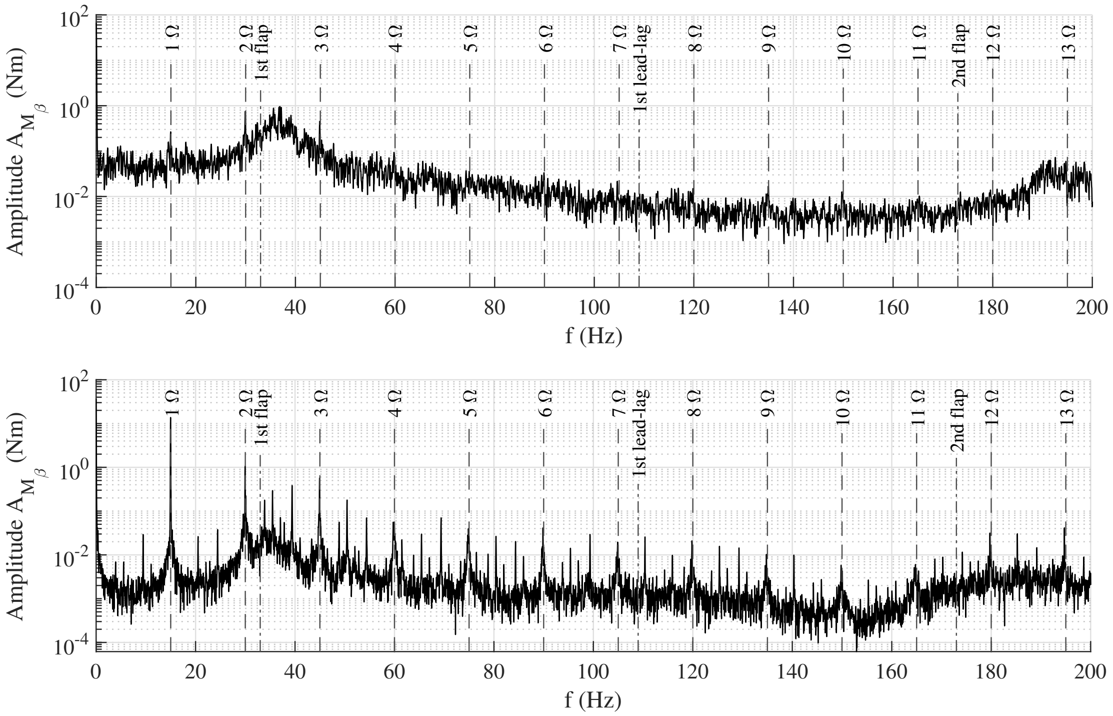

Figure 4.47: Amplitude spectrum as a function of frequency for the blade root flapping moment M_β at 900 RPM in static stall excitation at $\Theta_0 = 24°$ (top) and dynamic stall excitation at $\Theta = 14° \pm 8°$ (bottom), calculated blade modes and rotor harmonics indicated by dashed lines

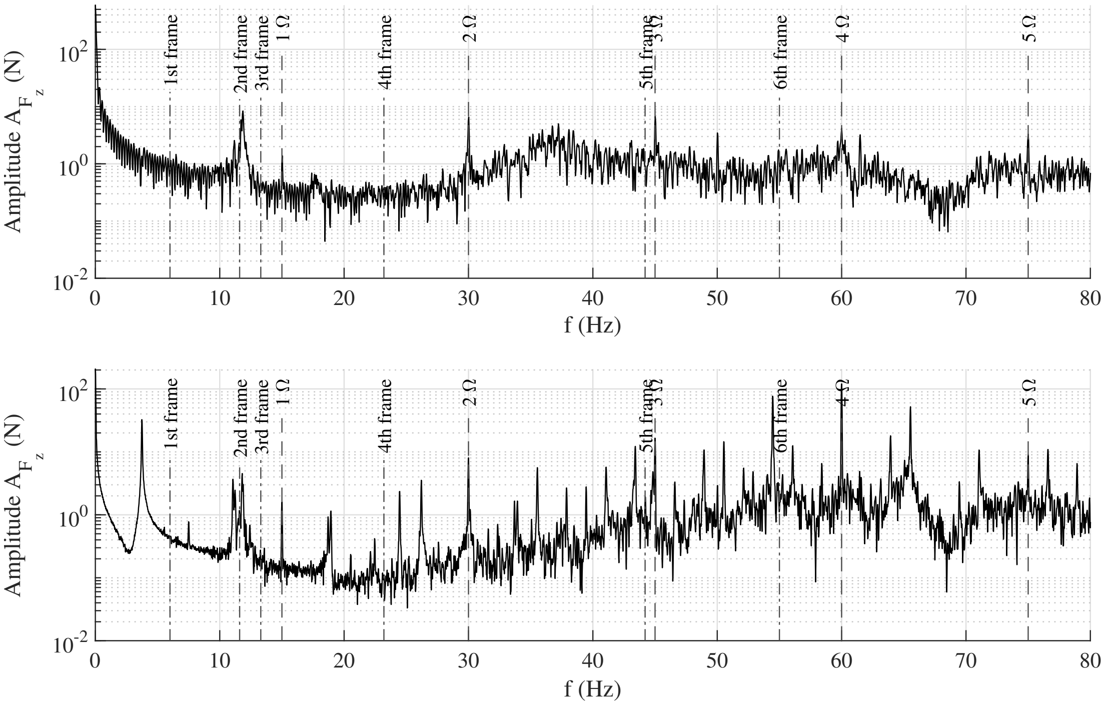

Figure 4.48: Amplitude spectrum as a function of frequency for the rotor thrust F_z at 900 RPM in static stall excitation at $\Theta_0 = 24°$ (top) and dynamic stall excitation at $\Theta = 14° \pm 8°$ (bottom), calculated frame modes and rotor harmonics indicated by dashed lines

5 Summary, Conclusions, and Recommendations

5.1 Summary

This thesis investigates the influence of rotor control parameters – collective pitch, cyclic pitch, and rotor speed – on structural rotor loads during dynamic stall in hover. While pitching airfoils and wings have been investigated in numerous studies in the past, rotating pitching blades have yet to be analyzed in depth. The present work takes the analysis of pitching airfoils in dynamic stall to the next level by examining the structural load dynamics of these airfoils in a rotating environment and under three-dimensional flow conditions. Early parameter studies (Mach number, Reynolds number, AoA range, mean AoA, reduced frequency) on pitching airfoils have identified load trends and regions of interest that have guided further research. Similarly, the influence of rotor control parameters on structural rotor loads in this thesis should provide a directional aid for further scientific work and reveal the effect of rotation on load dynamics during dynamic stall. As mentioned in section 1.1 of the introduction, the research questions behind the present investigation are:

1. *How does rotor speed affect the load dynamics of a rotating pitching airfoil in 3D flow conditions during dynamic stall?*
2. *How do collective and cyclic pitch angles affect the load dynamics of a rotating pitching airfoil in 3D flow conditions during dynamic stall?*
3. *To what extent do cycle-to-cycle variations of local aerodynamic loads affect integrated structural loads of a rotating pitching airfoil during dynamic stall?*

These questions are answered by an experimental approach. The experiments focus on hover tests on a two-bladed, hingeless rotor. The investigated rotating pitching airfoils are rigid rotor blades with a twist-free, rectangular planform and a NACA 0012 0° tab airfoil. The measured blade root moments and pitch link forces are used to examine the blade load dynamics. Several results emerge from the experimental dynamic stall analysis, which are explained and discussed in section 4.3. The advantages and limitations of this approach are discussed in section 5.3.

The chosen research method requires a Mach-scaled rotor test rig capable of withstanding the high load amplitudes and vibrations during dynamic stall. A rotor test rig is therefore developed as part of this work to serve as a research platform for dynamic stall on a rotor in hover and forward flight. The rotor test rig is designed for the presented analysis and for long-term studies of future rotor configurations and geometries. It contains a high-resolution rotating and stationary measurement system to acquire sensor data, such as integrated rotor forces and moments, rotor torque and speed, and any kind resistance-based sensor data. A corresponding numerical rotor model in CAMRAD II supports the estimation of design loads and the validation of measured static loads. The structural blade model is defined using sectional properties of an elastic Timoshenko beam and a surrogate flapping hinge to account for the blade attachment stiffness. The sectional beam properties are validated with static deformation, while the stiffness of the flapping hinge is adjusted using rotating blade deformation.

Rotor performance and static stall polars are measured at the three rotor speeds 900, 1200, and 1500 RPM. Static stall onset on the MERIT blade occurred between 19° and 21° collective pitch at 900, 1200, and 1500 RPM with a slight tendency of lower pitch angles at higher rotor speeds. Moreover, stall location was ambiguous in some steady control cases and even varying dependent on the rising or falling section of the polar. A comparison of measured and predicted loads shows a very satisfactory correlation for thrust and power data, with no significant differences between the rigid and elastic blade models. However, both models predict stall at about 4° higher pitch angles than the experiments. The elastic blade model takes into account the moment-relieving effect of the centrifugal force. While the rigid blade model overestimates the blade loads by far, the elastic blade model predicts the structural blade root moments very well, although the MERIT blades have a high stiffness and thus their deformation is small (5.3 mm flap displacement at 900 RPM and 12° collective pitch).

Ten dynamic stall cases are selected to observe load trends for collective and cyclic pitch variation. These are: $14, 16, 18, 20^\circ \pm 6^\circ$ and $14^\circ \pm 4, 5, 6, 7, 8, 9, 10^\circ$. All dynamic stall cases are performed at 900, 1200, and 1500 RPM. The measured loads are compared to the corresponding static stall polar. Dynamic stall on the MERIT rotor sets in when the local maximum pitch angle, consisting of collective and cyclic pitch, exceeds the static stall pitch angle, confirming prevalent studies on pitching airfoils and wings. Three different evaluation entities describe the load trends of the revolution-averaged data: dynamic load increase (load overshoot), load range, and load hysteresis. These are used to analyze structural loads (blade root flapping moment, lead-lag moment, torsion, and axial pitch link forces). The parameter study shows a clear increasing influence of rotor speed and pitch control on structural load dynamics.

The dynamic stall load evaluations in this thesis are based on phase averages. Significant cycle-to-cycle variations with bifurcation in structural loads are detected in only two out of ten dynamic stall cases with moderate collective pitch angles, i.e. at $14^\circ \pm 6^\circ$ at 1500 RPM and $14^\circ \pm 9^\circ$ at 1200 RPM. The probability density plots of all other cases show random data scatter around the phase-average without furcation. Nevertheless, individual outliers with very high deviation (50-170%) occur in almost all cases with increasing trend for higher speed and higher control angles.

The frequency analysis of the structural load data reveals that deep dynamic stall excites many more eigenmodes at low and high frequencies (up to at least 300 Hz) compared to static stall. In addition to the integral multiples of the rotor speed, rotor blade and test rig frame eigenmodes are detected.

5.2 Conclusions

With the chosen experimental approach and the gained results, the answers to the research questions (section 1.1) and the conclusions that can be drawn thereof are:

1. *The effects of rotor speed on a rotating pitching airfoil are opposite to the effects of Mach number on a pitching airfoil for the cases analyzed.* Increasing rotor speed shows an increasing trend in dynamic load increase, load range, and hysteresis of all measured structural loads, while increasing Mach number decreases the load overshoot on pitching airfoils. The variation of Mach number, Reynolds number, and reduced frequency along the blade radius seem to be a major influence on the dynamic stall vortex location at different speeds. However, local flow investigation is needed to locate the dynamic stall vortex and its movement on the blade's surface as in [18].

2. *The collective and cyclic pitch variations confirm the trends from the mean AoA and AoA range variation of pitching airfoils and wings.*
   Collective and cyclic pitch have an increasing effect on dynamic load peaks and hystereses during dynamic stall. Cyclic pitch has an even stronger effect than collective pitch when comparing different combinations of collective and cyclic pitch for the same maximum pitch angle. For the rotating pitching blade, the maximum pitch rate – resulting from the combination of rotor speed and cyclic pitch control – seems to play an important role for the strength of dynamic load increase.

3. *Two of the ten dynamic cases analyzed show significant cycle-to-cycle variations with bifurcation.* These are dynamic stall cases with moderate collective pitch ($14^\circ \pm 6^\circ$ at 1500 RPM and $14^\circ \pm 9^\circ$ at 1200 RPM). All other cases show significantly lower data scatter with a normal distribution around the phase average. Bifurcation is not only restricted to the stall onset and reattachment areas, especially in the lead-lag moment. These findings have strong similarities with those on pitching airfoils. The clustering methods examined by Ramasamy et al. [28, 33] for a different evaluation of similar load paths of pitching airfoils at a given control setting are therefore not considered necessary for the dynamic load trend analysis in this thesis.

5.3 Evaluation of Research Design

The chosen method to investigate parameter trends on a rotating pitching blade in dynamic stall compared to a pitching airfoil is the following: the experimental analysis of rotor control parameter effects on structural loads (blade root moments, pitch link forces) during cyclic pitch-induced dynamic stall in hover on a hingeless, rigid rotor blade with a rectangular blade geometry and a NACA 0012 0° tab airfoil.

Over the past few decades, computational capabilities have improved tremendously, making high-fidelity modeling an increasingly suitable choice for predicting dynamic stall loads. Nevertheless, an experimental approach has been preferred to a numerical one because it provides fast and reliable data for a wide range of parameters once it is set up. Furthermore, experiments take into account the complexity of the flow field (vortex interactions, recirculation, local unsteady effects) and the three-dimensional flow effects on the rotor blade. Numerical and experimental investigations should go hand in hand to provide meaningful research results. Both approaches have strengths and weaknesses; a well-planned and targeted combination of both methods will lead to a better understanding and predictive capability of the phenomenon. In addition, the MERIT test facility is a platform for future experiments that will facilitate the investigation of different rotor configurations, blade shapes, and flight states. The advantage of a laboratory environment over flight testing is the applicability of high-resolution and high-quality measurement equipment at a relatively low cost compared to fully equipped flight tests. Although the MERIT rotor is Mach-scaled to account for compressibility effects that significantly affect dynamic stall loads, it does not represent the exact parameter conditions that occur simultaneously on a full-scale helicopter in flight (e.g., Mach number, and Reynolds number). Neither does it represent the effects of aeroelasticity and modern blade geometries with taper, sweep, and twist. The structural load analysis in this thesis allows for a quick and comprehensive parameter study. It focuses on loads that are most relevant to the end of life of the rotor components. The main advantage of its hingeless rotor attachment, structural rigidity, rectangular geometry, and airfoil is the comparability with pitching airfoil data. Therefore, it is a research platform for flow morphology and parameter trend analysis.

The research results presented have directional implications for future research. They reveal regions of interest for future work by highlighting areas of critical load dynamics and unexpected trend changes. In addition, the created test platform provides a basis for further research in wind tunnels and with easily applicable measurement techniques (e.g., surface pressure measurements, PIV, PSP) to examine local flow in detail. These data are necessary for CFD validation and further development of three-dimensional, semi-empirical dynamic stall models.

5.4 Recommendations

The information presented provides the basis for simulations and tests; it should help future investigators determine the most appropriate approach for their particular areas of interest. Based on the research findings of this thesis, the recommendations for future dynamic stall investigations and measurement techniques are as follows:

1. In order to detect local flow mechanisms and validate CFD results, such as radial and chordwise stall location and vortex formation and size, it is necessary to measure the surface pressure on the rotor blade. This can be achieved by using transient pressure sensors embedded in the blade, which was already demonstrated for the MERIT blade in [159], or pressure sensitive paint applied on the blade surface.

2. Local flow visualization techniques, such as PIV, are helpful in accurately describing the dynamic stall vortex shape, size, and expansion along the blade radius. Global flow analysis of the rotor wake and inflow can help to detect recirculation, inflow perturbation, or the

interaction of the rotor with the casing elements and the test rig steel frame to identify stall triggers.

3. Although the MERIT blades are designed with high rigidity, their remaining elasticity must be considered when validating numerical calculations, such as CFD or CSD simulations. In particular, torsional twist combined with flapping deflection can have a noticeable effect on the thrust polar. Therefore, the author recommends the measurement of blade deformation, e.g. by optical methods such as DIC or photogrammetry, or embedded strain sensors such as FBG sensors, see [160–164].

4. A reliable assignment of the eigenmodes is only possible by analyzing the corresponding eigenvectors, which can be obtained by measuring the deformation, surface strain, or acceleration of the blades and the steel frame of the test rig. FBG sensors embedded into the blade are especially useful for blade mode shape analysis and experimental identification of the rotor fan plot.

5. All rotor experiments in this thesis have been performed in hover. The next step is of course to study the rotor in the wind tunnel to create simulate forward flight conditions. The rotor can be trimmed to zero phase average hub moments using the four stationary load cells.

6. To analyze compressibility effects and shock-induced stall, further increases in rotor speed and pitch range can be tested.

7. Variations in rotor configuration provide a deeper insight into dynamic stall sensitivity. Increasing the blade elasticity or introducing a flapping hinge to allow for blade movement can greatly affect the development and strength of the dynamic stall vortex. In addition, the effect of different blade geometries, such as sweep, taper, and twist, on dynamic stall can be studied.

8. Cycle-to-cycle bifurcation checks and (if necessary) data clustering methods, as shown in [156], should be applied when evaluating surface pressure and validating CFD simulations.

Bibliography

[1] L. W. Carr, K. W. McAlister, and W. J. McCroskey, “Analysis of the development of dynamic stall based on oscillating airfoil experiments,” *NASA Technical Note D-8382, Washington D.C., January*, 1977.

[2] J. G. Leishman, “Principles of helicopter aerodynamics, second edition,” *Cambridge University Press, New York, NY*, 2006.

[3] K. Mulleners and M. Raffel, “Dynamic stall development,” *Experiments in Fluids*, vol. 54, pp. 1469–1477, 2013.

[4] B. Wei, Y. Gao, and S. Hu, “Experimental and numerical study on dynamic stall under a large Reynolds number,” *Advances in Aerodynamics*, vol. 5, pp. 1–20, 2023.

[5] L. W. Carr and M. S. Chandrasekhara, “Compressibility effects on dynamic stall,” *Progress in Aerospace Sciences*, vol. 32, pp. 523–573, 1996.

[6] ——, “A study of compressibility effects on dynamic stall of rapidly pitching airfoils,” *Computer Physics Communications*, vol. 65, pp. 62–68, 1991.

[7] P. F. Lorber, “Compressibility effects on the dynamic stall of a three-dimensional wing,” *AIAA 92-0191, 30th Aerospace Sciences Meeting and Exhibit, Reno, NV, January 6-9*, 1992.

[8] T. Schwermer, “Experimentelle Untersuchung des Dynamischen Strömungsabrisses an einem Rotor mit Axialer Zuströmung,” *Dissertation, Gottfried Wilhelm Leibniz Universität Hannover*, 2018.

[9] T. Schwermer, K. Richter, and M. Raffel, “Development of a rotor test facility for the investigation of dynamic stall,” *19th DGLR-Fachsymposium der STAB, Munich, Germany*, vol. 132, 2014.

[10] V. Rhagav, “Radial flow effects on a retreating rotor blade,” *Dissertation, Georgia Institute of Technology, May*, 2014.

[11] S. Surrey, B. Ortun, K.-V. Truong, and F. Wienke, “Investigation of the structural blade dynamics and aeroelastic behavior of the 7a rotor,” *AHS 72nd Annual Forum, West Palm Beach, Florida, May 17–19*, 2016.

[12] K. Kindler, K. Mulleners, and M. Raffel, “Dynamic stall on a fully equipped helicopter model,” *36th European Rotorcraft Forum, 07.-09. Sept, Paris, France*, 2010.

[13] K. Mulleners, K. Kindler, and M. Raffel, “Dynamic stall on a fully equipped helicopter model,” *Aerospace Science and Technology*, vol. 19, pp. 72–76, 2012.

[14] T. Schwarz and K.-D. Pahlke, “Goahead generation of advanced helicopter experimental aerodynamic database for cfd code validation - publishable final activity report,” *Aerodays, Madrid, Spain, March 30th – April 1st*, 2011.

[15] W. G. Bousman, “A qualitative examination of dynamic stall from flight test data,” *Journal of the American Helicopter Society*, vol. 43, pp. 279–295, 1998.

[16] T. R. Norman, P. Shinoda, R. L. Peterson, and A. Datta, “Full-scale wind tunnel test of the UH-60A airloads rotor,” *American Helicopter Society 67th Annual Forum, Virginia Beach, VA, May 3-5*, 2011.

[17] A. H. Lind, L. N. Trollinger, F. H. Manar, I. Chopra, and A. R. Jones, “Flowfield measurements of reverse flow on a high advance ratio rotor,” *Experiments in Fluids*, vol. 59, p. 185, 2018.

[18] M. M. Müller, A. Weiss, and J. N. Braukmann, “Dynamic stall investigation on a rotating semielastic double-swept rotor blade at the rotor test facility göttingen,” *Journal of the American Helicopter Society*, vol. 68, p. 22007, 2023.

[19] W. G. Bousman, “Uh-60 airloads program tutorial,” *Proceedings of the American Helicopter Society 65th Annual Forum, May 27-29, Grapevine, Texas*, 2009.

[20] J. Letzgus, M. Keßler, and E. Krämer, “Cfd-simulation of three-dimensional dynamic stall on a rotor with cyclic pitch control,” 2015.

[21] M. Pulfer, “Numerische Untersuchung des Einflusses der Seiferth-Flügel auf die Strömung in der offenen Messstrecke von Windkanal A der TUM,” *Master’s Thesis, Technical University of Munich*, 2017.

[22] V. Heuschneider, F. Berghammer, T. Pflumm, and M. Hajek, “Development and initial hover testing of the mach scaled rotor test rig merit,” *47th European Rotorcraft Forum, Virtual, September 6-9*, 2021.

[23] T. Pflumm, L. Gaugelhofer, V. Heuschneider, F. Berghammer, and M. Hajek, “Hybrid experimental measurement of sectional stiffness properties of the merit rotor blade with digital image correlation,” *47th European Rotorcraft Forum, Virtual, September 6-9*, 2021.

[24] V. Heuschneider, F. Berghammer, and M. Hajek, “Numerical and experimental study on the modal characteristics of a rotor test rig,” *Topics in Modal Analysis and Testing, Volume 8, Conference Proceedings of the Society for Experimental Mechanics Series*, 2020.

[25] N. Pfanner, “Fatigue test procedures of torsion-tension straps of a helicopter rotor test rig: Planning and execution,” *Master’s Thesis, Technical University of Munich*, 2021.

[26] S. Keil, “Dehnungsmessstreifen,” *Dehnungsmessstreifen, Springer Vieweg Wiesbaden, February*, 2017.

[27] L. Dadone, “U.s. army helicopter design datcom volume i - airfoils,” *U.S. Army Air Mobility Research and Development Laboratory USAAMRDL CR 76-2, Aviation Systems Command, Ames Research Center, Moffett Field, California*, 1976.

[28] M. Ramasamy, A. Sanayei, J. S. Wilson, P. B. Martin, T. Harms, P. Nikoueeyan, and J. Naughton, “Reducing uncertainty in dynamic stall measurements through data-driven clustering of cycle-to-cycle variations,” *Journal of the American Helicopter Society*, vol. 66, p. 12003, 2021.

[29] A. Sanayei, M. Ramasamy, J. S. Wilson, and P. B. Martin, “Development of modal analysis based clustering technique using pitching airfoil measurements,” *AIAA Scitech 2019 Forum*, 2019.

[30] T. Harms, P. Nikoueeyan, and J. Naughton, “Experimental evaluation of the cycle-to-cycle variation of dynamic stall on the SC1094R8 airfoil,” *AIAA Aerospace Sciences Meeting*, 2018.

[31] K. A. Henschel, “Biocomposites in aviation structures on the example of flax and its hybrids,” *Dissertation, Technical University of Munich*, 2019.

[32] W. Johnson, “Helicopter theory,” *Dover Books on Aeronautical Engineering Series, Dover Publications*, 1994.

[33] M. Ramasamy, J. S. Wilson, W. J. McCroskey, and P. B. Martin, “Measured characteristics of cycle-to-cycle variations in dynamic stall,” *AHS Technical Meeting on Aeromechanics Design for Vertical Lift*, 2016.

[34] R. W. Prouty, “Helicopter performance, stability, and control,” *Krieger Publishing Company, Malabar, Florida*, pp. 1–731, 2002.

[35] B. G. V. D. Wall, “Grundlagen der Hubschrauber-Aerodynamik,” *Springer-Verlag Berlin Heidelberg*, 2015.

[36] ——, “Grundlagen der Dynamik von Hubschrauber-Rotoren,” *Springer-Verlag GmbH Deutschland*, 2018.

[37] M. J. Smith, A. D. Gardner, R. Jain, D. Peters, and F. Richez, “Rotating wing dynamic stall: State of the art and future directions,” *76th Annual Forum of the Vertical Flight Society, Virtual, Oct 10*, 2020.

[38] W. J. McCroskey, L. W. Carr, and K. W. McAlister, “Dynamic stall experiments on oscillating airfoils,” *AIAA Journal*, vol. 14, pp. 57–63, 1976.

[39] W. J. McCroskey, “Unsteady airfoils,” *Annual Review of Fluid Mechanics*, vol. 14, pp. 285–311, 1982.

[40] R. Jain, A. L. Pape, A. Grubb, M. Costes, F. Richez, and M. Smith, “High-resolution computational fluid dynamics predictions for the static and dynamic stall of a finite-span oa209 wing,” *Journal of Fluids and Structures*, vol. 78, pp. 126–145, 2018.

[41] K. W. McAlister, L. W. Carr, and W. J. McCroskey, "Dynamic stall experiments on the naca 0012 airfoil," *NASA Technical Paper 1100, AN 78N17000*, 1978.

[42] W. J. McCroskey, "The phenomenon of dynamic stall," *NASA Technical Memorandum 81264*, pp. 1–28, 1981.

[43] W. G. Bousman and W. R. Mantay, "A review of research in rotor loads," *NASA/Army Rotorcraft Technology Conference, NASA Ames Research Center, March 14-16*, 1987.

[44] L. W. Carr, "Progress in analysis and prediction of dynamic stall," *Journal of Aircraft*, vol. 25, pp. 6–17, 1988.

[45] L. W. Carr and W. J. McCroskey, "A review of recent advances in computational and experimental analysis of dynamic stall," *Fluid Dynamics of High Angle of Attack*, pp. 3–33, 1993.

[46] M. J. Smith, A. R. Jones, F. Ayancik, K. Mulleners, and J. W. Naughton, "An assessment of the state of the art from the 2019 aro dynamic stall workshop," *AIAA Aviation 2020 Forum, Virtual, June 15-19*, 2020.

[47] A. D. Gardner, A. R. Jones, K. Mulleners, J. W. Naughton, and M. J. Smith, "Review of rotating wing dynamic stall: Experiments and flow control," *Progress in Aerospace Sciences*, vol. 137, p. 100887, 2023.

[48] M. Kramer, "Increase in the maximum lift of an airplane wing due to a sudden increase in its effective angle of attack resulting from a gust," *NACA-TM-678*, 1932.

[49] R. Katzmayr, "Effect of periodic changes of angle of attack on behavior of airfoils," *NACA-TM-147*, 1922.

[50] H. Wagner, "Über die Entstehung des dynamischen Auftriebes von Tragflügeln," *Zeitschrift für angewandte Mathematik und Mechanik*, vol. 5, p. 17, 1925.

[51] F. J. Bailey and F. B. Gustafson, "Observations in flight of the region of stalled flow over the blades of an autogiro rotor," *National Advisory Committee for Aeronautics, Technical Note No. 741, Washington, December*, 1939.

[52] J. Liiva, F. J. Davenport, L. Gray, and I. C. Walton, "Two-dimensional tests of airfoils oscillating near stall - volume 1 - summary and evaluation of results," *Technical Report AD0670957, Philadelphia, Pennsylvania*, 1968.

[53] J. Liiva and F. J. Davenport, "Dynamic stall of airfoil sections for high-speed rotors," *24th Annual National Forum of the American Helicopter Society, May*, 1968.

[54] J. Liiva, "Unsteady aerodynamic and stall effects on helicopter rotor blade airfoil sections," *Journal of Aircraft*, vol. 6, pp. 46–51, 1969.

[55] L. Gray and J. Liiva, "Wind tunnel tests of thin airfoils oscillating near stall - volume 2 - data report," *USAAVLABS TR 68-89B*, 1969.

[56] L. W. Carr, W. J. McCroskey, K. W. McAlister, S. L. Pucci, and O. Lambert, "An experimental study of dynamic stall on advanced airfoil sections volume 3. hot-wire and hot-film measurements," *NASA Technical Memorandum 84245*, 1982.

[57] M. S. Chandrasekhara and L. W. Carr, "Flow visualization studies of the Mach number effects on dynamic stall of an oscillating airfoil," *Journal of Aircraft*, vol. 27, pp. 516–522, 1990.

[58] M. Chandrasekhara, "Compressibility effects on dynamic stall of oscillating airfoils," *Progress in Aerospace Sciences*, vol. 32, pp. 523–573, 1994.

[59] K. W. McAlister, S. L. Pucci, W. J. McCroskey, and L. W. Carr, "An experimental study of dynamic stall on advanced airfoil sections volume 2. pressure and force data," *NASA Technical Memorandum 84245, USAAVRADCOM TR-82-A-8*, 1982.

[60] W. McCroskey and R. K. Fisher, "Detailed aerodynamic measurements on a model rotor in the blade stall regime," *Journal of the American Helicopter Society*, vol. 17, pp. 20–30, 1972.

[61] W. J. McCroskey and S. L. Pucci, "Viscous-inviscid interaction of oscillating airfoils in subsonic flow," *AIAA Journal*, vol. 20, p. 167, 1982.

[62] W. J. McCroskey, K. W. McAlister, L. W. Carr, S. L. Pucci, O. Lambert, and R. F. Indergand, "Dynamic stall on advanced airfoil sections," *Journal of the American Helicopter Society*, vol. 26, pp. 40–50, 1981.

[63] W. J. McCroskey, K. W. McAlister, L. W. Carr, and S. L. Pucci, "An experimental study of dynamic stall on advanced airfoil sections volume 1. summary of the experiment," *NASA Technical Memorandum 84245*, p. 92, 1982.

[64] R. M. Scruggs, J. F. Nash, and R. E. Singleton, "Analysis of flow-reversal delay for a pitching foil," *AIAA 12th Aerospace Sciences Meeting, Washington D.C., January 30 - February 1*, 1974.

[65] P. F. Lorber and F. O. Carta, "Airfoil dynamic stall at constant pitch rate and high Reynolds number," *Journal of Aircraft*, vol. 25, pp. 548–556, 1988.

[66] F. O. Carta, "A comparison of the pitching and plunging response of an oscillating airfoil," *NASA Contractor Report 3172*, 1979.

[67] J. M. Martin, R. W. Empey, W. J. McCroskey, and F. X. Caradonna, "An experimental analysis of dynamic stall on an oscillating airfoil," *Journal of the American Helicopter Society*, pp. 26–32, 1974.

[68] R. A. Piziali, "2-D and 3-D oscillating wing aerodynamics for a range of angles of attack including stall," *NASA Technical Memorandum 4632, USAATCOM Technical Report 94-A-001*, 1994.

[69] K. Mulleners and M. Raffel, "The onset of dynamic stall revisited," *Experiments in Fluids*, vol. 52, pp. 779–793, 2012.

[70] M. Acharya and M. H. Metwally, "Unsteady pressure field and vorticity production over a pitching airfoil," *AIAA Journal*, vol. 30, pp. 403–411, 1992.

[71] J. M. Akkala and J. H. J. Buchholz, "Vorticity transport mechanisms governing the development of leading-edge vortices," *Journal of Fluid Mechanics*, vol. 829, pp. 512–537, 2017.

[72] J. Boutet, G. Dimitriadis, and X. Amandolese, "Dynamic stall onset variation with reduced frequency for three stall mechanisms," *International Forum on Aeroelasticity and Structural Dynamic (IFASD), Como, Italy, 25-28 June*, 6 2017.

[73] J. Deparday and K. Mulleners, "Critical evolution of leading edge suction during dynamic stall," *Journal of Physics: Conference Series*, vol. 1037, p. 022017, 6 2018.

[74] A. Zanotti and G. Gibertini, "Experimental investigation of the dynamic stall phenomenon on a naca 23012 oscillating airfoil," *Proceedings of the Institution of Mechanical Engineers, Part G: Journal of Aerospace Engineering*, vol. 227, pp. 1375–1388, 2013.

[75] A. Zanotti, S. Melone, R. Nilifard, and A. D'Andrea, "Experimental-numerical investigation of a pitching airfoil in deep dynamic stall," *Proceedings of the Institution of Mechanical Engineers, Part G: Journal of Aerospace Engineering*, vol. 228, pp. 557–566, 2014.

[76] T. S. Beddoes, "Onset of leading edge separation effects under dynamic conditions and low Mach number," *34th Annual National Forum of the American Helicopter Society, Washington D.C., May 15-17*, 1978.

[77] P. B. Martin, K. W. McAlister, M. S. Chandrasekhara, and W. Geissler, "Dynamic stall measurements and computations for a vr-12 airfoil with a variable droop leading edge," *American Helicopter Society 59th Annual Forum, Phoenix, Arizona, May 6 – 8*, 2003.

[78] W. Geißler, G. Dietz, H. Mai, J. Bosbach, and H. Richard, "Dynamic stall and its passive control investigations on the oa209 airfoil section," *31th European Rotorcraft Forum, 13-15 September, Florence, Italy*, 2005.

[79] H. F. Müller-Vahl, C. Strangfeld, C. N. Nayeri, C. O. Paschereit, and D. Greenblatt, "Control of thick airfoil, deep dynamic stall using steady blowing," *AIAA Journal*, vol. 53, pp. 277–295, 2015.

[80] P. F. Lorber, A. F. Covino, and F. O. Carta, "Dynamic stall experiments on a swept three-dimensional wing in compressible flow," *AIAA 22nd Fluid Dynamics, Plasma Dynamics and Lasers Conference*, 1991.

[81] P. F. Lorber, F. O. Carta, and A. F. Covino, "An oscillating three-dimensional wing experiment: Compressibility, sweep, rate, waveform, and geometry effects on unsteady separation and dynamic stall," *UTRC Report R92-958325-6*, 1992.

[82] P. F. Lorber and F. O. Carta, “Unsteady transition measurements on a pitching three-dimensional wing,” *Fifth Symposium on Numerical and Physical Aspects of Aerodynamic Flows*, 1992.

[83] F. N. Coton and R. A. D. Galbraith, “Experimental study of dynamic stall on a finite wing,” *Aeronautical Journal*, vol. 103, pp. 229–236, 1999.

[84] F. N. Coton, R. A. Galbraith, and R. B. Green, “The effect of wing planform shape on dynamic stall,” *The Aeronautical Journal, Cambridge University Press*, vol. 105, pp. 151–159, 2001.

[85] F. N. Coton and R. A. M. Galbraith, “An examination of dynamic stall on an oscillating rectangular wing,” *21st AIAA Applied Aerodynamics Conference, Orlando, Florida, June 23-26*, 2003.

[86] A. Bauknecht, X. Wang, J. A. Faust, and I. Chopra, “Wind tunnel test of a rotorcraft with lift compounding,” *Journal of the American Helicopter Society*, vol. 66, pp. 1–16, 2021.

[87] M. Bross and D. Rockwell, “Flow structure on a simultaneously pitching and rotating wing,” *Journal of Fluid Mechanics, Cambridge University Press*, vol. 756, pp. 354–383, 2014.

[88] Z. R. Carr, A. C. DeVoria, and M. J. Ringuette, “Aspect-ratio effects on rotating wings: circulation and forces,” *Journal of Fluid Mechanics, Cambridge University Press*, vol. 767, pp. 497–525, 2015.

[89] T. Schwermer, A. D. Gardner, and M. Raffel, “A novel experiment to understand the dynamic stall phenomenon in rotor axial flight,” *Journal of the American Helicopter Society*, vol. 64, pp. 1–11, 2019.

[90] ——, “Dynamic stall experiments on a rotor with high cyclic setting in axial inflow,” *The American Helicopter Society’s 73rd Annual Forum at the Fort Worth Convention Center, Fort Worth, Texas, USA, May 9-11*, 2017.

[91] M. M. Müller, T. Schwermer, H. Mai, and C. Stieg, “Development of an innovative double-swept rotor blade tip for the rotor test facility goettingen,” *DLRK 2018 - Deutscher Luft- und Raumfahrtkongress*, 2018.

[92] M. Müller, “Untersuchung der dreidimensionalen dynamischen Strömungsablösung an Rotorblättern,” *DLR-Interner Bericht. DLR-IB-AE-GO-2021-64*, 2021.

[93] M. Raffel, F. D. Gregorio, K. D. Groot, O. Schneider, W. Sheng, G. Gibertini, and A. Seraudie, “On the generation of a helicopter aerodynamic database,” *The Aeronautical Journal*, vol. 115, pp. 103–112, 2011.

[94] D. Petot, G. Arnaud, R. Harrison, J. Stevens, O. Dieterich, B. G. V. D. Wall, C. Young, and E. Széchényi, “Stall effects and blade torsion - an evaluation of predictive tools,” *Journal of the American Helicopter Society*, vol. 44, pp. 320–331, 1999.

[95] F. Richez, R. Jain, M. Smith, A. Grubb, and C. Castells, “Validation and analysis of aeroelastic simulations of the UH-60A rotor from pre- to post-stall flight conditions,” *Vertical Flight Society’s 76th Annual Forum, Virtual, Oct. 5-8*, 2020.

[96] J. Letzgus, M. Keßler, and E. Krämer, “Simulation of dynamic stall on an elastic rotor in high-speed turn flight,” *Journal of the American Helicopter Society*, vol. 65, p. 22002, 2020.

[97] A. D. Gardner, C. C. Wolf, and M. Raffel, “Review of measurement techniques for unsteady helicopter rotor flows,” *Progress in Aerospace Sciences*, vol. 111, 11 2019.

[98] ——, “A new method of dynamic and static stall detection using infrared thermography,” *Experiments in Fluids*, vol. 57, p. 149, 2016.

[99] A. D. Gardner and K. Richter, “Boundary layer transition determination for periodic and static flows using phase-averaged pressure data,” *Experiments in Fluids*, vol. 56, pp. 1–13, 2015.

[100] A. D. Gardner, C. Eder, C. C. Wolf, and M. Raffel, “Analysis of differential infrared thermography for boundary layer transition detection,” *Experiments in Fluids*, vol. 58, p. 122, 2017.

[101] A. Gardner, C. Wolf, and M. Raffel, “Review of measurement techniques for unsteady helicopter rotor flows,” *Progress in Aerospace Sciences*, vol. 111, p. 100566, 2019.

[102] P. J. Ansell and K. Mulleners, “Multiscale vortex characteristics of dynamic stall from empirical mode decomposition,” *AIAA Journal*, vol. 58, pp. 600–617, 2020.

[103] D. G. Coleman, F. O. Thomas, S. Gordeyev, and T. C. Corke, “Parametric modal decomposition of dynamic stall,” *AIAA Journal*, vol. 57, pp. 176–190, 2019.

[104] S. Mariappan, A. D. Gardner, K. Richter, and M. Raffel, “Analysis of dynamic stall using dynamic mode decomposition technique,” *AIAA Journal*, vol. 52, pp. 2427–2439, 2014.

[105] K. J. Asztalos, S. T. Dawson, and D. R. Williams, “Modeling the flow state sensitivity of actuation response on a stalled airfoil,” *AIAA Journal*, vol. 59, pp. 2901–2915, 2021.

[106] J. Kou and W. Zhang, “Data-driven modeling for unsteady aerodynamics and aeroelasticity,” *Progress in Aerospace Sciences*, vol. 125, p. 100725, 2021.

[107] K. Taira and A. G. Nair, “Network-based analysis of fluid flows: Progress and outlook,” *Progress in Aerospace Sciences*, vol. 131, pp. 376–421, 2022.

[108] M. Ramasamy, A. Sanayei, J. S. Wilson, P. B. Martin, T. Harms, P. Nikoueeyan, and J. Naughton, “Data-driven optimal basis clustering to characterize cycle-to-cycle variations in dynamic stall measurements,” *The Vertical Flight Society’s 75th Annual Forum, Philadelphia, Pennsylvania, May 13–16*, 2019.

[109] P. Nikoueeyan, T. Harms, J. Naughton, and V. Ahuja, “Experimental assessment of an airfoil optimized to delay the onset of dynamic stall,” *Proceedings of the Vertical Flight Society 75th Annual Forum, Philadelphia, Pennsylvania, May 13-16*, pp. 1–14, 2019.

[110] F. Richez, “Numerical analysis of dynamic stall for different helicopter rotor flight conditions,” *AHS International 73rd Annual Forum and Technology Display, Fort Worth, Texas, USA, May 9-11*, 2017.

[111] J. Hodara, A. H. Lind, A. R. Jones, and M. J. Smith, “Collaborative investigation of the aerodynamic behavior of airfoils in reverse flow,” *Journal of the American Helicopter Society*, vol. 61, p. 32001, 2016.

[112] A. Klein, K. Richter, A. Gardner, A. Altmikus, T. Lutz, and E. Krämer, “Numerical comparison of dynamic stall for 2d airfoils and an airfoils model in the dnw-twg,” *37th European Rotorcraft Forum, Vergiate and Gallarate, Italy, September 13-15*, 2011.

[113] R. Nilifard, A. Zanotti, G. Gibertini, A. Guardone, and G. Quaranta, “Numerical investigation of three-dimensional effects on deep dynamic stall experiments,” *71st American Helicopter Society International Annual Forum, Virginia Beach, VA, USA, May 5-7*, 2015.

[114] A. Spentzos, G. Barakos, K. Badcock, B. Richards, P. Wernert, S. Schreck, and M. Raffel, “Investigation of three-dimensional dynamic stall using computational fluid dynamics,” *AIAA Journal*, vol. 43, pp. 1023–1033, 2005.

[115] K. Kaufmann, M. Costes, F. Richez, A. D. Gardner, and A. L. Pape, “Numerical investigation of three-dimensional dynamic stall on an oscillating finite wing,” *AHS 70th Annual Forum, Montréal, Québec, Canada, May 20-22*, 5 2014.

[116] A. D. Gardner and K. Richter, “Influence of rotation on dynamic stall,” *American Helicopter Society 68th Annual Forum, Fort Worth Convention Center, Fort Worth, Texas, May 1-3*, 2012.

[117] Y. Ruan and M. Hajek, “Numerical investigation of dynamic stall on a single rotating blade,” *Aerospace*, vol. 8, pp. 1–27, 2021.

[118] Y. Ruan, “Numerical investigation of dynamic stall on a retreating helicopter blade,” *Dissertation, Technical University of Munich*, 2022.

[119] J. Letzgus, A. D. Gardner, T. Schwermer, M. Keßler, and E. Krämer, “Numerical investigations of dynamic stall on a rotor with cyclic pitch control,” *Journal of the American Helicopter Society*, vol. 64, 1 2019.

[120] J. Letzgus, “High-fidelity simulation of dynamic stall on helicopter rotors,” *Dissertation, University of Stuttgart*, 2021.

[121] A. Weiss, C. C. Wolf, K. Kaufmann, J. N. Braukmann, J. T. Heineck, and M. Raffel, “Unsteady boundary-layer transition measurements and computations on a rotating blade under cyclic pitch conditions,” *Experiments in Fluids*, vol. 61, 2 2020.

[122] S. R. Hirshorn, “Nasa systems engineering handbook,” *National Aeronautics and Space Administration NASA Headquarters, Washington, D.C.*, 2007.

[123] A., G. Heller, E. Krämer, and C. D. Wagner, “New results in numerical and experimental fluid mechanics xiii: Contributions to the 22nd stab/dglr symposium,” *Notes on Numerical Fluid Mechanics and Multidisciplinary Design, Springer International Publishing*, 2021.

[124] W. Johnson, “Camrad ii comprehensive analytical model of rotorcraft aerodynamics and dynamics,” *Palo Alto, California*, 1994.

[125] H. Sixt, “Konzeptentwurf, Auslegung und Konstruktion von Rotormast, Lagerung und Stahlrahmengestell eines Hubschrauberrotorprüfstands,” *Master’s Thesis, Technical University of Munich*, 2017.

[126] *Mechanical vibration - Rotor balancing - Part 11: Procedures and tolerances for rotors with rigid behaviour*, ISO 21940-11:2016, 2016.

[127] V. Heuschneider, F. Berghammer, A. Abdelmoula, M. Hajek, and J. Sirohi, “Model based blade attachment stiffness evaluation of the merit rotor in hover with photogrammetry and digital image correlation,” *The Vertical Flight Society’s 78th Annual Forum, Ft. Worth, Texas, May 10-12*, 2022.

[128] K. Strohrmann, N. André, and M. Hajek, “Hybrid natural fiber composites in a helicopter cabin door-mechanical properties and ecological efficiency,” *AIAA SciTech, San Diego, CA, USA*, 2019.

[129] T. Pflumm, “Numerical and experimental structural beam analysis for the development of helicopter rotor blades,” *Dissertation, Technical University of Munich*, 2022.

[130] N. Roth, “Concept and design of a balancing device for rotor blades of the munich experimental rotor investigation testbed merit,” *Bachelor’s Thesis, Technical University of Munich*, 2020.

[131] F. Berghammer, “Modellierung und Analyse des Eigenschwingverhaltens eines Hubschrauberrotorprüfstands,” *Master’s Thesis, Technical University of Munich*, 2019.

[132] ——, “Modeling and finite element simulation of a helicopter rotor test rig,” *Mid Term Thesis, Technical University of Munich*, 2018.

[133] B. Sosa, “Real-time sensor data acquisition and synchronization for the rotor test rig merit,” *Mid Term Thesis, Technical University of Munich*, 2021.

[134] HBK, “Strain gauge installation on fiber-reinforced plastics,” https://www.hbm.com/en/3180/tips-and-tricks-strain-gage-installation-on-fiber-reinforced-plastics/, 2008, [Online; accessed 01-May-2023].

[135] L. Gaugelhofer, “Hybrid experimental measurement of sectional stiffness properties of a com-posite rotor blade with digital image correlation,” *Master’s Thesis, Technical University of Munich*, 2020.

[136] M. T. Heath, "Chapter 2: Systems of linear equations," *Classics in Applied Mathematics*, pp. 48–103, 11 2018.

[137] C. G. Cameron, "Comprehensive aeromechanical measurements of a model-scale, coaxial, counter-rotating rotor system," *Dissertation, The University of Texas at Austin*, 2016.

[138] M. Grabe, "Measurement uncertainties in science and technology: Second edition," *Springer International Publishing*, vol. 9783319048888, pp. 1–401, 2014.

[139] S. V. Gupta, *Measurement Uncertainties - Physical Parameters and Calibration of Instruments*. Springer-Verlag Berlin Heidelberg, 2012.

[140] A. E. Fridman, "The quality of measurements - a metrological reference," *Springer Science and Business Media, LLC*, 2012.

[141] D., T. Gerhold, , and V. S. Hannemann, "On the validation of the dlr-tau code, new results in numerical and experimental fluid mechanics ii," *Springer Vieweg*, pp. 426–433, 1999.

[142] P. Spalart and S. Allmaras, "A one-equation turbulence model for aerodynamic flows," in *30th Aerospace Sciences Meeting and Exhibit*. Reno, NV, USA: AIAA, 1992.

[143] D. Komp, S. Kumar, M. Hajek, and J. Rauleder, "Effect of active camber morphing on rotor performance and control loads," *Aerospace Science and Technology*, vol. 108, p. 106311, 2021.

[144] T. Pflumm, W. Garre, and M. Hajek, "A preprocessor for parametric composite rotor blade cross-sections," *44th European Rotorcraft Forum, Delft, The Netherlands, September 18-21*, 2018.

[145] C. Cesnik and D. Hodges, "Vabs: A new concept for composite rotor blade cross-sectional modeling," in *American Helicopter Society 51st Annual Forum*. The American Helicoper Society, 1995.

[146] W. Johnson, "Rotorcraft aeromechanics," *Cambridge University Press*, 2013.

[147] A. Barth, K. Kondak, and M. Hajek, "Design, analysis and flight testing of a high altitude synchropter uav," *American Helicopter Society 74th Annual Forum, Phoenix, AZ, May 14-17*, 2018.

[148] W. Sutherland, "The viscosity of gases and molecular force," *The London, Edinburgh, and Dublin Philosophical Magazine and Journal of Science*, vol. 36, pp. 507–531, 1893.

[149] A. U. Barth, "Auslegung, Simulation, Bau und Flugerprobung eines unbemannten, elektrischen Hubschraubers mit kämmenden Rotoren für extreme Flughöhen," *Dissertation, Technical University of Munich*, 2020.

[150] T. Pflumm, A. Barth, K. Kondak, and M. Hajek, "Auslegung und konstruktion eines hauptrotorblattes für ein in extremen flughöhen operierendes drehflügel-uav," *Deutscher Luft- und Raumfahrtkongress, Rostock, Germany*, 2015.

[151] V. Heuschneider, I. Yavrucuk, and M. Hajek, “Structural blade loads of a mach-scaled rotor during dynamic stall in hover,” in *The Vertical Flight Society ´s 80th Annual Forum and Technology Display, Montréal, Québec, Canada, May 7-9*, 2024.

[152] M. Mitropoulos, V. Heuschneider, A. Barth, and I. Yavrucuk, “Experimental whirl tower tests approaching and surpassing stall for a variety of tip speeds and rotor blades,” in *The Vertical Flight Society ´s 80th Annual Forum and Technology Display, Montréal, Québec, Canada, May 7-9*, 2024.

[153] M. Ramasamy, J. S. Wilson, W. J. Mccroskey, and P. B. Martin, “Characterizing cycle-to-cycle variations in dynamic stall measurements,” *Journal of the American Helicopter Society*, vol. 63, p. 22002, 2018.

[154] J. Sangwan, T. K. Sengupta, and P. Suchandra, “Investigation of compressibility effects on dynamic stall of pitching airfoil,” *Physics of Fluids*, vol. 29, p. 076104, 2017.

[155] K. K. Tsang, R. M. So, R. C. Leung, and X. Q. Wang, “Dynamic stall behavior from unsteady force measurements,” *Journal of Fluids and Structures*, vol. 24, pp. 129–150, 2008.

[156] M. Ramasamy, R. Jain, and T. R. Norman, “Data-driven analysis of cycle-to-cycle variations, scatter, and furcation in the UH-60A wind tunnel rotor airloads measurements,” *Journal of the American Helicopter Society*, vol. 67, p. 42011, 2022.

[157] U. Diwekar and A. David, “Probability density functions and kernel density estimation,” *BONUS Algorithm for Large Scale Stochastic Nonlinear Programming Problems, Springer New York, NY*, pp. 27–34, 2015.

[158] O. A. Bauchau, “Dymore a finite element based tool for the analysis of nonlinear flexible multibody systems,” 2006.

[159] M. A. Smialy, “Analyse und Bewertung des stationären und instationären Verhaltens piezoresisti-ver Drucksensoren mit Integration in eine Rotorblattstruktur,” *Master’s Thesis, Technical University of Munich*, 2018.

[160] S. Manner, “Validierung eines hybriden Sensornetzwerks im Hubschrauberrotorblatt,” *Dissertation, Technical University of Munich*, 2016.

[161] S. Suesse and M. Hajek, “Rotor blade displacement and load estimation with fiber-optical sensors for a future health and usage monitoring system,” *American Helicopter Society 74th Annual Forum, Phoenix, AZ, USA, May 14-17*, 2018.

[162] F. Berghammer, V. Heuschneider, and M. Hajek, “Development and integration of a fiber-optical sensor system for rotor blade state observation,” *The Vertical Flight Society’s 78th Annual Forum, Ft. Worth, Texas, May 10-12*, 2022.

[163] F. Berghammer, B. Sosa, V. Heuschneider, I. Yavrucuk, and M. Hajek, “Testing of a fiber-optical sensor system for rotor blade hums,” *The Vertical Flight Society’s 79th Annual Forum, West Palm Beach, FL, USA, May 16-18*, 2023.

[164] B. Sosa, "Testing of an integrated fiber-optical sensor system for rotor blade state observation," *Master's Thesis, Technical University of Munich*, 2023.

A Tables

A.1 Mechanical Test Rig Components

Component	Installation Location	Manufacturer	Designation
Bearings			
Grooved ball bearing	Rotor shaft	*SKF*	6220-2Z
Angular contact ball bearings	Rotor shaft	*Schaeffler*	7322-B-XL-MP
Needle bearing	Blade holder	*Schaeffler*	HK4020-2RS-A-L271
Thin section bearing	Swashplate	*Silverthin*	SC 055 ARO
Grooved ball bearing	Swashplate and driver	*SKF*	626-2Z
Pivot bearing	Swashplate and driver	*Schaeffler*	GE6-PW
Swivel head	Actuator and pitch links	*Fluro*	GAXSW 8
Friction bearing	Actuator linear slide	*SKF*	PSM 121612 A51
Connecting Components			
Clamping set	Rotor head - rotor shaft	*Ringfeder*	RfN 7013.1 090x130
Coupling	Drive shaft - rotor shaft	*KTR*	Radex-N 60
Bolts	Rotor, swashplate	*Ganter*	ISO 7379 fitting screw
Sealing Components			
Radial shaft seal	Rotor shaft ball bearing	*SKF*	95X130X12 CRW1 R
O-ring seal	Spherical bearing	*HUG*	53,00 x 2,50 mm NBR70

Table A.1: Off-the-shelf mechanical components used for the rotor test rig, their installation location, manufacturer, and part number or designation

A.2 Materials and Surface Treatments

Component	Designation	Alloy	Number	Surface Treatment
Rotor				
Rotor shaft	tempered steel	42CrMo4 +QT	1.7225	nitrided
Rotor head	tempered steel	42CrMo4 +QT	1.7225	nickeled
Mounting rings	tempered steel	42CrMo4 +QT	1.7225	nickeled
Bearing sleeve	tempered steel	42CrMo4 +QT	1.7225	nickeled
Blade holder	tempered steel	42CrMo4 +QT	1.7225	nitrided, oxidized
Hall sensor holder	tempered steel	42CrMo4 +QT	1.7225	nickeled
Pitch links	tempered steel	42CrMo4 +QT	1.7225	nickeled
Tension-torsion strap	stainless feather steel	X10CrNi18-8	1.4310	-
	tempered steel	42CrMo4 +QT	1.7225	-
Swashplate				
Rotating star	aluminum	AlZn5,5MgCu	3.4365	hard-anodized
Stationary star	aluminum	AlZn5,5MgCu	3.4365	hard-anodized
Spherical sleeve	brass	CuSn8	2.1030	-
Spherical bearing	tempered steel	42CrMo4 +QT	1.7225	-
Labyrinth sealing	aluminum	AlZn5,5MgCu	3.4365	hard-anodized
Push rods	silver steel	115CrV3	1.2210	-
Drivers				
Stationary driver	aluminum	AlZn5,5MgCu	3.4365	hard-anodized
Rotating driver	aluminum	AlZn5,5MgCu	3.4365	hard-anodized
Steel Frame				
Wind tunnel adaptor	non-alloy steel	-	S355	painted
Engine cradle	non-alloy steel	-	S355	painted
Middle frame	non-alloy steel	-	S355	painted
Upper frame	non-alloy steel	-	S355	painted
Various Components				
Adapter	aluminum	AlZn5,5MgCu	3.4365	hard-anodized
Cover	aluminum	AlZn5,5MgCu	3.4365	hard-anodized
Bearing containment	aluminum	AlZn5,5MgCu	3.4365	hard-anodized

Table A.2: Materials and surface treatments of designed mechanical components used for the rotor test rig

A.3 CFD Computation Parameters

Entity	Symbol	Reference Parameter	Validation Parameter	Unit
Reference pressure	p_{ref}	101325	101325	Pa
Reference temperature	T_{ref}	288.15	288.15	K
Gas constant	κ	1.4	1.4	-
Reference Mach number	M_{ref}	0.4	0.4	-
Chord length	c	0.13	0.508	m
Reference density	ρ_{ref}	1.225	1.225	kg/m^3

Table A.3: Parameters used in the CFD calculation of the MERIT airfoil polars and the validation case

A.4 Strain Gauge Properties

		Blade root		Push rod
		LM16 Linear	**XM46 Torsion**	**LA13 Linear**
Measuring grid foil	-	Modco (CrNi)	Modco (CrNi)	Constantan
Gauge factor k	-	$2.19 \pm 1.0\%$	$2.26 \pm 1.0\%$	$2.0 \pm 1\%$
Temperature compensation	$10^{-6}/K$	0.5	0.5	23
Resistance R	Ω	$1000 \pm 0.3\%$	$1000 \pm 0.3\%$	$350 \pm 0.3\%$
Measuring grid length	mm	6	6	3
Fatigue strength, 10^7 cycles	$\mu m/m$	$\pm 2,000$	$\pm 2,000$	$\pm 1,200$
Max. elongation	$\mu m/m$	$+10,000/-15,000$	$+10,000/-15,000$	$\pm 50,000$

Table A.4: Strain gauge properties for linear and torsional sensors used on the carbon blade root and on the designed aluminum pitch link load cells

B Graphs

B.1 Tensile Strength Tests

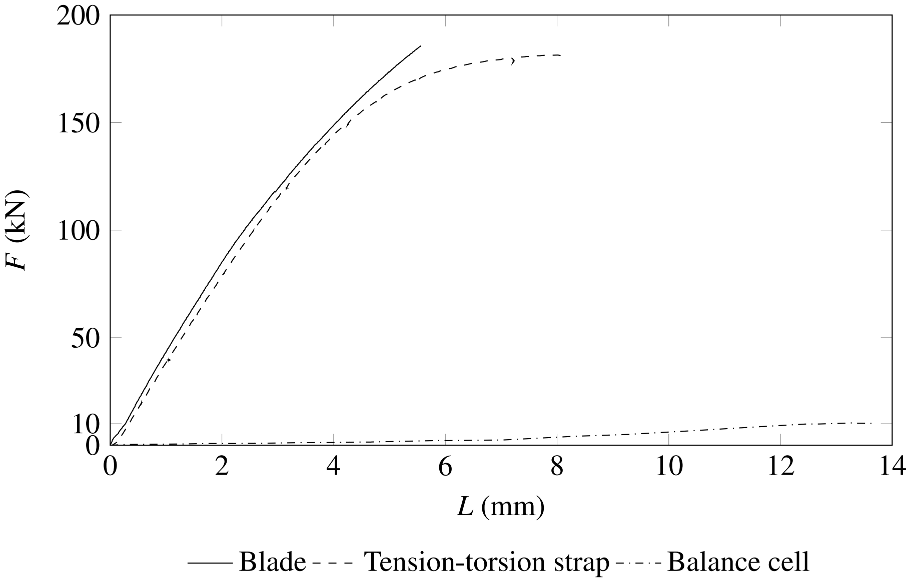

Figure B.1: Results from tensile strength tests [22]

B.2 Dynamic Stall Azimuth and Convergence Graphs

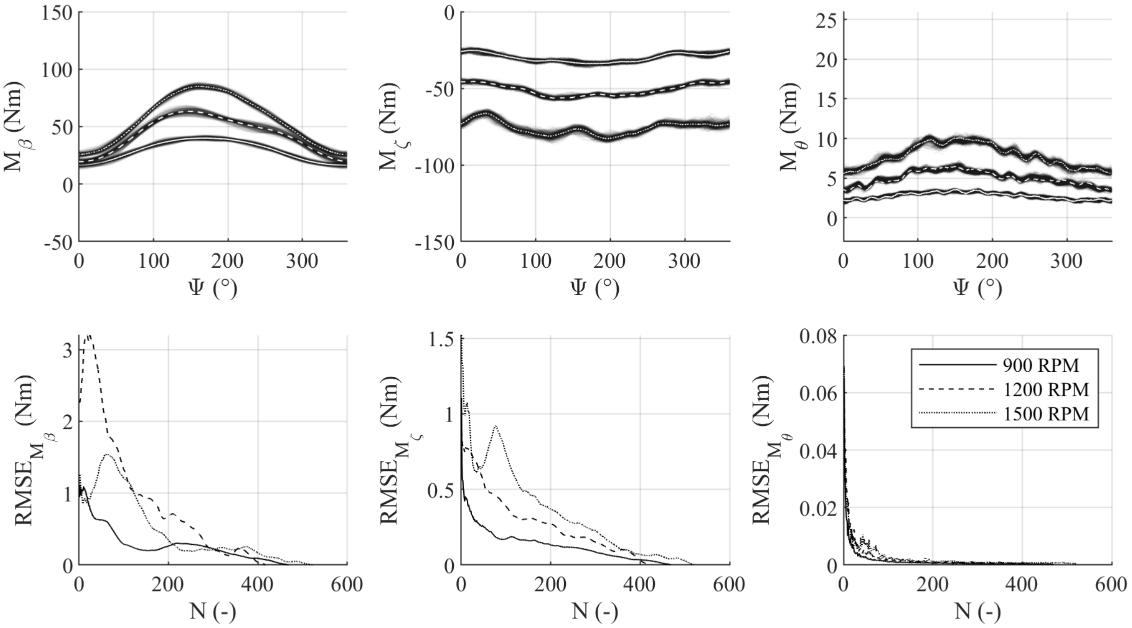

Figure B.2: Flapping, lead-lag, and torsional moment as function of rotor azimuth at 900, 1200, and 1500 RPM (upper row) and the RMSE between each revolutional data set and the phase averaged mean of the last revolutions as function of number of recorded revolutions N (lower row) for the dynamic stall case 14° ± 4°

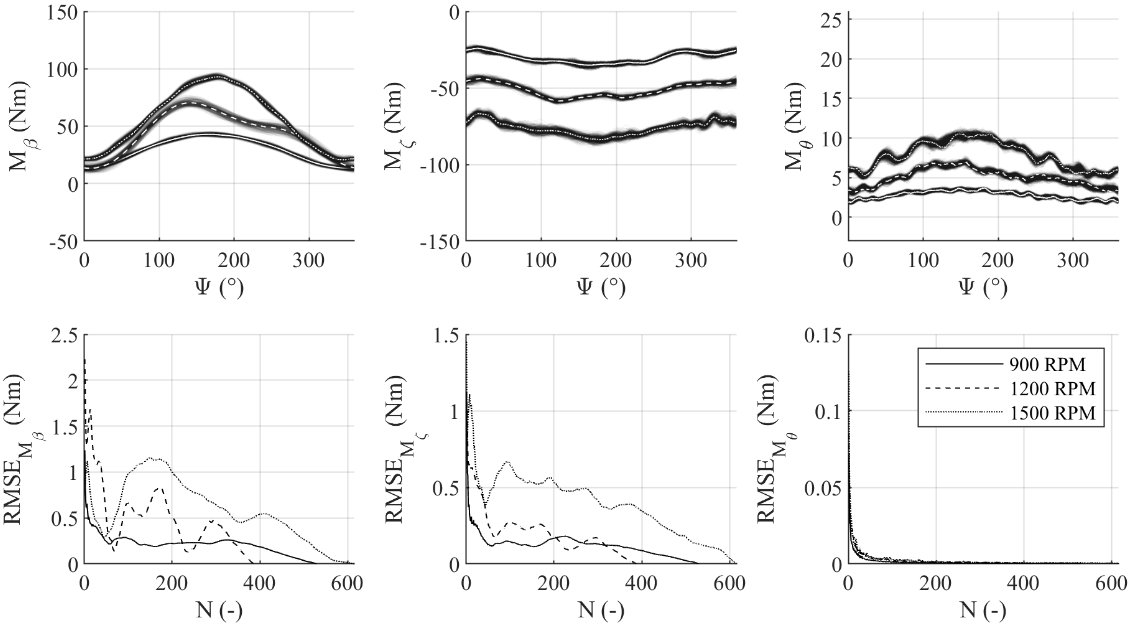

Figure B.3: Flapping, lead-lag, and torsional moment as function of rotor azimuth at 900, 1200, and 1500 RPM (upper row) and the RMSE between each revolutional data set and the phase averaged mean of the last revolutions as function of number of recorded revolutions N (lower row) for the dynamic stall case 14° ± 5°

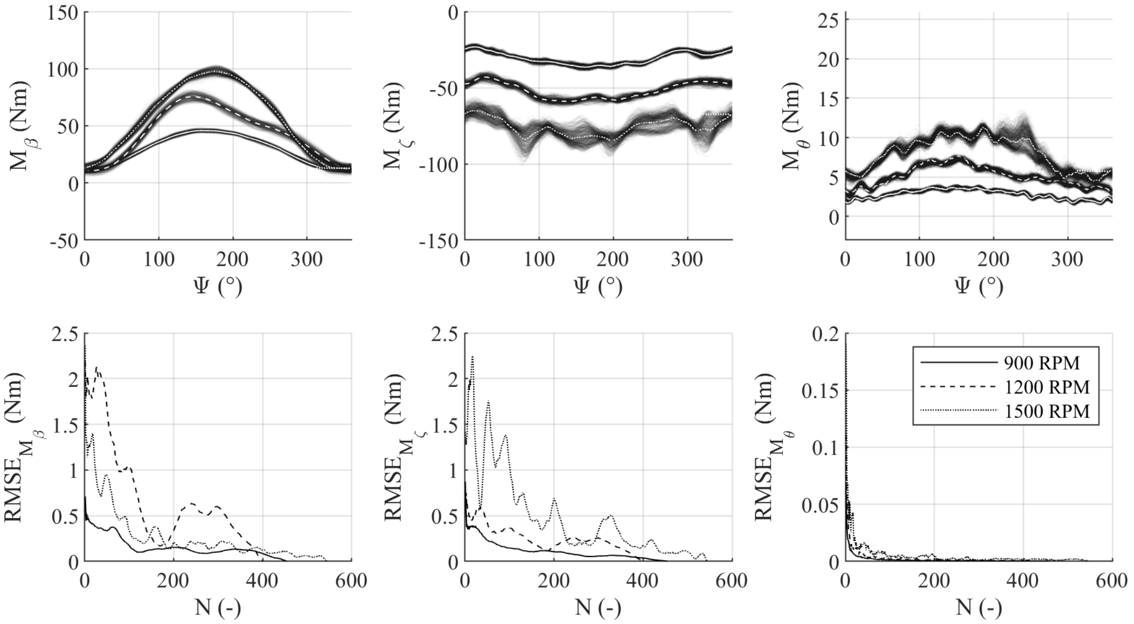

Figure B.4: Flapping, lead-lag, and torsional moment as function of rotor azimuth at 900, 1200, and 1500 RPM (upper row) and the RMSE between each revolutional data set and the phase averaged mean of the last revolutions as function of number of recorded revolutions N (lower row) for the dynamic stall case 14° ± 6°

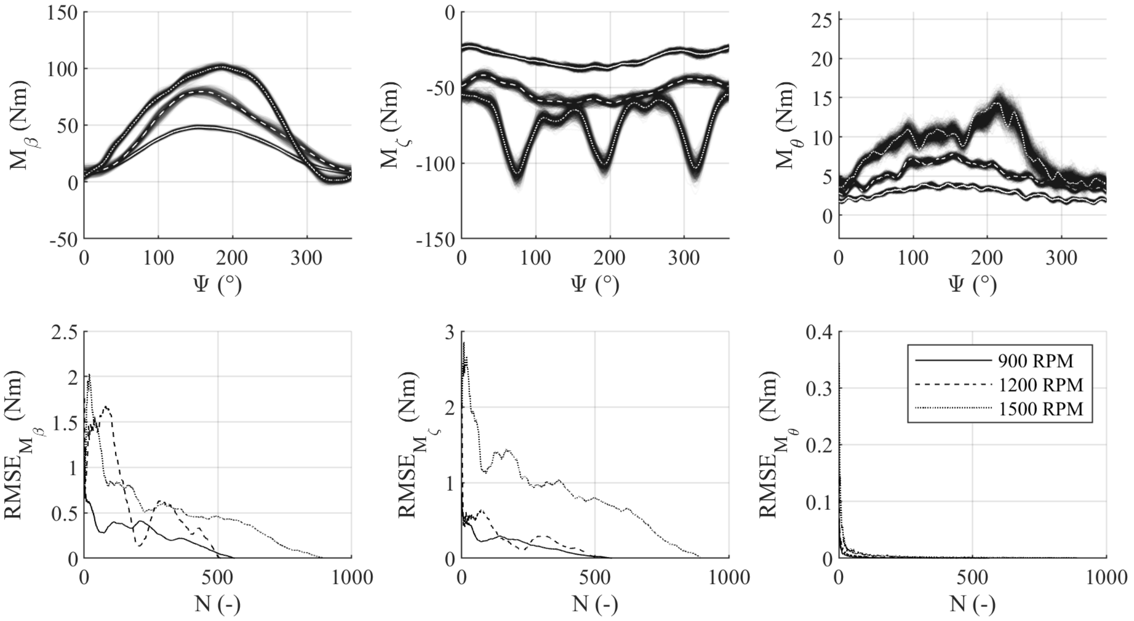

Figure B.5: Flapping, lead-lag, and torsional moment as function of rotor azimuth at 900, 1200, and 1500 RPM (upper row) and the RMSE between each revolutional data set and the phase averaged mean of the last revolutions as function of number of recorded revolutions N (lower row) for the dynamic stall case 14° ± 7°

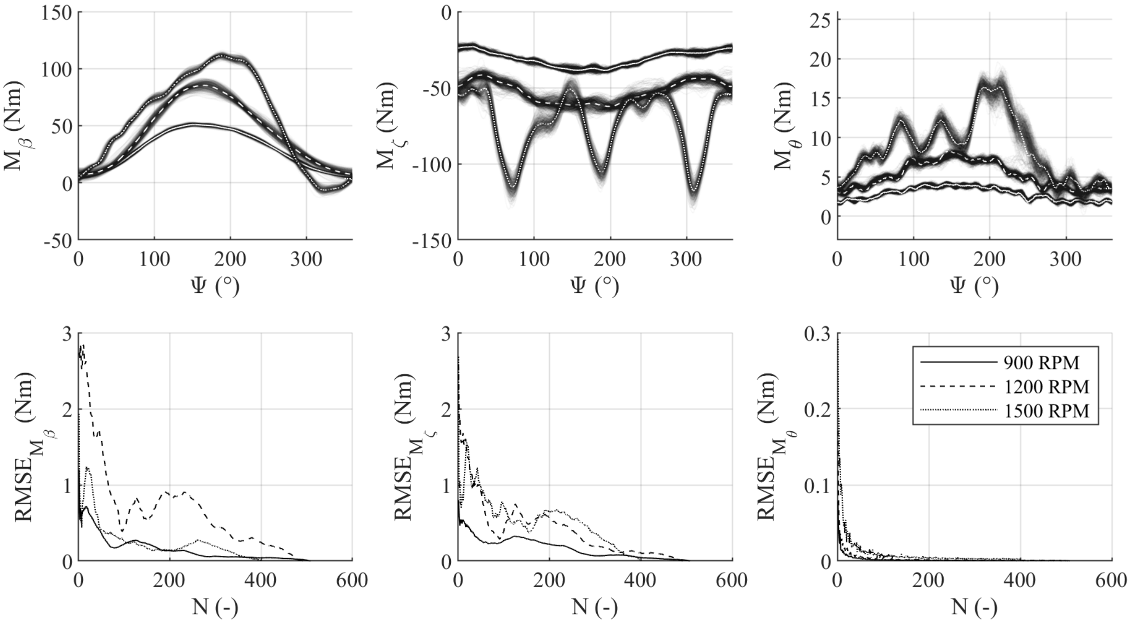

Figure B.6: Flapping, lead-lag, and torsional moment as function of rotor azimuth at 900, 1200, and 1500 RPM (upper row) and the RMSE between each revolutional data set and the phase averaged mean of the last revolutions as function of number of recorded revolutions N (lower row) for the dynamic stall case 14° ± 8°

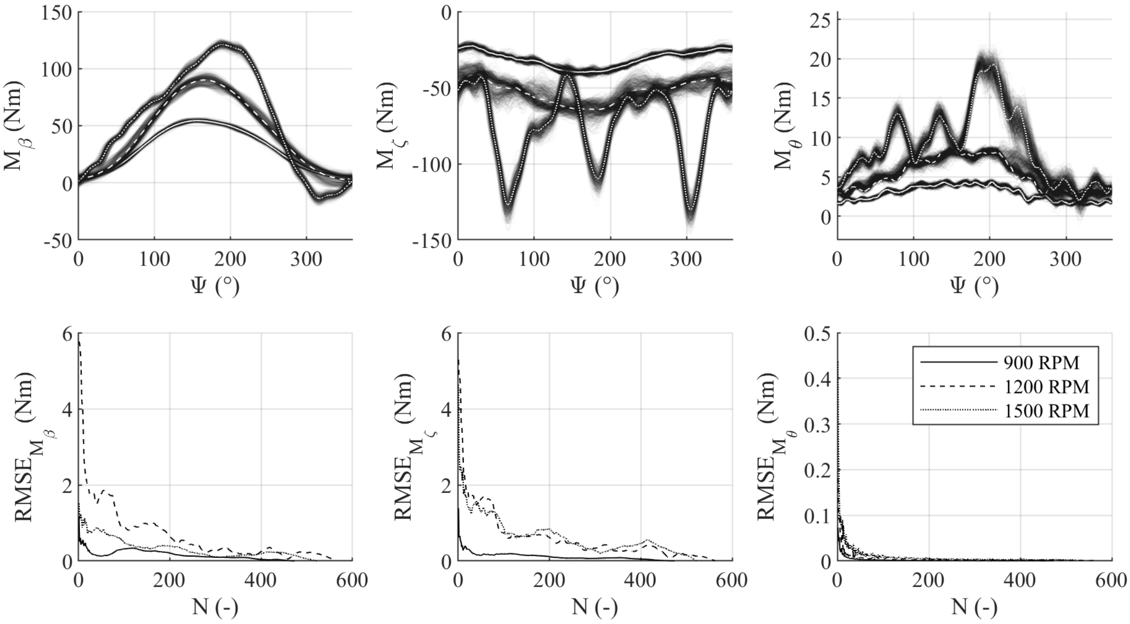

Figure B.7: Flapping, lead-lag, and torsional moment as function of rotor azimuth at 900, 1200, and 1500 RPM (upper row) and the RMSE between each revolutional data set and the phase averaged mean of the last revolutions as function of number of recorded revolutions N (lower row) for the dynamic stall case 14° ± 9°

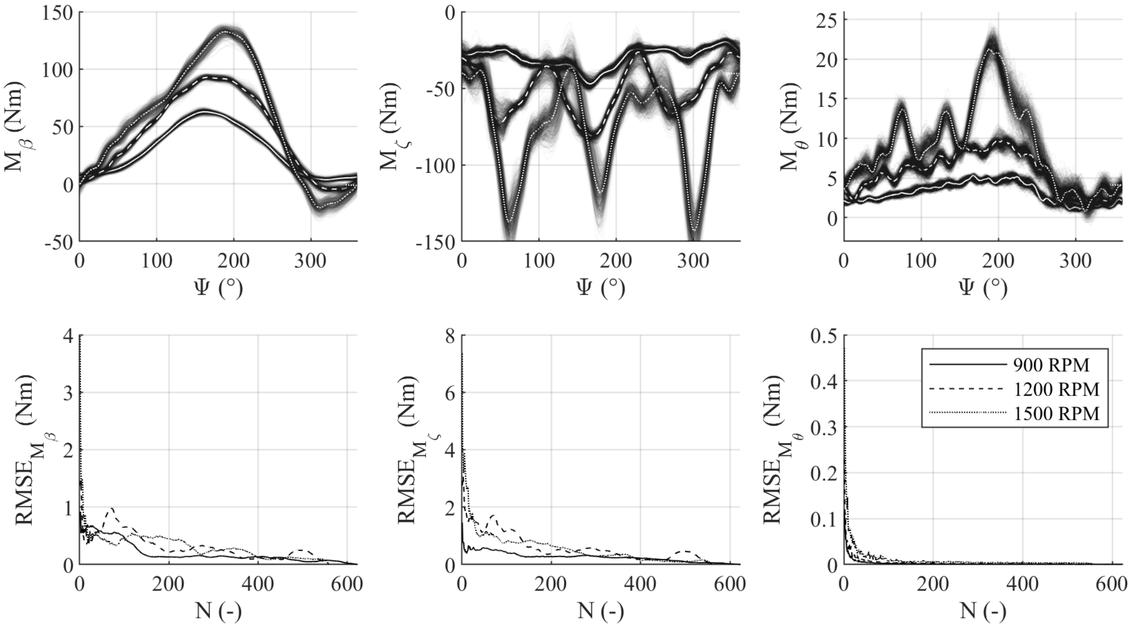

Figure B.8: Flapping, lead-lag, and torsional moment as function of rotor azimuth at 900, 1200, and 1500 RPM (upper row) and the RMSE between each revolutional data set and the phase averaged mean of the last revolutions as function of number of recorded revolutions N (lower row) for the dynamic stall case 14° ± 10°

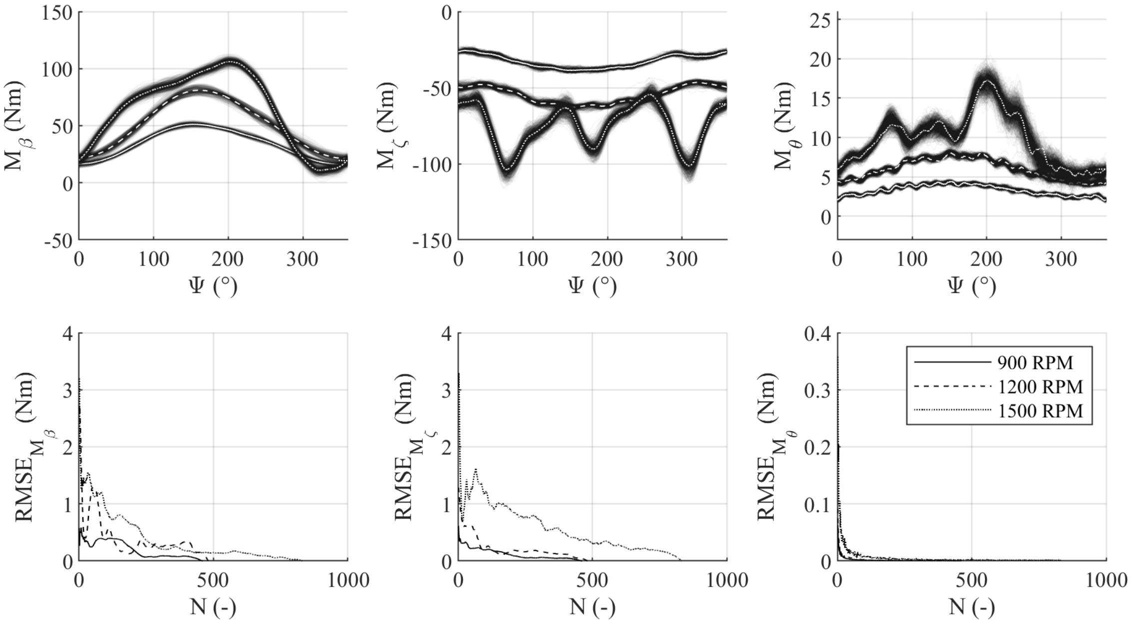

Figure B.9: Flapping, lead-lag, and torsional moment as function of rotor azimuth at 900, 1200, and 1500 RPM (upper row) and the RMSE between each revolutional data set and the phase averaged mean of the last revolutions as function of number of recorded revolutions N (lower row) for the dynamic stall case 16° ± 6°

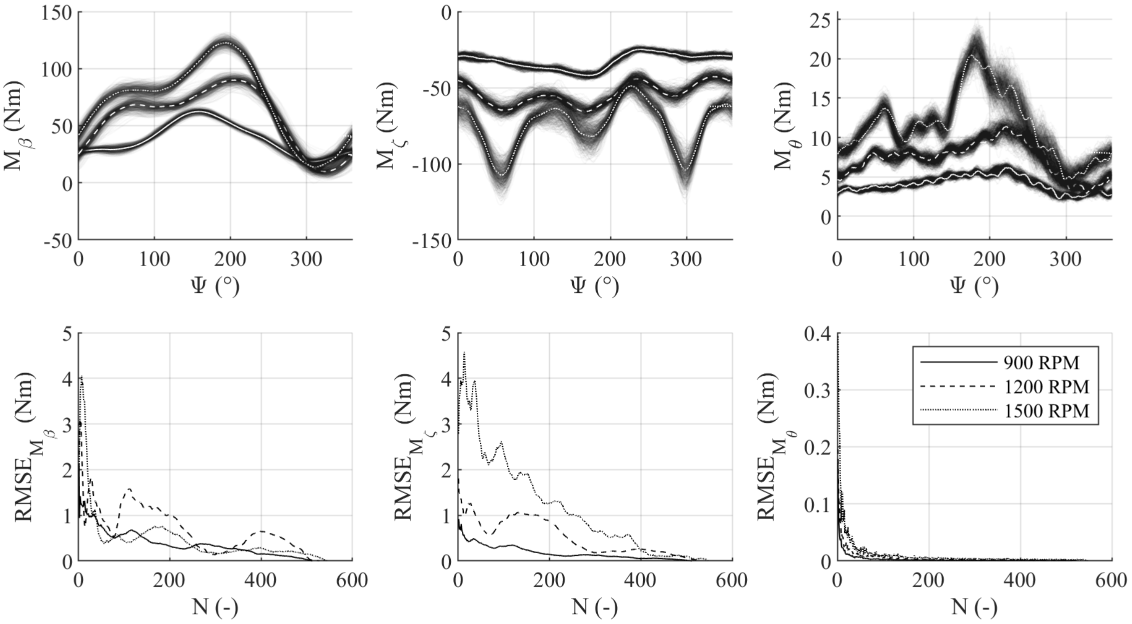

Figure B.10: Flapping, lead-lag, and torsional moment as function of rotor azimuth at 900, 1200, and 1500 RPM (upper row) and the RMSE between each revolutional data set and the phase averaged mean of the last revolutions as function of number of recorded revolutions N (lower row) for the dynamic stall case 18° ± 6°

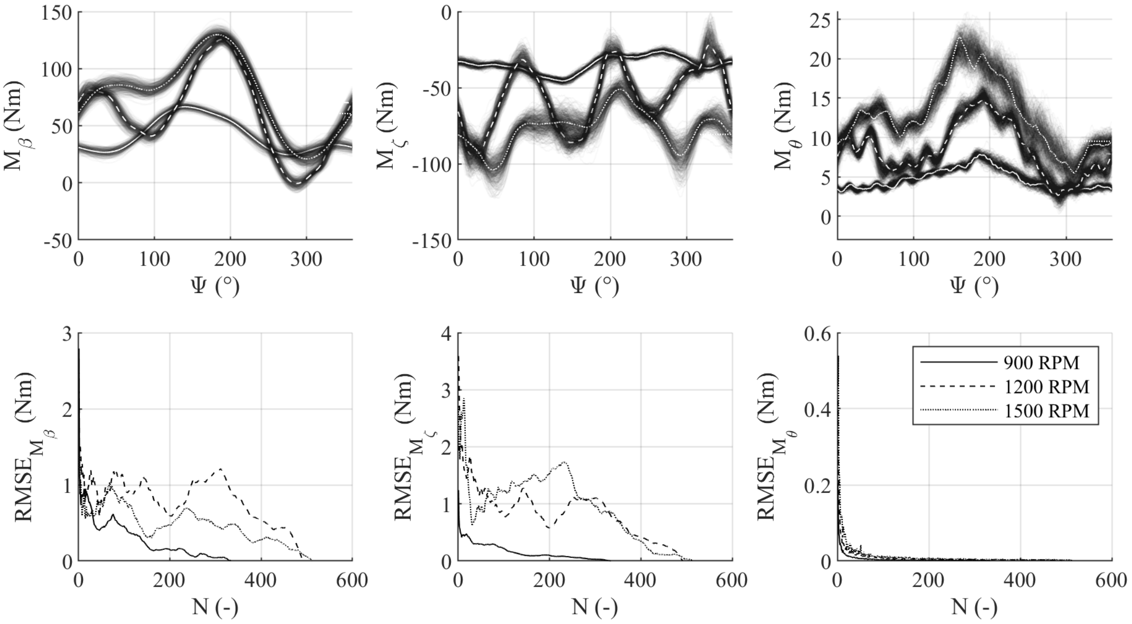

Figure B.11: Flapping, lead-lag, and torsional moment as function of rotor azimuth at 900, 1200, and 1500 RPM (upper row) and the RMSE between each revolutional data set and the phase averaged mean of the last revolutions as function of number of recorded revolutions N (lower row) for the dynamic stall case 20° ± 6°

B.3 Dynamic Stall Repeatability Check

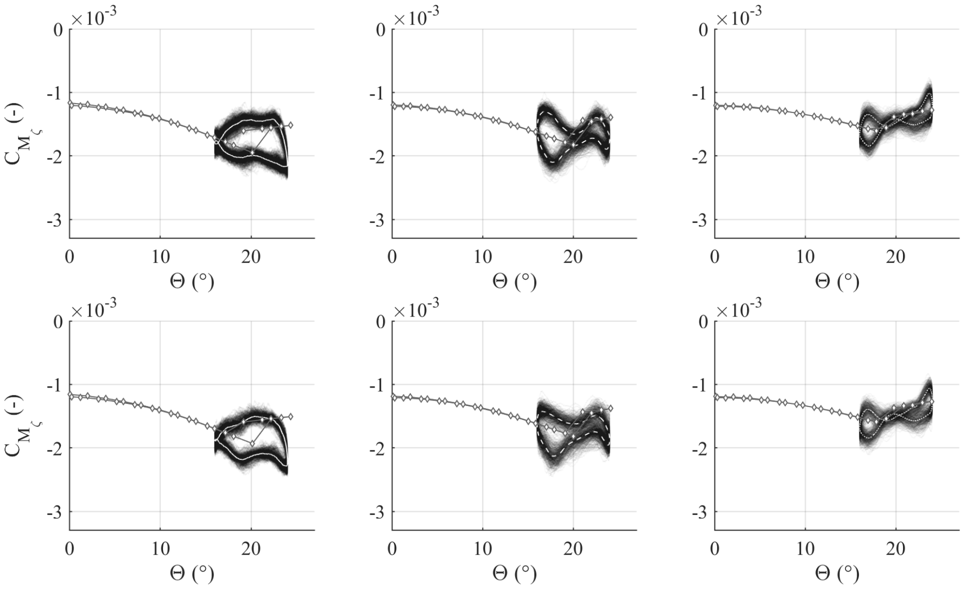

Figure B.12: Repeatability test for the dynamic stall case 20° ± 4° at 900, 1200, and 1500 RPM and the non-dimensionalized blade root lead-lag moment as a function of pitch angle; upper graphs recorded on day 1, 17.5°C, 943 hPa; lower graphs recorded on day 2, 18.2°C, 953.3 hPa.

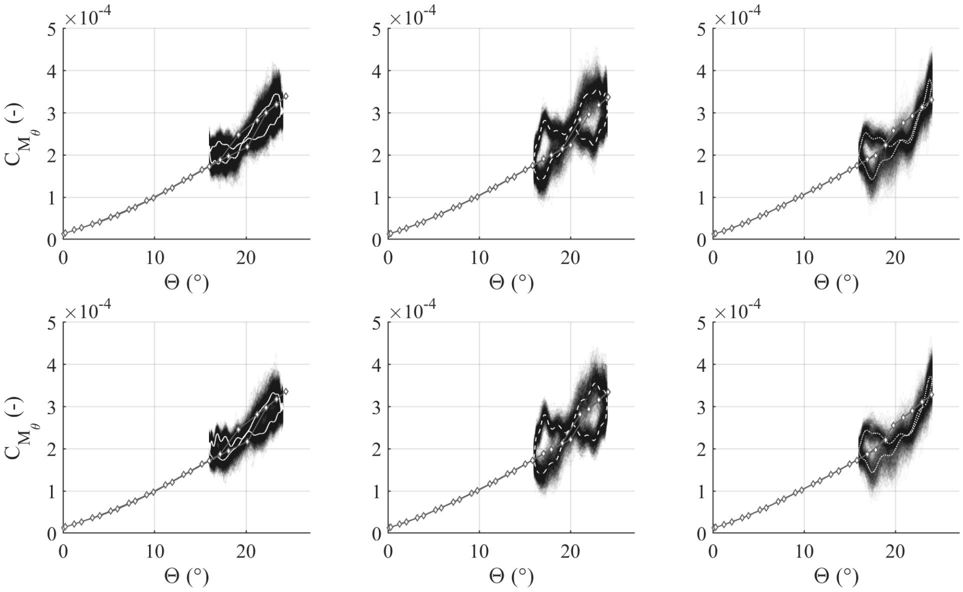

Figure B.13: Repeatability test for the dynamic stall case 20° ± 4° at 900, 1200, and 1500 RPM and the non-dimensionalized blade root torsion as a function of pitch angle; upper graphs recorded on day 1, 17.5°C, 943 hPa; lower graphs recorded on day 2, 18.2°C, 953.3 hPa.

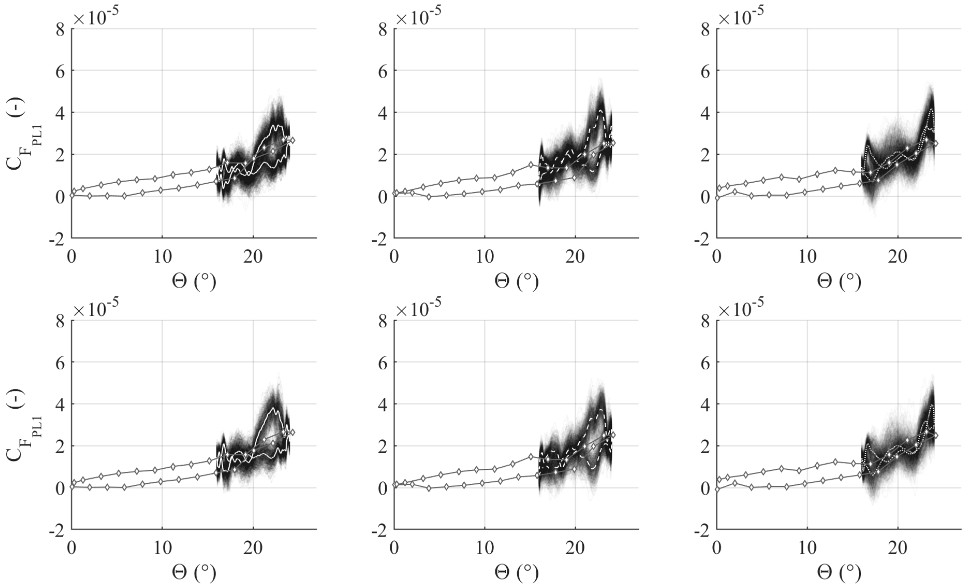

Figure B.14: Repeatability test for the dynamic stall case 20° ± 4° at 900, 1200, and 1500 RPM and the non-dimensionalized pitch link 1 force F_{PL1} as a function of pitch angle; upper graphs recorded on day 1, 17.5°C, 943 hPa; lower graphs recorded on day 2, 18.2°C, 953.3 hPa.

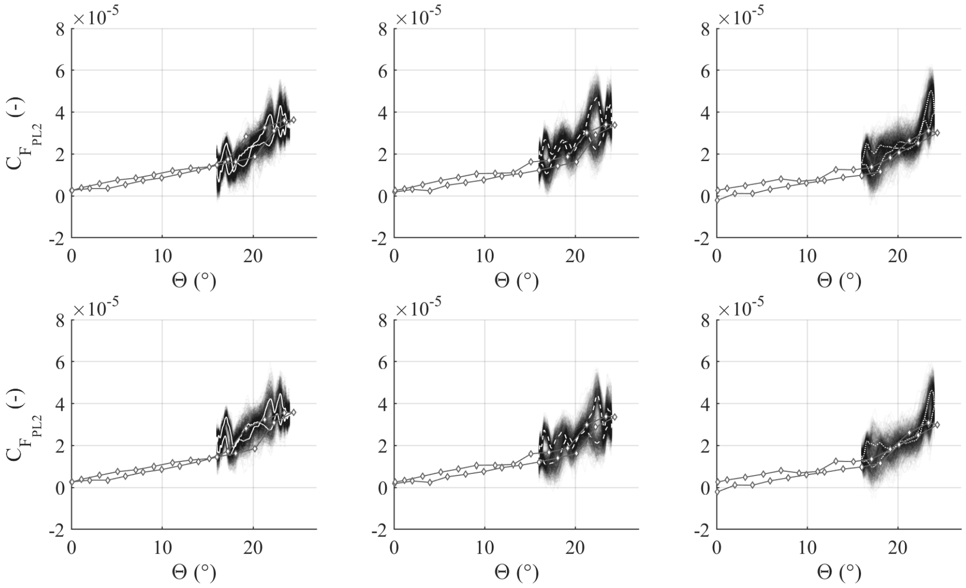

Figure B.15: Repeatability test for the dynamic stall case 20° ± 4° at 900, 1200, and 1500 RPM and the non-dimensionalized pitch link 2 force F_{PL2} as a function of pitch angle; upper graphs recorded on day 1, 17.5°C, 943 hPa; lower graphs recorded on day 2, 18.2°C, 953.3 hPa.

B.4 Dynamic Stall Graphs

B.4.1 Collective Pitch Variation

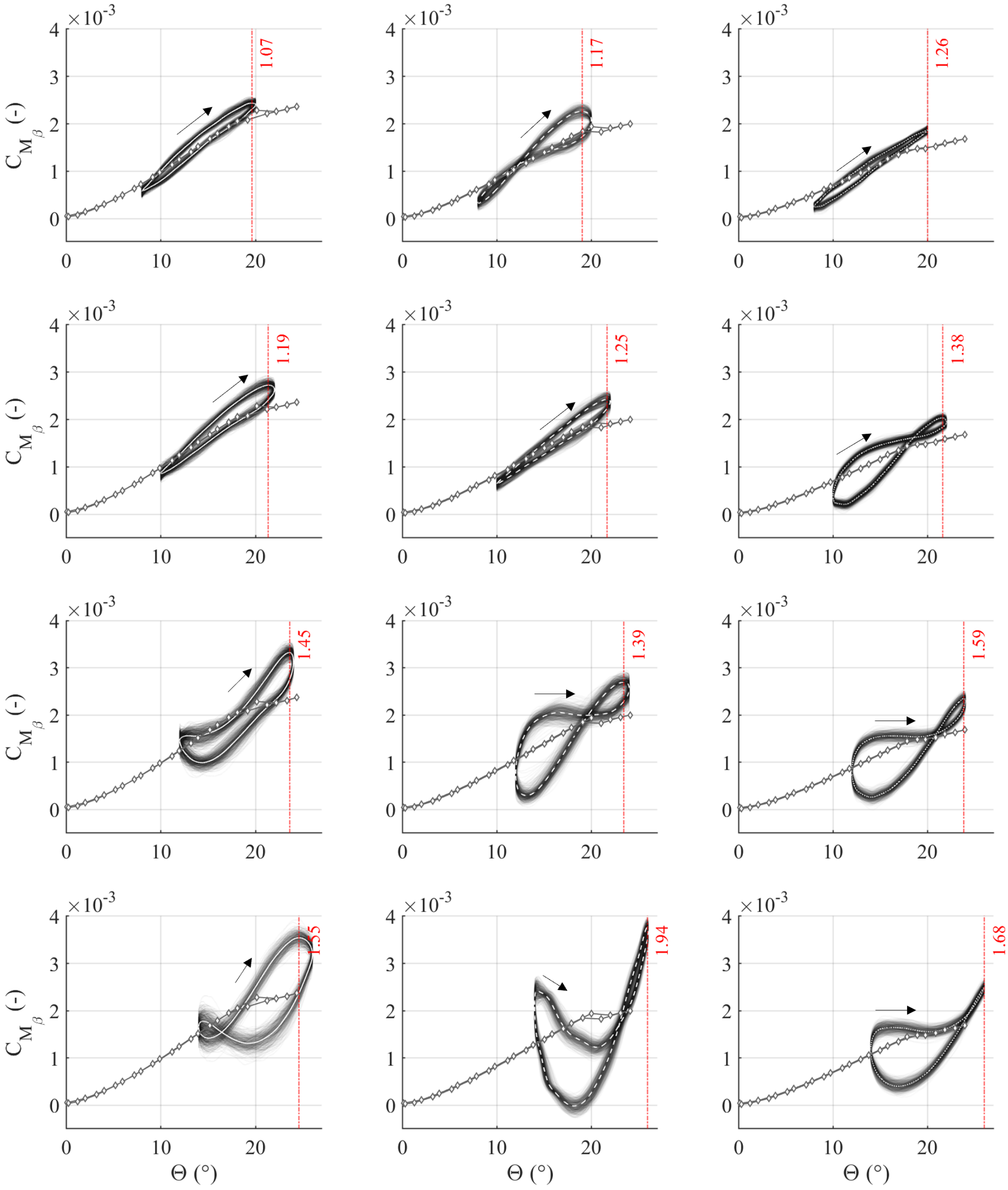

Figure B.16: Blade root flapping moments for $14, 16, 18, 20 \pm 6°$ from top to bottom at 900, 1200, 1500 RPM from left to right

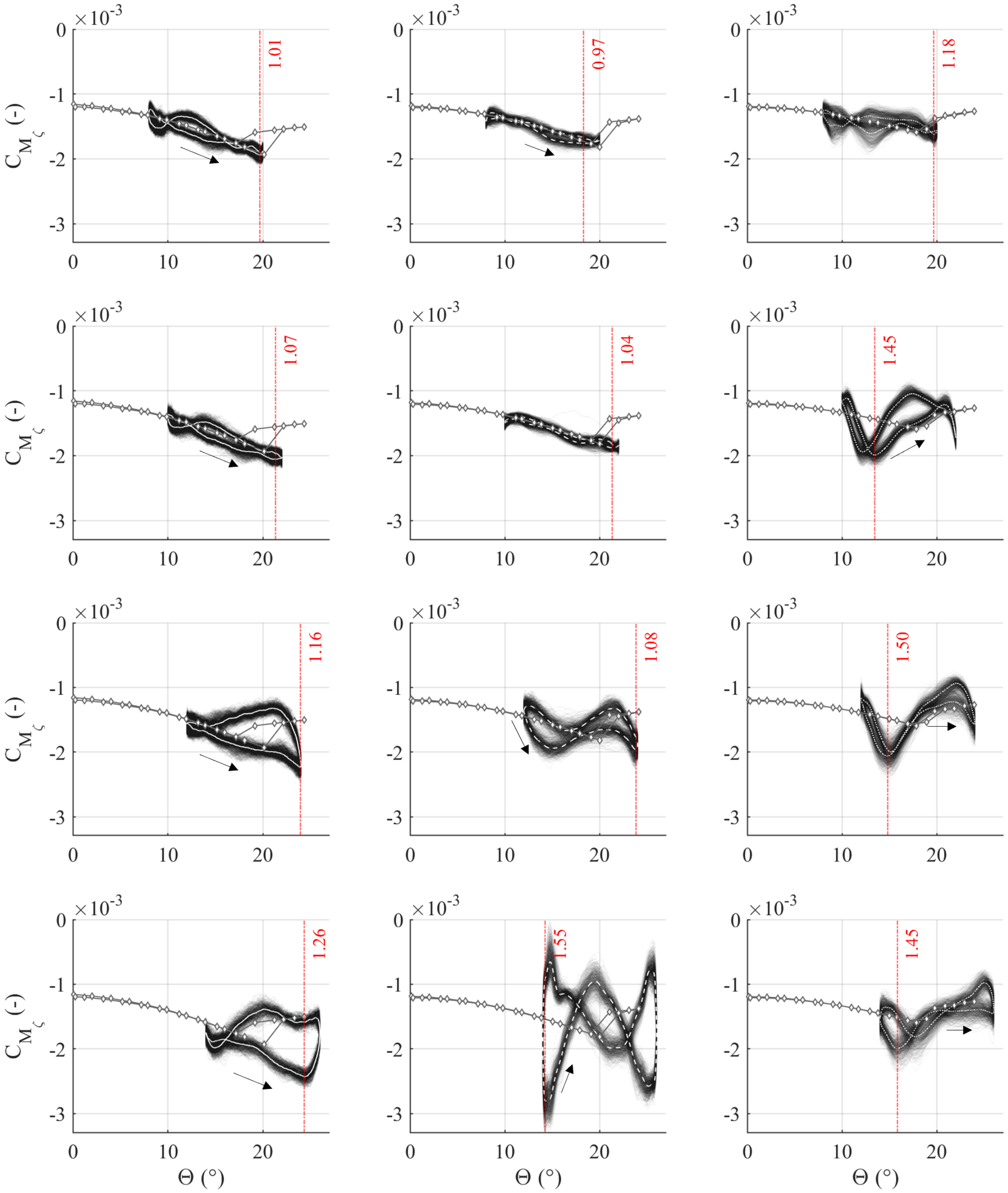

Figure B.17: Blade root lead-lag moments for 14, 16, 18, 20 ± 6° from top to bottom at 900, 1200, 1500 RPM from left to right

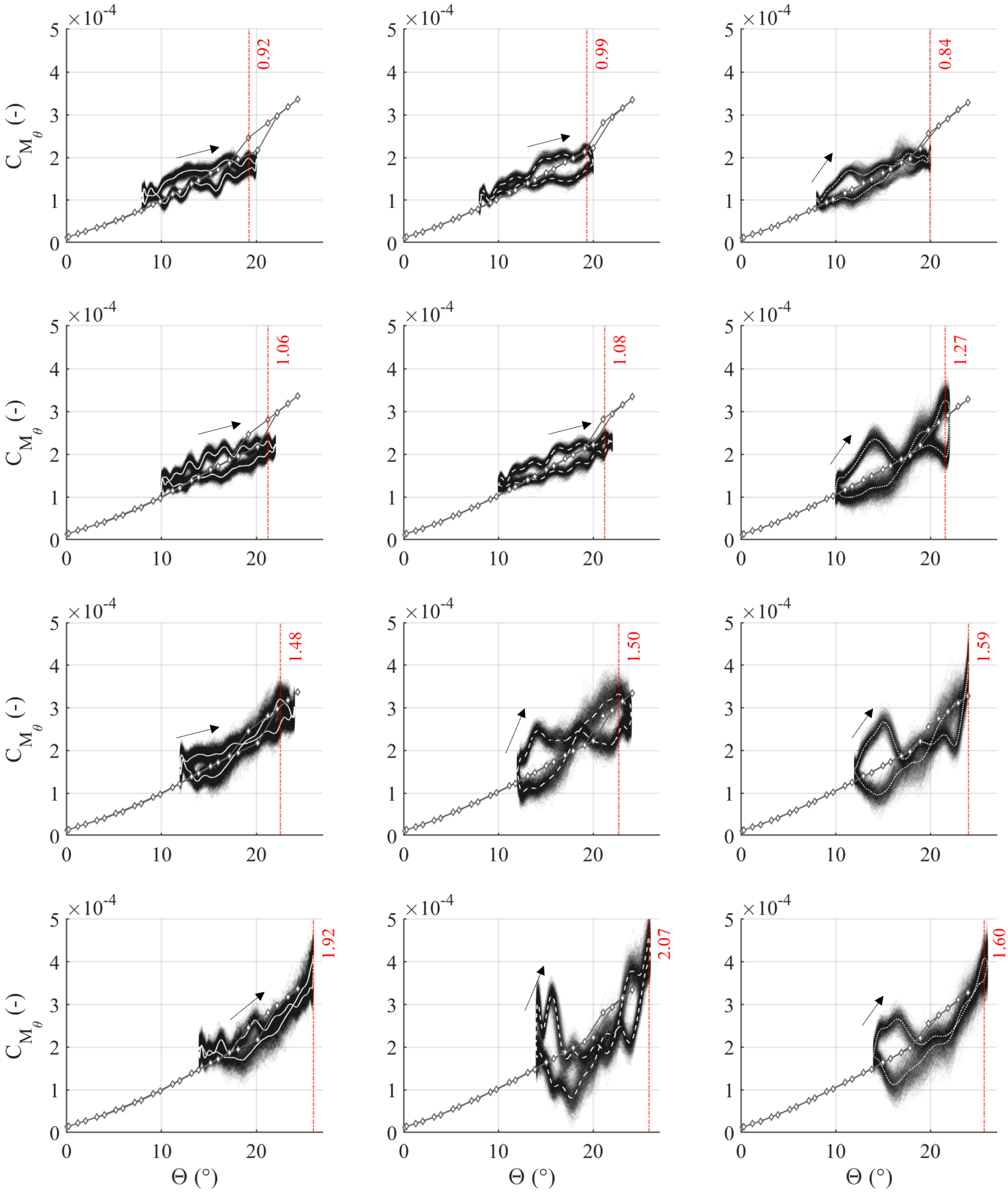

Figure B.18: Blade root torsion for $14, 16, 18, 20 \pm 6°$ from top to bottom at 900, 1200, 1500 RPM from left to right

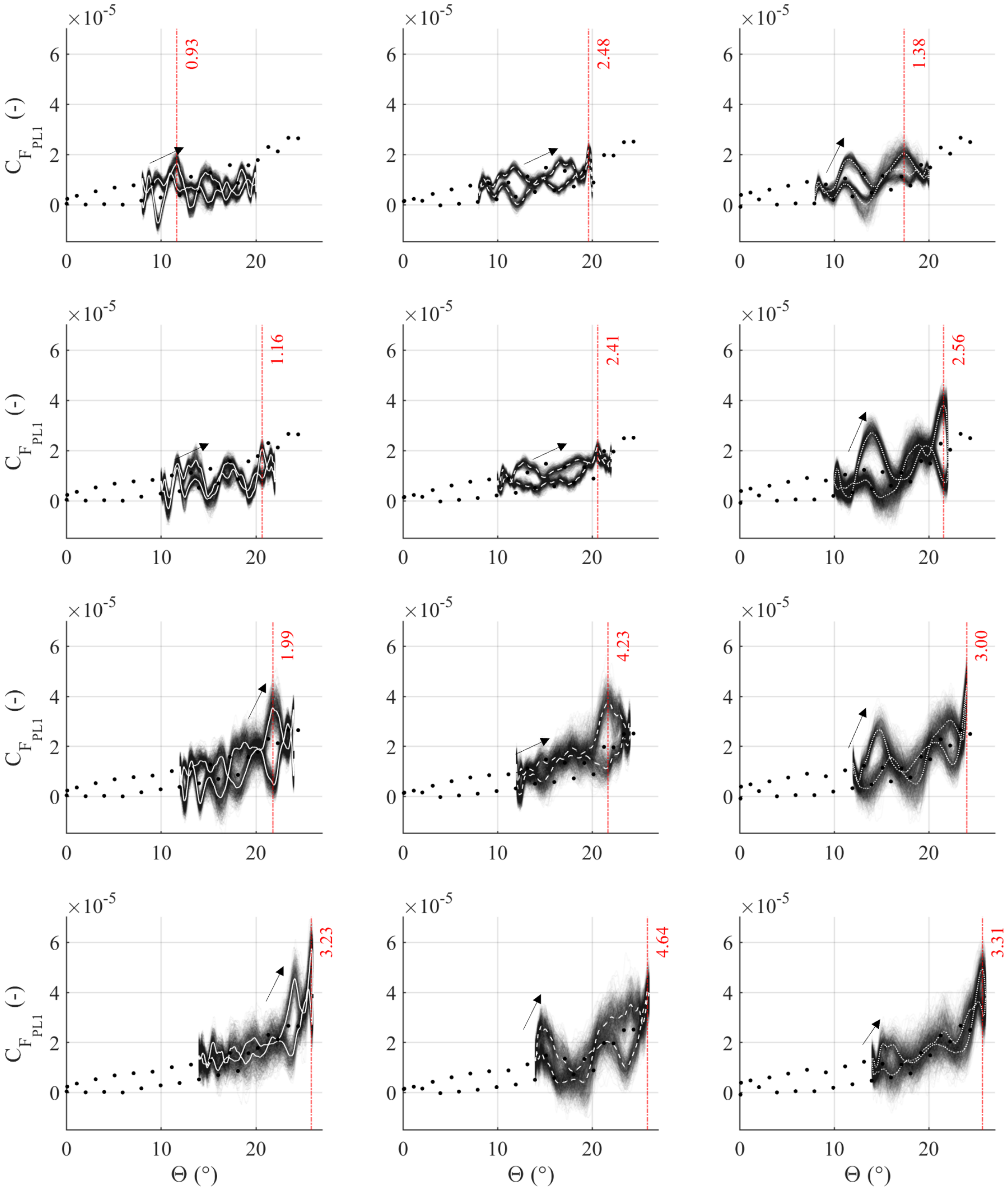

Figure B.19: Pitch link 1 force $F_{PL,1}$ for $14, 16, 18, 20 \pm 6°$ from top to bottom at 900, 1200, 1500 RPM from left to right

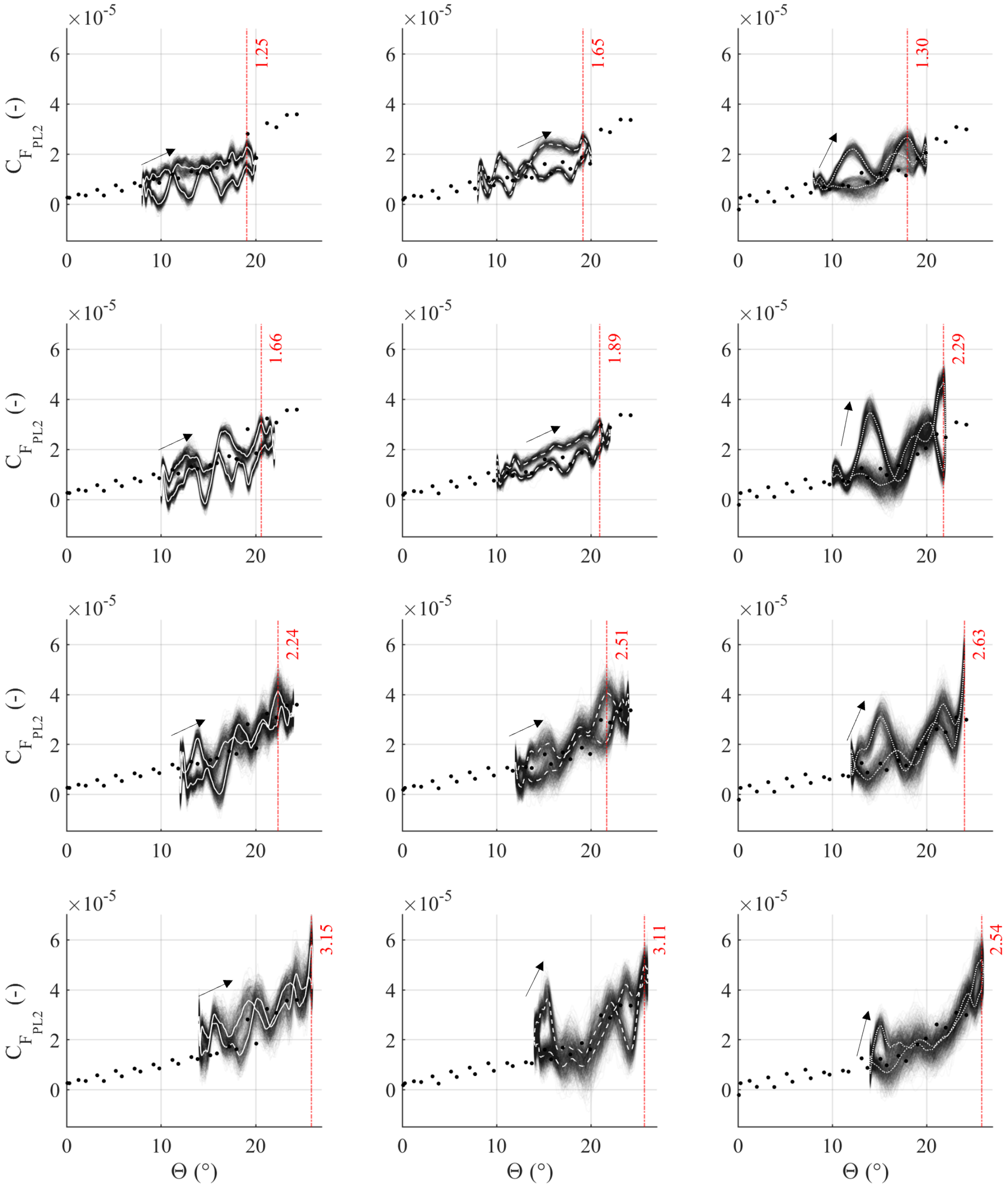

Figure B.20: Pitch link 2 force $F_{PL,2}$ for $14, 16, 18, 20 \pm 6°$ from top to bottom at 900, 1200, 1500 RPM from left to right

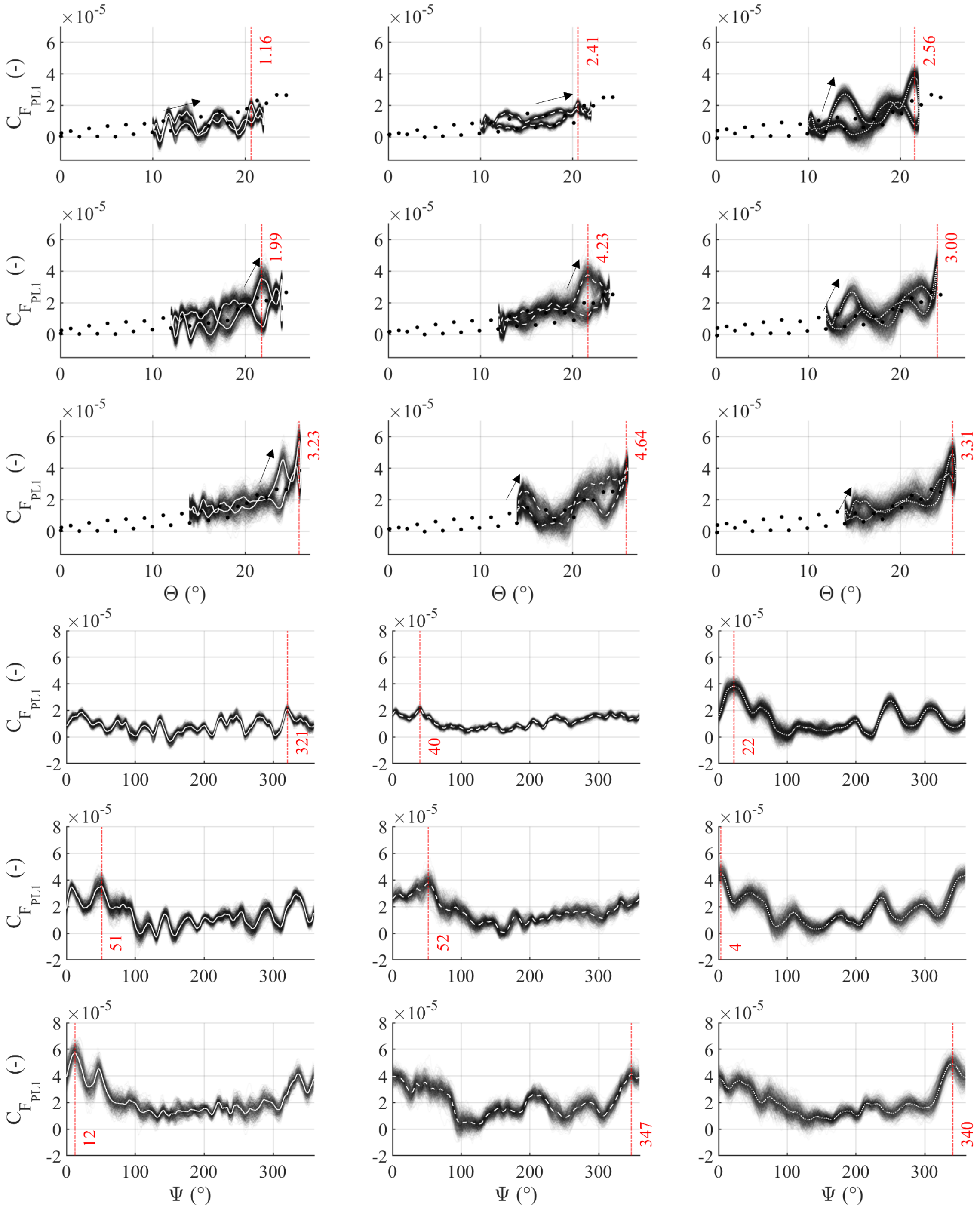

Figure B.21: Non-dimensionalized pitch link 1 force $C_{F_{PL1}}$ for three dynamic stall cases with varying collective pitch and constant cyclic pitch at $16^\circ \pm 6^\circ, 18^\circ \pm 6^\circ, 20^\circ \pm 6^\circ$ from top to bottom and 900, 1200, 1500 RPM from left to right; loads shown as a function of pitch (upper three rows) and as a function of azimuth (lower three rows)

B.4.2 Cyclic Pitch Variation

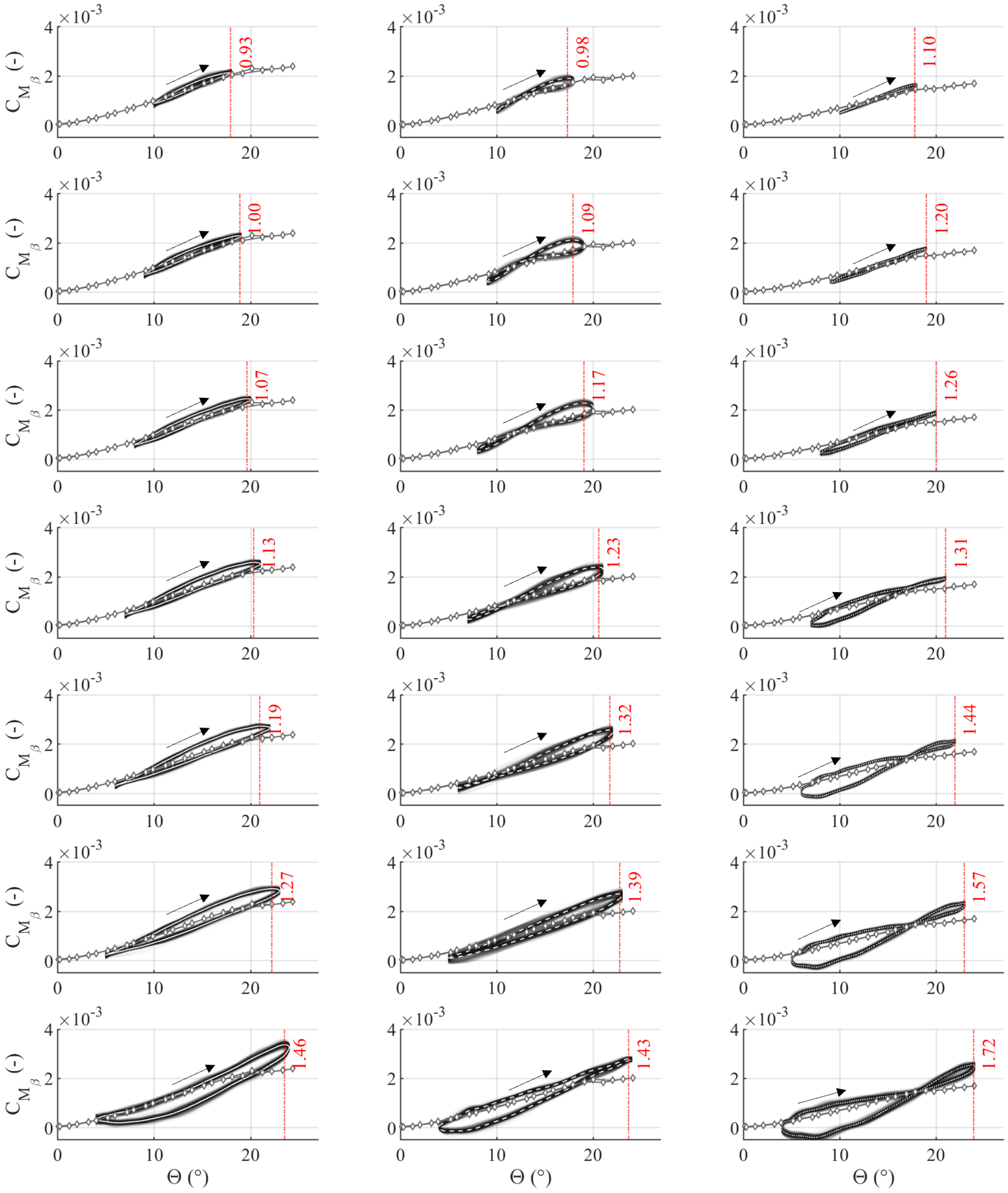

Figure B.22: Blade root flapping moment for 14 ± 4, 5, 6, 7, 8, 9, 10° from top to bottom at 900, 1200, 1500 RPM from left to right

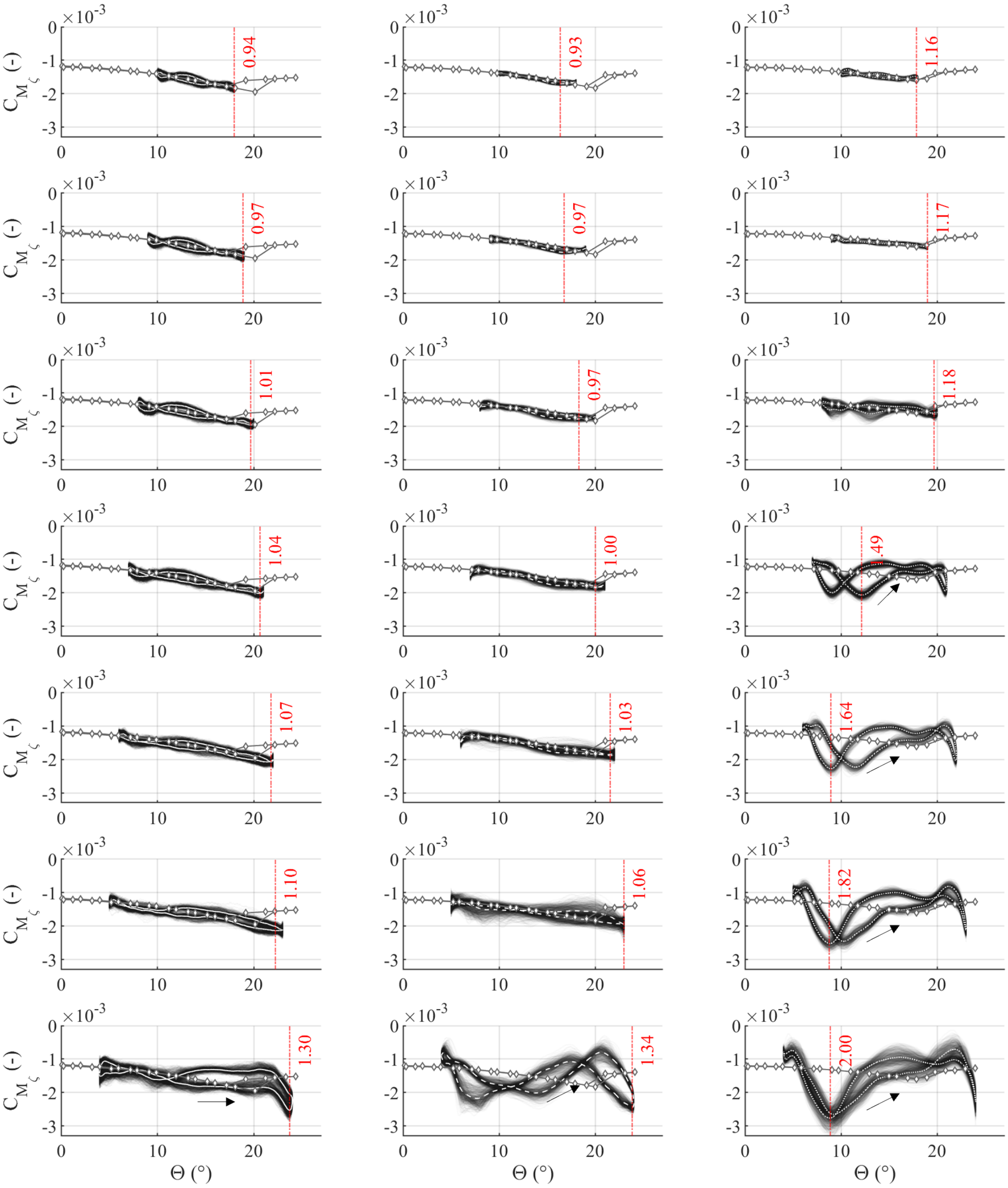

Figure B.23: Blade root lead-lag moment for $14 \pm 4, 5, 6, 7, 8, 9, 10^{\circ}$ from top to bottom at 900, 1200, 1500 RPM from left to right

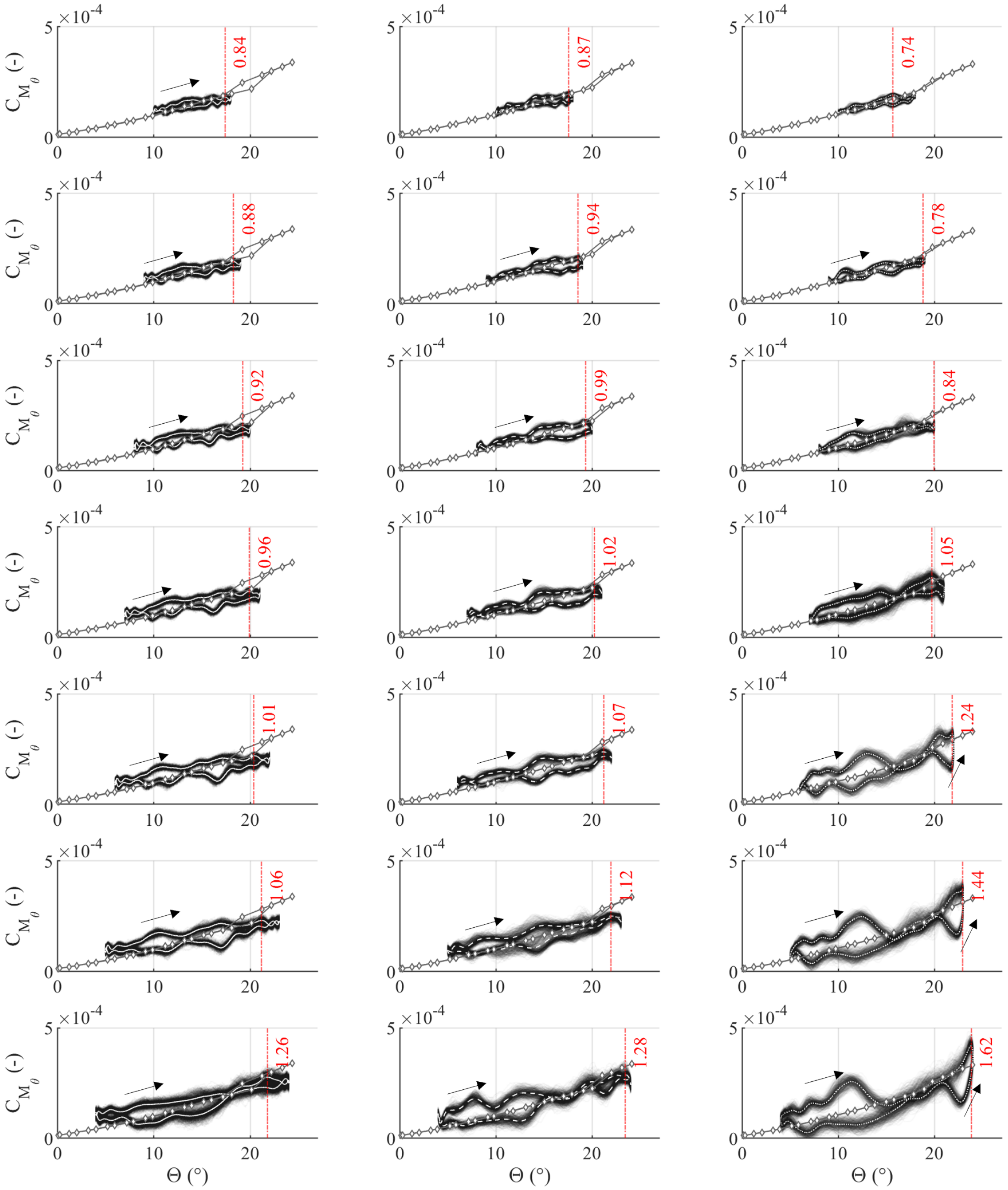

Figure B.24: Blade root torsion for 14 ± 4, 5, 6, 7, 8, 9, 10° from top to bottom at 900, 1200, 1500 RPM from left to right

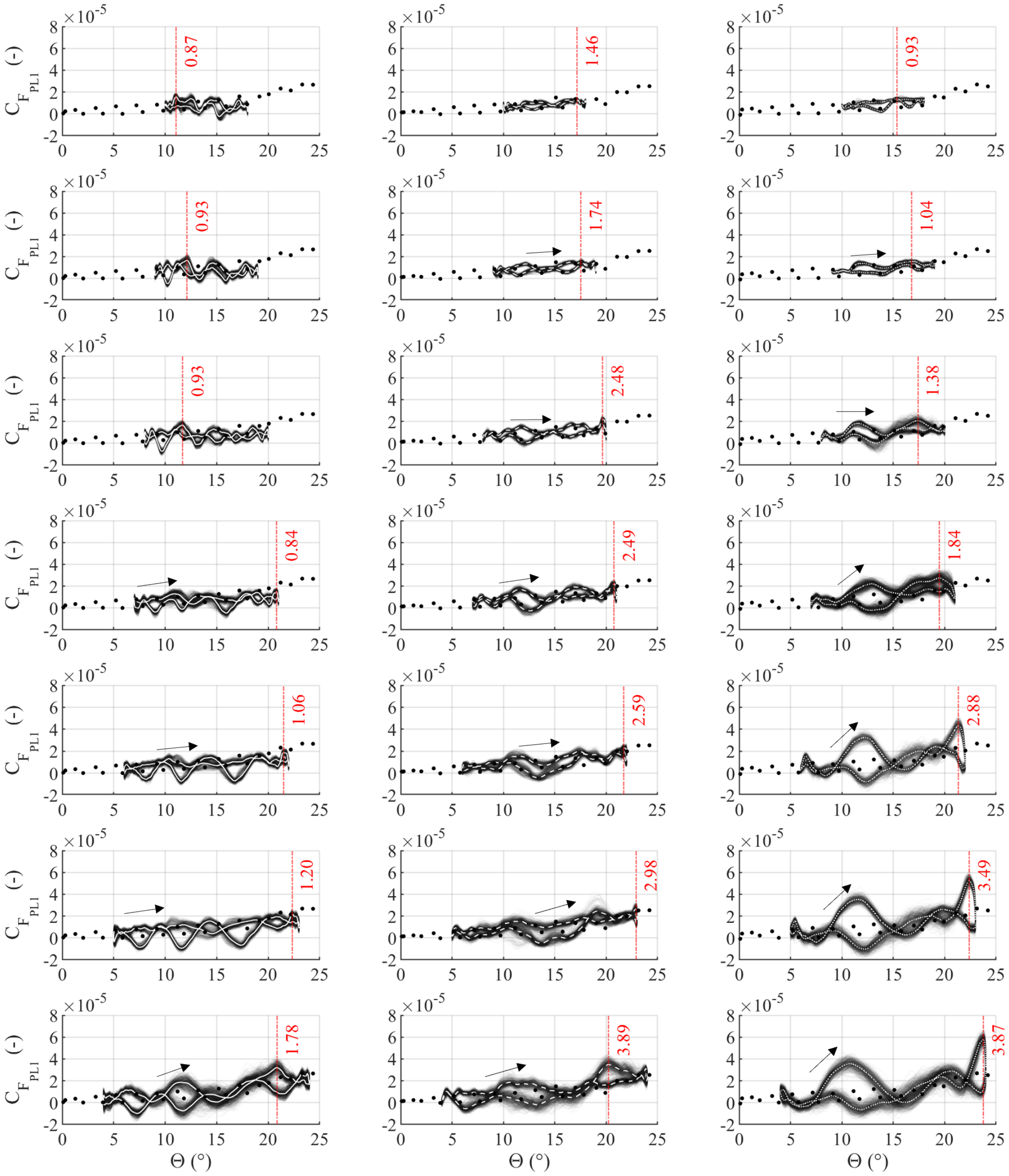

Figure B.25: Pitch link 1 force $F_{PL,1}$ from top to bottom for $14 \pm 4, 5, 6, 7, 8, 9, 10°$ at 900, 1200, 1500 RPM from left to right

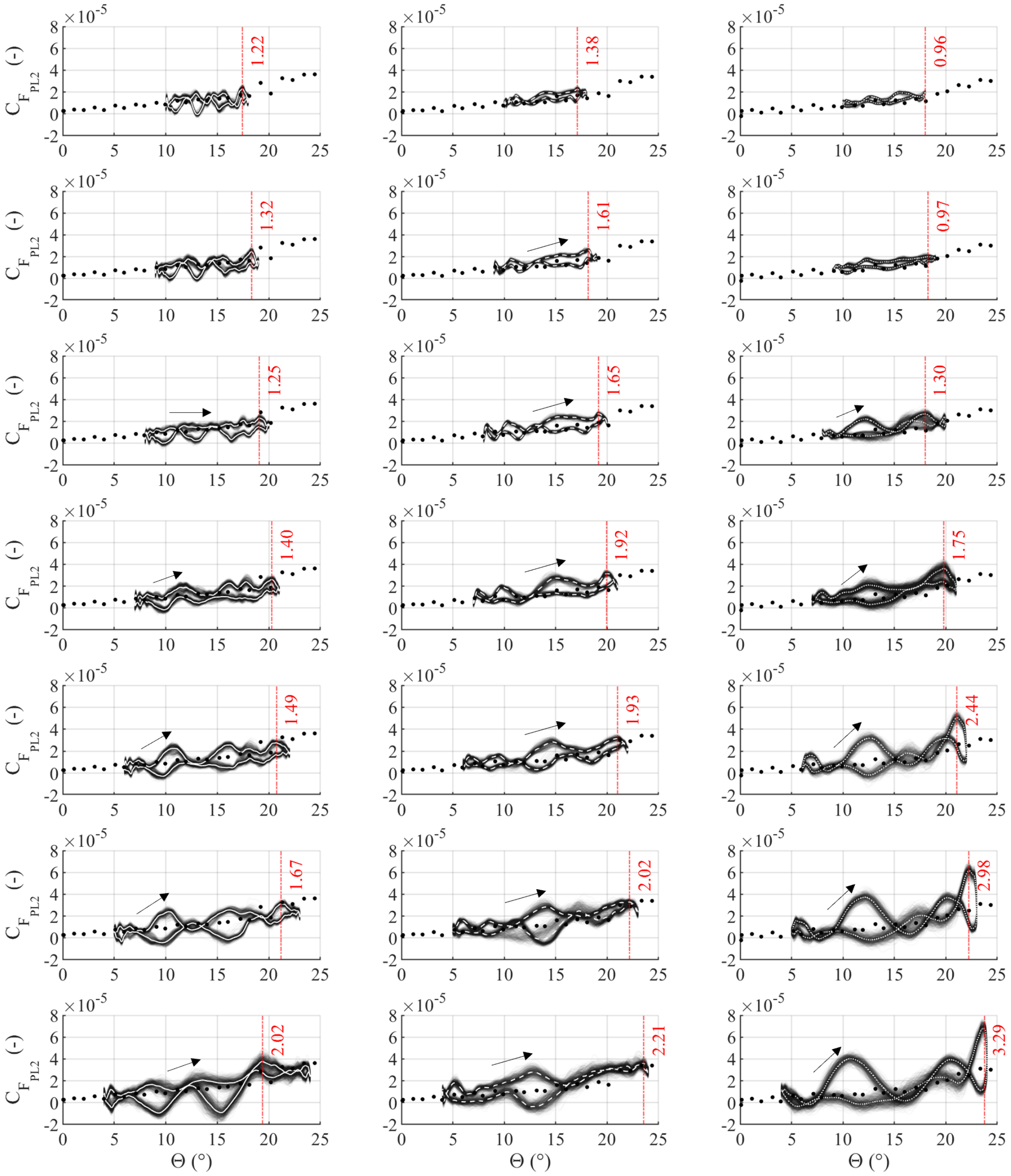

Figure B.26: Pitch link 2 force $F_{PL,2}$ from top to bottom for $14 \pm 4,5,6,7,8,9,10°$ at 900, 1200, 1500 RPM from left to right

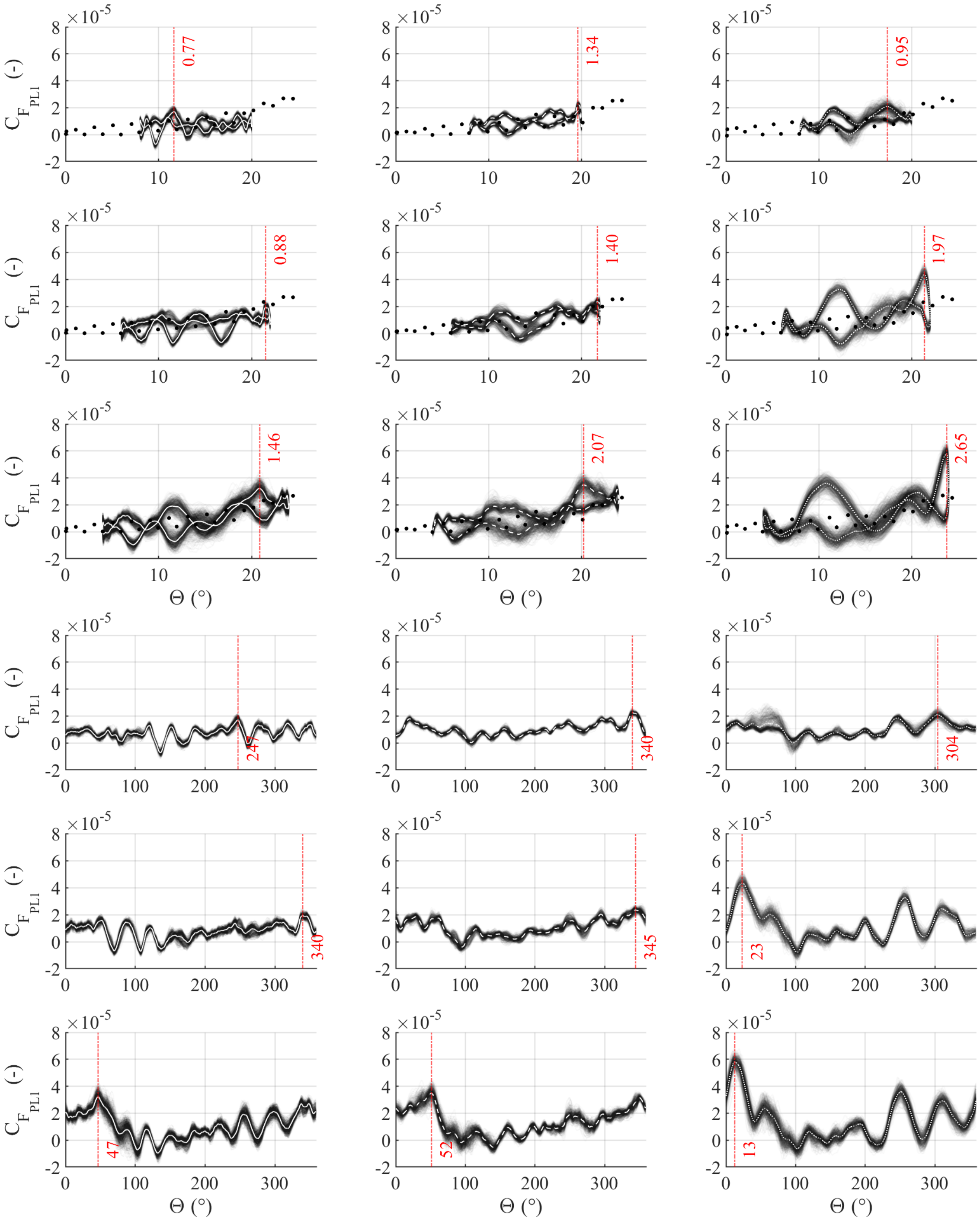

Figure B.27: Non-dimensionalized pitch link 1 force $C_{F_{PL1}}$ for three dynamic stall cases with varying cyclic pitch and constant collective pitch at $14^\circ \pm 6^\circ, 14^\circ \pm 8^\circ, 14^\circ \pm 10^\circ$ from top to bottom and 900, 1200, 1500 RPM from left to right; loads shown as a function of pitch (upper three rows) and as a function of azimuth (lower three rows)

B.5 Amplitude Spectrum Graphs

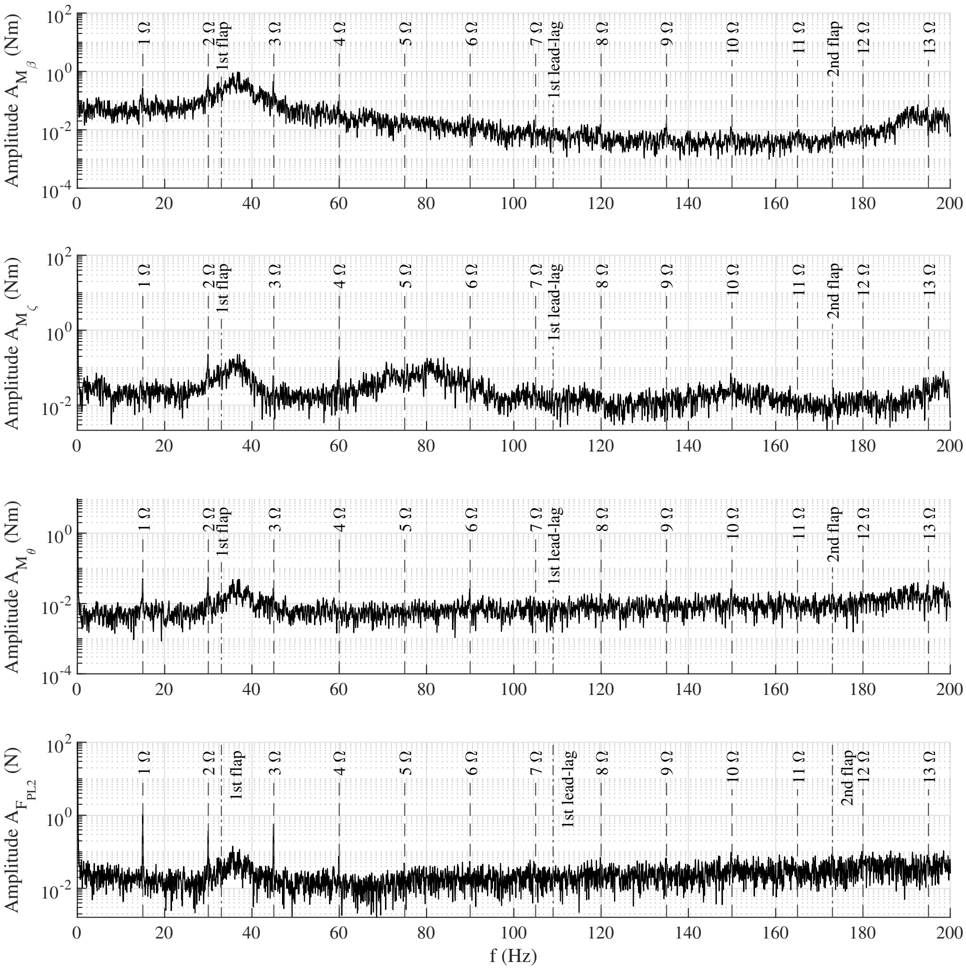

Figure B.28: Amplitude spectrum as a function of frequency for the blade root flapping, lead-lag and torsion moment $M_\beta, M_\zeta, M_\theta$ and pitch link 2 force $F_{PL,2}$ in static stall excitation at 900 RPM and $\Theta_0 = 24°$

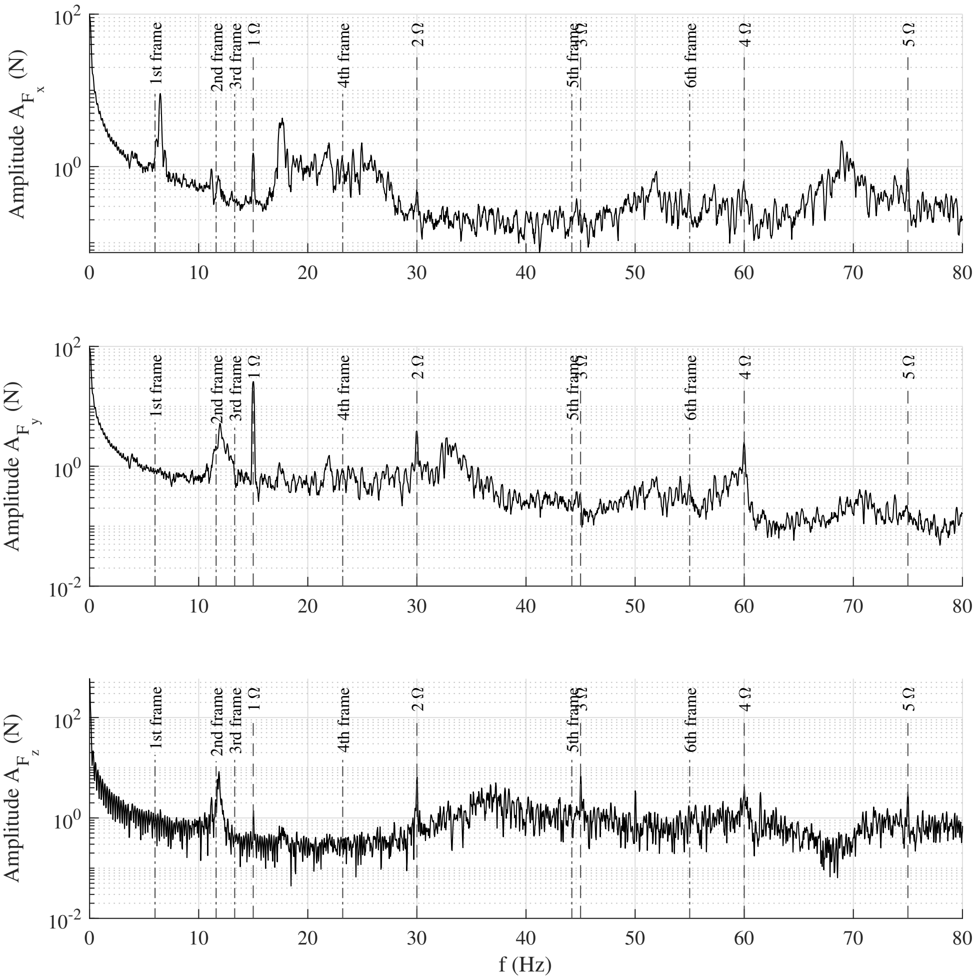

Figure B.29: Amplitude spectrum as a function of frequency for the rotor forces F_x, F_y, F_z in static stall excitation at 900 RPM and $\Theta_0 = 24°$

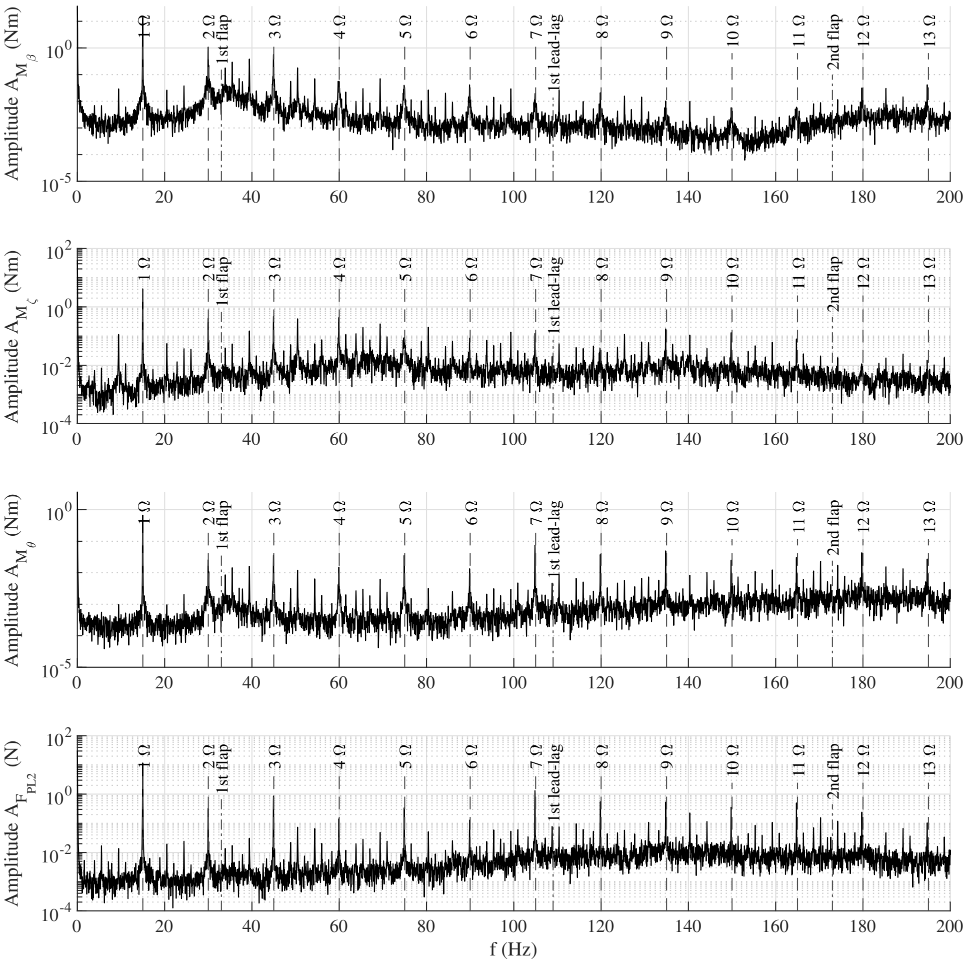

Figure B.30: Amplitude spectrum as a function of frequency for the blade root flapping, lead-lag and torsion moment $M_\beta, M_\zeta, M_\theta$ and pitch link 2 force $F_{PL,2}$ in dynamic stall excitation at 900 RPM and $\Theta = 14^\circ \pm 8^\circ$

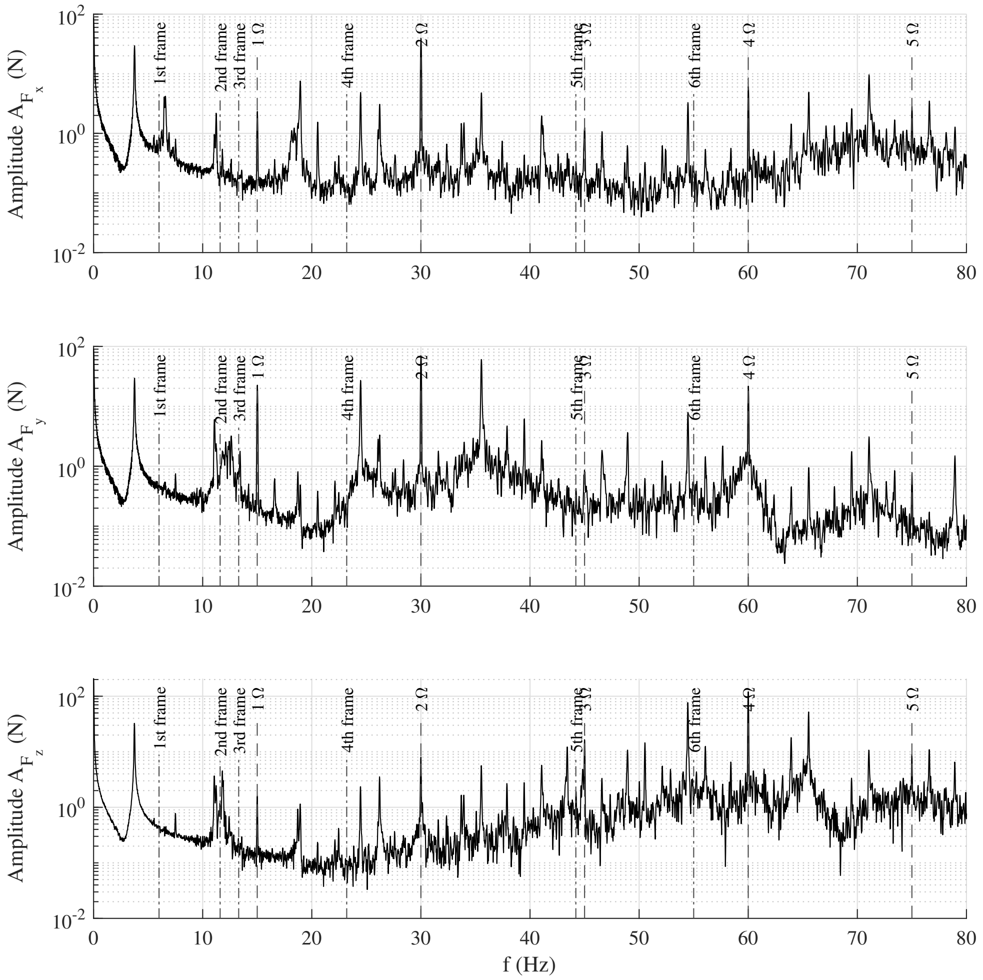

Figure B.31: Amplitude spectrum as a function of frequency for the rotor forces F_x, F_y, F_z in dynamic stall excitation at 900 RPM and $\Theta = 14° \pm 8°$

B.6 Joint Probability Density Graphs

B.6.1 Collective Pitch Variation

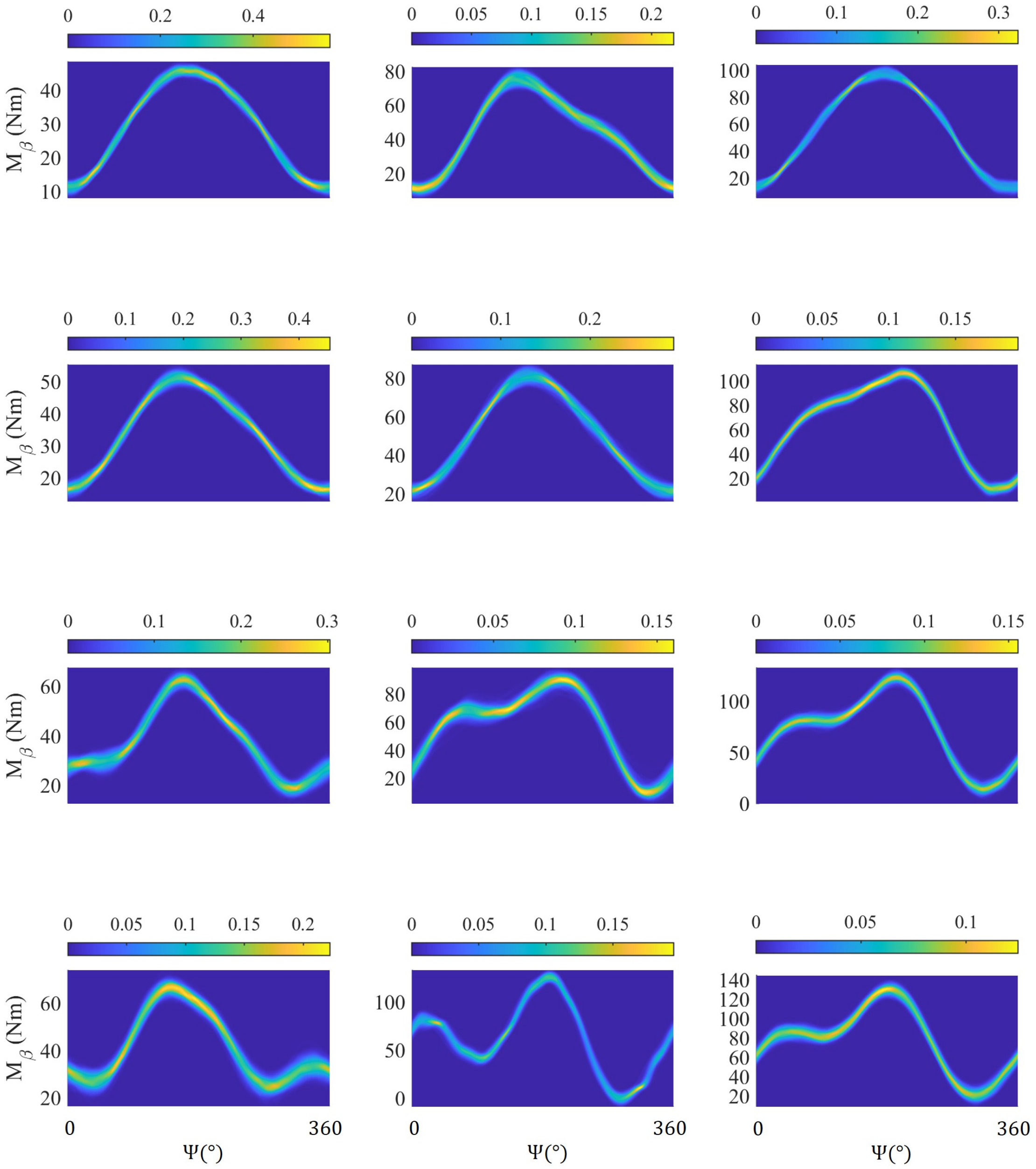

Figure B.32: Joint probability density function of the blade root flapping moment for $14, 16, 18, 20 \pm 6°$ (from top to bottom) at 900, 1200, 1500 RPM (from left to right)

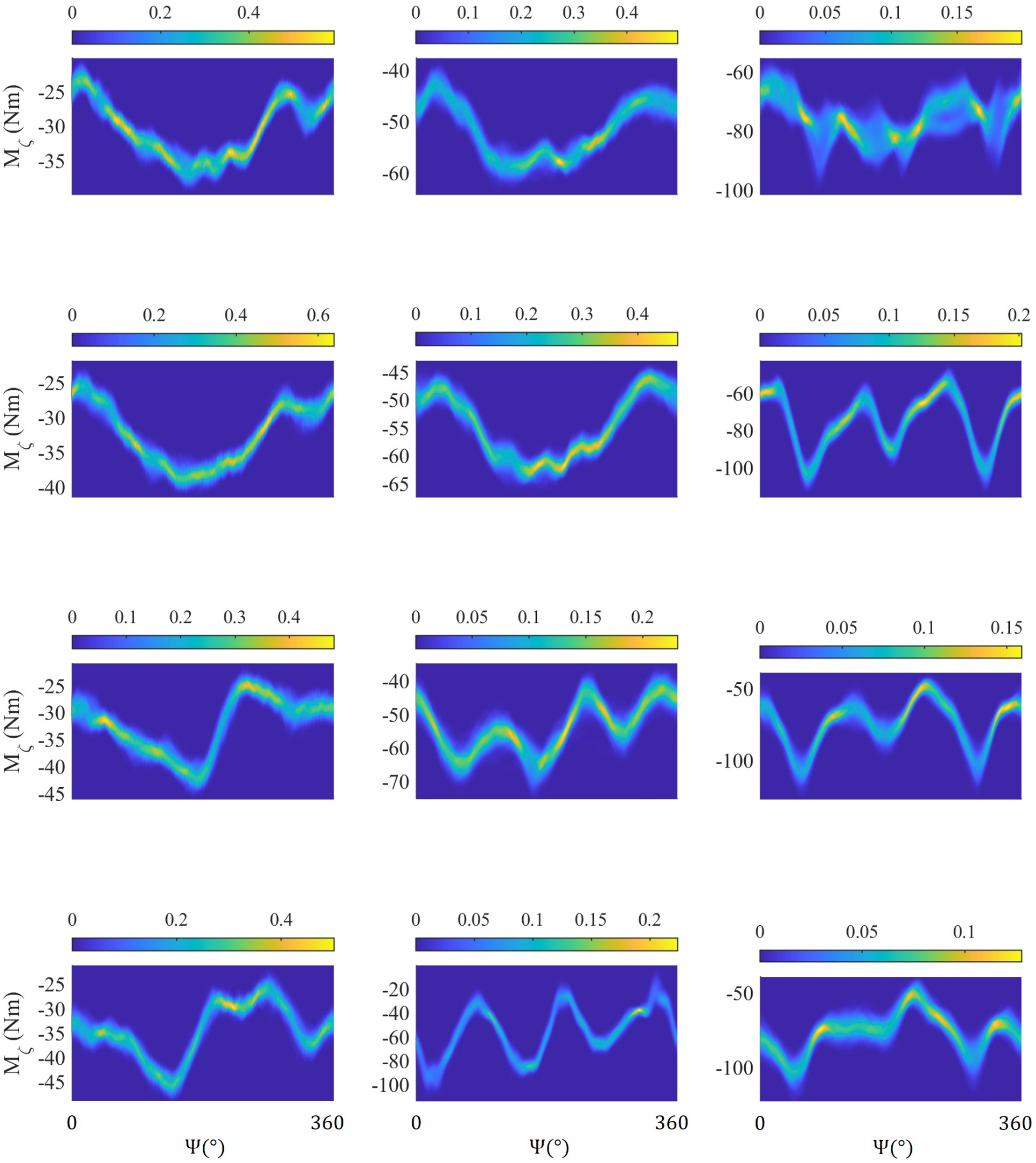

Figure B.33: Joint probability density function of the blade root lead-lag moment for $14, 16, 18, 20 \pm 6°$ (from top to bottom) at 900, 1200, 1500 RPM (from left to right)

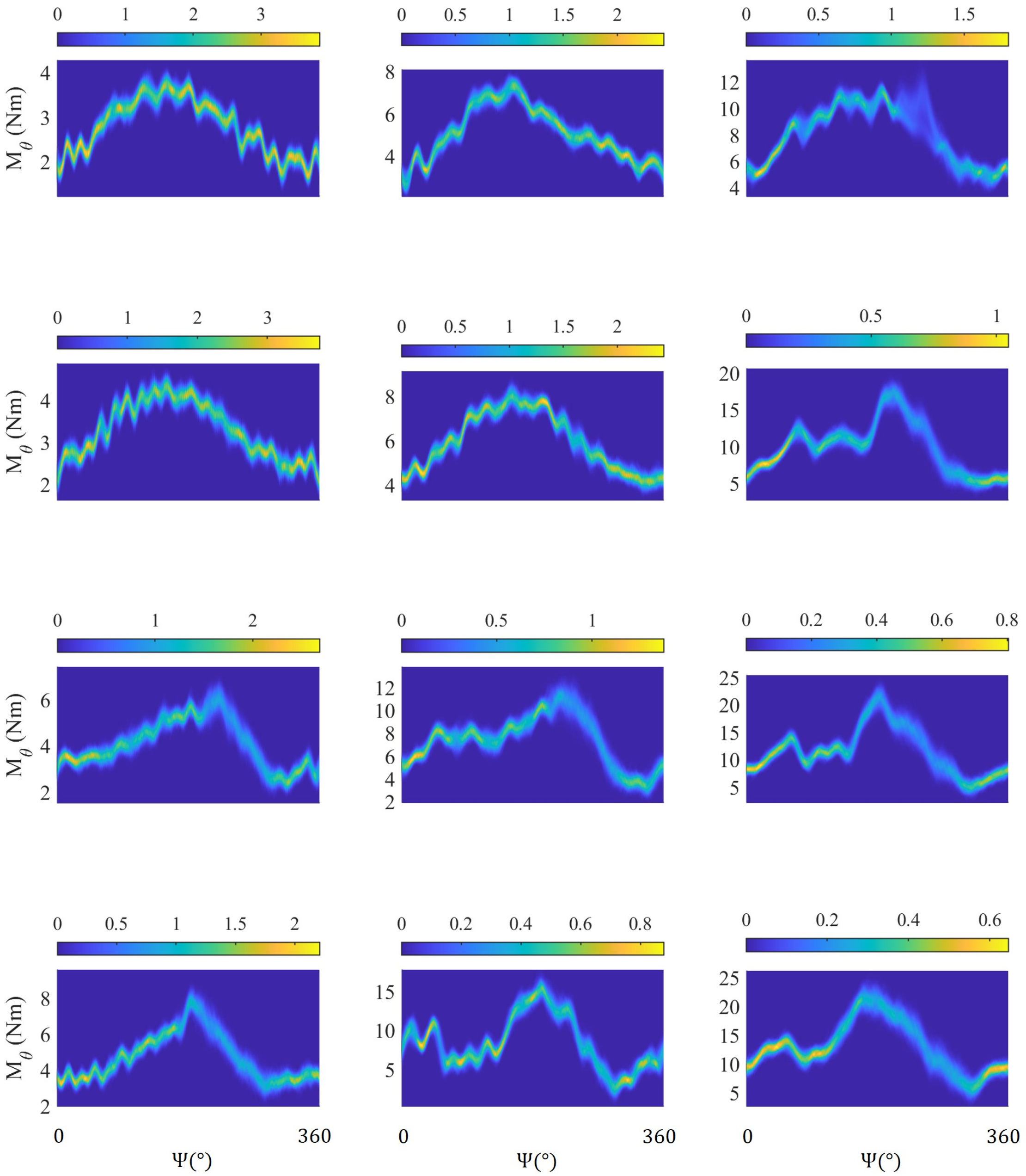

Figure B.34: Joint probability density function of the blade root torsion for $14, 16, 18, 20 \pm 6^\circ$ (from top to bottom) at 900, 1200, 1500 RPM (from left to right)

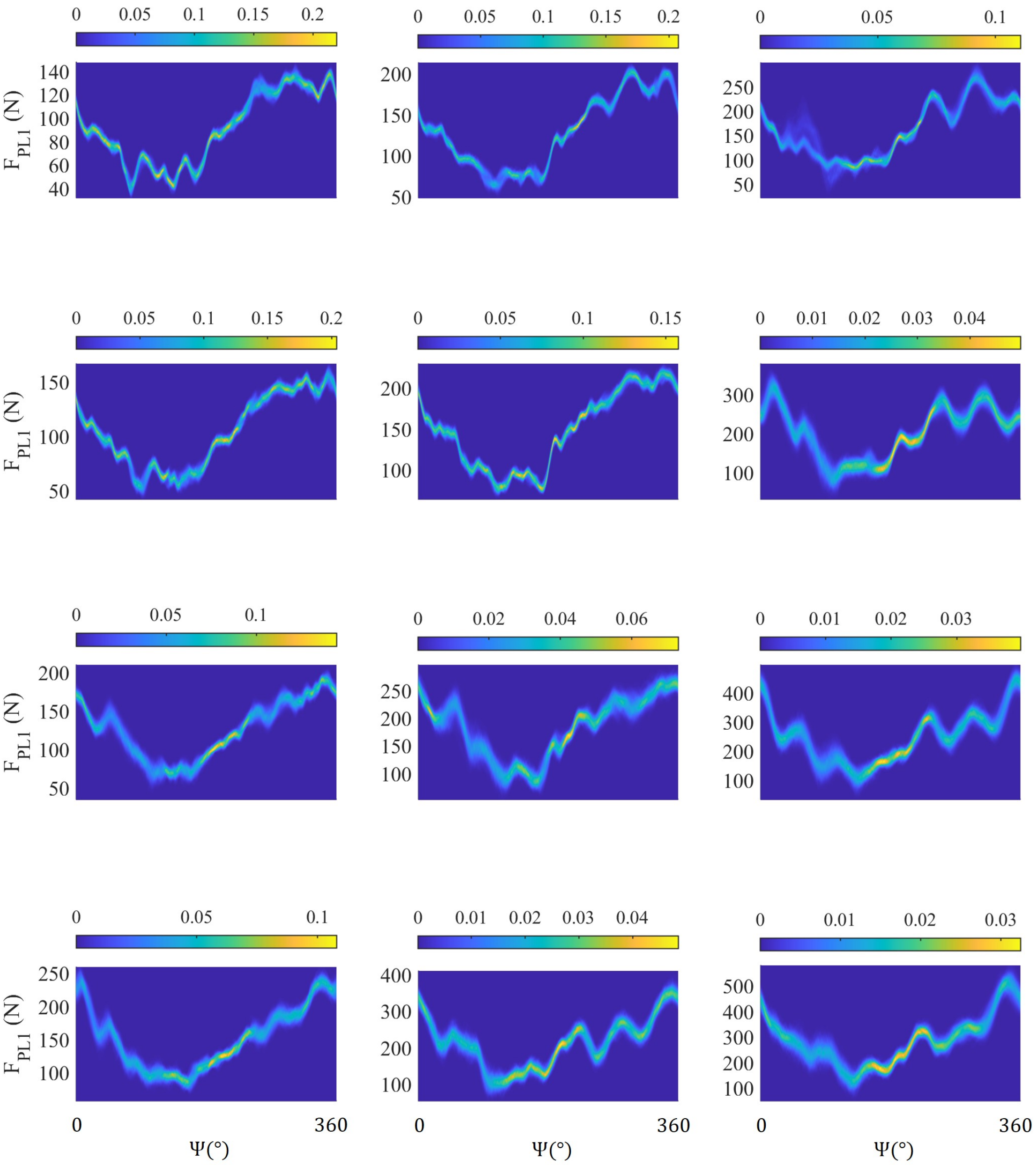

Figure B.35: Joint probability density function of the pitch link 1 force for 14, 16, 18, 20 ± 6° (from top to bottom) at 900, 1200, 1500 RPM (from left to right)

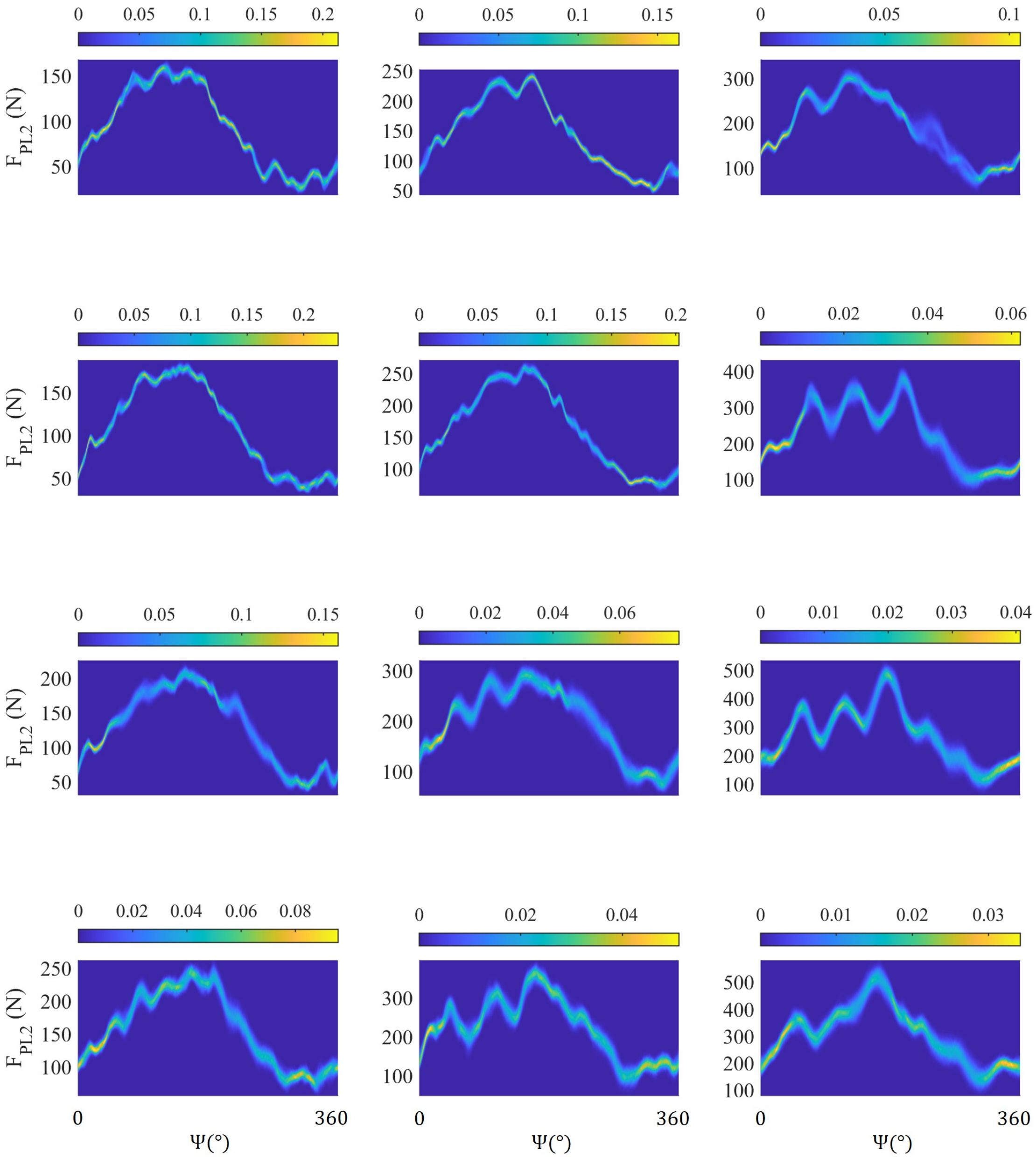

Figure B.36: Joint probability density function of the pitch link 2 force for $14, 16, 18, 20 \pm 6°$ (from top to bottom) at 900, 1200, 1500 RPM (from left to right)

B.6.2 Cyclic Pitch Variation

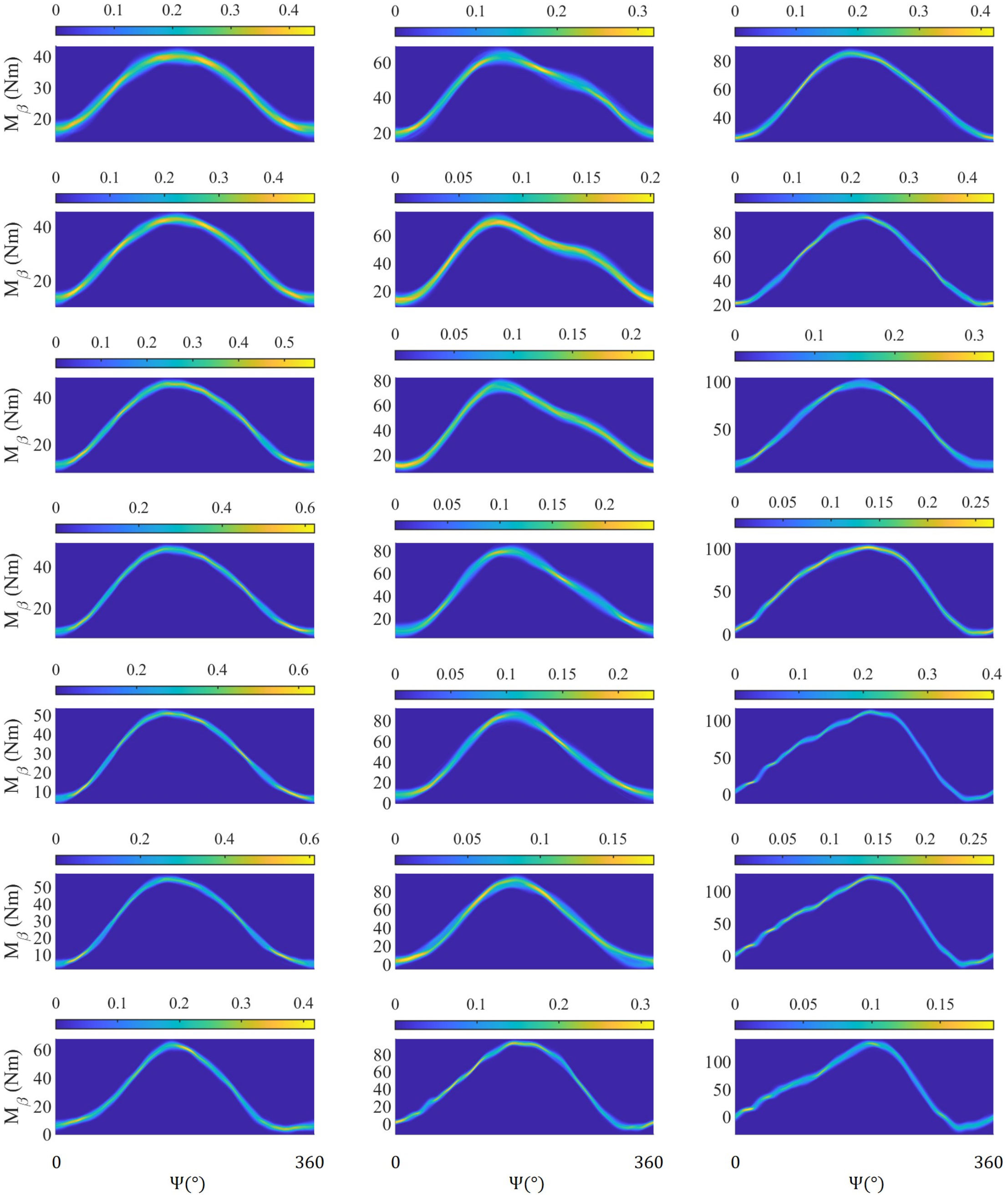

Figure B.37: Joint probability density function of the blade root flapping moment for $14 \pm 4, 5, 6, 7, 8, 9, 10^\circ$ (from top to bottom) at 900, 1200, 1500 RPM (from left to right)

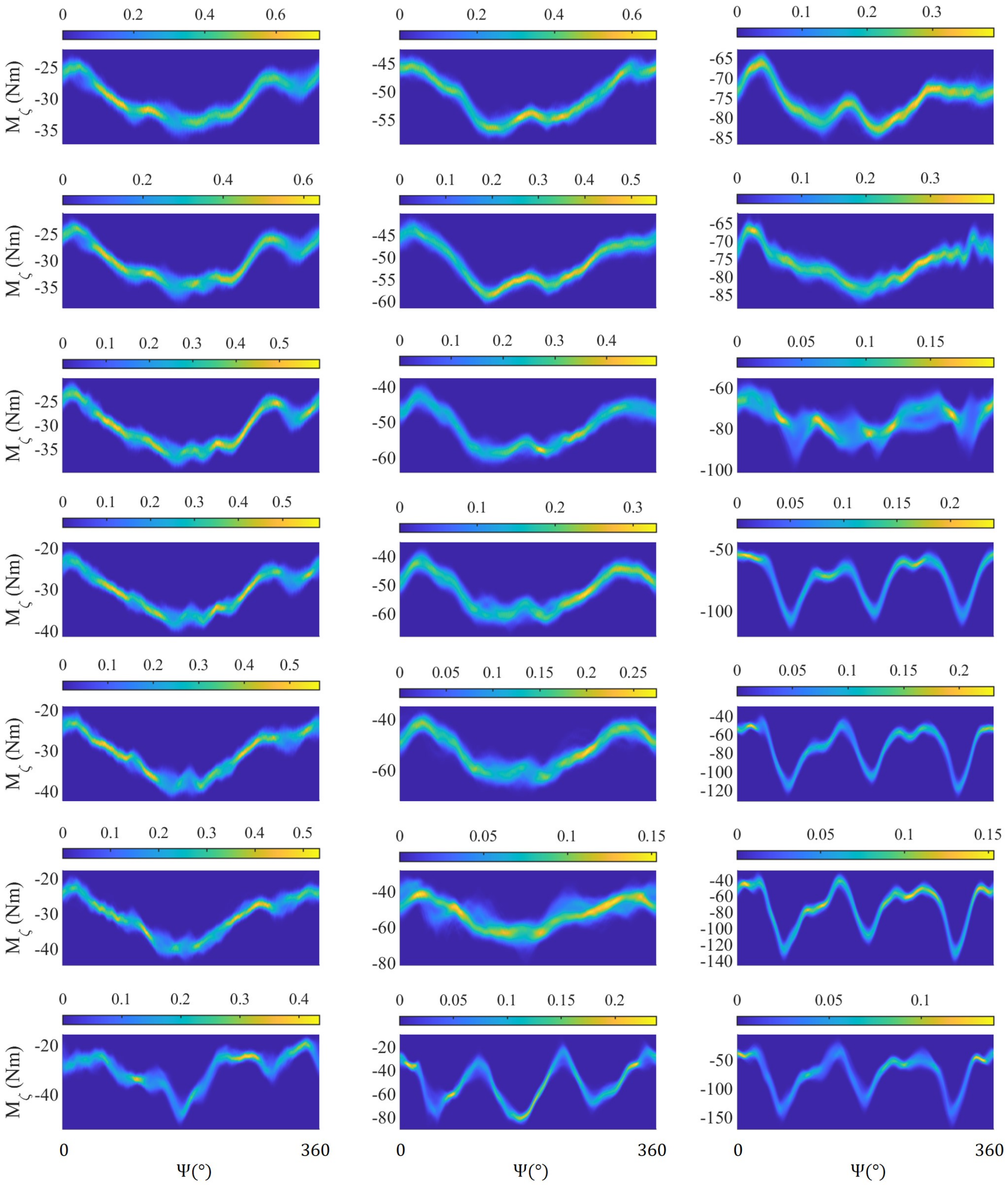

Figure B.38: Joint probability density function of the blade root lead-lag moment for 14 ± 4, 5, 6, 7, 8, 9, 10° (from top to bottom) at 900, 1200, 1500 RPM (from left to right)

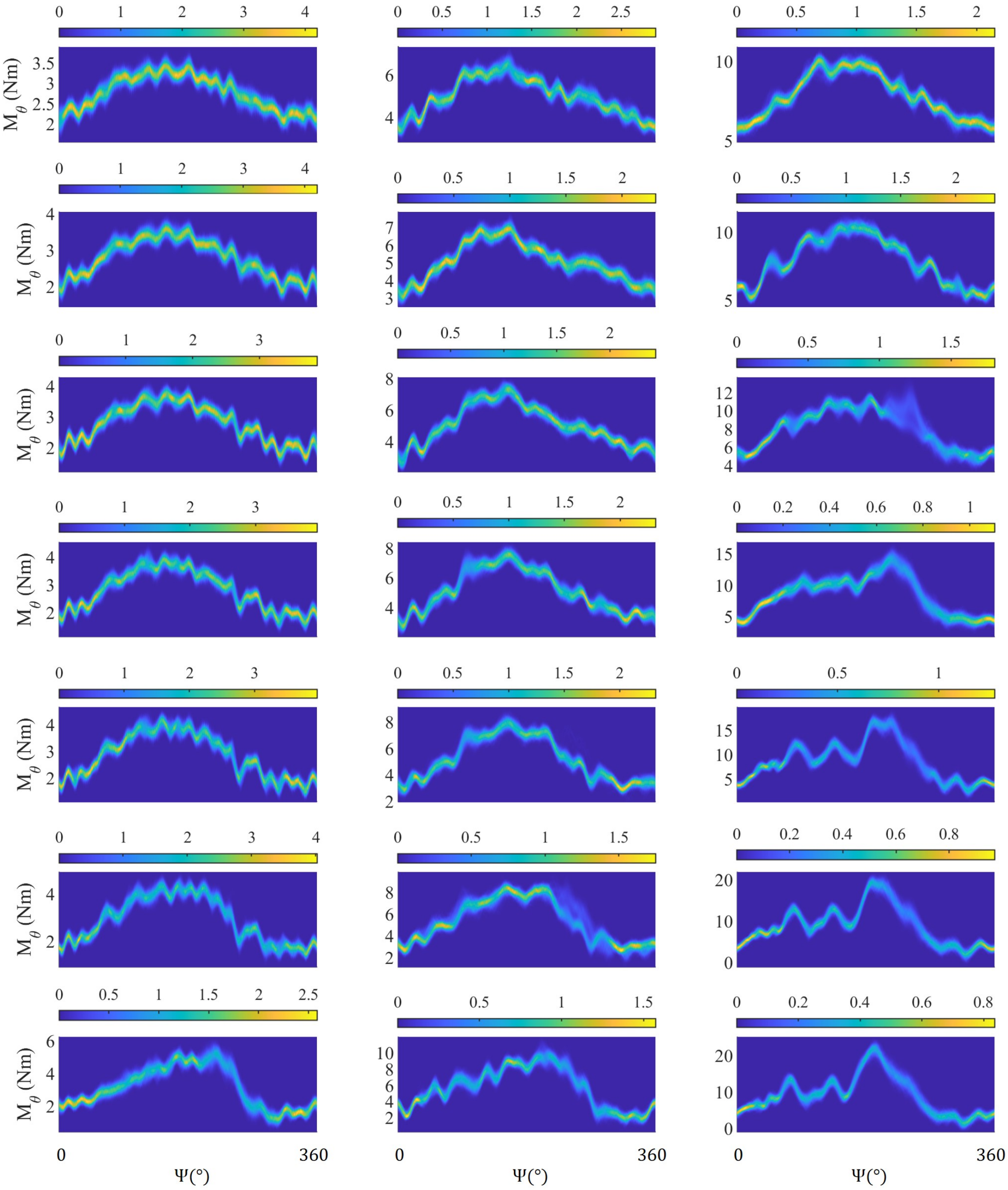

Figure B.39: Joint probability density function of the blade root torsion for 14 ± 4, 5, 6, 7, 8, 9, 10° (from top to bottom) at 900, 1200, 1500 RPM (from left to right)

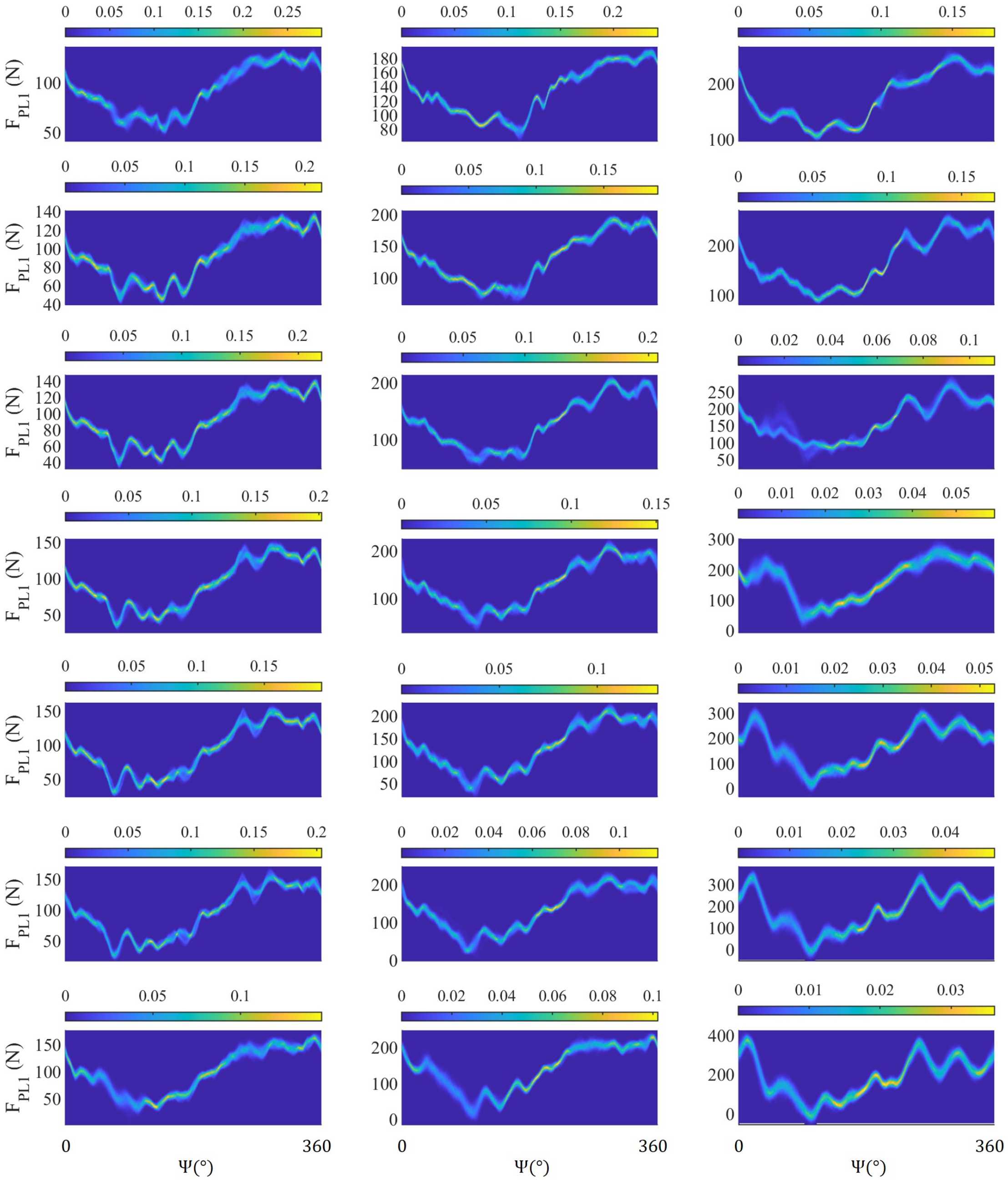

Figure B.40: Joint probability density function of the pitch link 1 force for 14 ± 4, 5, 6, 7, 8, 9, 10° (from top to bottom) at 900, 1200, 1500 RPM (from left to right)

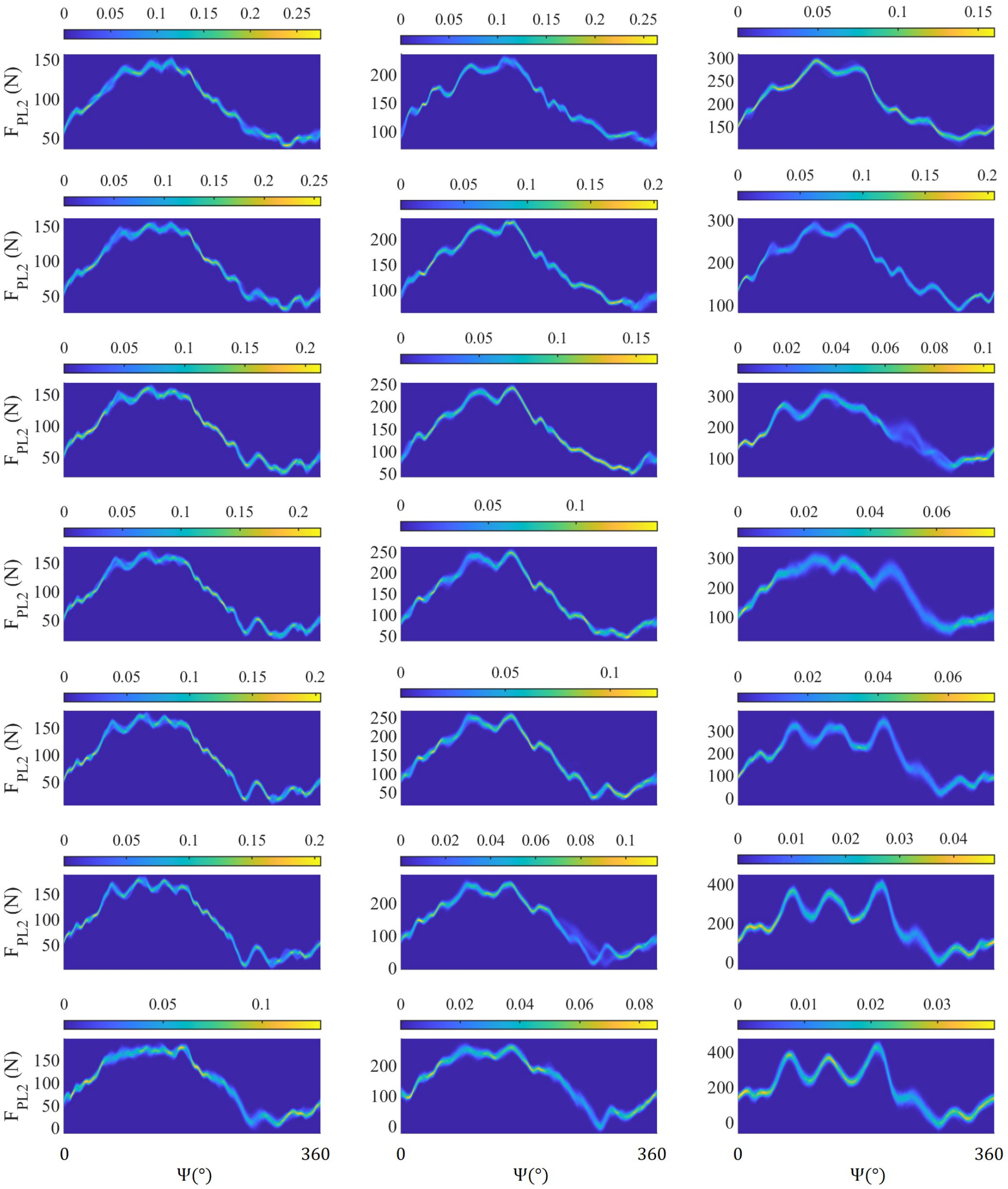

Figure B.41: Joint probability density function of the pitch link 2 force for $14 \pm 4, 5, 6, 7, 8, 9, 10^\circ$ (from top to bottom) at 900, 1200, 1500 RPM (from left to right)

B.7 Probability Density and Maximum Relative Error Graphs

B.7.1 Collective Pitch Variation

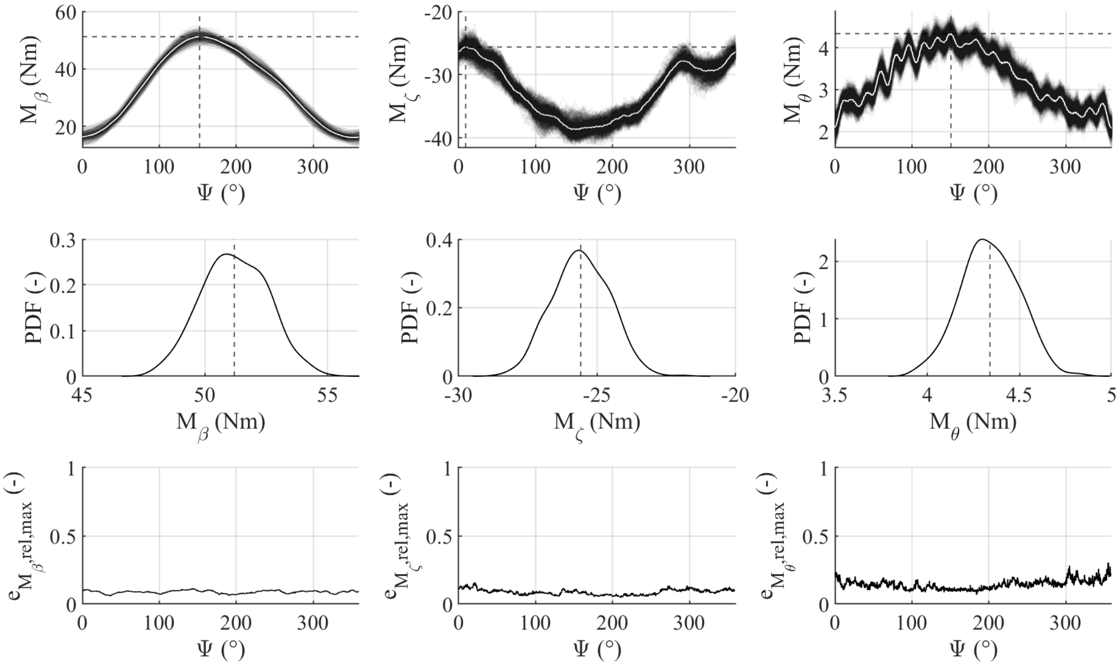

Figure B.42: Probability density function and maximum relative deviations of the blade root moments for 16 ± 6° and 900 RPM

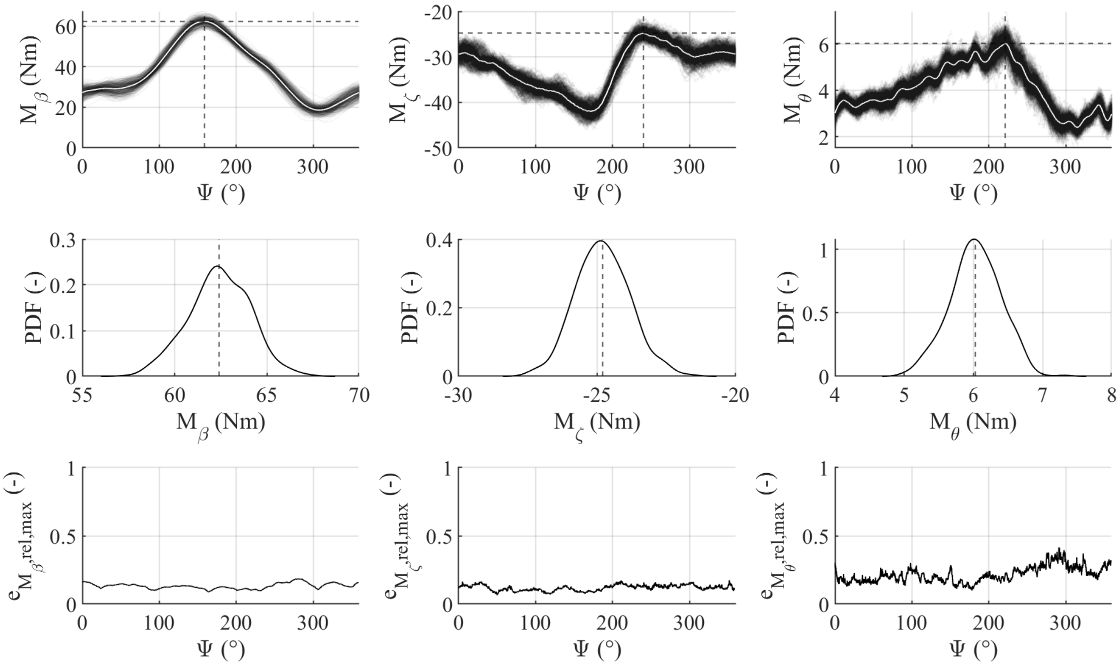

Figure B.43: Probability density function and maximum relative deviations of the blade root moments for 18 ± 6° and 900 RPM

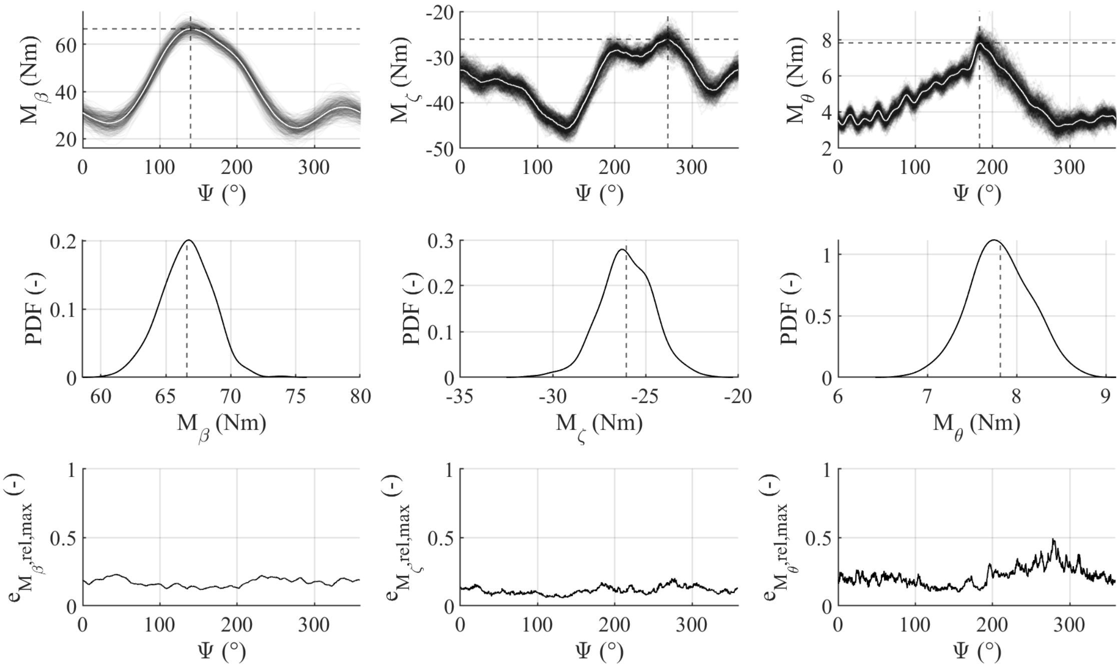

Figure B.44: Probability density function and maximum relative deviations of the blade root moments for 20 ± 6° and 900 RPM

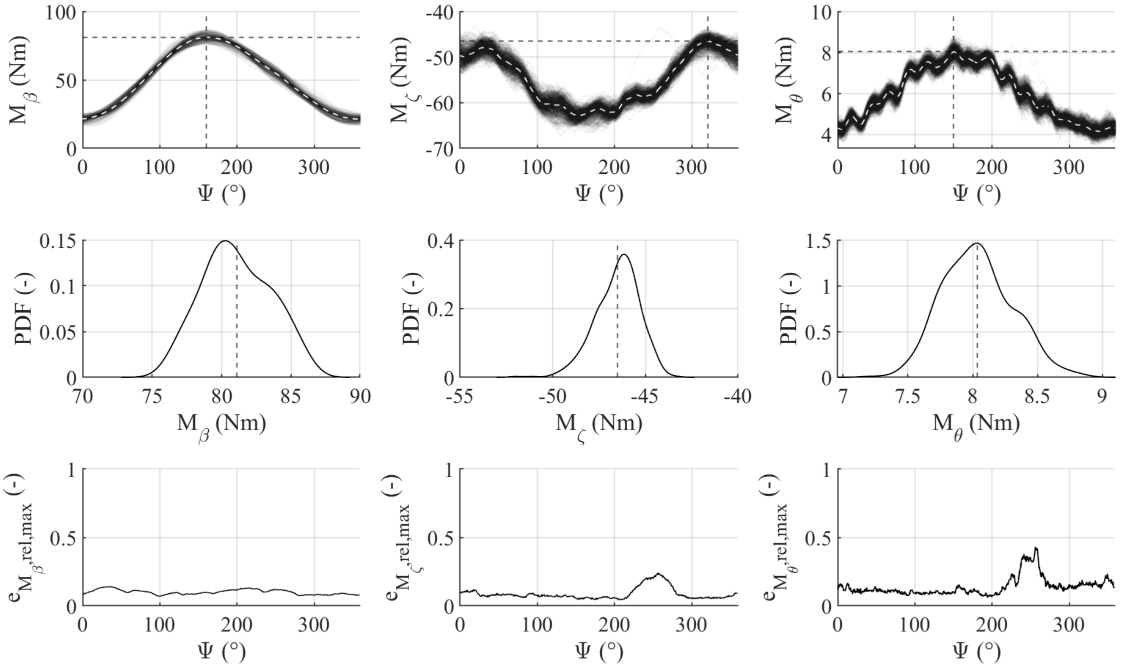

Figure B.45: Probability density function and maximum relative deviations of the blade root moments for $16 \pm 6°$ and 1200 RPM

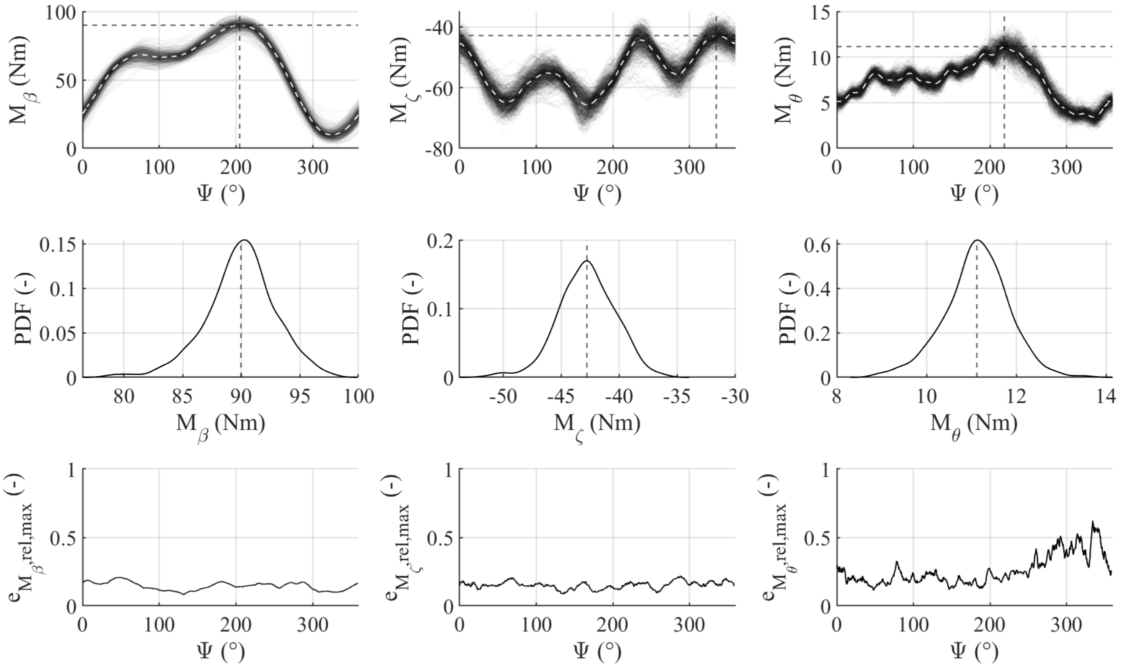

Figure B.46: Probability density function and maximum relative deviations of the blade root moments for $18 \pm 6°$ and 1200 RPM

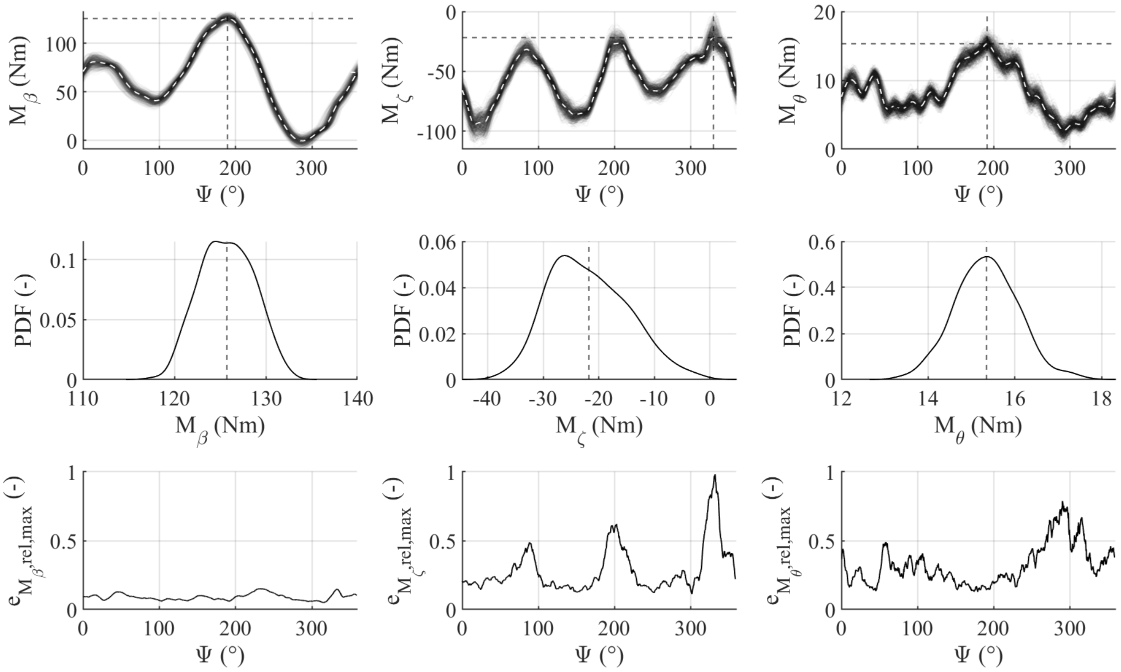

Figure B.47: Probability density function and maximum relative deviations of the blade root moments for 20 ± 6° and 1200 RPM

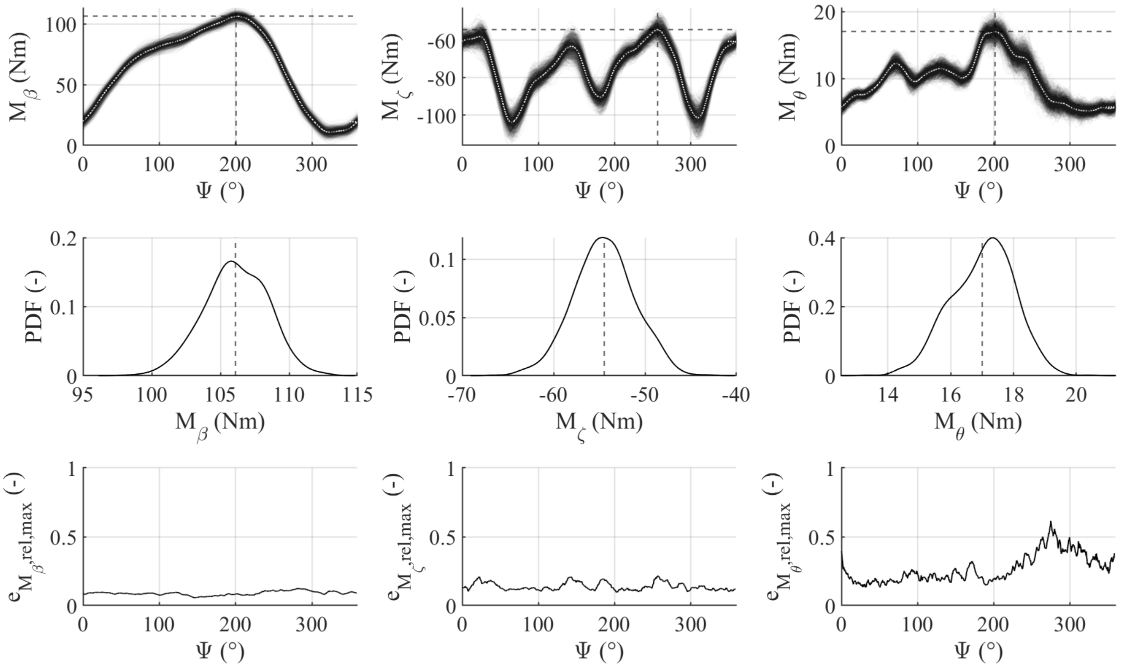

Figure B.48: Probability density function and maximum relative deviations of the blade root moments for 16 ± 6° and 1500 RPM

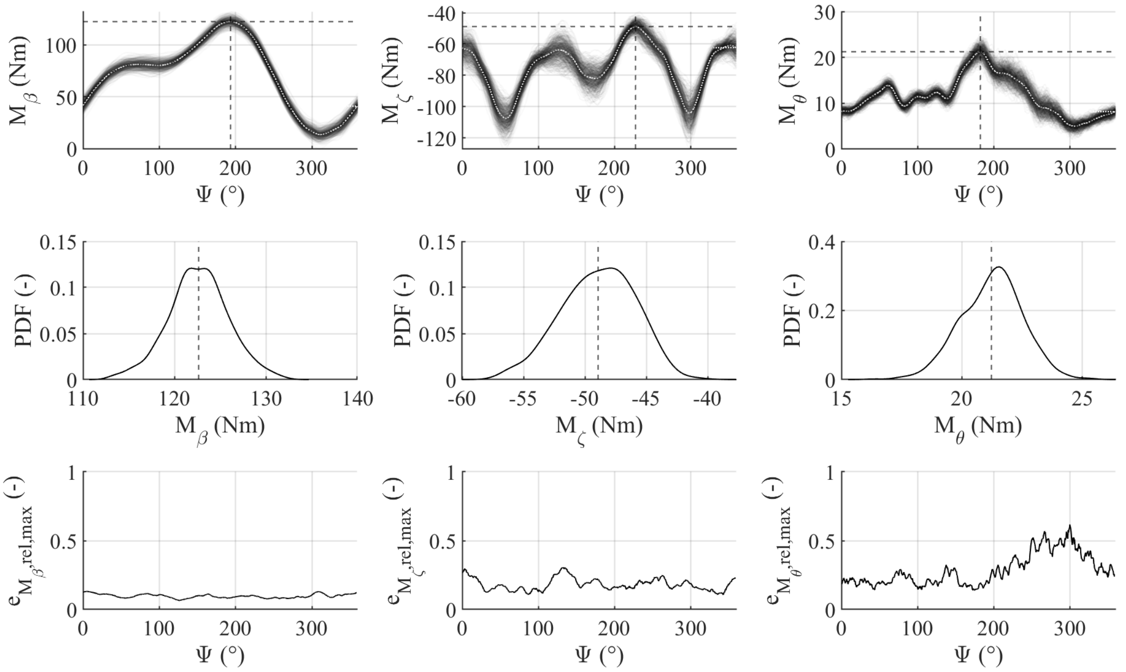

Figure B.49: Probability density function and maximum relative deviations of the blade root moments for 18 ± 6° and 1500 RPM

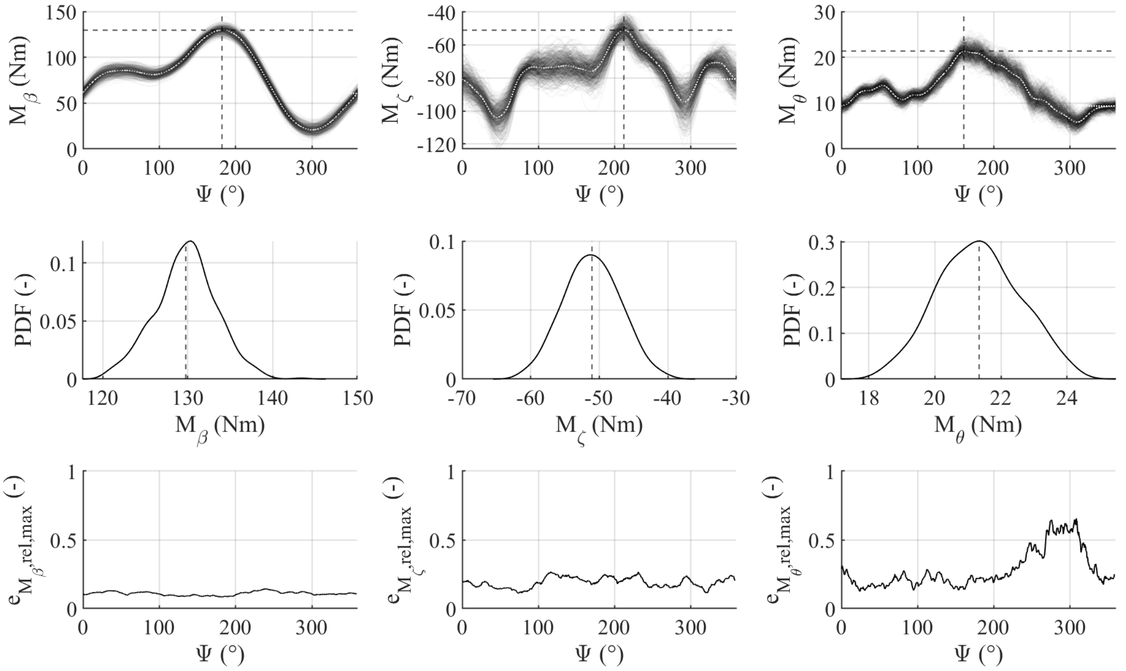

Figure B.50: Probability density function and maximum relative deviations of the blade root moments for 20 ± 6° and 1500 RPM

B.7.2 Cyclic Pitch Variation

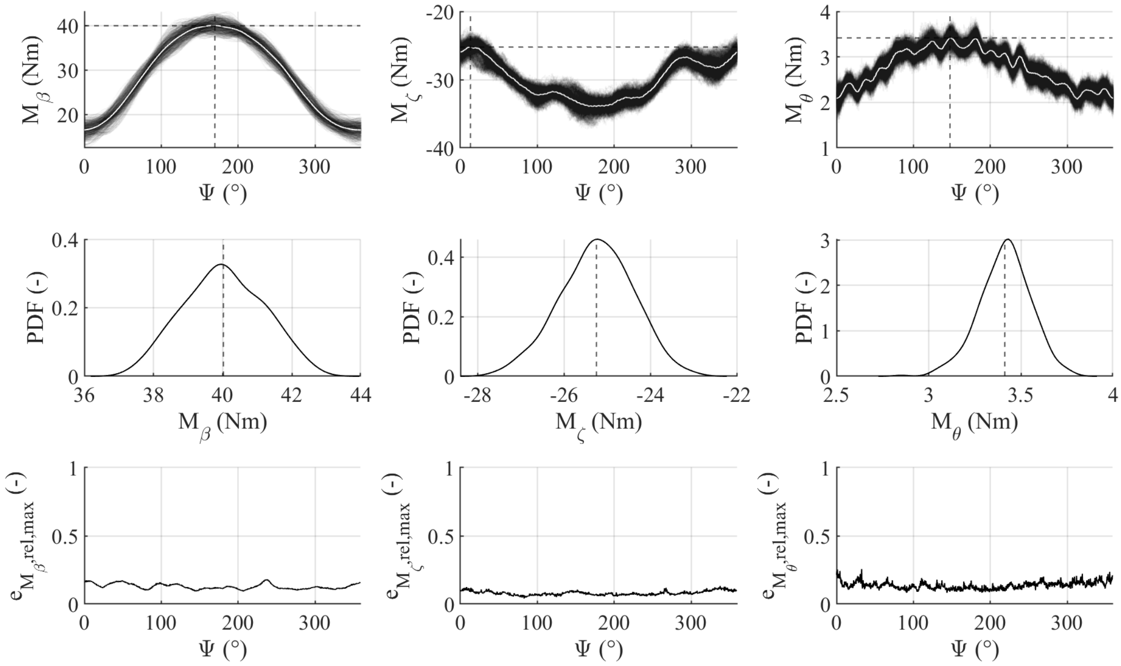

Figure B.51: Probability density function and maximum relative deviations of the blade root moments for 14 ± 4° and 900 RPM

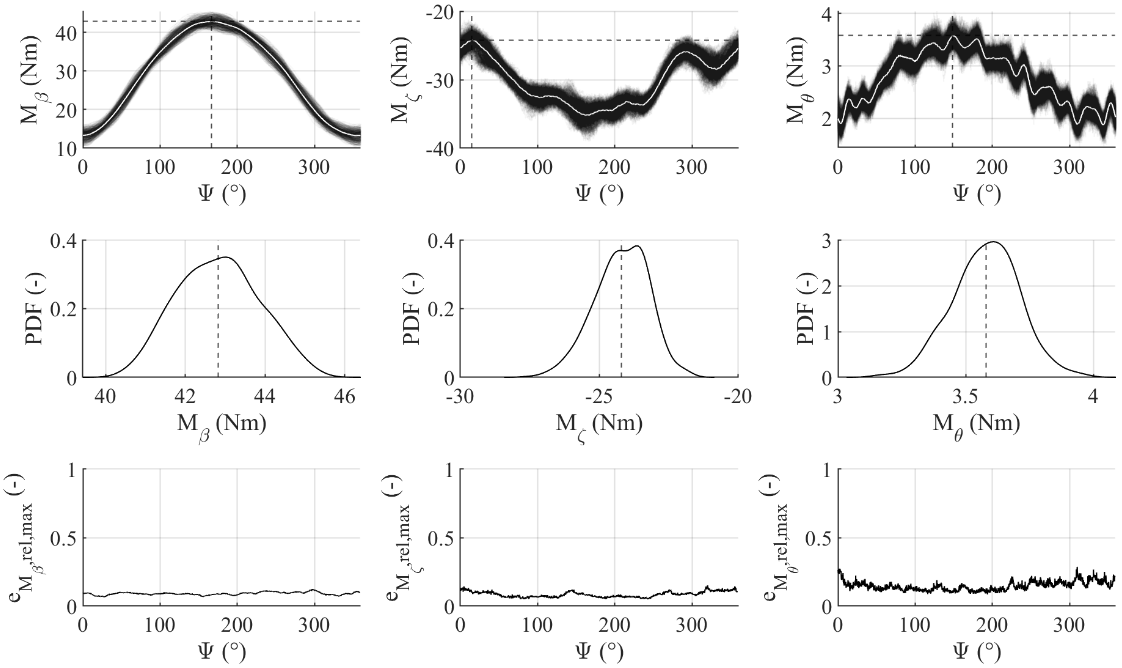

Figure B.52: Probability density function and maximum relative deviations of the blade root moments for 14 ± 5° and 900 RPM

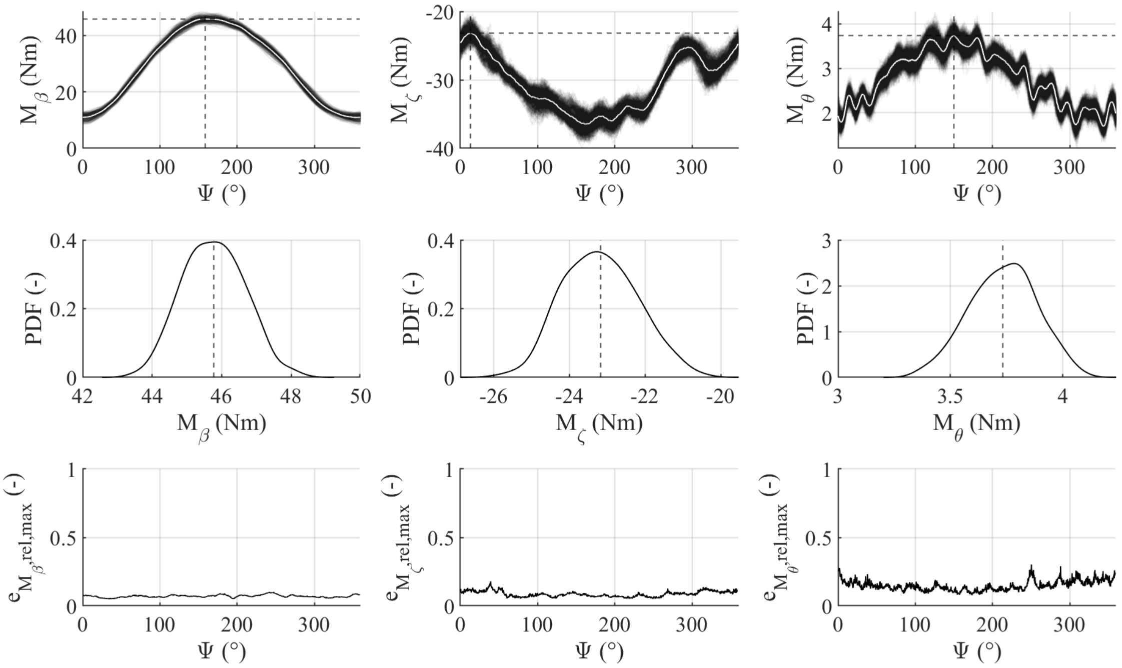

Figure B.53: Probability density function and maximum relative deviations of the blade root moments for 14 ± 6° and 900 RPM

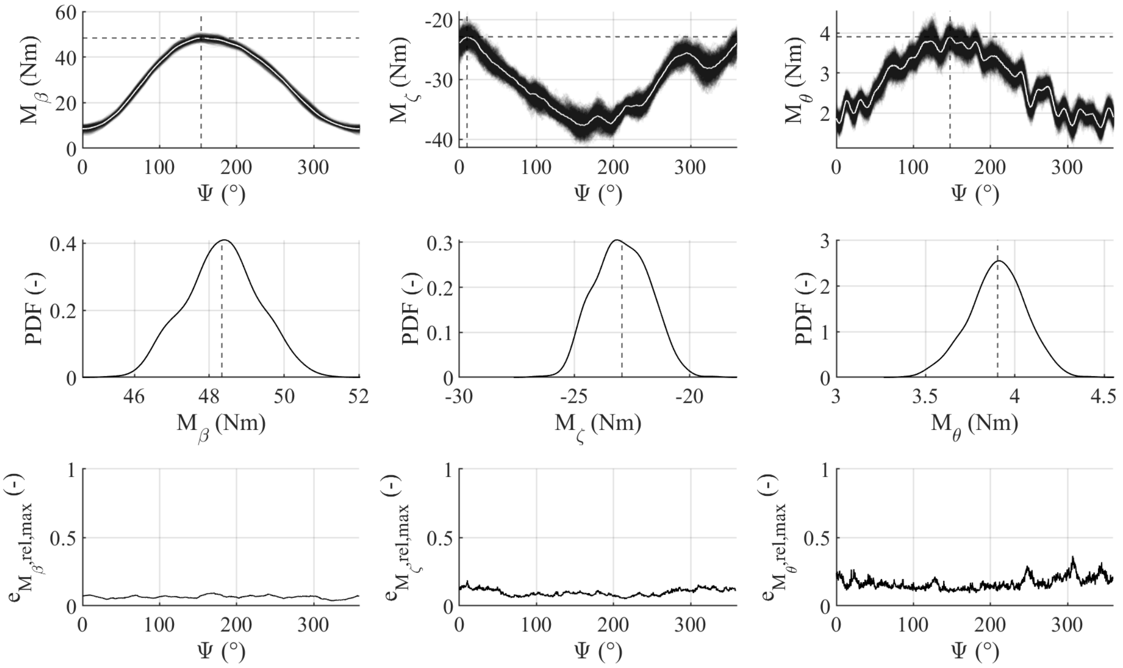

Figure B.54: Probability density function and maximum relative deviations of the blade root moments for 14 ± 7° and 900 RPM

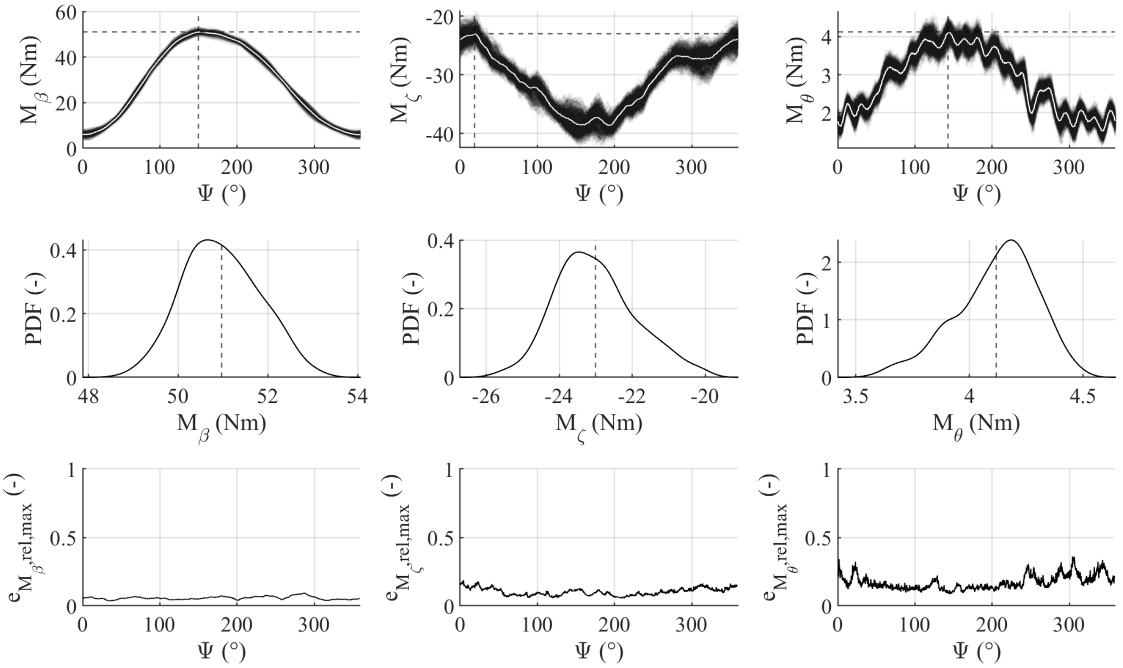

Figure B.55: Probability density function and maximum relative deviations of the blade root moments for 14 ± 8° and 900 RPM

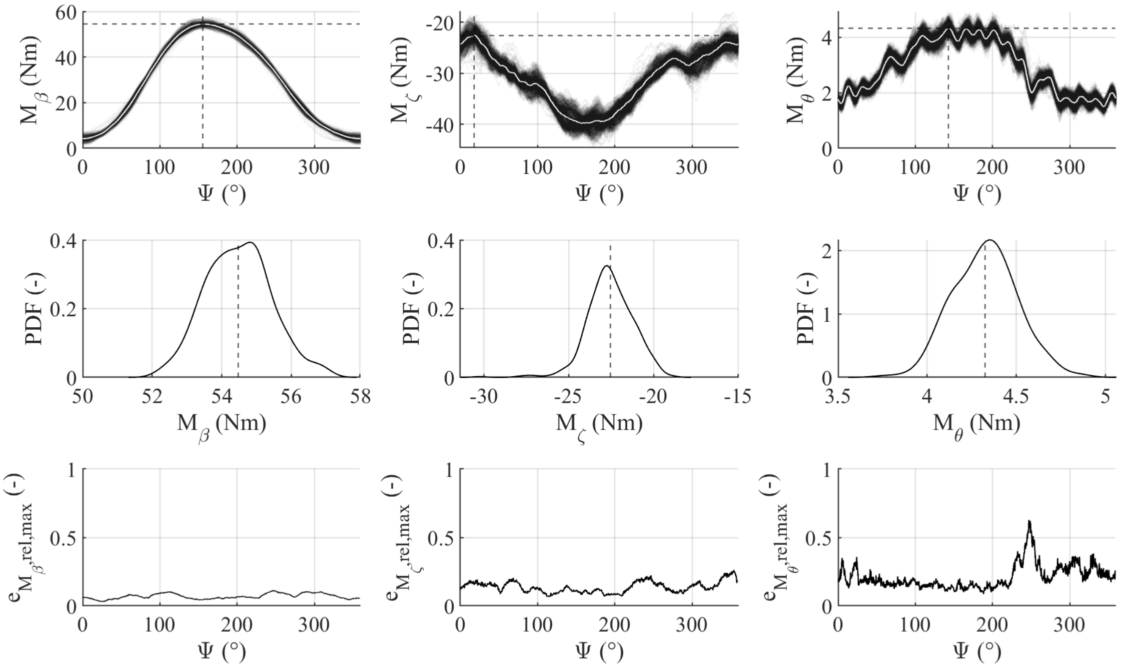

Figure B.56: Probability density function and maximum relative deviations of the blade root moments for 14 ± 9° and 900 RPM

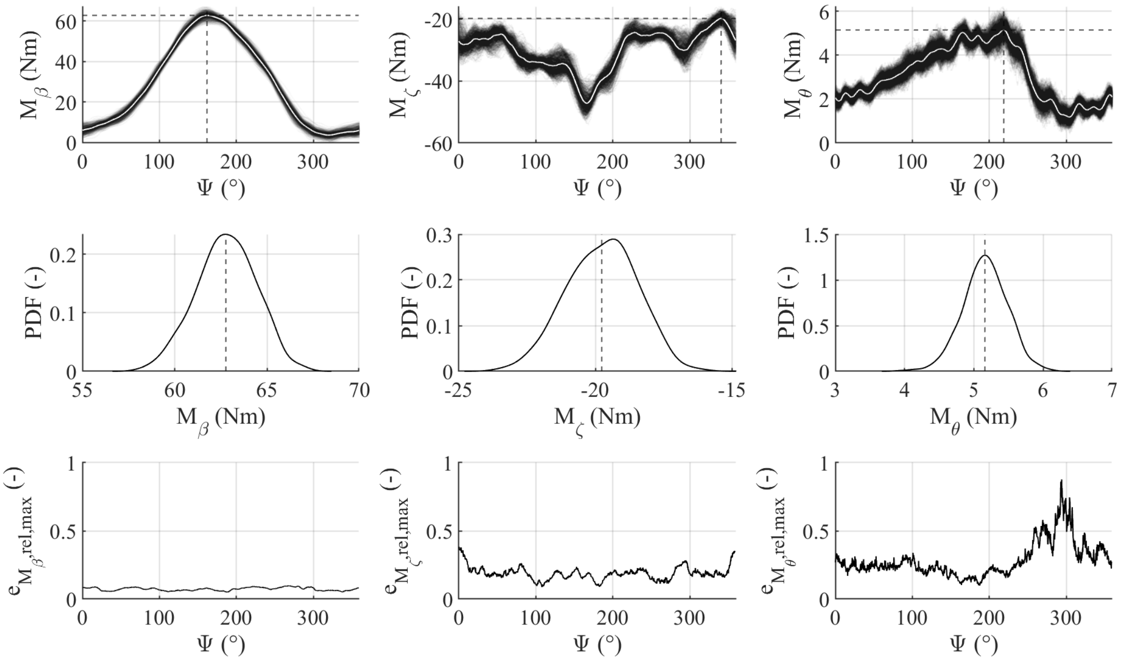

Figure B.57: Probability density function and maximum relative deviations of the blade root moments for 14 ± 10° and 900 RPM

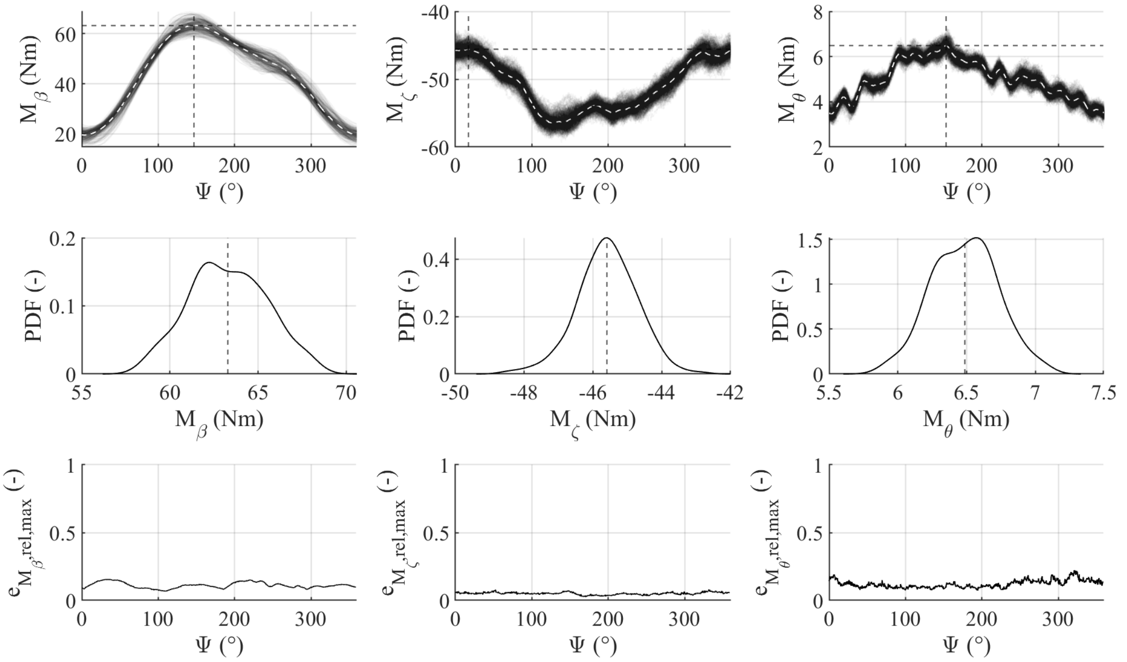

Figure B.58: Probability density function and maximum relative deviations of the blade root moments for 14 ± 4° and 1200 RPM

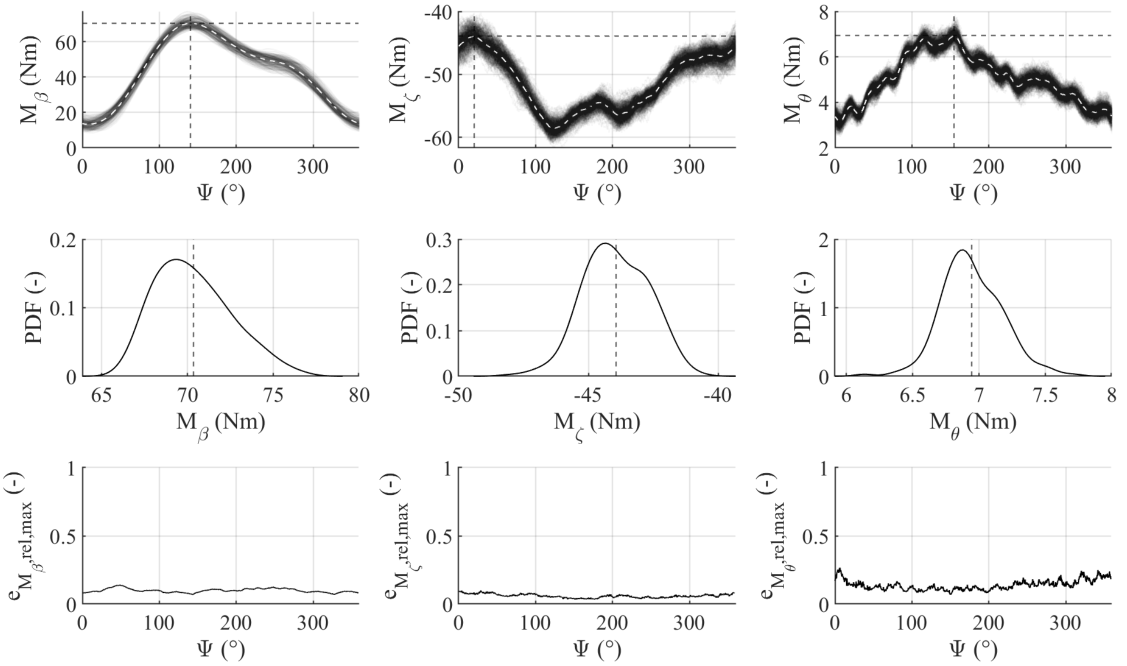

Figure B.59: Probability density function and maximum relative deviations of the blade root moments for 14 ± 5° and 1200 RPM

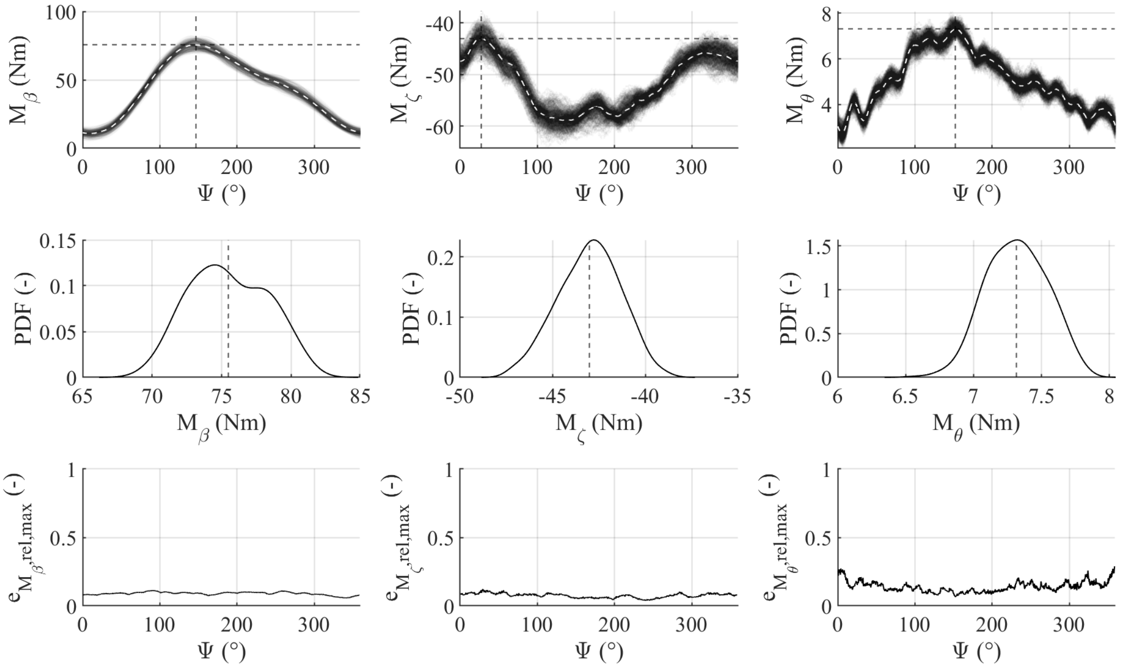

Figure B.60: Probability density function and maximum relative deviations of the blade root moments for 14 ± 6° and 1200 RPM

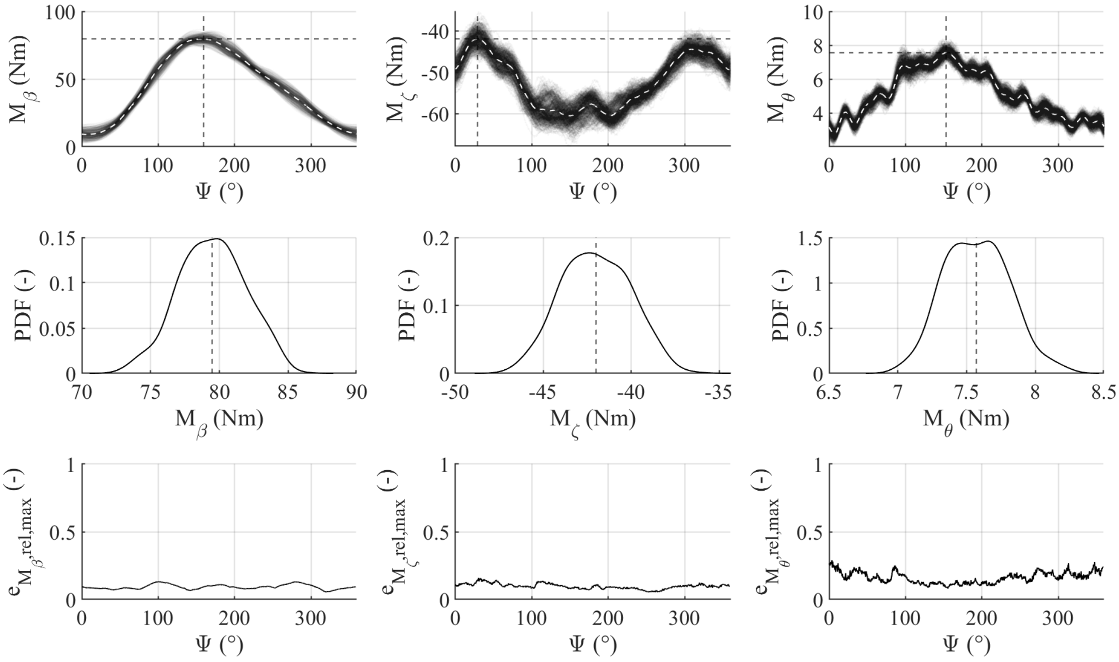

Figure B.61: Probability density function and maximum relative deviations of the blade root moments for 14 ± 7° and 1200 RPM

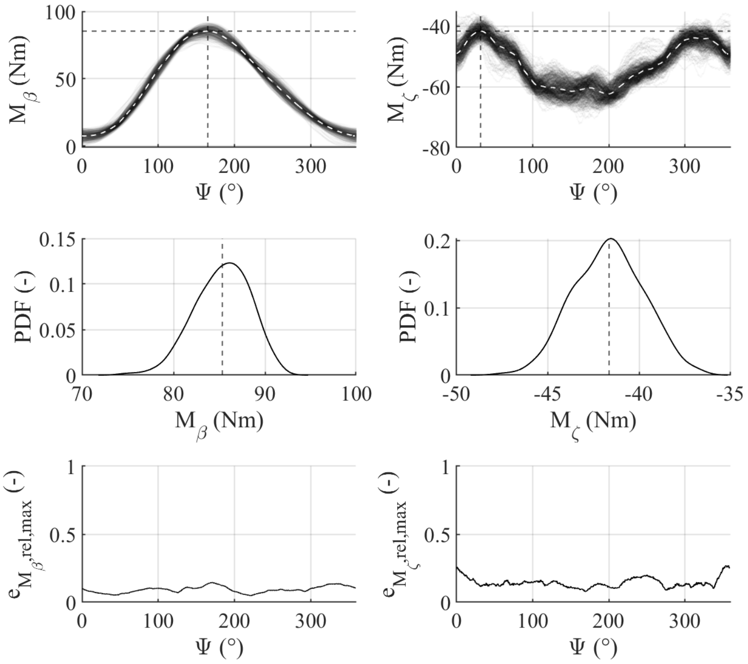

Figure B.62: Probability density function and maximum relative deviations of the blade root moments for 14 ± 8° and 1200 RPM

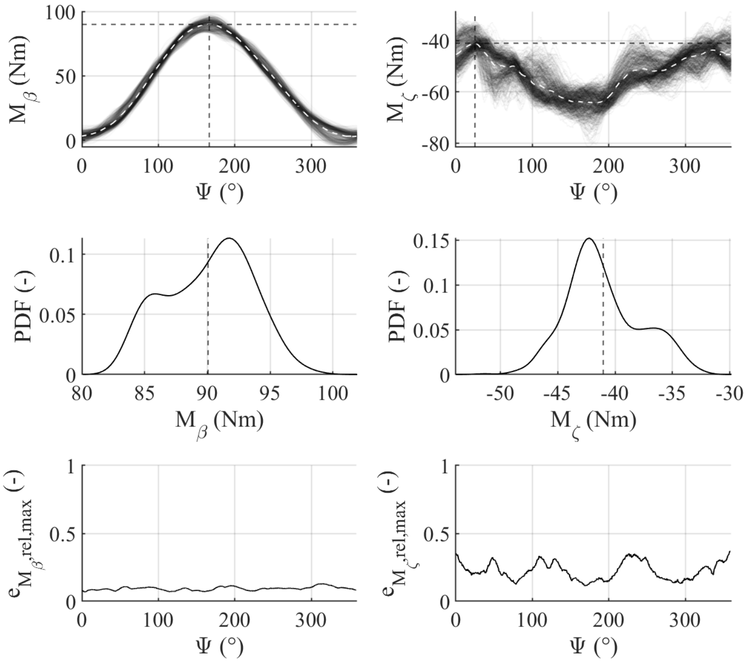

Figure B.63: Probability density function and maximum relative deviations of the blade root moments for 14 ± 9° and 1200 RPM

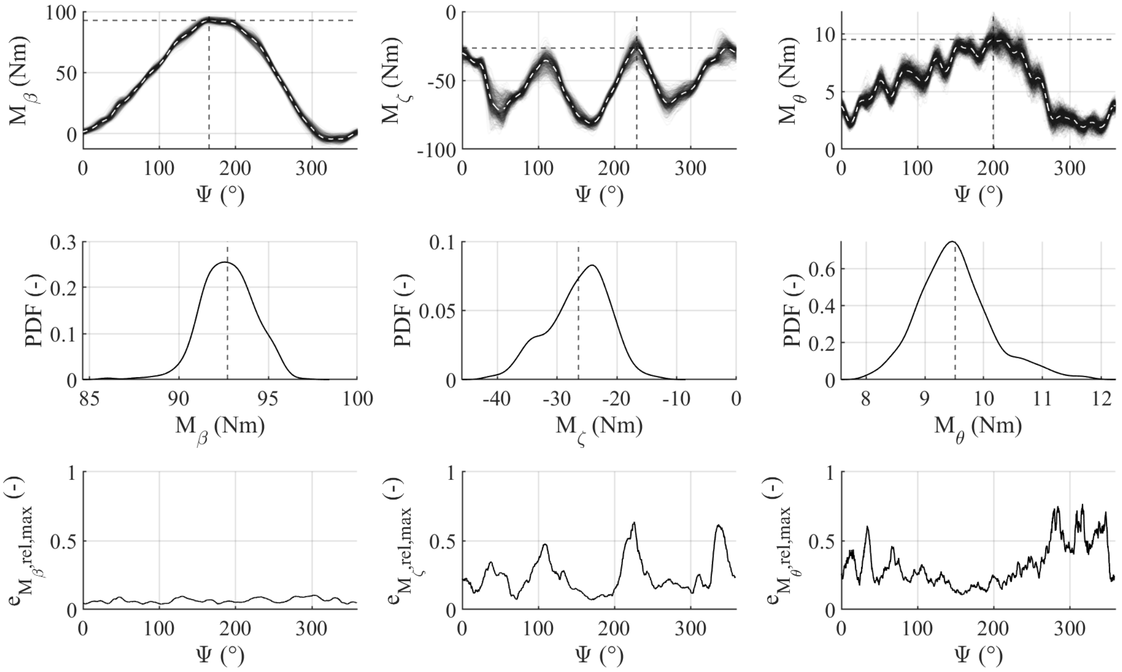

Figure B.64: Probability density function and maximum relative deviations of the blade root moments for 14 ± 10° and 1200 RPM

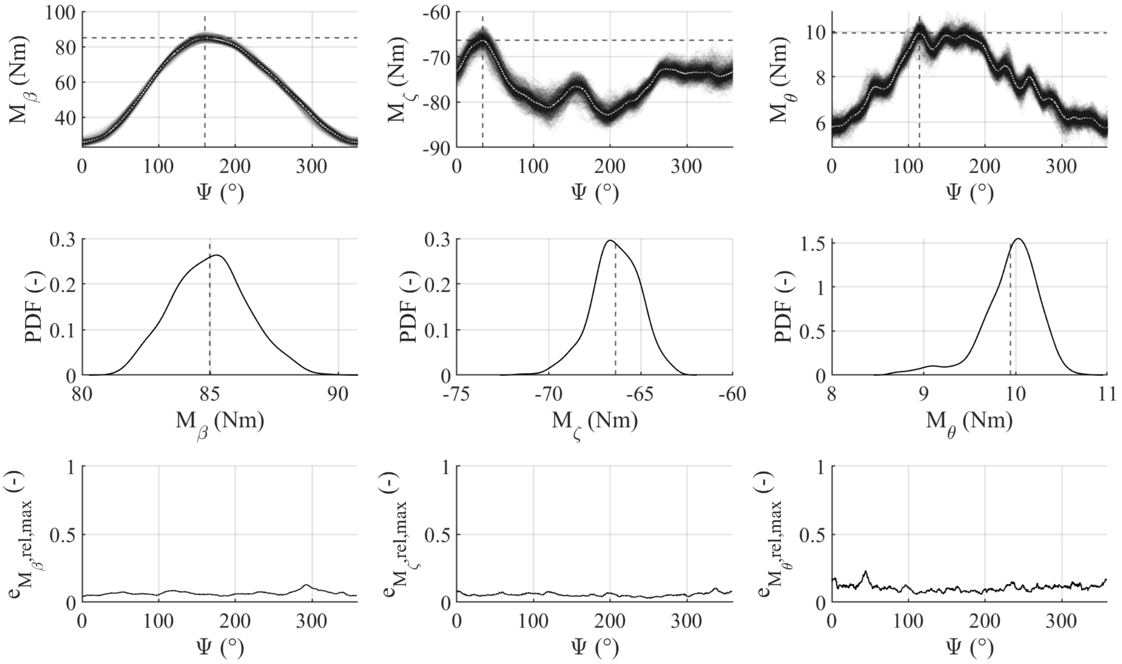

Figure B.65: Probability density function and maximum relative deviations of the blade root moments for 14 ± 4° and 1500 RPM

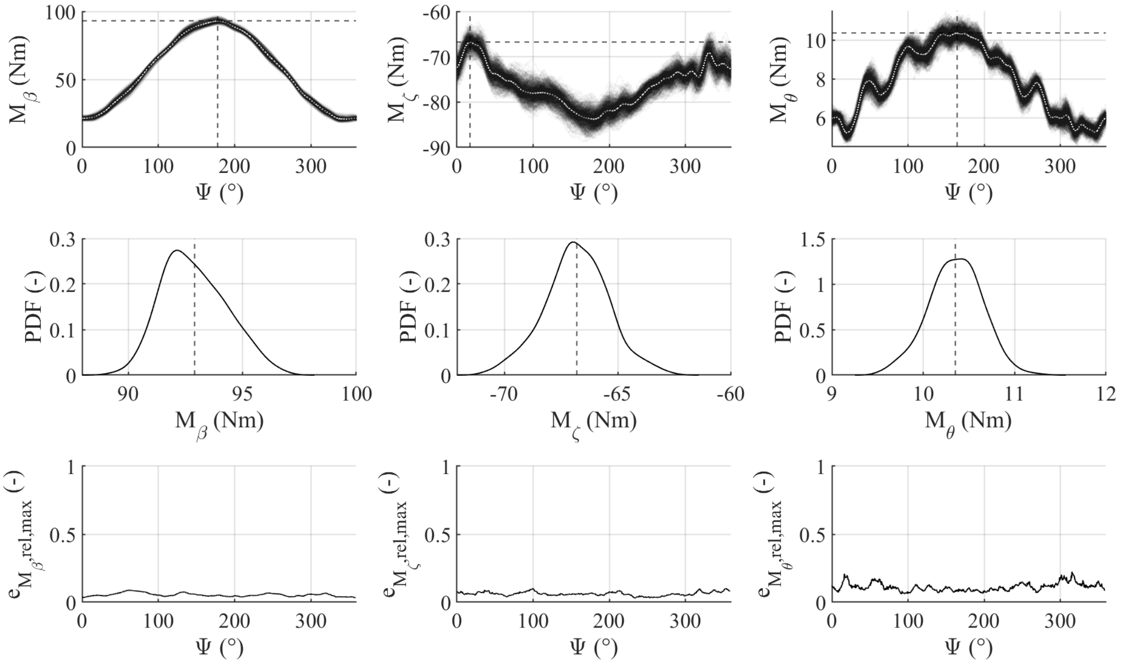

Figure B.66: Probability density function and maximum relative deviations of the blade root moments for 14 ± 5° and 1500 RPM

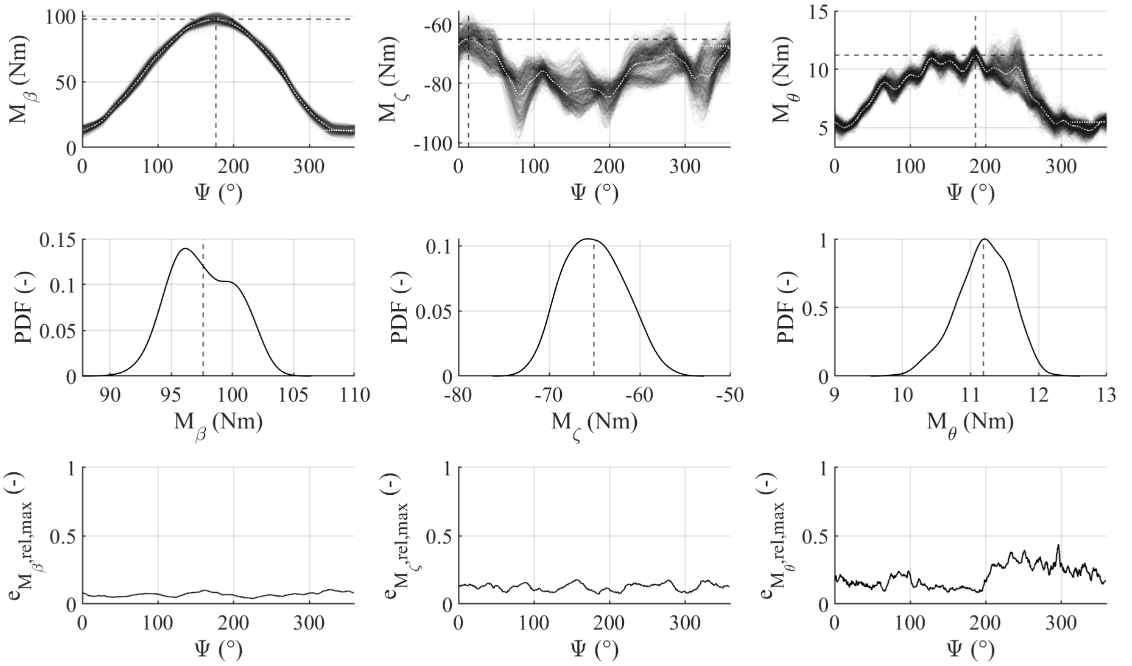

Figure B.67: Probability density function and maximum relative deviations of the blade root moments for 14 ± 6° and 1500 RPM

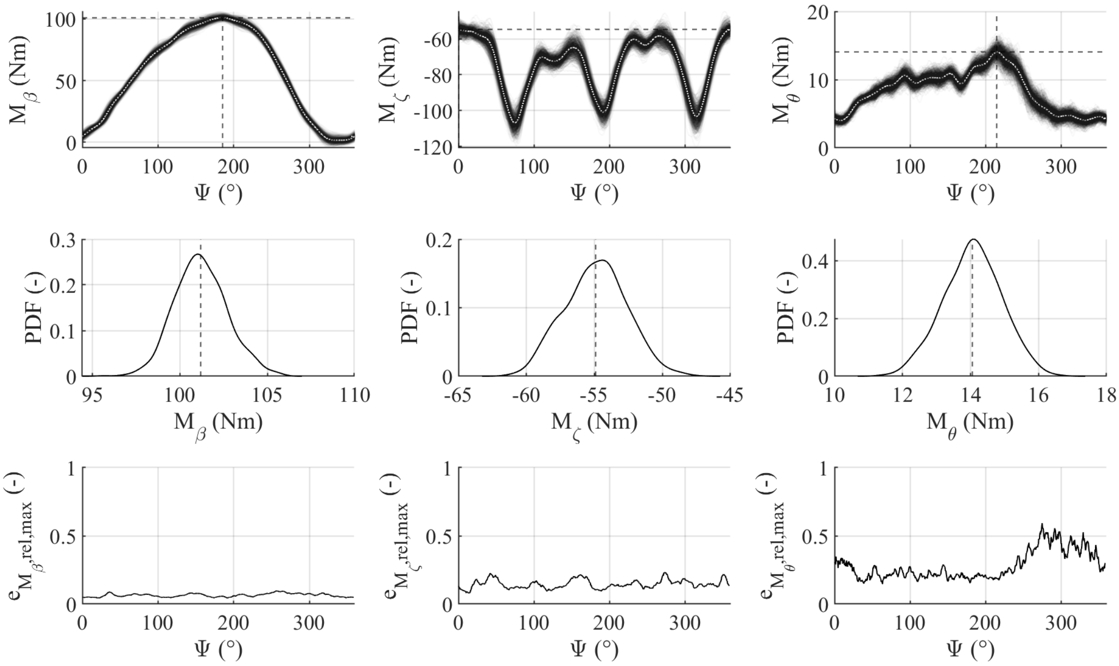

Figure B.68: Probability density function and maximum relative deviations of the blade root moments for 14 ± 7° and 1500 RPM

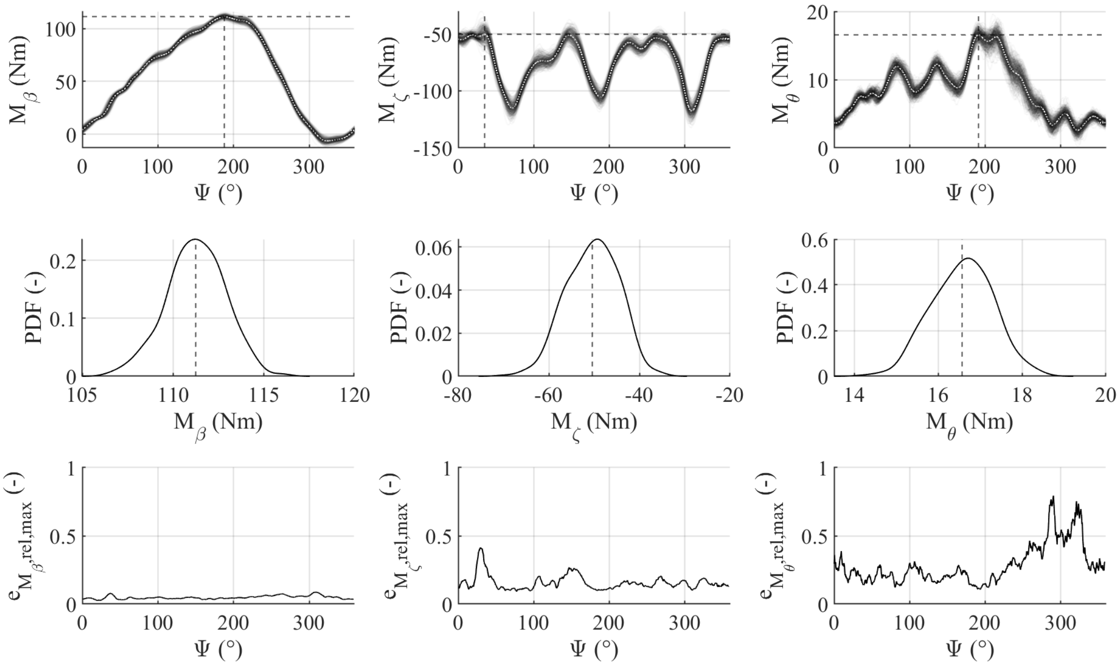

Figure B.69: Probability density function and maximum relative deviations of the blade root moments for 14 ± 8° and 1500 RPM

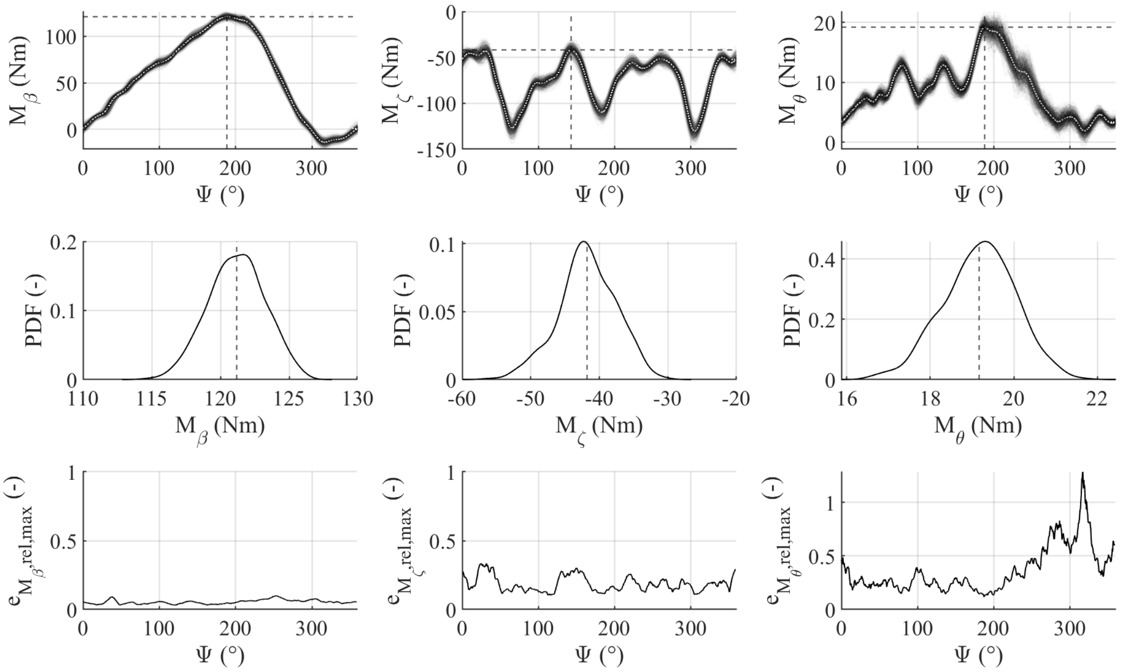

Figure B.70: Probability density function and maximum relative deviations of the blade root moments for 14 ± 9° and 1500 RPM

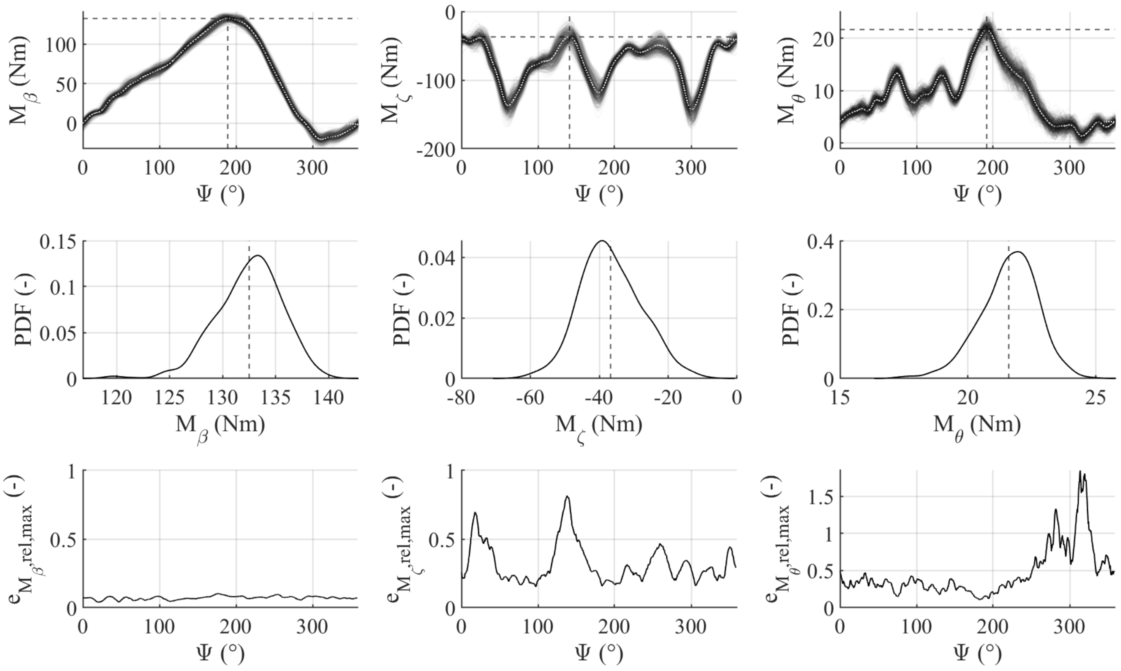

Figure B.71: Probability density function and maximum relative deviations of the blade root moments for 14 ± 10° and 1500 RPM